# Electron Spin Resonance Investigations of Organic Spin Chains and Two-Dimensional Organic Conductors

Von der Fakultät Mathematik und Physik der Universität Stuttgart zur Erlangung der Würde eines Doktors der Naturwissenschaften (Dr. rer. nat) genehmigte Abhandlung


Vorgelegt von

Belal Salameh

geboren in Al Baq'ah, Jordanien


| | |
|---|---|
| Hauptberichter | Prof. Dr. D. Schweitzer |
| Mitberichter | Prof. Dr. M. Dressel |

Tag der mündlichen Prüfung: 13. Juli 2005

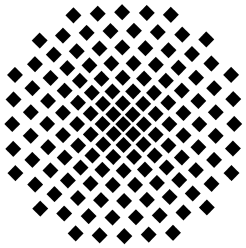


3. Physikalisches Institut der Universität Stuttgart

Juli 2005

# Contents

**Contents**

# Abbreviations and Symbols

| | |
|---|---|
| 1, 2, 3-D | one, two, three dimensional |
| A | acceptor |
| AC | alternating current |
| AFE | antiferroelectric |
| AFM | antiferromagnetic |
| AFMR | antiferromagnetic Resonance |
| AO | anion ordering |
| BEDT-TTF | bisethylenedithio-tetrathiafulvalene [$(CH_2)_4C_6S_8$] |
| BCS | Bardeen, Cooper and Schrieffer (theory) |
| CD | charge disproportionation |
| CDW | charge density wave |
| CGS | centimetre-gram-second (units system) |
| CO | charge order |
| CW | continuous wave |
| $d_1$ | intradimer distance |
| $d_2$ | interdimer distance |
| D | donor |
| DC | direct current |
| DI-DCNQI | 2,5-diiodo-dicyanoquinonediimine |
| DPPH | 1,1-diphenyl- 2-picryl- hydrazyl |
| $E_a$ | activation energy |
| EAT-model | Eggert, Affleck and Takahashi-model |
| EPR | electron paramagnetic resonance |
| ESR | electron spin resonance |
| FE | ferroelectric |
| FMR | ferromagnetic Resonance |

**Abbreviations and Symbols**

| | |
|---|---|
| g | g-value |
| $g_1$, $g_2$, $g_3$ | components of the g-tensor ($g_1$: maximum, $g_2$: intermediate and $g_3$: minimum) |
| $H_1$ | microwave magnetic field |
| $H_o$ | static magnetic field |
| HOMO | highest occupied molecular orbitals |
| HWHM | half width at half maximum |
| J | antiferromagnetic exchange constant |
| $J_1$ | intradimer antiferromagnetic exchange constant |
| $J_2$ | interdimer antiferromagnetic exchange constant |
| $k_F$ | Fermi wave vector |
| Loc | localized state |
| MF | mean field (theory) |
| NMR | nuclear magnetic resonance |
| $P_{abs}$ | absorbed microwave power |
| PP | peak-to-peak |
| $q_{AO}$ | anion ordering wave vector |
| Q-factor | quality factor |
| SC | superconductivity |
| SDW | spin density wave |
| SI | international system (units system) |
| SOMO | single occupied molecular orbital |
| SP | spin-Peierls |
| SQUID | superconducting quantum interference device |
| $T_1$ | spin lattice relaxation time |
| $T_2$ | spin spin relaxation time |
| $t_a$, $t_b$, $t_c$ | transfer integrals |
| $T_{AO}$ | anion ordering transition temperature |
| $T_c$ | superconducting transition temperature |
| TCNQ | tetracyanoquinodimethane |

| | |
|---|---|
| $T_{CO}$ | charge ordering transition temperature |
| TE | transverse electric (cavity mode) |
| THF | tetrahydrofurane |
| TMTSF | tetramethyltetraselenafulvalene $[(CH_3)_4C_6Se_4]$. |
| TMTTF | tetramethyltetrathiafulvalene $[(CH_3)_4C_6S_4]$. |
| TMTCF | TMTSF and TMTTF |
| $T_N$ | antiferromagnetic transition temperature (Neel temperature) |
| $T_{SP}$ | spin Peierls transition temperature |
| TTF | Tetrathiofulvalene |
| TTF-TCNQ | tetrathiafulvalene tetracyanoquinodimethane |
| $T_\rho$ | localization temperature |
| $t_\parallel$ | transfer integral parallel to the highest conduction direction |
| $t_\perp$ | transfer integral perpendicular to the highest conduction direction |
| U | on-site Coulomb repulsion |
| V | inter-site Coulomb repulsion |
| $V_c$ | critical inter-site Coulomb repulsion |
| $\gamma$ | alternation parameter |
| $\Delta g$ | g-shift (g-2.002319) |
| $\Delta H$ | ESR linewidth (half width at half maximum) |
| $\Delta H_{CO}$ | ESR linewidth induced by the charge ordering |
| $\Delta H_{pp}$ | ESR linewidth (peak to peak) |
| $\Delta_\rho$ | localization energy gap |
| $\Delta_\sigma$ | singlet triplet energy gap |
| $\varepsilon'$ | dielectric constant |
| $\lambda_{SO}$ | spin-orbit coupling constant |
| $\rho_a, \rho_b, \rho_c$ | electrical resistivity along a, b and c-axes |
| $\rho_{rt}$ | electrical resistivity at room temperature |
| $\rho_\parallel$ | electrical resistivity parallel to the conduction plane |
| $\rho_\perp$ | electrical resistivity perpendicular to the conduction plane |
| $\sigma$ | electrical conductivity |

**Abbreviations and Symbols**

| | |
|---|---|
| $\tau_{\parallel}$ | on-chain scattering time |
| $\tau_{\perp}$ | interchain tunnelling time |
| $\chi_{core}$ | spin susceptibility due to the core electrons |
| $\chi_s$ | spin susceptibility |
| $(\chi_s)_p$ | spin susceptibility at constant pressure |
| $(\chi_s)_v$ | spin susceptibility at constant volume |

# Kurzfassung

Das Phänomen korrelierter Elektronen in niedrigdimensionalen Festkörpern stellt eine der großen Herausforderungen der modernen Physik dar. Elektronische Korrelationen sind insbesondere in niedrigdimensionalen Festkörpern relevant. Abhängig von der Bandfüllung und der Stärke der Korrelationen, gibt es niedrigdimensionale Supraleiter mit neuartigen symmetriebrechenden Eigenschaften, Metalle, Halbleiter und Isolatoren. Sowohl das quasi eindimensionale Metall (TMT*C*F)$_2$X (*C*=S, Se) als auch das quasi zweidimensionale Metall (BEDT-TTF)$_2$X werden derzeit als Beispiele für niedrigdimensionale Systeme korrelierter Elektronen angesehen. Diese organischen Leiter gehören zu einer Kategorie von Kristallen, in denen große organische Moleküle in Ketten oder Lagen arrangiert sind und die somit niedrigdimensionale Systeme darstellen. Sie sind schon für sich genommen wissenschaftlich interessant, man erhofft sich jedoch auch, dass man aus den gewonnenen Erkenntnissen auch Fortschritte im Verständnis von Hochtemperatursupraleitern erzielt. Dies gründet darauf, dass die Phasendiagramme der Hochtemperatursupraleiter und der niedrigdimensionalen organischen Leiter viele Ähnlichkeiten aufweisen. Basierend auf den fortschreitenden Erkenntnissen über die elektronischen Phasen dieser Materialien können systematisch hochkorrelierte niedrigdimensionale Systeme erforscht werden.

Die Ladungstransfersalze der Zusammensetzung (TMTTF)$_2$X sind quasi-eindimensionale organische Leiter, die in Abhängigkeit von dem Anion X oder des externen Drucks p unterschiedliche Grundzustände besitzen, beispielsweise Spin-Peierls, kommensurable und inkommensurable Spindichtewellen (SDW) sowie unter hohen externen Druck Supraleitung. Bei Temperaturen unterhalb von 300 K sind diese Verbindungen Halbleiter mit Spinlokalisation auf den TMTTF-Dimeren. Der isolierende Grundzustand bei tiefen Temperaturen wird als Mott-Hubbard-Isolator angesehen.

In (TMTTF)$_2$PF$_6$, (TMTTF)$_2$AsF$_6$ und (TMTTF)$_2$SbF$_6$ wurde vor kurzem ein neuartiger Phasenübergang entdeckt: bei Temperaturen von ca. 100 K Ladungsordnung beobachtet, welche zu einer Ungleichverteilung der Ladungsträger entlang der molekularen Stapelrichtung führt [1,2]. Der Zustand der Ladungsträgerordnung ist ein ferroelektrischer Grundzustand [1]. Experimentelle und theoretische Arbeiten der zurückliegenden Jahre zeigten, dass Ladungsordnung

in einer Reihe ein- und zweidimensionaler organischer Ladungstransfersalze auftritt. Experimente wie NMR [3,4,5], Messungen der dielektrischen Permittivität [1,4,5] und der optische Reflektivität [6] wurden an den Verbindungen $(TMTTF)_2X$ (X = $SbF_6$, $AsF_6$, $BF_4$ und SCN) durchgeführt, um die Spin- und Ladungsordnungsphänomene zu erforschen. Es liegen bis jetzt jedoch noch keine systematischen Elektronenspinresonanz (ESR)-Messungen der Ladungsordnung in den obengenannten Salzen vor. Dabei ist eine verlässliche ESR-Studie, insbesondere besonders des neuen Ordnungszustandes, dringend erforderlich.

In dieser Arbeit wird eine detaillierte ESR- und SQUID-Studie vorgestellt, die an Einkristallen der $(TMTTF)_2X$-Salze durchgeführt wurde und deren Schwerpunkt auf der Untersuchung der Spin- und Ladungsordnung liegt. Ebenso werden die Transport- und die magnetischen Eigenschaften des quasi-zweidimensionalen organischen Supraleiters $\Theta$-$(BEDT\text{-}TTF)_2I_3$ und des neu synthetisierten organische Leiter $(BEDT\text{-}TTF)_2(B_{12}H_{12})(CH_2Cl_2)$ vorgestellt und diskutiert. Diese wurden durch ESR-, SQUID- und Gleichstromwiderstands-Messungen ermittelt.

Alle ESR-Spektren wurden mit einem Bruker ESP 300 X-Band-Spektrometer bei einer Arbeitsfrequenz von 9,5GHz aufgenommen. Für alle ESR-Messungen waren relativ kleine Einkristalle für ein gutes Signal-Rausch-Verhältnis ausreichend. Um die Messungen in einem Temperaturbereich von 300K bis 4,2K durchzuführen wurde ein Helium-Durchflusskryostat verwendet. Die Messungen über den gesamten Temperaturbereich erfolgten für jeden Kristall derart, dass das statische Magnetfeld jeweils parallel zu einer der drei Kristallachsen anlag. Für orientierungsabhängige Messungen wurden die Einkristalle bei einer festen Temperatur mit Hilfe eines Goniometers um die jeweilige Kristallachse gedreht. Zur Berechnung der Linienbreite und des Resonanzfeldes wurde die Least-Square-Methode auf die ESR-Spektren angewendet. Um den g-Faktor zu bestimmen, wurde das gemessene Resonanzfeld mit dem von DPPH verglichen. Die DC magnetische Suszeptibilität der Proben wurde mit einem Quantum Design SQUID Magnetometer gemessen. Anschließend wurde die Spinsuszeptibilität durch Subtraktion der diamagnetischen Suszeptibilität der inneren Elektronen aus dem Messwert bestimmt. Die Gleichstromleitfähigkeit wurde mit Hilfe einer 4-Punkt-Standardmessung bestimmt, wobei die Kristalle in diesem Fall über Golddrähte mit einem Durchmesser von 25µm und Kohlenstoff-Leitlack kontaktiert wurden.

Die Spinsuszeptibilitäten bei konstantem Volumen $(\chi_s)_v$ der vier untersuchten Salze können für Temperaturen T >100K mit den Modellen von Bonner und Fisher [7] bzw. Eggert, Affleck und Takahashi (EAT) [8] für eine antiferromagnetische (AFM) S=1/2 Heisenberg-Spinkette beschrieben werden. Die Werte für die AFM

Austauschkonstante |J|, welche mit Hilfe von numerischen Fits von $(\chi_s)_v$(T) nach dem EAT-Modell bestimmt wurden, sind 400K, 410K, 430K bzw. 460K für $(TMTTF)_2X$, X=$SbF_6$, $AsF_6$, $BF_4$ bzw. SCN. Die Werte für $(\chi_s)_v$ aller untersuchten Verbindungen weichen unterhalb 100K vom EAT-Modell ab, dort wird die gemessene Suszeptibilität kleiner als die theoretischen Werte. Diese Abweichung kann auf die Kopplung zwischen den Spinketten zurückgeführt werden. Diese Kopplung wird durch das Zwischenketten-Transferintegral $t_b$ beschrieben, welches in dem Fall von $(TMTTF)_2X$ $t_b \approx 12meV \approx 130K$ beträgt. Die Konsequenz davon ist, dass die $(TMTTF)_2X$-Salze unterhalb 130K ein zunehmend zweidimensionales Leitungsverhalten aufweisen und die Spinsuszeptibilität im quasi-zweidimensionalen Fall kleiner wird.

Im paramagnetischen Bereich bei höheren Temperaturen wurde festgestellt, dass die g-Faktoren und die ESR Linienbreiten $\Delta H$ aller untersuchten $(TMTTF)_2X$-Salze eine charakteristische Anisotropie aufweisen. Die größten Linienbreiten und g-Faktoren wurden bei statischem Magnetfeld $B_0$ parallel zur c*-Richtung beobachtet. Diese liegt parallel zur Längsachse der TMTTF-Moleküle. Senkrecht zur Molekülebene, entlang der a-Richtung, traten die kleinsten Linienbreiten und g-Faktoren auf. Es folgt also $g_{c*}>g_{b'}>g_a$ sowie $\Delta H_{c*}>\Delta H_{b'}>\Delta H_a$. Die Anisotropie der g-Faktoren wird durch die Anisotropie der Spin-Bahn-Kopplung hervorgerufen. Aufgrund der Symmetriebeschränkung dieser Materialien weisen die Linienbreiten dasselbe anisotrope Verhalten wie die g-Faktoren auf, da die Spin-Bahn-Streuung entlang der Stapelrichtung deutlich kleiner ist als diejenige zwischen den Stapeln. Dies beruht darauf, dass die Spin-Bahn-Wechselwirkung keine elektronischen Übergänge innerhalb von Stapeln, die aus denselben und identisch orientierten punktsymmetrischen Molekülen bestehen, verursachen können.

Die ESR-Linienbreiten nehmen bei den TMTTF-Salzen im paramagnetischen Bereich bei Temperaturerniedrigung ab, während die g-Faktoren temperaturunabhängig sind. Es wurde bei den hier untersuchten Kristallen ein linearer Abfall der Linienbreite mit der Temperatur im Bereich höherer Temperaturen (300-180K) beobachtet, und dies entlang aller drei Kristallachsen. Dabei besitzt der Verlauf von $\Delta H(T)$ entlang c* die größte, entlang a die kleinste Steigung. Bei linearer Extrapolation der Messwerte zu niedrigen Temperaturen hin kreuzen sie sich alle im negativen Temperaturbereich bei einer Temperatur $T_0$, die zwischen –120 und –150K liegt. Der lineare Abfall der Linienbreiten im paramagnetischen Bereich bei Temperaturabsenkung scheint eine generelle Eigenschaft dieser Klasse von Verbindungen zu sein. Die physikalische Bedeutung der negativen Temperatur $T_0$ ist jedoch noch nicht verstanden.

**Kurzfassung**

Die Linienbreiten nehmen in $(TMTTF)_2AsF_6$ und $(TMTTF)_2SbF_6$ unterhalb der Ladungsordnungstemperatur $T_{CO}$ langsamer ab, und nehmen in $(TMTTF)_2SCN$ unterhalb von $T_{CO}$ sogar zu. $T_{CO}$ liegt für die Verbindungen in obiger Reihenfolge bei 103K, 156K und 160K. Ebenso ändert sich unterhalb $T_{CO}$ die Anisotropie der Linienbreiten, wobei es Unterschiede zwischen den Salzen mit punktsymmetrischen Anionen ($AsF_6$, $SbF_6$) und dem nicht-punktsymmetrischen Anion SCN gibt: Im ersten Fall gilt $\Delta H_{c*} > \Delta H_{b'} > \Delta H_a$, für SCN jedoch $\Delta H_{c*} \approx \Delta H_{b'} > \Delta H_a$. Dieses Verhalten wird dem Verlust der Punktsymmetrie unterhalb $T_{CO}$ zugeschrieben, wie bereits mit Kernspinresonanzexperimenten (NMR) [3] und durch Messungen der dielektrischen Permittivität [1,4,5] gezeigt wurde. Da das Symmetriezentrum der TMTTF-Moleküle entlang der Ketten unterhalb $T_{CO}$ verloren geht, erwartet man eine Zunahme der Elektronenstreuung und dadurch eine Zunahme und Änderung der Anisotropie der ESR-Linienbreiten. Es wurde festgestellt, dass die Linienverbreiterung durch Ladungsträgerordnung in $(TMTTF)_2SbF_6$ eine größere Rolle spielt als in $(TMTTF)_2AsF_6$, was auf einen höheren Grad an Ladungs-Ungleichverteilung im Fall von $(TMTTF)_2SbF_6$ hindeutet. Diese Erkenntnis bestätigt bisherige Ergebnisse aus der NMR [2,3].
Die Winkelabhängigkeit bzw. Abhängigkeit der Linienbreiten und der g-Faktoren von den drei Kristallachsen bei den $(TMTTF)_2X$-Salzen kann im gesamten Temperaturbereich durch folgende Beziehungen beschrieben werden:

$$\Delta H(\theta) = \left[ \Delta H_{\min}^2 \cos^2(\theta) + \Delta H_{\max}^2 \sin^2(\theta) \right]^{1/2} \quad (1)$$

$$g(\theta) = \left[ g_{\min}^2 \cos^2(\theta) + g_{\max}^2 \sin^2(\theta) \right]^{1/2} \quad (2)$$

Hierbei ist θ der Winkel zwischen dem statischen Magnetfeld $B_0$ und den kristallinen Achsen, entlang derer die minimalen Linienbreiten und g-Faktoren beobachtet werden. $\Delta H_{min}$ und $g_{min}$ sind die Linienbreiten bzw. g-Werte entlang der a-Achse im Falle einer orientierungsabhängigen Messung in der ab′- bzw. der ac*-Ebene, für den Fall der b′c*-Ebene sind dies die entsprechenden Werte parallel zur b′-Richtung. $\Delta H_{max}$ sowie $g_{max}$ sind die Werte in c*-Richtung für eine orientierungsabhängigen Messung in der b′c*- und der ac*-Ebene und parallel zur b′-Achse bei einer Messung in der ab′-Ebene.
Charakteristische Veränderungen in den Orientierungsabhängigkeiten der Linienbreiten in der ab′-Ebene treten in der Ladungsordnungsphase der $(TMTTF)_2SbF_6$- und $(TMTTF)_2AsF_6$-Salze auf: es bilden sich dort zwei Maxima bei 45° und 135° aus, während oberhalb $T_{CO}$ ein Maximum bei 90° beobachtet wird. Die beiden

Maxima sind bei tiefen Temperaturen stärker ausgeprägt. Bei den tiefsten gemessenen Temperaturen kann die Winkelabhängigkeit durch Gleichung (3) angenähert werden.

$$\Delta H_{\text{doubling}}(\theta) = \left[ \Delta H^2(a)\cos^2(2\theta) + \Delta H^2(45^\circ)\sin^2(2\theta) \right]^{1/2} \qquad (3)$$

Hierbei sind ΔH(a) bzw. ΔH(45°) die Linienbreiten in a-Richtung bzw. entlang der Winkelhalbierende zwischen a- und b′-Richtung. θ ist der Winkel zwischen der a-Achse und der Feldrichtung von $B_0$. Für Temperaturen, die etwas unterhalb von $T_{CO}$ liegen, ist die Orientierungsabhängigkeit der Linienbreiten durch eine Kombination der Gleichungen 1 und 3 beschreibbar. Das bedeutet, dass ein neuartiger Streuprozess unterhalb $T_{CO}$ existiert, der eine Verdopplung der Periodizität des Orientierungsschemas der Linienbreiten entlang der ab′-Ebene hervorruft. Dies gilt für Kristalle mit punktsymmetrischem Anionen. Die Verdopplung der Periodizität der Orientierungsabhängigkeit könnte durch die Koexistenz zweier ungleichartiger magnetischer TMTTF-Gitterplätze verursacht werden, die im Ladungsordnungsbereich mit NMR bereits nachgewiesen wurden [2,3,9].

Mit weiter abnehmender Temperatur beobachtet man eine stärkere Zunahme der ESR-Linienbreite sobald die Temperatur in die Nähe der AFM-Ordnungstemperatur kommt, und zwar in den Verbindungen $(TMTTF)_2SbF_6$ und $(TMTTF)_2SCN$. Dieses kritische Verhalten von ΔH ist ein Kennzeichen für den magnetischen Charakter der antiferromagnetischen Ordnung. In diesem Regime ist die Linienbreite proportional zu $(T - T_N)^{-(3-d/2)}$ , wobei d die Dimensionalität der antiferromagnetischen Fluktuationen und μ = 3 − d/2 der kritische Exponent ist. Der experimentell bestimmte Wert von μ =1,5 in $(TMTTF)_2SCN$ bestätigt den 3D Charakter der antiferromagnetischen Fluktuationen. Überraschenderweise findet man in $(TMTTF)_2SbF_6$ μ = 0,5; dieser Unterschied kann durch eine unterschiedliche Anisotropie des Spinfreiheitsgrades zustande kommen, ebenso kommen aber auch unterschiedliche relative Größenordnungen der Dipol-Dipol-Wechselwirkungen und Spin-Bahn-Kopplung in Betracht. In $(TMTSF)_2NO_3$ wurde ein ähnliches Verhalten beobachtet [10].

Die Spinsuszeptibilität von $(TMTTF)_2AsF_6$ fällt unterhalb $T_{SP}$ = 13K stark ab. In diesem Temperaturbereich kann die Spinsuszeptibilität mit dem Bulaevskii-Modell für alternierende Spinketten beschrieben werden [11]. Mit diesem Fit erhält man den Alternierungsparameter $\gamma = J_2/J_1 = 0{,}94$, die intradimere antiferromagnetische Austauschkonstante $|J_1| = 423\,\text{K}$ und die interdimere antiferromagnetische Austauschkonstante $|J_2| = 397\,\text{K}$. Die Singulett-Triplett-Energielücke im T = 0 K-

Grenzfall, $\Delta_\sigma(0)$, kann über $\Delta(0)=0{,}8615\left|J\right|\delta^{2/3}=34{,}8\,\mathrm{K}$ nach [12] berechnet werden. Der Wert des Verhältnisses zwischen der Singlet-Triplett-Energielücke und $T_{SP}$, welcher in Störungstheorie zweiter Ordnung berechnet wurde [12], beträgt $\Delta_\sigma(0)/T_{SP}=2{,}47$. Dieser Wert ist in gute Übereinstimmung mit dem experimentellen Resultat $\Delta_\sigma(0)/T_{SP}=2{,}67$ für $(TMTTF)_2AsF_6$. Unterhalb der Anionenordnung in $(TMTTF)_2BF_4$ ($T_{AO}$ = 41 K) tritt zunächst ein sprungartigen Abfall und dann eine exponentieller Abnahme der Spinsuszeptibilität mit fallender Temperatur auf. Der sprungartige Abfall ist darauf zurückzuführen, dass die Ordnung der nicht punktsymmetrischen Anionen in eine Superstruktur, welche zu einer Dimerisierung der Spinkette führt, ein Phasenübergang 1. Ordnung ist. Die Spinsuszeptibilität bei konstantem Volumen kann unterhalb $T_{AO}$ wiederum mit dem Bulaevskii-Modell für alternierende Spinketten [11] beschrieben werden. Die Fitparameter sind: $\gamma=0{,}90$, $\left|J_1\right|=$ 452,6 K $\left|J_2\right|=$ 407,4 K. Die Singulett-Triplett-Anregungsenergie beträgt $\Delta_\sigma=52{,}0$ K.

An mehreren Kristallen des organischen Supraleiters Θ-$(BEDT\text{-}TTF)_2I_3$ wurde der Gleichstromwiderstand in einem Temperaturbereich von Raumtemperatur bis hinab zu 1,6 K gemessen. Der spezifische Widerstand lag bei Raumtemperatur typischerweise bei $0{,}04\,\Omega\cdot\mathrm{cm}$ entlang der leitenden Ebene, bei 4K lag er bei $8\times10^{-5}\,\Omega\cdot\mathrm{cm}$. Das Verhältnis der spez. Widerstände ρ(300 K) / ρ(4 K) ≈ 500 deutet auf die hohe Qualität der Θ-$(BEDT\text{-}TTF)_2I_3$-Kristalle hin. Der spezifische Widerstand nimmt bei Temperaturerniedrigung von Raumtemperatur an bis zur Übergangstemperatur zur Supraleitung $T_c$=3,6K stetig ab. Dort fällt der Widerstand sehr stark ab. Bei hohen Temperaturen ist die Spinsuszeptibilität temperaturunabhängig, wie dies für die Pauli-Spinsuszeptibilität von Metallen zu erwarten ist. Das es sich bei der Supraleitung um eine Volumenerscheinung handelt, wurde mit der Beobachtung des Abschirmungssignals durch das Herausdrängen des magnetischen Flusses im supraleitenden Zustand nachgewiesen. Die Proben, die noch einen Restwiderstand zeigten, wiesen im gesamten Temperaturbereich eine von der Temperatur unabhängige Spinsuszeptibilität auf. Der Übergang zur Supraleitung trat in etwa 30% der untersuchten Kristalle auf. Das Anisotropieverhältnis beträgt $\rho_\perp/\rho_\parallel=500$ bei Raumtemperatur, dabei bezeichnet $\rho_\perp$ den spezifischen Widerstand senkrecht und $\rho_\parallel$ den spez. Widerstand parallel zur leitenden Ebene. Diese Werte deuten auf das stark zweidimensionale Leitungsverhalten der Kristalle hin.

Im Raumtemperaturspektrum der ESR werden eine dysonförmige Linien beobachtet, wenn die magnetische Komponente des Mikrowellenfeld senkrecht zur leitenden ab-Ebene zeigt. Diese Linieform entsteht durch die Abschirmung des elektrischen

Wechselfeldes durch Leitungselektronen, d.h. den Skineffekt, was zu einer Beimischung eines dissipativen Anteils zur Mikrowellenabsorption führt. Die Dyson-Form bei Raumtemperatur wurde ausschließlich in dieser speziellen Orientierung gefunden. Entlang der anderen Orientierungsrichtungen wurden bei Raumtemperatur symmetrische Lorentzlinien festgestellt. Die Lorentz-Linienform geht schrittweise in eine Dyson-Form über, sobald durch Temperaturerniedrigung die Leitfähigkeit zunimmt und damit die Skin-Tiefe abnimmt. g-Wert und Linienbreite sind innerhalb der ac-Ebene anisotrop, dahingegen in der ab-Ebene isotrop. Das Maximum des g-Faktors mit 2,0111 wurde entlang der c-Achse gemessen, das Minimum von 2,0030 innerhalb der ab-Ebene. Das Maximum entspricht der Orientierung des statischen Magnetfeldes entlang der langen Molekülachse (der C = C -Doppelbindung) des BEDT-TTF-Moleküls. Innerhalb der ab-Ebene, in welcher der minimale g-Wert gemessen wurde, besitzen die BEDT-TTF-Moleküle eine Zick-Zack-Struktur. Da der g-Tensor von Θ-$(BEDT\text{-}TTF)_2I_3$-Kristallen axialsymmetrisch ist, kann man nur $g_1 = 2{,}0111$ bestimmen, die Werte $g_2$ und $g_3$ von 2,0030 stellen aufgrund besagter Zick-Zack-Struktur einen Mittelwert dar. Die Anisotropie der g-Faktoren kann anhand des g-Tensors des BEDT-TTF-Kations nachvollzogen werden. Die Winkelabhängigkeit der Peak-to-Peak-Linienbreite ($\Delta H_{pp}$) von Θ-$(BEDT\text{-}TTF)_2I_3$ bei Raumtemperatur (RT) verhält sich qualitativ so wie die g-Faktoren: hier tritt ein Maximum von 81 Oe entlang der c-Achse auf während der Wert innerhalb der ab-Ebene bei 61 Oe liegt. Die Linienbreite nimmt monoton von 82 bzw. 61Oe bei Raumtemperatur auf 9 bzw. 6 Oe bei 20 K ab. Entlang beider Orientierungen nimmt die Linienbreite unterhalb von 20K ab, ebenso die g-Faktoren, die bei höheren Temperaturen temperaturunabhängig sind.

Durch 3 stündiges tempern der Θ-$(BEDT\text{-}TTF)_2I_3$ Einkristalle bei 60-70 °C wurden die getemperten $\Theta_T$-$(BEDT\text{-}TTF)_2I_3$-Kristalle hergestellt. Dadurch änderte sich die ESR-Linienbreite von (81-62) Oe in der Θ-Phase zu (26,7-24,5) Oe in der $\Theta_T$-Phase, abhängig von der Orientierung. Alle vermessenen Kristalle zeigen metallisches Verhalten und einen scharfen Abfall des spezifischen Widerstandes bei ungefähr 5 K. Durch den Abschirmungseffekt in der Suszeptibilitätsmessung konnte nachgewiesen werden, dass unterhalb von 4K das gesamte Volumen supraleitend war. Die unterschiedlichen Übergangstemperaturen in den Gleichstrom- und Suszeptibilitätsmessungen bedeuten, dass bei 5K supraleitende Wege auf der Oberfläche vorliegen und erst unterhalb von 4K Volumensupraleitung vorliegt.

Temperatur- und orientierungsabhängige ESR-Messungen von $\Theta_T$-$(BEDT\text{-}TTF)_2I_3$ wurden entlang der ac-Ebene (magnetischer Mikrowellenfeldvektor $B_1$ parallel zur

leitenden Ebene) durchgeführt. Entlang aller Messrichtungen und in allen Temperaturbereichen wurde eine einzelne Absorptionslinie beobachtet, was darauf hindeutet, dass das gesamte Volumen in die getemperte Phase transformiert wurde. Die ESR-Spektren bei RT zeigen symmetrische Lorentzlinien. Die g-Faktoren liegen zwischen 2,0091 bis 2,0049 und die Linienbreiten zwischen 26,7 Oe bis 24,5 Oe. Die g-Faktoren und Linienbreiten haben dieselbe Orientierungsabhängigkeit, die minimalen bzw. maximalen Werte treten auf, wenn das statische Magnetfeld senkrecht bzw. parallel zur Leitungsebene angelegt wird. Die Lorentzlinie verändert sich zunehmend zu einer Dyson-Linie, wenn die Temperatur unterhalb von etwa 100K weiter erniedrigt wird. Dies ist auf eine signifikante Abnahme der Skin-Tiefe zurückzuführen. Die Linienbreite nimmt mit der Temperatur ab, während die g-Faktoren entlang beider Orientierungsrichtungen temperaturunabhängig sind.
Einkristalle des neuen organischen Leiters $(BEDT\text{-}TTF)_x(B_{12}H_{12})_y(CH_2Cl_2)_z$ wurden mit der elektrochemischen Kristallationstechnik gezüchtet. Die Kristalle konnten anhand der ESR-Linienbreiten bei Raumtemperatur von 1,7 Oe, 13 Oe und 45 Oe drei verschiedenen Phasen zugeordnet werden. Der spezifische elektrische Widerstand der drei Phasen zeigte halbleitendes Verhalten mit unterschiedlichen Anregungslücken. In den drei Phasen misst man Anregungsenergien von $\Delta$ = 0,14, 0,08 und 0,15 eV in obiger Reihenfolge. Für eine Phase, und zwar diejenige mit $\Delta H$ = 1,7 Oe und $\Delta$ = 0,14 eV, wurde mit Hilfe der Röntgenstrukturanalyse die Stöchiometrie zu $(BEDT\text{-}TTF)_2(B_{12}H_{12})(CH_2Cl_2)$ bestimmt. Die Peak-to-Peak-Linienbreite bei Raumtemperatur schwankt bei dieser Verbindung zwischen 1,4 Oe bis 1,8 Oe in Abhängigkeit von der Kristallorientierung. Die entsprechenden g-Werte liegen bei Raumtemperatur zwischen g = 2,0105 und 2,0067. Die Linienbreiten nehmen beinahe linear mit der Temperatur im gesamten Temperaturbereich ab, dagegen sind die g-Faktoren temperaturunabhängig.

# Introduction

Physical properties of low dimensional systems such as surfaces, thin films, multilayers and low-dimensional inorganic and organic conductors are the focus of strong scientific research. Many of those properties are not observed in three dimensional systems, but are exclusive of the reduced dimensionality of those structures. The interest in these materials is related to their high anisotropy, i. e., the electrical conductivity is high along one or two directions, while it is smaller by several orders of magnitude along the perpendicular directions. The anisotropy influences not only the charge transport, but also leads to several kinds of unusual ground states.

One of the main challenges of condensed matter physics is posed by the competition between the kinetic energy of electrons, electron-phonon interactions, magnetic exchange interactions and electron-electron interactions in the low dimensional materials. As a result of this competition a large variety of different phases may occur at low temperatures. Examples are the Kondo-state, non-Fermi liquid states, superconductivity, spin and charge density waves, charge order state and spin-Peierls phase.

Benchmark systems for low-dimensional materials are organic charge-transfer salts, like the quasi-one dimensional salts $(TMTSF)_2X$ and $(TMTTF)_2X$ and the quasi-two dimensional metals from the (BEDT-TTF) family. Organic conductors belong to a class of crystals for which big organic molecules are combined in coupled chains or sheets. These materials yield realizations of low-dimensional solids. The magnetic, electronic properties and the dimensionality of these materials can be easily changed by exchanging the monovalent anion X or by applying external pressure, and therefore the ground states in the phase diagram can be easily tuned.

Electron spin resonance (ESR) spectroscopy is certainly one of the most powerful tools to investigate the magnetic properties and the charge dynamics of the organic conductors. The ESR spectra are observable in the most of the organic conductors, while few “ordinary” metals show detectable ESR signals, even at low temperature. Indeed, this feature results principally from the electronic low dimensionality of these systems which controls the spin-relaxation process. ESR is a major probe not only to investigate the paramagnetic state of these materials but also to probe different magnetic ground states and distinguish between them.

After the theoretical prediction of the charge ordering (CO) transition in the quasi-one dimensional organic conductors, the CO phenomenon in the spin chain compounds $(TMTTF)_2X$ has been investigated experimentally and theoretically. It turned out that the CO exists not only in quasi-1D compounds but also in quasi-2D organic compounds as well. A lot of experimental investigations like NMR, dielectric permittivity and optical reflectivity measurements were performed to study the spin and the charge ordered states of the organic spin chain compounds $(TMTTF)_2X$ (X = $SbF_6$, $AsF_6$, $BF_4$ and SCN). Nevertheless, detailed electron spin resonance studies - especially on the charge ordered state of these compounds - do not exist yet. Therefore, the reliable ESR study - especially of the charge order state - is highly needed.

In previous studies, the magnetic and the transport properties of single crystals of the organic conductor $\Theta$-$(BEDT\text{-}TTF)_2(I_3)_{1-x}(AuI_2)_x$ ($x<0.02$) were reported. It was shown that among several samples few were found to show a superconducting transition and the most not. The reason for the absence of superconductivity in some samples was not understood. Here, the transport and the magnetic properties of the neat quasi-two dimensional organic superconductor $\Theta$-$(BEDT\text{-}TTF)_2I_3$-which have almost identical structural properties as the $\Theta$-$(BEDT\text{-}TTF)_2(I_3)_{1-x}(AuI_2)_x$ crystals - and its tempered phase $\Theta_T$-$(BEDT\text{-}TTF)_2I_3$ are presented and discussed. Also the ESR, the SQUID and the electrical resistivity measurements of the new synthesized organic conductor $(BEDT\text{-}TTF)_2(B_{12}H_{12})(CH_2Cl_2)$ are reported.

The current project is devoted to explore the spin and charge ordered states in the quasi 1-D salts $(TMTTF)_2X$ (X = $SbF_6$, $AsF_6$, $BF_4$ and SCN) by performing detailed electron spin resonance experiments in these states. The second aim of this project is to study the transport and the magnetic properties of the neat organic superconductors $\Theta$- and $\Theta_T$-$(BEDT\text{-}TTF)_2I_3$ by means of ESR, SQUID and dc measurements.

This thesis is divided to six chapters as follow:

**Chapter 1**, the conduction mechanism in the organic conductors and the physical reason of the low dimensionality of these systems is explained. Then the studied materials and some of there properties are introduced.

**Chapter 2**, the physics of low dimensional conductors is introduced and discussed.

**Chapter 3,** the experimental techniques (ESR, the SQUID magnet- meter and the dc resistivity setup) used in this work are introduced and the detailed measurement procedures and results analysis is explained.

**Chapter 4,** the detailed ESR and SQUID measurements of four $(TMTTF)_2X$ salts ($X=SbF_6$, $AsF_6$, SCN and $BF_4$) are reported. In this chapter the general behaviour of these salts in the high temperature region and the low temperature ground state of each salt will be discussed and explained. Detailed measurements in the charge order state of the first three salts will be presented and discussed.

**Chapter 5**, the transport and the magnetic properties of the neat organic superconductor $\Theta$-$(BEDT\text{-}TTF)_2I_3$, its tempered phase ($\Theta_T$-$(BEDT\text{-}TTF)_2I_3$) and the new organic conductor $(BEDT\text{-}TTF)_2(B_{12}H_{12})(CH_2Cl_2)$ investigated by means of ESR, SQUID and dc measurements will be presented and discussed.

**Chapter 6,** the summary of the thesis and the possible future work are presented.

# Chapter 1

# Organic Conductors

Organic conductors are materials made of relatively large molecules which contain carbon often in association with hydrogen, oxygen, sulfur and selenium. These compounds have a considerable value of room temperature electric conductivity $\sigma_{rt} \geq 1 \quad (\Omega \cdot \mathrm{cm})^{-1}$ which can reach the conductivity of a normal metal. Structurally all existing organic conductors can be divided into two groups: organic charge-transfer radical salts, and conducting polymers. In this work we are dealing with the organic conductors from the first group.

The study of organic charge-transfer radical salts has always been intimately associated with low-dimensional physics: compounds involving planer molecules have anisotropic structures and associated anisotropic physical properties. This is one reason why organic conductors can offer a richer palette of properties than the simple metals, and why so much more can be learned from them. It turned out that the electronic properties of organic conductors are extraordinarily sensitive to marginal changes in the molecular structure. Due to this reason, organic conductors exhibit a large variety of behaviors and their properties can easily be tuned over a wide range. This range of structural and electronic properties, all of which can be controlled by the synthetic chemist, has attracted the interest of chemists and physicists alike, and promises to yield more interesting materials in the future.

A major breakthrough in the field of organic conductors came in the 1960's and the 1970's with the discovery of the molecules TCNQ (tetracyanoquinodimathane) and TTF (tetrathiafulvalene), respectively [13,14]. These two molecules were combined in 1973 [15] to form the TTF-TCNQ charge-transfer salts, where electrons are transferred from the TTF molecules (donors) to the TCNQ molecules (acceptors). In this salt the π-orbitals are strongly overlapping along the molecular stacks of the monoclinic structure, while there is only a weak overlap in the perpendicular directions. Thus the charge transport is anisotropic and TTF-TCNQ is a quasi one-dimensional conductor. The promising discovery of a rather large room-temperature conductivity of about 1000 $(\Omega \cdot \mathrm{cm})^{-1}$ in this compound and the increase of the

conductivity by more than one order of magnitude upon cooling to 60 K led to intense search for other conducting organic molecules. In this first generation of the charge-transfer salts, the metallic properties could not be maintained down to low temperatures because of the occurrence of a Peierls metal-insulator phase transition. In such one-dimensional (1-D) conductors this transition is driven by the instability of the electron gas towards the formation of charge-density waves (CDW) at the critical wave vector $2k_F$ ($k_F$ is the Fermi wave vector of the 1-D electron gas). A real break through occurred in 1980 with the discovery of superconductivity in $(TMTSF)_2PF_6$[I] at $T_c = 0.9\,K$ after applying pressure of 6.5 kbar [16], and in $(TMTSF)_2ClO_4$ ($T_c$ =1.4 K) at ambient pressure [17].

## 1.1 Conduction Mechanism in Organic Conductors

Crystalline organic conductors consist normally of donor accepter (D-A) complexes as shown in Figure 1.1. In many charge-transfer salts, each two donor molecules jointly donate an electron to one acceptor molecule to form the salt ($D_2A$). The transfer of one electron from each two donors to one acceptor serves to bind the charge-transfer salt together, and also leaves behind a hole shared between the two donor molecules. This means that the bands formed by the overlap of the donor molecules will be partially filled; leading one to expect that the charge-transfer salt will have metallic conductivity. In order to form the charge transfer radical salt, the donor molecules must be stacked next to each other so that the molecular orbitals overlap [18].

The donor molecules which are the building units of the organic conductors are arranged in linear columns or planer sheets. Thus, the resultant electron transfer and the electrical conduction become anisotropic, namely, the electrical conductivity along a unique crystalline direction is much higher than that in the other directions; such compounds are called quasi one-dimensional (1-D) conductors. In other compounds the conductivity is high in a given plane of the crystal and small perpendicular to the plane; these compounds are called quasi two-dimensional (2-D) conductors. The structure of these compounds determines the dimensionality and the shape of the crystal, where the quasi 1-D conductors normally grow in a needle like form with the highest conductive direction parallel to the long direction of the

[I] TMTSF denotes tetramethyltetraselenafulvalene and has a chemical composition $(CH_3)_4C_6Se_4$.

crystal. The quasi 2-D conductors have normally a plate or a cube shape with high and isotropic conductivity along the large crystal surface.

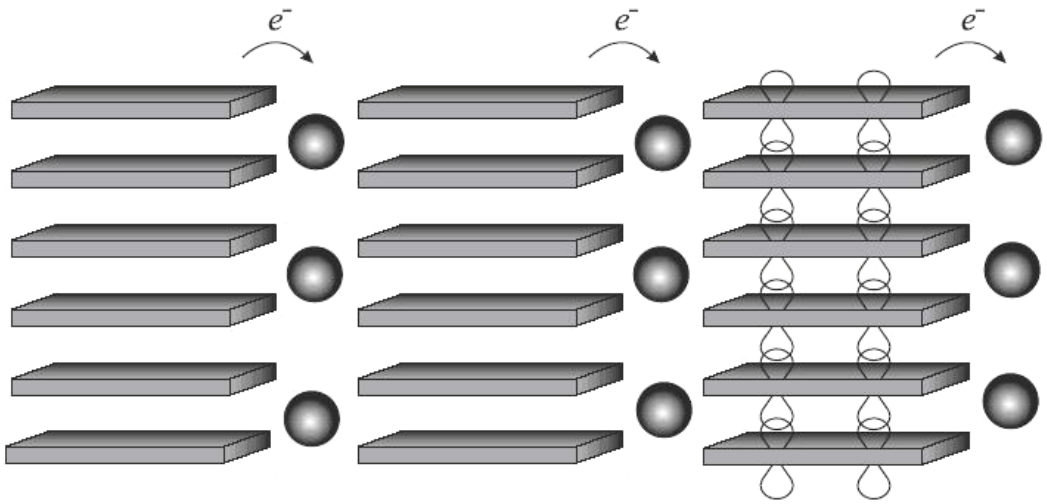


**Figure 1.1: Schematic representation of the charge transfer salt $D_2A$. The donor (cation) planer molecules are packed in stacks alternating with chains of accepter (anion) molecules shown as balls. The intermolecular overlap of π-orbitals between the donor molecules is shown in the right stack, as an example. From Ref. [19].**

This work is devoted to investigate quasi 1-D conductors from the TMTTF[I] family which are called Fabre salts, and the quasi 2-D superconductors Θ-(BEDT-TTF)$I_3$[II] and its tempered phase. In the following, these two types of organic conductors will be introduced.

## 1.2 Fabre Salts

The first $(TMTTF)_2X$ organic conductor was synthesized by J. M. Fabre in the late 1970's [20], where X represents an inorganic monovalent anion like $PF_6^-$, $AsF_6^-$, $SbF_6^-$, $ClO_4^-$, $BF_4^-$, SCN, etc. Bechgaard salts $(TMTSF)_2X$ are the selenium analogous of Fabre salts [21], see Figure 1.2.

[I] TMTTF denotes Tetramethyltetrathiafulvalene and has a chemical composition $(CH_3)_4C_6S_4$.
[II] BEDT-TTF which is know also as ET denotes Bisethylenedithio-tetrathiafulvalene and has a chemical composition $(CH_2)_4C_6S_8$.


**Figure 1.2: The structure of TMT*C*F molecule (*C*=S, Se)**

Both Bechgaard and Fabre charge- transfer salts have a similar structure. In general they are denoted by (TMT*C*F)$_2$X (C=S, Se), where TMTCF is a flat organic molecule. These salts are quasi one-dimensional conductors because of the flat shape of the TMTCF molecule. (TMT*C*F)$_2$X crystals are grown by electrochemical technique as described in the references [20,21].

## 1.2.1 Crystal Structure of Fabre Salts

All (TMTCF)$_2$X salts crystallize in the triclinic $P\bar{1}$ space group with two donors and one anion per unit cell, see Figure 1.3. The unit cell dimensions of the investigated Fabre salts ((TMTTF)$_2$X, X=AsF$_6$, SbF$_6$, BF$_4$ and SCN) are listed in Table 1.1.

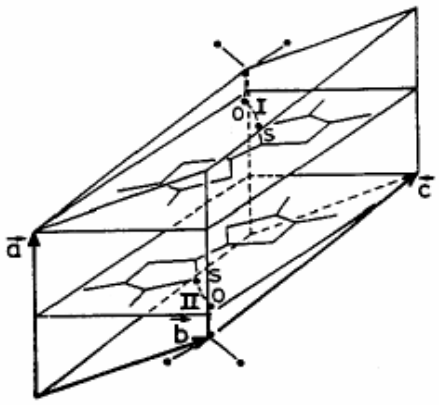


**Figure 1.3: The triclinic unit cell of (TMTCF)$_2$X salt with tetrahedral anion. From Ref. [22].**

| X | $SbF_6$ | $AsF_6$ | $BF_4$ | SCN |
|---|---|---|---|---|
| Anion symmetry | Octahedral | Octahedral | Tetrahedral | Linear |
| a (Å) | 7.195 | 7.178 | 7.112 | 7.053 |
| b (Å) | 7.622 | 7.610 | 7.468 | 7.598 |
| c (Å) | 13.45 | 13.317 | 12.946 | 12.750 |
| α ( ° ) | 81.19 | 82.03 | 85.56 | 89.08 |
| β ( ° ) | 96.65 | 95.75 | 94.05 | 92.61 |
| γ ( ° ) | 106.19 | 107.11 | 108.8 | 108.05 |
| V ($Å^3$) | 643.0 | 598.2 | 648.5 | 648.8 |
| M (g/mol) | 756.6 | 709.8 | 607.7 | 579.0 |
| ρ ($g/cm^3$) | 1.95 | 1.97 | 1.56 | 1.48 |
| Ref. | [23,24] | [24,25] | [26] | [26] |

**Table 1.1: The unit cell parameters of several Fabre salts at room temperature.**

Figure 1.4.a and b show two projections of the $(TMTTF)_2X$ crystal structure which have the same structure as the Bechgaard salts. The TMTTF molecules are related by inversion symmetry with inversion centers located between the molecules. A common feature of all Fabre salts is the zig-zag configuration of the molecular stacks along a-direction. They form layers in a-b plane which alternate with the anion X along the c-direction. Thus, the shortest interchain distances between the sulfur atoms are along b-direction. Moreover the stacks are not regular, in the sense that there are two different distances ($d_1$ and $d_2$) between consecutive molecules in the same stack, in other words TMTTF molecules form dimers along a-direction. Dimerization of the TMTTF molecules along the chain is one of the most important features of Fabre salts and it is more pronounced than in Bechgaard salts (see Table 1.2). Such a dimerization can have very drastic consequences on the electronic properties of these 2:1 salts, since the reciprocal periodicity $2\pi/a$ of the stack corresponds to the $4k_F$ critical wave vector of the 1-D correlated electron gas, this can enhance the charge localization phenomena which will be discussed in Section 1.2.2.

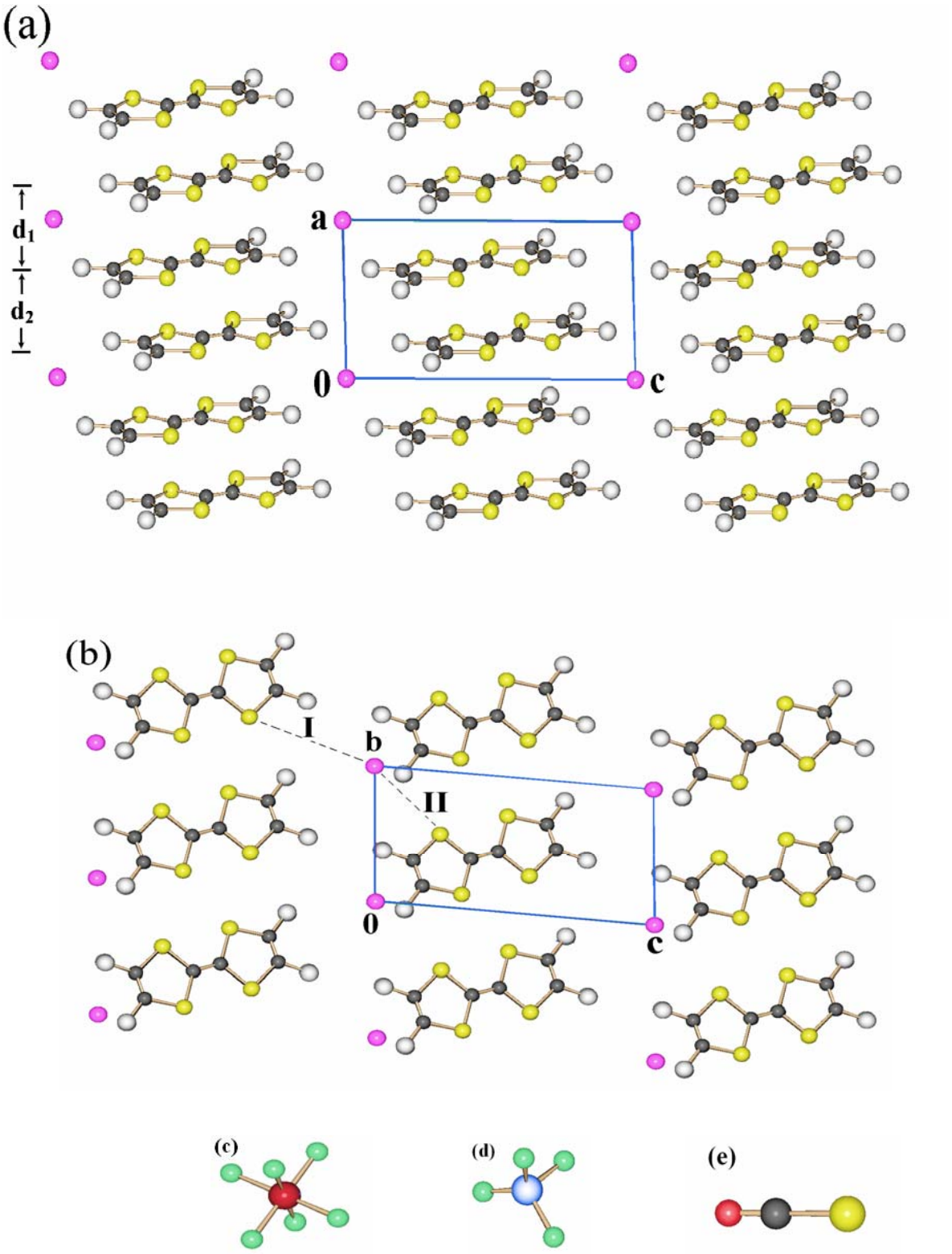


**Figure 1.4: Projection of the crystallographic structure of $(TMTTF)_2X$ along the a-c plane (a) and b-c plane (b), the zig-zag structure can be clearly seen. The violet spheres between the TMTTF molecules denote the anions. The tetrahedral, octahedral and linear anions are shown in c, d and e respectively. $d_1$ and $d_2$ in (a) are the intradimer and the interdimer spacing, respectively where $d_1 > d_2$ (see table 1.2).**

| X | $(TMTTF)_2X$ | | | | | | $(TMTSF)_2X$ | |
|---|---|---|---|---|---|---|---|---|
| | $SbF_6$ | $AsF_6$ | $PF_6$ | $BF_4$ | SCN | $ClO_4$ | $PF_6$ | $ClO_4$ |
| $d_1$ (Å) | — | 3.54 | 3.52 | 3.54 | 3.49 | 3.52 | 3.63 | 3.63 |
| $d_2$ (Å) | — | 3.64 | 3.62 | 3.56 | 3.56 | 3.59 | 3.66 | 3.64 |
| $\Delta d$ (Å) | — | 0.1 | 0.1 | 0.02 | 0.07 | 0.07 | 0.03 | 0.01 |
| $t_{a1}$ (meV) | 137 | 144 | 137 | — | — | 140 | 252 | 258 |
| $t_{a2}$ (meV) | 85 | 84 | 93 | — | — | 100 | 209 | 221 |
| $t_a$ (meV) | 111 | 114 | 115 | — | — | 120 | 231 | 240 |
| $\Delta t_a / t_a$ | 0.47 | 0.53 | 0.38 | | — | 0.33 | 0.19 | 0.15 |
| $\lvert C-C\rvert_{\min}$ (Å) | — | 4.01 | 3.99 | 3.88 | 4.08 | 3.96 | 3.88 | 3.77 |
| $\lvert C-C\rvert_{VdW}$ (Å) | 3.7 | 3.7 | 3.7 | 3.7 | 3.7 | 3.7 | 4.00 | 4.00 |
| $\gamma_c$ | — | 0.923 | 0.93 | 0.954 | 0.907 | 0.93 | 1.03 | 1.06 |
| $t_b$ (meV) | 12.2 | 13.9 | 12.3 | — | — | — | 33.5 | 27.0 |
| $t_a / t_b$ | 9.1 | 8.2 | 9.3 | — | — | — | 6.9 | 8.8 |

**Table 1.2: Some structural parameters and the transfer integrals for different TMTCF salts at room temperature and ambient pressure. $d_1$ and $d_2$ are the intradimer and interdimer spacing, respectively and $\Delta d$ is the difference between them ($\Delta d=d_1-d_2$). The intrachain transfer integrals $t_{a1}$, $t_{a2}$ as well as the average transfer integral $t_a$ , and the calculated degree of dimerization $\Delta t_a/t_a$ are given. $\lvert C\text{-}C\rvert_{min}$ is the shortest distance between the sulfur or selenium atoms along b-direction, $\lvert C\text{-}C\rvert_{vdw}$ is the double of the van der Walls radius of the sulfur or selenium atoms and $\gamma_c$ is the ratio between them. $t_b$ is the transfer integral along b-direction. The values are from Ref. [24,25, 27,28,29,30]. The dashes indicate that the data are not available.**

It is very common to quantify the dimerization by the difference of the distances between the average molecular planes along a-direction $[(d_2- d_1)/a)]$. However this analysis ignores that a significant dimerization can be also produced by a shift of the molecules transverse to the stack direction. Since both kinds of displacement can comparably affect the intrastack electronic interactions, the dimerization can be better quantified by the calculation of intermolecular transfer integrals along the $d_1$ ($t_{a1}$) and $d_2$ ($t_{a2}$) defined in Figure 1.4.a. Table 1.2 gives these $t_{ai}$ for some TMTCF salts for the donors HOMO in the framework of the extended Hückel model when the anionic potential is neglected [31]. The degree of dimerization of the stacks can be defined by the relative difference $2(t_{a1}-t_{a2})/(t_{a1}+t_{a2}) = \Delta t_a / t_a$ . Table 1.2 shows that the dimerization in TMTTF salts is larger than in TMTSF salts, and the dimerization changes with changing the anion.

The anions are placed in centrosymmetrical cavities delimited by the methyl groups of the TMTTF molecules [32]. The location of non-centrosymmetrical anions as $BF_4$, $ClO_4$ and SCN in these cavities introduces a substantial disorder in the structure, which will be more explicitly considered in the next chapter.

The anisotropy of TMT*C*F salts originates from the difference between the intermolecular interactions for different directions. The intrastack interactions (along the a-axis) are always strong enough to permit a strong intermolecular coupling, where both $d_1$ and $d_2$ are smaller than the double of the van der Walls radius of *C* atom (*C* = S or Se). The interstack interaction is weaker than the intrastack interaction in all TMT*C*F salts (the transfer integral along b-direction ($t_b$) is always smaller than that along a-direction ($t_a$) in all salts). Another important remark is that the interstack interaction in TMTSF salts is stronger than in TMTTF salts, because in the former ones the shortest Se-Se distance along b-direction is smaller than the double of the van der Walls radius of the selenium atom, while in TMTTF salts the shortest S-S distance along the b-axis is larger than the double of the van der Walls radius of the sulfur atom, this is the reason why TMTTF salts are more one dimensional than TMTSF salts. The importance of these interactions is measured by the value of $\gamma_C$, $\gamma_C = (C-C)_{VdW}/(C-C)_{\min}$ [33].

## 1.2.2 Electrical Properties of Fabre Salts

The electrical resistivity of TMTSF salts is very anisotropic. The room temperature resistivity ratio is about $\rho_{b'}/\rho_a \approx 100$ and $\rho_{c*}/\rho_a \approx 30000$ [34][I]. The room temperature resistivity ($\rho_{rt}$) of $(TMTSF)_2X$ parallel to the stacking direction is very low (about $10^{-2}\ \Omega\cdot\mathrm{cm}$) (see Figure 1.5) and decreases with decreasing the temperature down to about 20 K where the most TMTSF salts undergo a metal-insulator phase transition due to one dimensional instabilities [35,36]. However $(TMTSF)_2ClO_4$ undergoes a superconducting transition at about 1.4 K at ambient pressure [17].

This is not the case for $(TMTTF)_2X$ salts where the room temperature resistivity is about two orders of magnitude higher than that of TMTSF salts, and it increases upon cooling after a broad minimum at around 100-300K ($T_\rho$) [20,37] as shown in Figure 1.5.

[I] These values of the anisotropy ratio were obtained from the dc. resistivity measurements of $(TMTSF)_2ReO_4$ along the three crystal axes where the room temperature resistivity values: $\rho_a$, $\rho_{b'}$ and $\rho_{c*}$ are $1.45\times10^{-3}\ \Omega\cdot\mathrm{cm}$, $0.1777\ \Omega\cdot\mathrm{cm}$ and $44\ \Omega\cdot\mathrm{cm}$, respectively.

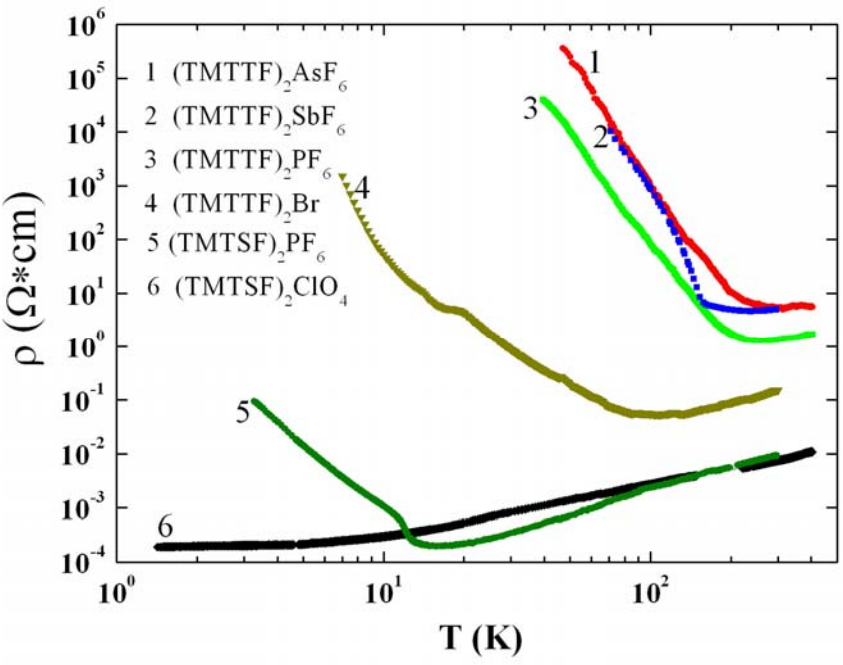


**Figure 1.5: Temperature dependence of the electrical resistivity of selected TMTCF salts.**

The dc resistivity parallel to the stacking direction of the TMTTF salts was extensively studied [38]. All $(TMTTF)_2X$ salts have a broad minimum in resistivity which occurs at the localization temperature ($T_\rho$) (see Table 1.3) for explanation see section 2.2. Below this temperature the conductivity become thermally activated with activation energy in the range (500-800) K.

| | $(TMTTF)_2X$ | | | |
|---|---|---|---|---|
| X | $AsF_6$ | $SbF_6$ | $BF_4$ | SCN |
| $T_\rho$ (K) | 220 | 155 | 210 | 250 |
| $\Delta_\rho$ (K) | 600 | 600 | — | — |
| Ref. | [37,39] | [39] | [37] | [37] |

**Table 1.3: The localization temperature and the localization energy gap of the investigated Fabre salts.**

For the salts with non-centrosymmetrical anions like SCN a clear anomaly was detected in the derivative of the conductivity versus temperature $\left[d\,\mathrm{Ln}\sigma/d(1/T)\right]$ at $T_{AO}$=160 K which is lower than the localization temperature ($T_\rho$ for the SCN salt =

250 K). This anomaly is not associated with a noticeable change of the slope of the resistivity; no such anomaly was detectable down to low temperatures in the salts with centrosymmetrical anions like $PF_6$, $AsF_6$ and $SbF_6$.

Infrared measurements of TMTTF salts showed that the activated behaviour of the resistivity is due to localization of the conduction electrons on the TMTTF molecules [40], implying the presence of a gap of charge ($\Delta_\rho$), whose effect becomes relevant below $T_\rho$. The values of $T_\rho$ for the investigated Fabre salts are tabulated in Table 1.3. In $Q_n(TCNQ)_2$[I], which has a similar charge localization phenomenon, X-ray diffuse scattering experiments were able to show that such a gap of charge is associated with the formation of a short range $4k_F$ CDW, leading to a local dimerization of the TCNQ stacks [41]. Nevertheless the same experiment could not detect $4k_F$ CDW in TMTTF salts because the $4k_F$ charge localization is associated with the lattice dimerization in these salts.

The energy gap $\Delta_\rho$ increases with increasing on-site Coulomb repulsion $U$ and the degree of dimerization. $\Delta_\rho$ was calculated using the reduced on site Coulomb repulsion $U/\langle t_a \rangle$ and the reduced dimerization $\Delta_D/\langle t_a \rangle$, in the framework of the 1-D dimerized Hubbard model at 1/4 band filling [42]. The charge gap is estimated to be $\langle t_a \rangle/25$ in $(TMTSF)_2PF_6$ and $\langle t_a \rangle/2$ in $(TMTTF)_2PF_6$ [42], where $t_a = (t_{a1} + t_{a2})/2$ is the average transfer integral along the stacks, (see Table 1.2).

From the previous discussion it is clear that due to the stronger dimerization and larger on-site Coulomb repulsion ($U$) of the TMTTF comparing with TMTSF salts, they are closer to the Mott-Hubbard insulting state. For more details see section 2.2.

### 1.2.3 Thermal Expansion of $(TMTCF)_2X$ Salts

Organic radical salts from the $(TMTCF)_2X$ family have relatively large expansion coefficient. For example, by heating a single crystal of $(TMTSF)_2PF_6$ from 4 K up to 300 K it was found that the expansion coefficient along the a-axis $\Delta a/a = 0.03$, along the b-axis $\Delta b/b = 0.01$ and along the c-axis $\Delta c/c = 0.01$ [43]. The expansion coefficient along the a-axis for $(TMTSF)_2PF_6$ was found to increase linearly with increasing the temperature above 100 K with a slope of $(\Delta a/a)/T = 10^{-4}\,K^{-1}$ [44]. To compare experimental measurements, as for the spin susceptibility (which is measured normally at constant pressure (p = 1 bar)), with theoretical calculations which are obtained for constant volume, the effect of the expansion of the unit cell have to be taken into account. For the spin susceptibility, the difference between the

[I] $Q_n(TCNQ)_2$ denotes the quinolinium ditetracyanoquinodimeth-anide.

spin susceptibility at constant pressure $(\chi_s)_p$ and at constant volume $(\chi_s)_v$ is given by the relation [45]:

$$(\chi_s)_p - (\chi_s)_v = \int_0^T \left(\frac{\partial \chi_s}{\partial T}\right)_T \left(\frac{a\partial p}{\partial a}\right)_T \left(\frac{\partial a}{a\partial T}\right)_p dT \qquad (1.1)$$

The second and the third terms in equation 1.1 represent the compressibility and the thermal expansion coefficient of the salt which are known for $(TMTSF)_2PF_6$ from temperature and pressure dependence X-ray measurements [46]. The first factor can be obtained by measuring the spin susceptibility as a function of temperature and pressure. The experimental data for the first term is not available, however using the scaling relation which was derived by Bourbonnais [47]

$$\frac{1}{\sqrt{T_1 T}} \propto \chi_s(T) \qquad (1.2)$$

and using the temperature and pressure dependent measurements of the nuclear spin lattice relaxation time $T_1$ which were obtained by NMR measurements by Wzietek *et. al.* [45] the first term can be obtained. Finally using the X-ray and NMR measurements under pressure for $(TMTSF)_2PF_6$ the spin susceptibility at constant volume can be calculated. Figure 1.6 shows the calculated temperature dependence of $(T_1T)^{1/2}$ for $(TMTSF)_2PF_6$ at constant volume using equation 1.1 and the measured values at constant pressure. Using Figure 1.6 the susceptibility $(\chi_s)_v$ can be calculated from the $(\chi_s)_p$.

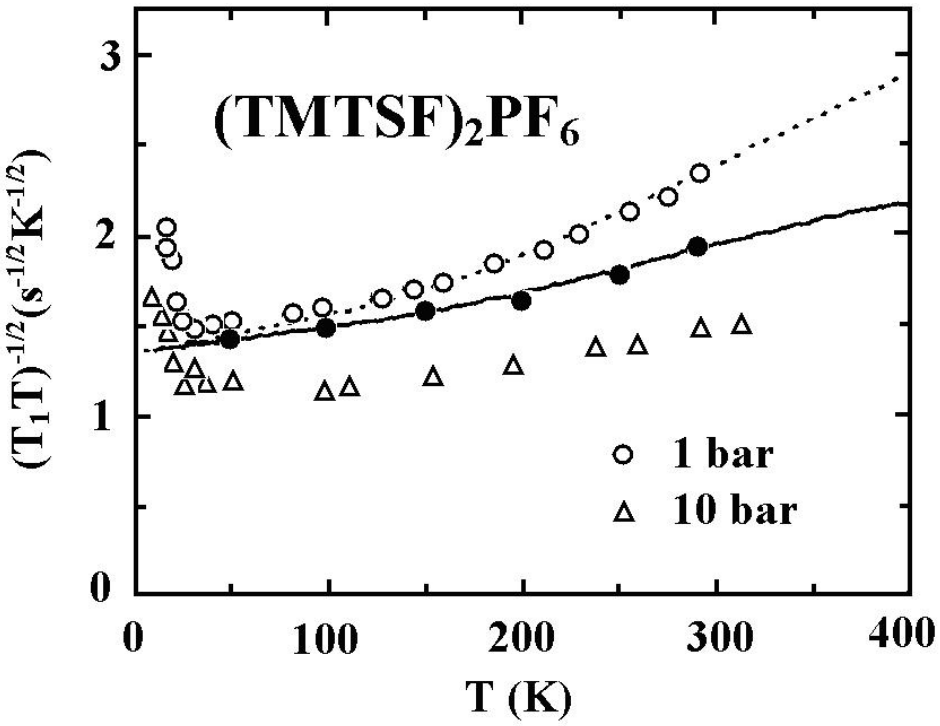


**Figure 1.6: Temperature dependence of $(T_1T)^{-1/2}$ for $^{77}Se$ of $(TMTSF)_2PF_6$ under hydrostatic pressure of 1 bar and 10 bar. The closed symbols represent the corrected data for constant volume. From Ref. [48].**

## 1.2.4 The Phase Diagram of $(TMTCF)_2X$ Salts

Quasi one-dimensional materials are found to be more sensitive to certain instabilities than two or three-dimensional systems with comparable coupling as mentioned above. A direct consequence of the one-dimensional behaviour of the $(TMTCF)_2X$ salts is the wide variety of ground states of this family.

The ground state of the Fabre and Bechgaard salts depends on the chemical composition of the organic donor or the inorganic anion and the external applied pressure. The electronic state of these salts can be summarized as a function of temperature and pressure in the so-called "generalized phase diagram", as illustrated in Figure 1.7.

A series of ground states (spin-Peierls, spin-density wave and superconductivity) appear upon the elevation of chemical pressure (i.e. the size of the anion X and the exchange of the chalcogen atom of the donor molecule (Se or S)) and/or external pressure [49].

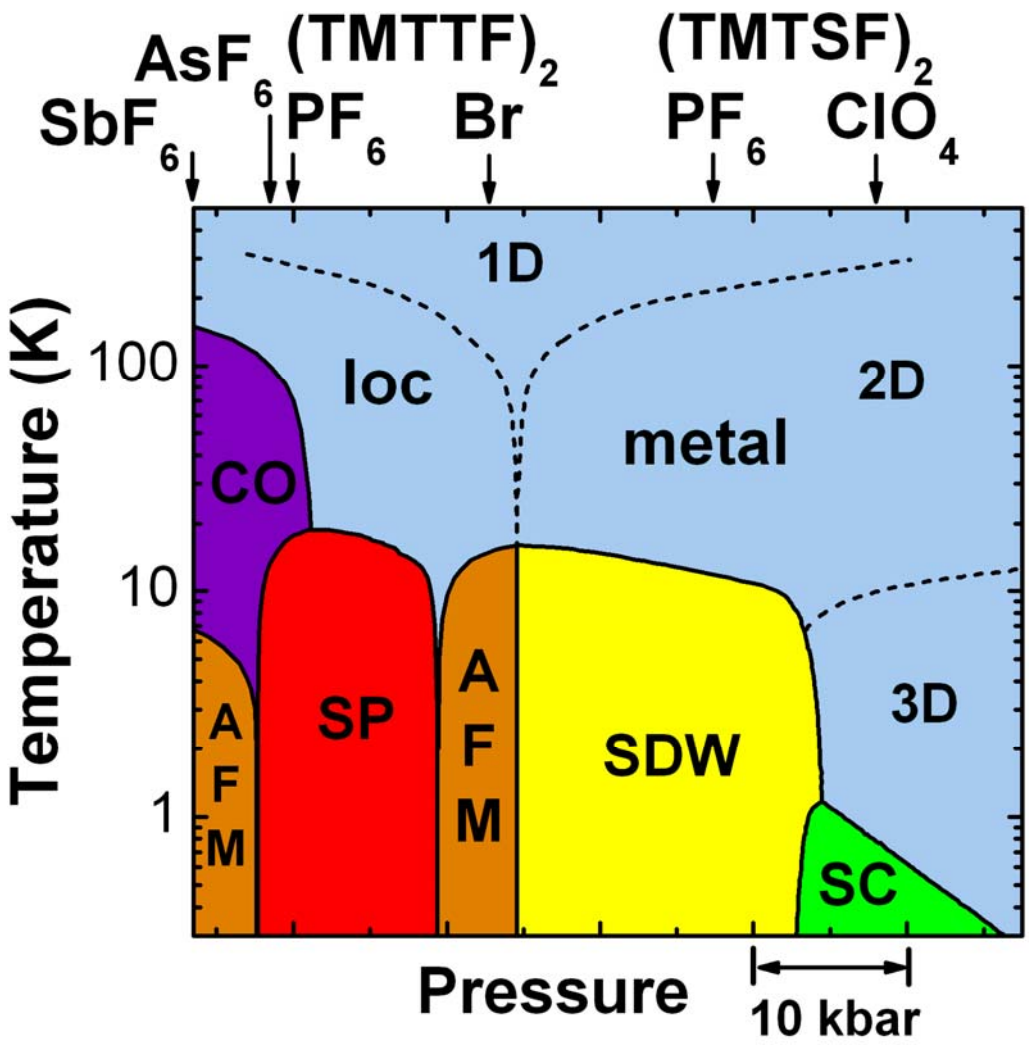


**Figure 1.7:** **Generalized temperature-pressure phase diagram for the $(TMTCF)_2X$ salts after Ref. [48,50,51] determined for example by pressure dependent resistivity and NMR measurements. The notations loc, CO, SP, AFM, SDW and SC refer to Mott localized, charge ordered, spin-Peierls, antiferromagnetic (commensurate SDW), spin density wave (incommensurate), and superconducting ground sates, respectively. The ambient pressure position of the different compounds in the phase diagram is indicated by the arrows.**

Applying pressure mainly enhances the interchain coupling (increase the interchain transfer integral $t_b$) and this results in increasing the dimensionality, in agreement with the fact that $(TMTTF)_2PF_6$ is more one-dimensional than its selenium analogous.
For example $(TMTTF)_2PF_6$ is located in the left side of the phase diagram, at a temperature of about 230 K this salt shows a smooth transition to the insulating state caused by opening of a dimerization gap. It is then found to develop a charge-ordered (CO) state at about 63 K and a lattice distorted spin-Peierls (SP) state at 19 K. The SP state is suppressed under moderate pressure and is replaced by an antiferromagnetic (AFM) Néel state similar to the one found in the $(TMTTF)_2Br$ salt at ambient pressure; the Mott state of $(TMTTF)_2PF_6$ is in turn suppressed under pressure of 13 kbar and the salt is then fully metallic and undergoes a SDW phase transition similar to $(TMTTSF)_2PF_6$ [52]. By applying a pressure of 40 kbar to $(TMTTF)_2PF_6$ [53], the SDW state is then removed and the salt goes into superconducting state which closes the sequence of ground states.

Within the next chapter, we will not attempt a detailed discussion of the whole structure of the phase diagram but rather place a selected emphasis on the description of the ground states observed in the Fabre salts (the left side of the phase diagram).

## 1.3 The 2-D Organic Conductors $(BEDT\text{-}TTF)I_3$

The search of organic superconductors was stimulated by the idea of W. A. Little [54] that the pairing of electrons via their coupling to highly polarisable side-chains in organic materials could yield superconductors with transition temperatures ($T_c$) above room temperature. After it turned out that the superconducting transition temperature in quasi 1-D TMTSF salts was rather small ($T_c \leq 3$ K), and that most of these salts undergo a metal-insulator transition at low temperatures due to the one-dimensional instabilities, and that the pairing mechanism is most likely different from the one proposed by Little, special efforts were made to increase the dimensionality of the organic conductors from 1-D to 2-D in order to enhance $T_c$ and to avoid the one-dimensional instabilities. This was achieved in the late 1970's by synthesizing the nonplanar donor molecule BEDT-TTF (Bisethylenedithio-tetrathiafulvalene) (abbreviated as ET) by Mizuno *et al* [55]. The structure of the BEDT-TTF molecule is depicted in Figure 1.8.

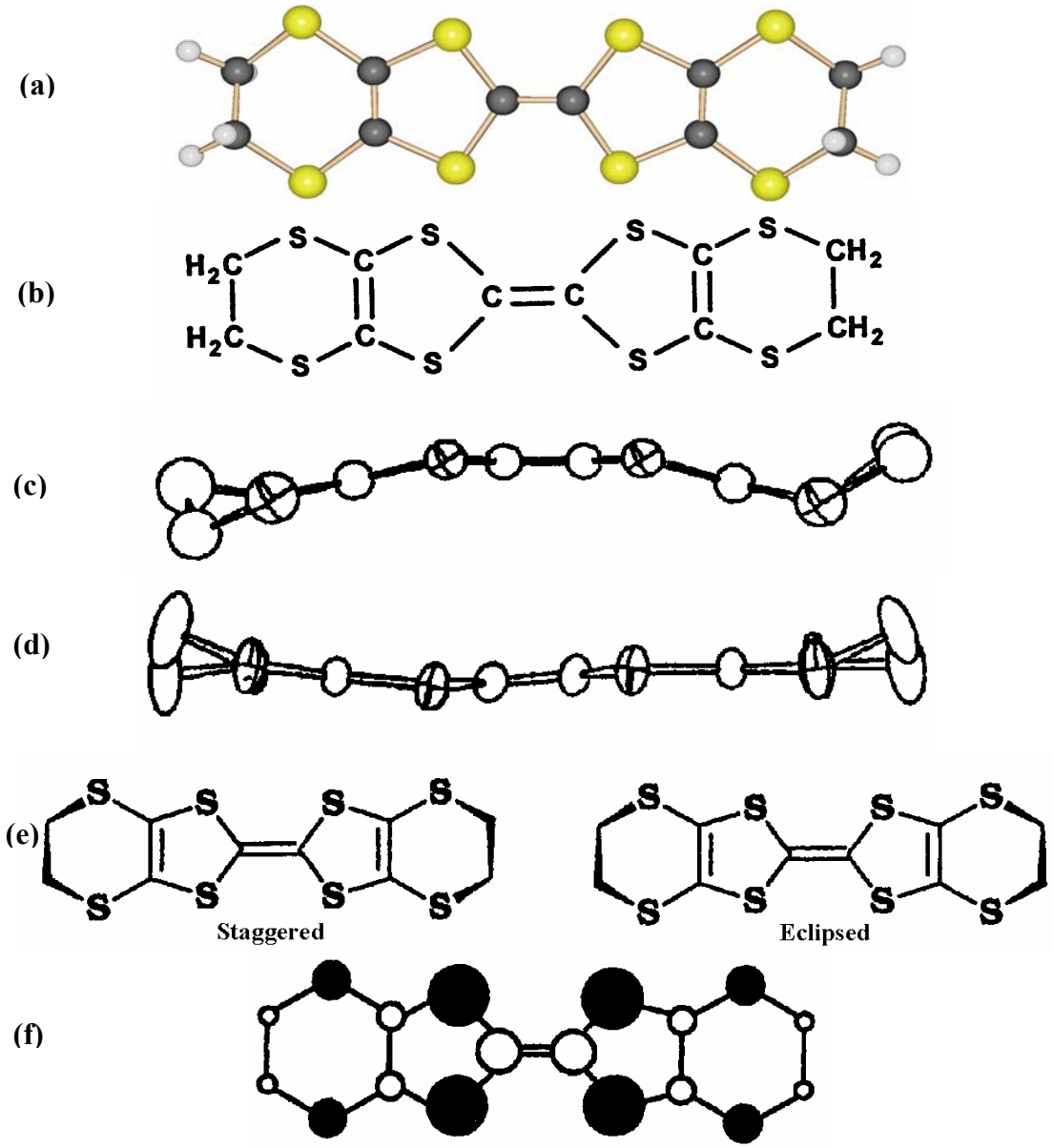


**Figure 1.8: The structure of the BEDT-TTF molecule (a) and (b), the molecule is shown in a neutral solid (c), and in a radical salt (staggered form) (d). The main conformations of the terminal ethylene groups of the BEDT-TTF molecule are shown in (e), and the calculated HOMO coefficients where the magnitude of the coefficient is shown by the radius of the circle (f).**

The electronic properties of the BEDT-TTF molecule indicate that while it is a slightly weaker donor than the TMTSF molecule[I] it is better in yielding conductive charge transfer complexes down to low temperatures because of the higher dimensionality in the BEDT-TTF salts [56]. Because of the non planer shape of the

[I] The room temperature conductivity of TMTSF salts is higher than that of BEDT-TTF salts.

neutral BEDT-TTF molecule (Figure 1.8.c) it can produce quasi 2-D salts. On complex formation it becomes nearly planar (Figure 1.8.d) except for the terminal ethylene groups which are thermally disordered at high temperatures. The terminal ethylene groups can have two main conformations where they can be either staggered or eclipsed (Figure 1.8.e).

The conformation of the ethylene groups is one of the key parameters in BEDT-TTF salts. The BEDT-TTF molecules in the charge transfer salt form stacks leaving cavities along the direction of the molecular long axis, where the counteranions reside. This tendency leads to a comparatively small transfer integral $t_{\|}$ and, hence, BEDT-TTF complexes are poorly conductive compared with TMTSF salts. For example the room temperature conductivity of β-( BEDT-TTF $)_2I_3$ is (20-70) $(\Omega \cdot \mathrm{cm})^{-1}$ parallel to the high conductive plane [57, 58] compared to about 500 for both $(TMTSF)_2ClO_4$ and $(TMTSF)_2PF_6$ [59,60] parallel to the stacking direction. On the other hand, the BEDT-TTF molecule has a strong tendency to form proximate intermolecular $S \cdots S$ contacts along the side-by-side direction leading to an increment of the transfer integral $t'_{\|}$ , see Figure 1.9.

The outer S atoms contribute significantly to the network formation; although the electron densities on the outer S atoms of the HOMO are substantially lower than those of the inner ones (Figure 1.8.f). The anions form layers which sandwich the donor layers. Significant donor-anion interactions are recognized by the short atomic contacts between the ethylene groups of the BEDT-TTF molecules and the anions. However, the donor-donor interactions through the anion opening along the long side of the BEDT-TTF molecules are very small because of the fact that the electron densities on the outer ethylene groups are negligible and the distance between the BEDT-TTF molecules along this direction is large. Therefore, the transfer integral along this direction ($t_{\perp}$) is the smallest.

These competing different kinds of intermolecular interactions and the large conformational freedom of the ethylene groups together with the rather flexible molecular framework give a variety of BEDT-TTF salts. They show 1-D to 2-D character, a number of morphologies, and a variety of molecular compositions.

It has been pointed out that BEDT-TTF salts exhibit a wide variety of electronic properties, depending on the anion present in the material. In addition a lot of phases exist for the same anion with vast different physical properties; these phases can be formed simultaneously in the crystallization. The different physical properties are derived primarily from the packing of the donor-radical cations in their crystal structure. The donor-packing pattern, which determines the electronic structure of the salt, are classified into α, β, κ, Θ, γ, phases etc. The spatial

arrangements of BEDT-TTF molecules in the unit cell of some of these phases are schematically shown in Figure 1.10.

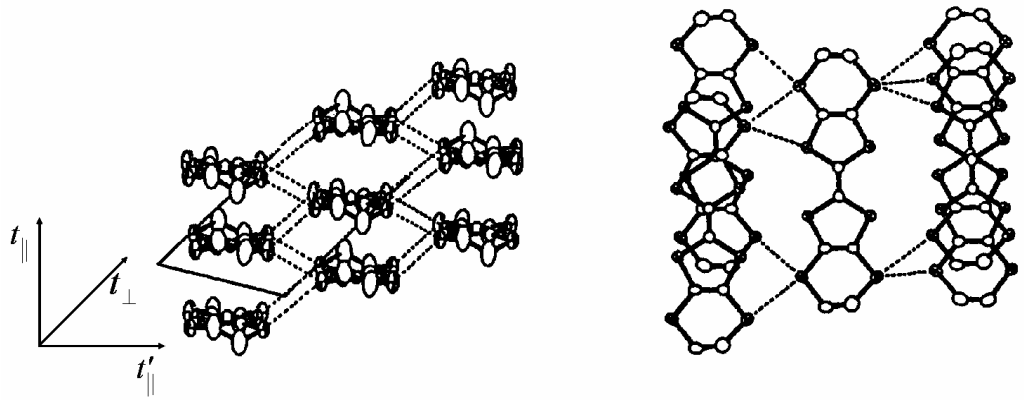


**Figure 1.9: The intermolecular short S···S atomic contacts in β-(BEDT-TTF)$I_3$.**

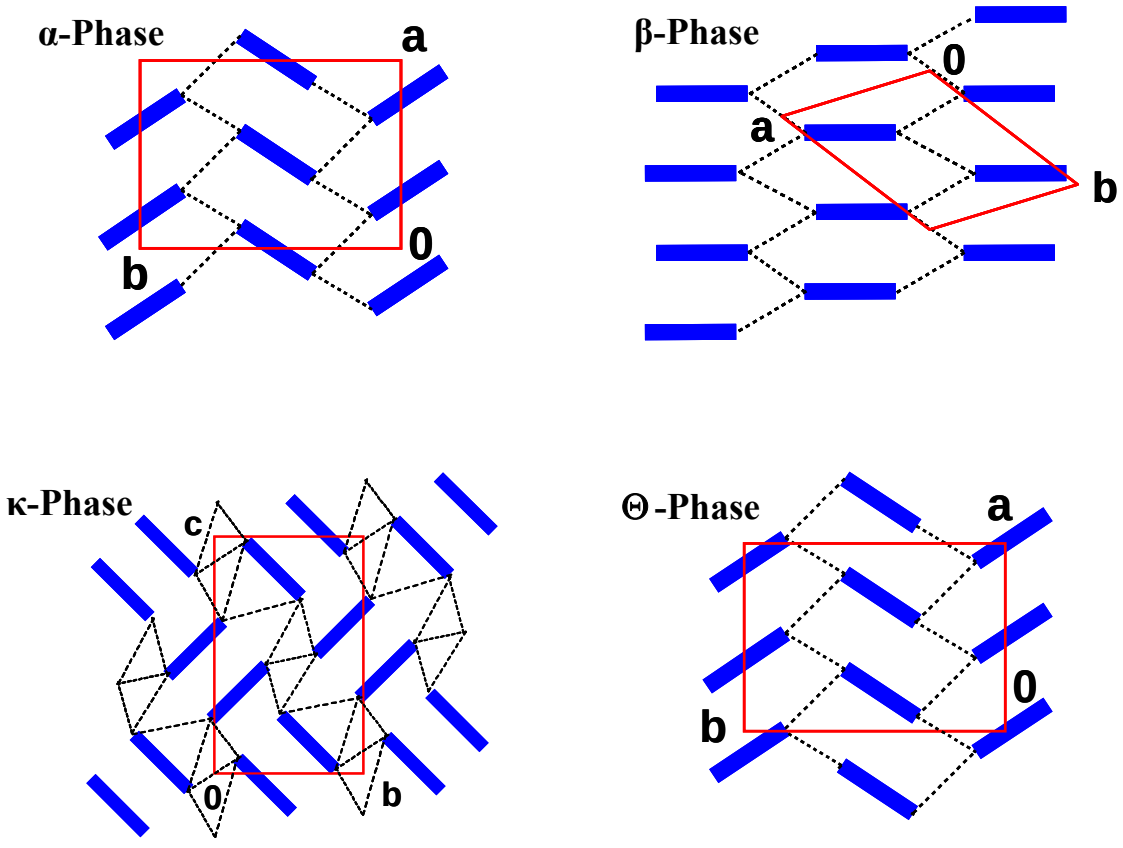


**Figure 1.10: Schematic representation of the spatial arrangement of the BEDT-TTF molecules in the most common phases (α, β, κ, Θ) of the BEDT-TTF salts. The blue rectangles and the red ones represent the BEDT-TTF molecules and the unit cells, respectively. The dashed lines represent the π-orbital overlaps.**

From the viewpoint of superconductivity, (BEDT-TTF)$_2$X salts with linear anions are interesting ones. One class of the most important salts of this family is formed using $I_3^-$ anion giving the different charge transfer salts (BEDT-TTF)$_2$I$_3$. This salt has four main phases. Among them, only α-(BEDT-TTF)$_2$I$_3$ undergoes a metal-insulator phase transition at 135 K and exhibits metallic behavior from 135 K up to room temperature [61,62]. The other three phases (β, κ and Θ) exhibit superconductivity at ambient pressure. The β-(BEDT-TTF)$_2$I$_3$ salt is the second ambient pressure-superconductor that was found with $T_c$ = (1.5 and 8) K [63,64,65]. κ-(BEDT-TTF)$_2$I$_3$ is one of the best 2-D organic metals known until now and it has a superconducting transition at 4 K [66]. The Θ-phase of this salt which is the less studied phase yet between all the (BEDT-TTF )$_2$I$_3$ phases was synthesized in 1986 [67,68] as mixed anion salt Θ-(BEDT-TTF)$_2$(I$_3$)$_{1-x}$(AuI)$_x$. This phase is also a 2-D metal and it was shown that among several samples a few were found to show a superconducting transition at 3.6 K, some samples show partial superconductivity, and most of them show no indication of superconductivity.
In this work the transport and magnetic properties of neat crystals of the organic superconductor Θ-(BEDT-TTF)$_2$I$_3$ will be presented.

### 1.3.1 Crystal Structure of Θ-(BEDT-TTF)$_2$I$_3$

Single crystals of Θ-(BEDT-TTF)$_2$I$_3$ were prepared using standard electrochemical techniques in a 100 ml electrochemical cell of 3 compartments [69]. Glass filters were used to separate the components from each other. 0.1 g BEDT-TTF and 0.5 g $Bu_4NI_3$ ($Bu_4N^+$ = tetrakis (n-butyl) ammonium ion) were dissolved in 100 ml tetrahydrofurane (THF) and saturated with dry nitrogen. The crystals were grown using a constant current of 15 μA at room temperature and under exclusion of light. During the electrochemical crystallization $AuI_2^-$ anions were not used as reported before for growing Θ-(BEDT-TTF)$_2$(I$_3$)$_{1-x}$(AuI$_2$)$_x$ (x<0.02) crystals [70,71]. The obtained neat Θ-(BEDT-TTF)$_2$I$_3$ crystals are plates with nearly rectangular shape; the crystals have dimensions up to (2.5×2×0.2) mm$^3$. The investigated samples of the neat Θ-(BEDT-TTF)$_2$I$_3$ crystals belong to the monoclinic system with P2(1)/c symmetry. The lattice parameters at room temperature are: a = 9.93Å, b = 10.07Å, c = 34.2Å, β = 98.27°. The packing motive of the BEDT-TTF molecules and the structure data are very similar to those of Θ-(BEDT-TTF)$_2$(I$_3$)$_{1-x}$(AuI$_2$)$_x$ crystals, whereby most of the Θ-(BEDT-TTF)$_2$(I$_3$)$_{1-x}$(AuI$_2$)$_x$ crystals are twinned to form a pseudo-orthorhombic structure with half the length in a-direction compared to the monoclinic cell. In Θ-(BEDT-TTF)$_2$I$_3$ crystals, each $I_3^-$ anion occupies one of two

independent positions on the mirror plane *m* in a channel formed by the BEDT-TTF molecules with the occupancy probability of 50%. The two types of the $I_3^-$ are statistically disordered in the structure as shown in Figure 1.11. Figure 1.12 shows the structure of the Θ-(BEDT-TTF)$_2$I$_3$ crystal, the BEDT-TTF molecules form a 2-D conduction network parallel to the ab-plane. The dihedral angle between the planes of the neighbouring molecules connected by short $S\cdots S$ contacts is about 80° [71,72].

The structure of Θ-(BEDT-TTF)$_2$I$_3$ crystals is very similar to that of α-(BEDT-TTF)$_2$I$_3$ except that the Θ-phase salt has two crystallographically unique donor-molecule layers in the unit cell. Even though the symmetry in the Θ-phase layer is higher, and all BEDT-TTF molecules are centrosymmetrical.

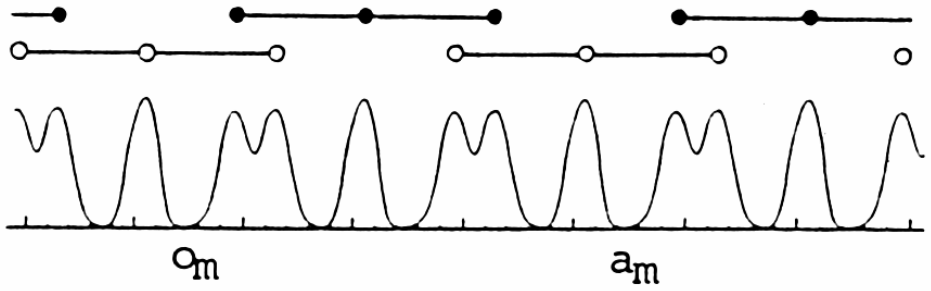


**Figure 1.11: Fourier peaks show the arrangement of the $I_3$ anions in the Θ-(BEDT-TTF)$_2$I$_3$ crystals. The opened and closed circles indicate two possible ordered arrangements of the $I_3$ anions. From ref. [67].**

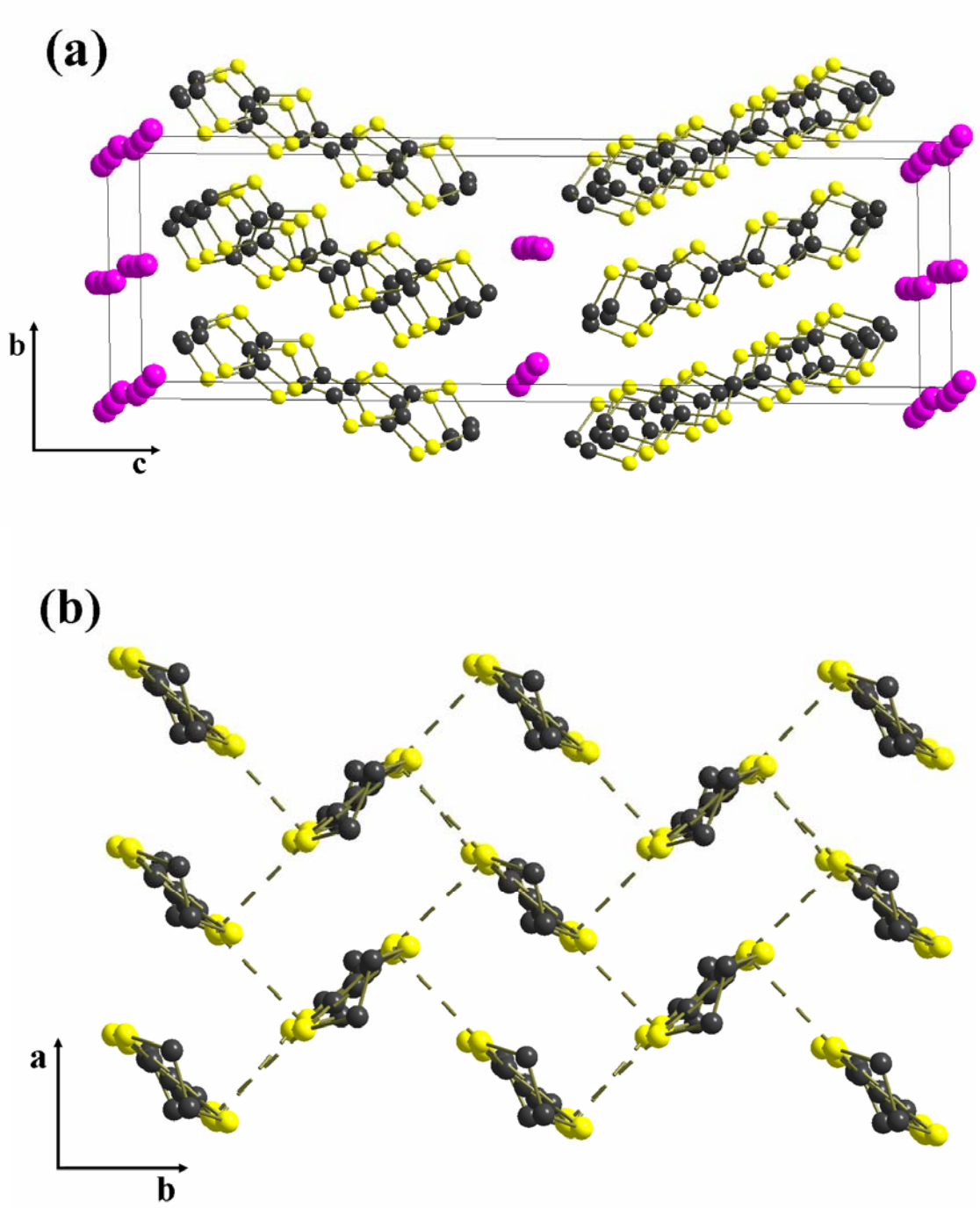


**Figure 1.12: The crystal structure of Θ-(BEDT-TTF)$_2$I$_3$ shown along ac-plane (a), and the arrangement of (BEDT-TTF) molecules in the conduction plane (ab-plane) (b). The dashed lines represent the S···S contacts.**

# Chapter 2

# Physics of Low Dimensional Conductors

Because of their intrinsic low dimensionality, organic conductors show more diversified physical properties than three dimensional conductors. First we have to distinguish between strictly 1-D systems, for which no phase transitions are possible at finite temperature ($T \neq 0$), and quasi 1-D and 2-D systems which do display phase transitions at $T \neq 0$. In organic conductors, the interactions between the chains or the sheets are responsible for finite temperature transitions. This is the reason for labeling systems of chains or sheets as quasi-one or two-dimensional. First let us concentrate on the electronic properties.

## 2.1 Band Structure and Electronic Properties

The conduction bands of organic conductors are constructed from π-molecular orbitals. The conduction π-electrons can move from one orbital to the nearest one with strength $t$ (the transfer integral). Since the donor molecules in the organic conductors are stacking in columns (in quasi 1-D conductors) or in sheets (in quasi 2-D conductors), this will introduce anisotropy in the transfer integral $t$, the anisotropy of the transfer integral along the different crystallographic direction derives the shape of the Fermi surface. The electron band structure can be described within the tight-binding single electron Hamiltonian. The linearized energy dispersion is given by the relation [73].

$$\varepsilon(\vec{K}) = -2t_a \cos(k_a \cdot a) - 2t_b \cos(k_b \cdot b) - 2t_c \cos(k_c \cdot c) \qquad (2.1)$$

Where $t_a$, $t_b$ and $t_c$ are the transfer integrals between the nearest neighbor molecules along the a, b, and c axis respectively, $k_i$ is the electron wave vector in the $i^{th}$

direction. The Fermi surfaces for 1-D, 2-D and 3-D conductors are illustrated in Figure 2.1. The shape of these surfaces changes depending on the ratio between the transfer integrals along the different crystallographic directions.

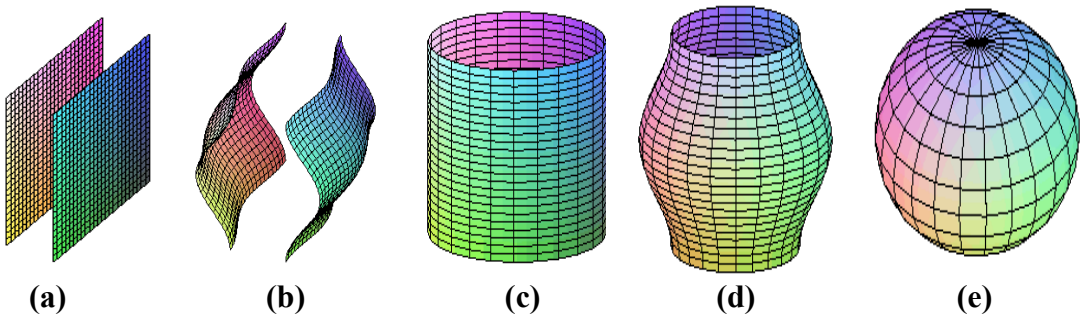


**Figure 2.1: The shape of the Fermi surface for different dimensionality for: (a) One-dimensional $t_b=t_c=0$, (b) quasi one-dimensional ($t_a>>t_b>t_c$), (c) isotropic two-dimensional ($t_a=t_b$, $t_c=0$), (d) quasi two-dimensional $t_a \approx t_b>>t_c$, (e) isotropic three dimensional $t_a=t_b=t_c$).**

The shape of the Fermi surface has high significance for explaining and evaluating many physical quantities of solids and for principle understanding of their behavior. For example, the Fermi surface of the one-dimensional system consists of two parallel planes separated by the wave vector $2k_F$ (Figure 2.1.a). This surface is perfectly nested by the wave vector $Q=(2k_F,0,0)$ [I]. When the transverse overlap $t_b$ is not negligible, this introduces some warping of the Fermi surface as shown in Figure 2.1.b, and then the wave vector $Q=(2k_F,0,0)$ no longer nests the Fermi surface. The new nesting vector $Q=(2k_F,\pi/b,\pi/c)$ of this Fermi surface deviates from the perfect nesting vector with terms of the order $(t_b/t_a)^2$ [18]. With increasing $t_b/t_a$ the nesting condition applies for smaller amount of electron hole pairs and the system will more likely stay metallic and will not undergo a metal insulator transition at low temperatures. This can explain the general trend to increase the ratio $t_b/t_a$ (increasing the dimensionality from 1-D to 2-D) to avoid the one dimensional instabilities and to increase the probability to get organic superconductors. In the following sections a brief theoretical background about quasi 1-D and quasi 2-D systems will be given.

[I] Perfect nesting of the Fermi surface means $\varepsilon_K = \varepsilon_{K+Q}$ for all k on the Fermi surface. This means that all the sites (one full, one empty) which differ by $Q=2k_F$ have the same energy and are paired.

## 2.2 Mott Hubbard Transition

In $(TMTCF)_2X$ salts, the transfer of one electron from two donor molecules to each anion leaves 0.5 hole on average per donor molecule. Therefore the TMTCF salts are expected to be metals with a 3/4 filled conduction bands in terms of electrons ($1/4$ filled band in terms of holes) in absence of dimerization. However the dimerization of TMTCF molecules along the chain direction give rise to two HOMO (higher occupied molecular orbitals) like bands per Brillouin zone, the upper band is half filled (i. e. $k_F = \pm\pi/2a$, see Figure 2.2). Thus in the case of strong dimerization (as in TMTTF salts) the conduction band can be considered as half filled with one hole per each TMTTF dimer.

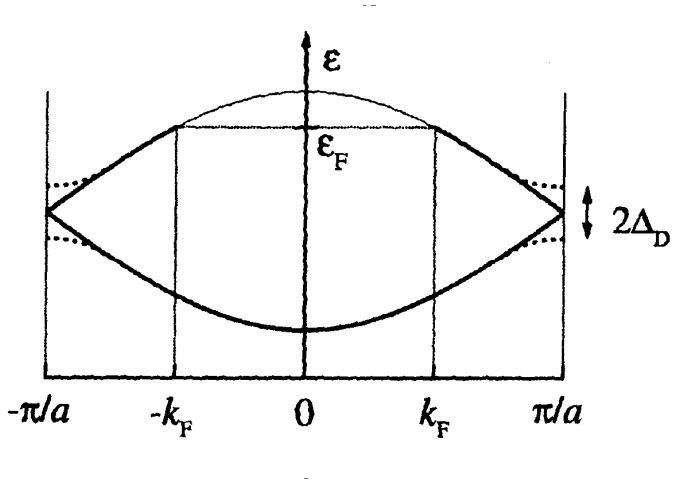


**Figure 2.2: Schematic representation of the one electron band dispersion of TMTTF salts in chain direction. The band structure is folded at $\pm\pi/a$ because of the stack dimerization. At the Brillouin zone boundaries, the gap $2\Delta_D$ is due the inequivalence between $d_1$ and $d_2$.**

Mott and Hubbard have introduced this transition [74,75,76], where it was shown that an incompletely filled band will not necessarily show metallic conduction. The essence of the idea of Mott-Hubbard insulting state can be seen by examining the half-filled chain shown in Figure 2.3.

If the on-site Coulomb repulsion $U$ (the electrostatic repulsion ($e^2/r_{12}$) between a pair of electrons) becomes comparable to the bandwidth $W$ [I], then the probability of the two electrons being on the same site will decrease. At a critical value of

[I] The band width $W$ for the one dimensional material equals $4t_a$, where $t_a$ is the transfer integral parallel to the stacking direction.

$U/W \sim 1$, there will be a sudden transition to a nonmetallic state. The band gap is predicted to change discontinuously from zero to some positive value as $U/W$ changes. Opening this energy gap gives raise to an activated electrical conductivity [77].

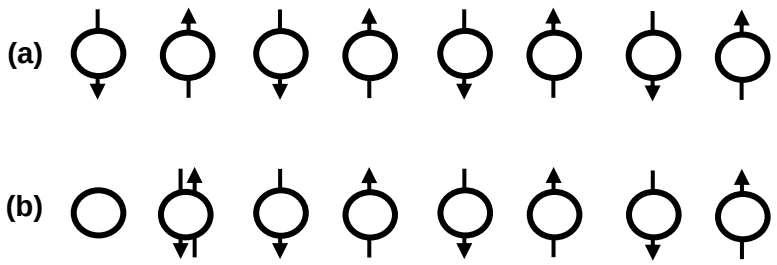


**Figure 2.3: (a) Ordered array of radicals with one unpaired electron per each site (half filled band). (b) The case of double occupancy of a single site exists. If the on-site Coulomb repulsion (U) is nonzero, the activation energy $2\Delta_D$ will separate configuration (a) from configuration (b).**

## 2.3 Magnetism of Organic Conductors

The application of an external magnetic field $H$ on a material induces a spin magnetization M defined as the spin magnetic moment per unit volume. The spin susceptibility $\chi_s$ ($\chi_s = M/H$) of the conduction electrons in conventional metals is temperature independent within the free-electron Fermi model, and is called Pauli susceptibility. The Pauli susceptibility is given by the relation:

$$\chi_s = \frac{\mu_0 N g^2 \mu_B^2}{2} D(E_F) \tag{2.2}$$

where $D(E_F)$ is the density of states at the Fermi level ($D(E_F) = mk_F / 2\pi^2 \hbar^2$).

In the limit of strong coupling (for strong electron-electron correlation), the exchange interaction between the spins should be taken into account. The exchange interaction between two spin operators at sites i and j ($S_i$ and $S_j$) can be described by the Hamiltonian:

$$\hat{H} = -J \vec{S}_i \cdot \vec{S}_j \tag{2.3}$$

where $J$ is the coupling constant of the exchange interaction between the two spin operators $\vec{S}_i$ and $\vec{S}_j$. Ferromagnetism, in which the spins are aligned parallel, is

observed when $J$ is positive, whereas negative $J$ gives antiferromagnetism with spins arranged antiparallel to each other.
At high temperatures, the TMTTF molecules form an isotropic antiferromagnetic (AFM) spin 1/2 chain in general. The AFM spin chain can be described by three different models depending on the dimensionality of the order parameter (n)[I] [78]:

- For n = 1 the spin-spin interaction can be described by the Ising model

$$\hat{H}_{\text{Ising}} = -J\sum_{i=1}^{N} S_i^z S_{i+1}^z \tag{2.4}$$

- For n = 2 the spin-spin interaction can be described by the xy-model

$$\hat{H}_{xy} = -J\sum_{i=1}^{N} (S_i^x S_{i+1}^x + S_i^y S_{i+1}^y) \tag{2.5}$$

- For n = 3 the spin-spin interaction can be described by the Heisenberg model

$$\hat{H}_{Heisenberg} = -J\sum_{i=1}^{N} \overrightarrow{S_i} \cdot \overrightarrow{S_j} \tag{2.6}$$

In TMTTF salts at high temperatures the spin can be aligned along any direction (n=3) and thus they form S=1/2 AFM Heisenberg chain as depicted in Figure 2.4.

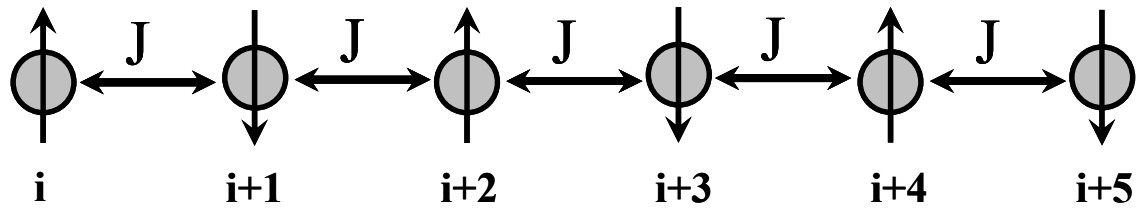


**Figure 2.4: Schematic view of the isotropic S=1/2 AFM Heisenberg chain of localized electrons with AFM coupling constant J.**

[I] The order parameter n=1 if the spins can only be aligned along one specific direction, n = 2 if the spins can be aligned in one plane and n=3 if they can be aligned along any direction in the space.

### 2.3.1 Bonner-Fisher Model

If the AFM Heisenberg chain of N spins $\vec{S_i}$ is inserted in a magnetic field $\vec{H}$, it can be described by the Hamiltonian:

$$\hat{H} = -J\sum_{i=1}^{N} \vec{S}_i \cdot \vec{S}_{i+1} - g\mu_B \sum_{i=1}^{N} \vec{H} \cdot \vec{S}_i \qquad (2.7)$$

The temperature dependence of the spin susceptibility of isotropic finite spin chain with $(3 \le N \le 11)$ was calculated numerically by Bonner and Fisher [7]. The results were extrapolated to get the spin susceptibility of the infinite ($N \to \infty$) chain. The obtained temperature dependence of the spin susceptibility for the infinite chain is shown in Figure 2.5.

They found that the spin susceptibility has a smooth maximum value of $\chi_{\max} = 0.1469\,\Gamma/|J|$ at $T_{\max}/|J| = 0.641$. Below the maximum, the susceptibility decreases with decreasing temperature down to low temperatures to approach a finite non-zero value at zero Kelvin $\chi(T \to 0) = \Gamma/\pi^2|J|$. This implies that there is no energy gap between the ground state and the first excited state.

The constant $\Gamma$ was introduced [48] for easy conversion between the different unit systems. For S=1/2 chain $\Gamma = 4C$ with C Curie constant. $\Gamma$ is given for the different unit system as follow:

- In SI unit system $\Gamma = \mu_o N g^2 \mu_B / k_B$ = 18865 $m^2$K/mol.
- In CGS unit system $\Gamma = N g^2 \mu_B / k_B$ = 15012 K/mol.
- In the most of the theoretical papers $\Gamma = 1$.

Using the Bethe ansatz, Eggert, Affleck and Takahashi [8] developed an advanced model (EAT-model) which describes the temperature dependence of the spin susceptibility of the S=1/2 Heisenberg AFM chain at low temperatures (T<0.25J) more accurately. The obtained susceptibility using this model at low temperatures is larger than that of the Bonner-Fisher model, as shown in Figure 2.5.

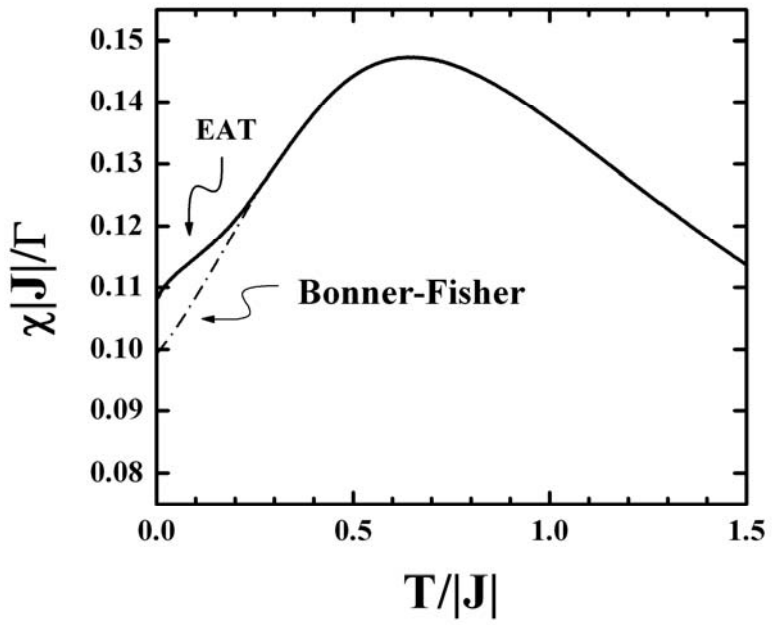


**Figure 2.5: Temperature dependence of the spin susceptibility for S=1/2 antiferromagnetic spin chain obtained by the Bonner-Fisher model [7] and EAT model (Eggert, Affleck and Takahashi ) [8].**

For both models the temperature dependence of the spin susceptibility at high temperatures (T > 0.3J) can be approximated numerically using the following relation [79].

$$\chi(T) = \frac{\Gamma}{T}\frac{0.25 + 0.74975x + 0.075235x^2}{1.0 + 0.9931x + 0.172135x^2 + 0.757825x^3}, \qquad x = \left|J\right|/T \qquad (2.8)$$

From equation (2.8) and the obtained $\chi_{\max}$ the AFM exchange constant J for a spin chain can be derived independently.

## 2.3.2 Spin-Peierls Transition

The spin-Peierls (SP) transition is a second order phase transition which occurs at a critical temperature $T = T_{SP}$ in a regular $S = 1/2$ Heisenberg antiferromagnetic chain of localized electrons. This transition results from a $2k_F$ instability.

In the TMTTF salts the spins are arranged in a regular chain of dimers at high temperatures, with one spin per dimer, see Figure 2.6.a. The spin-Peierls transition

results in a tetramerization of the molecular chains (dimerization of the dimers) as shown in Figure 2.6.b. This means that below the SP transition the spin chain forms singlet pairs by alternating the spacing between the spins. This results in forming two different AFM exchange constants $J_1$ and $J_2$. Here $J_1$ is the intradimer exchange constant and $J_2$ is the interdimer one and $|J_1| > |J_2|$. The resultant chain is then called alternating spin chain where the alternation parameter $\gamma(T)$ is given by the relation [11]:

$$\gamma(T) = \frac{1-\delta(T)}{1+\delta(T)} = \frac{J_2(T)}{J_1(T)}; \quad J_{1,2} = J[1 \pm \delta] \tag{2.9}$$

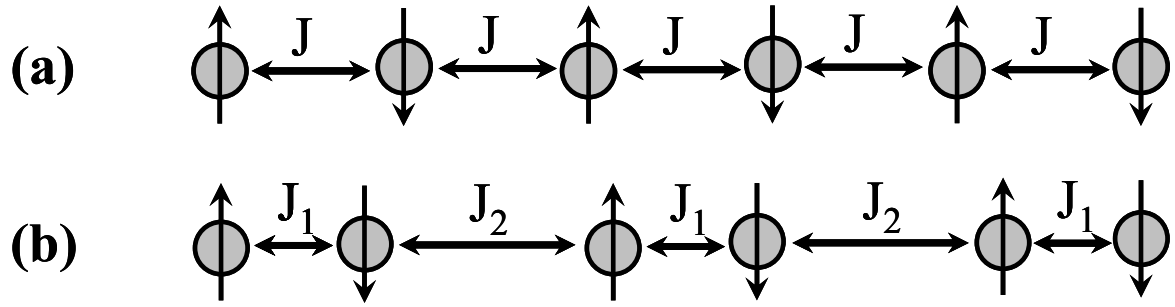


**Figure 2.6: The equidistant AFM Heisenberg spin chain with a uniform coupling constant J (a), and the distorted chain below $T_{SP}$ with two different AFM exchange constants $J_1$ and $J_2$ (b).**

This transition can be detected by measuring the temperature dependence of the spin susceptibility. The susceptibility of a uniform $S = 1/2$ 1-D antiferromagnetic chain has a finite value in the limit of $T \to 0$, indicating that this spin system is gapless. When the chain is elastically distorted to form dimers, the susceptibility of the resulting alternated chain approaches zero as $T \to 0$ even though the alternation is weak. This indicates that the tetramerization produces an energy gap $\Delta_\sigma$ between the singlet nonmagnetic ground state and the triplet excited state. When the energy gained in the formation of the singlet triplet energy gap exceeds the lattice distortion energy, the spin-Peierls phase transition takes place. The net effect of the distortion is to couple the $S = 1/2$ electronic spins of the chain into nonmagnetic $S = 0$ pairs. The singlet triplet gap was described by the mean field theory and can be calculated using the relation [12][I]:

[I] In this reference the factor is 1.723 and not 0.8615 as shown in equation 2.10, the difference here is due to the different definition of J, where J here equals 2J used in the reference.

$$\Delta_\sigma(T) = 0.8615 \ |J| * [\delta(T)]^{2/3} \tag{2.10}$$

The spin-Peierls transition is driven by one-dimensional structural fluctuations (spin Peierls fluctuations), such fluctuations start to develop at some temperature $T_{SP}^0$ above $T_{SP}$ [80]. The effect of these fluctuations is to induce a local pairing of the spins which leads to an observable deviation of the magnetic susceptibility below $T_{SP}^0$ from the general Bonner–Fisher behaviour. These fluctuations are of one-dimensional nature at $T_{SP}^0$ and become three dimensional on cooling from $T_{SP}^0$ to $T_{SP}$. Below $T_{SP}$ a long-range order is finally achieved, this long range-order causes a doubling of the lattice periodicity and the susceptibility decreases exponentially to the lowest temperatures. Below the SP transition the temperature dependent spin susceptibility can be described by the result which Bulaevskii [11] obtained from a Hartree-Fock approximation for an alternating 1-D AFM Heisenberg $S = 1/2$ chain.

$$\chi_s = \frac{\alpha(\gamma)}{T} \exp\left(-\frac{|J_1|\beta(\gamma)}{T}\right) \tag{2.11}$$

where α and β are tabulated in Ref. [11] for different values of the alternation parameter γ. For very low temperatures ($T \ll T_{SP}$) the alternation parameter is temperature independent, thus the spin susceptibility can be fitted as alternating spin chain with temperature independent alternation.

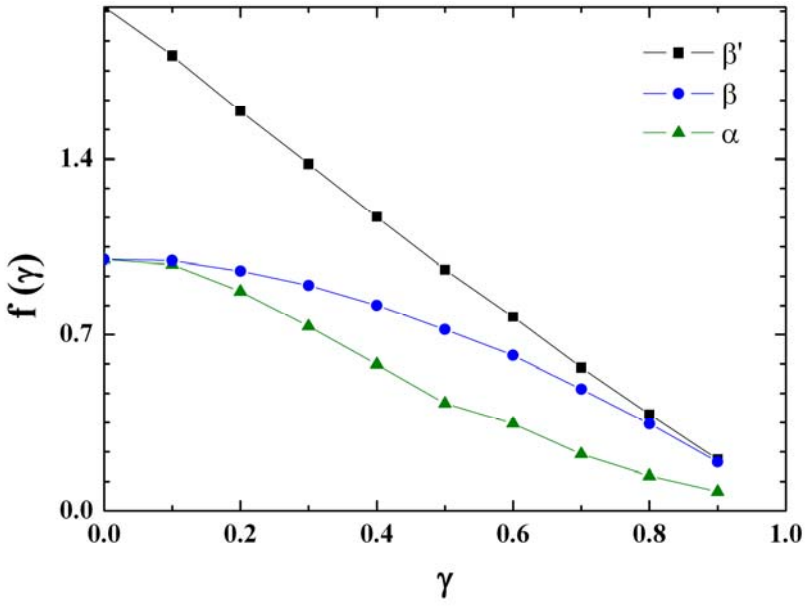


**Figure 2.7: The parameters α, β and β′ as function of the alternation parameter γ as given in Ref. [11]**

To fit the measured spin susceptibility using equation (2.11), the numerator of the exponential function $J_1\beta(\gamma)$ can be replaced by $J\left[1+\delta(\gamma)\right]\beta(\gamma) = J\beta'(\gamma)$ where $J_1 = J\left[1+\delta(\gamma)\right]$ and $\beta' = \left[1+\delta(\gamma)\right]\beta$. The value of $\beta'$ as a function of $\gamma$ for a given value of $\beta$ can be calculated using the previous relation and equation (2.9). The values of $\alpha, \beta$ and $\beta'$ as function of $\gamma$ are plotted in Figure 2.7.

## 2.4 Anion Ordering Transition

Although most of the physics of (TMT*C*F)$_2$X salts is governed by the organic molecules (the donors). Nevertheless, the anions, the presence of which is essential for electric neutrality may in some cases suppress the stability of the conducting phase and introduce a lot of physical phenomena. As a matter of fact, the possibility for (TMT*C*F)$_2$X compounds with non-centrosymmetrical anions to undergo a structural phase transition can modify the band structure and the topology of the Fermi surface. At room temperature non-centrosymmetrical anions such as $ClO_4$, $BF_4$, $ReO_4$, $NO_3$ and SCN have two (or more) equivalent orientations corresponding to short and long contacts between the Se or the S atoms of the TMTSF or TMTTF molecule, respectively and the peripheral electronegative atom of the anion, and so the inversion center is present on average only as shown in Figure 2.8.

This means that non-centrosymmetrical anions incorporated in the cavities delimited by the TMT*C*F molecules are disordered at room temperature. The room temperature orientational disorder is a unique property of the TMT*C*F salts because of the weak anion-donor interactions, probably due to the location of the anion in a well isolated cavity. At room temperature the tetrahedral anion has to choose its orientation between one of the two orientations, labeled I and II in Figure 2.8.a. The local potential experienced by each anion from its surrounding is thus composed of two symmetrical wells, as schematically shown Figure 2.8.b. The anion will be able to change its orientation if it can overcome the barrier potential $V_o$. An orientational ordering of the anions generally occurs upon cooling [81]. This ordering is achieved by the formation of superstructure through a structural phase transition (anion ordering transition). This phase transition affects strongly the electronic structure. The anion ordering critical temperature ($T_{AO}$), the critical wave vector ($q_{AO}$) and the order of this phase transition (1$^{st}$ or 2$^{nd}$ order) of some Fabre salts are summarized in Table 2.1.

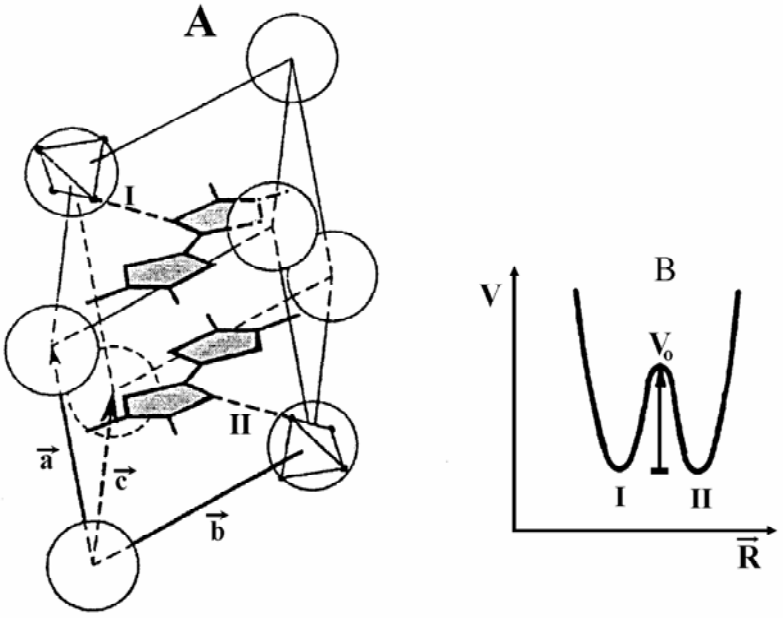


**Figure 2.8: The two possible orientations of a tetrahedral anion in TMTTF salt (a), and schematic representation of the potential experienced by such an anion from its surrounding (b). I and II label the contacts (bonds) between the outer (O or F) atoms of the anion with the sulfur atoms of the two inversion symmetry related organic molecules. These contacts determine the orientation of the anion in the cavity. From Ref. [31].**

| X | $T_{AO}$ (K) | Order | $q_{AO}$ | Ref. |
|---|---|---|---|---|
| $ReO_4$ | 154 | 1st | (1/2,1/2,1/2) | [82, 83] |
| $BF_4$ | 40 | 1st | (1/2,1/2,1/2) | [84] |
| $ClO_4$ | 70 | 1st | (1/2,1/2,1/2) | [85] |
| $NO_3$ | 50 | 2nd | (1/2,0,0) | [84] |
| SCN | 160 | 2nd | (0,1/2,1/2) | [86] |

**Table 2.1: The anion ordering phase transition parameters for some Fabre salts. $T_{AO}$ stands for the anion ordering transition temperature and $q_{AO}$ for the critical wave vector of the transition.**

Structural X-ray studies have shown that the anions adopt a well defined orientation below the anion ordering transition temperature. This transition is also accompanied by a shift of the anion from the center of the cavity delimited by the organic molecules; this causes a sizeable tetramerization (molecular displacements of about 0.1 Å in the case of the (1/2,1/2,1/2) superstructure) of the organic stacks. This is not the case in $(TMTTF)_2SCN$ which has an anion ordering transition at

160 K with (0,1/2,1/2) critical wave vector, where no superstructure reflections or diffuse scattering at the $a^*/2$ ($2k_F$) wave vector could be detected down to 18 K [86]. This means that the crystals are not perturbated along the stacking direction and there is no tetramerization of the organic stacks accompanied with this type of anion ordering. For TMTTF salts the anion ordering critical wave vector ($q_{AO}$) of the superstructure seems to depend on the shape of the anion. The $(1/2,0,0)$ AO is only found in the triangular $NO_3^-$ anion, but the $(1/2,1/2,1/2)$ AO is found in all the TMTTF salts with a tetrahedral anion and the $(0,1/2,1/2)$ wave vector is only found in $(TMTTF)_2SCN$ ($SCN^-$ is a linear anion).

In addition the AO is generally accompanied by an elastic deformation of the $P\bar{1}$ symmetry of the triclinic lattice and variations of the lattice parameters. Therefore the AO transition influences the electronic properties of the salt where it changes the electrostatic potential seen by the conduction electrons on the donor stacks. In the case of $(0,1/2,1/2)$ (as in $(TMTTF)_2SCN$) the anions establish long and short contacts with the TMTTF molecules along the stacks so that the inversion symmetry is lost. A $4k_F$ site potential is thus created by this AO periodicity. It adds in quadrature to the $4k_F$ bond potential as show in the following equation [31].

$$\Delta_D = \sqrt{(\Delta_D^b)^2 + (\Delta_D^s)^2} \tag{2.12}$$

where $\Delta_D^b$ is the $4k_F$ energy gap due to bond dimerization with inversion symmetry and $\Delta_D^s$ is the $4k_F$ energy gap due to bond dimerization without inversion symmetry. This increase of $\Delta_D$ leads to an enhancement of the charge gap $2\Delta_\rho$, this means it increases the charge localization phenomena. As the charge and spin degree of freedom are decoupled in Fabre salts, no change of the spin susceptibility is observed at $T_{AO} = 160$ K when the resistivity abruptly increases [20, 87].

In the case of $(1/2,1/2,1/2)$ AO wave vector (as in $(TMTTF)_2BF_4$) the stacks are tetramerized and this leads to a considerable deformation of the organic stacks. The tetramerization of the donor stacks leads to an exponentially decrease of the spin susceptibility below $T_{AO}$ because each two TMTTF dimers with spin 1/2 will be coupled and the system will go into a non-magnetic S = 0 ground state.

## 2.5 Charge Ordering (CO) in Fabre Salts

Charge order is self-organization of charge carriers in a superstructure, i. e. the charge carriers arrange themselves in distinct patterns. In case of static charge order

and if it includes all charge carriers of the conduction band, the charge ordered state is insulating. Most well known example is the stripe order in transition metal oxides like $La_{2-x-y}Nd_ySr_xCuO_4$ or $La_{2-x}Sr_xNiO_4$. Holes are accumulating in one-dimensional stripes in the domain walls separating antiferromagnetic regions. Spin and charge order in these materials has attracted attention of many scientists because they are closely related to high-temperature superconductors. In high-temperature superconductors like $La_{2-x}Sr_xCuO_4$ indications of fluctuation of spin and charge stripes were observed, which however do not order statically.

The charge ordering (CO) state was observed experimentally in the quasi-two dimensional conductor α-$(BEDT\text{-}TTF)_2I_3$ by IR spectroscopy [88][I] and in the quarter-filled molecular crystals $(DI\text{-}DCNQI)_2Ag$[II] by NMR measurements [89]. On the other hand, independently, Seo and Fukuyama [90] predicted the existence of charge disproportionation (CD) theoretically among the TMTTF molecules in Fabre salts. Afterward, the CO phenomenon has been extensively investigated hand in hand both experimentally and theoretically, and it turned out that CO frequently exists not only in quasi-1D compounds but also in quasi-2D organic compounds as well.

In order to study the charge ordering in 1/4 filled 1-D dimerized systems theoretically, the intersite Coulomb repulsion $V$ has to be introduced. This is done by the 1-D dimerized extended Hubbard model for quarter filled system (two spins per four sites as schematically show in Figure 2.9) which is defined by the following Hamiltonian [90].

$$\hat{H} = t_1 \sum_{i\ even,\ \sigma} (a_{i\sigma}^{+} a_{i+1\,\sigma} + h.c.) + t_2 \sum_{i\ odd,\sigma} (a_{i\sigma}^{+} a_{i+1\,\sigma} + h.c.) + U \sum_i n_{i\uparrow} n_{i\downarrow} + V \sum_i n_i n_{i+1} \quad (2.13)$$

where $\sigma$ is the spin index which takes $\uparrow$ and $\downarrow$, $n_{i\sigma}$, $a_i^{+}$ and $a_i$ are the number, the creation and the annihilation operators of the electron at the i[th] site and $n_i = n_{i\uparrow} + n_{i\downarrow}$, $U$ and $V$ are the onsite and the nearest neighbor (intersite) Coulomb interactions, respectively. $t_1$ is the intradimer transfer integral and $t_2$ is the interdimer one.

Using the Hamiltonian (2.13) and the mean field (MF) approximation, the existence of charge ordering in TMTTF compounds was predicted theoretically [90]. These calculations were carried out at T = 0 and fixed electron density at quarter filling. It

[I] In that time this phase transition was not called charge ordering phase.
[II] DI-DCNQI is 2,5-diiodo-dicyanoquinonediimine

was assumed that $t_1 \geq t_2$ so that the pairs of molecules (1-2) and (3-4) can be considered as dimers, see Figure 2.9.

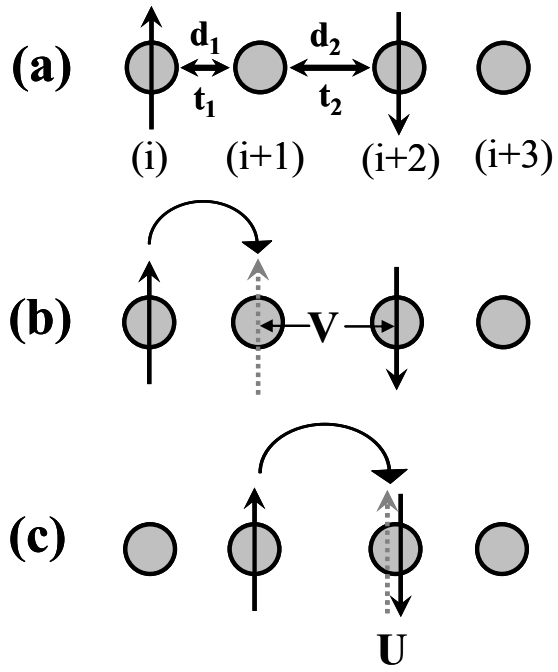


**Figure 2.9: Schematic view of the quarter-filled dimerized one dimensional antiferromagnetic spin chain (a), the sites 1 and 2 form one dimer; $t_1$ and $t_2$ are the intradimer and interdimer transfer integral, respectively. The intersite (V) and the onsite (U) Coulomb interactions are represented in (b) and (c), respectively.**

In the $t_1 >> V$ limit, the electron will be able to move within the dimer, this means the spin moment in each site will be the same ($S_Z(1) = S_Z(2) = -S_Z(3) = -S_Z(4)$), where $S_Z(i)$ is the spin moment at the $i^{th}$ site, and also the charge will be equally distributed between the sites (each TMTTF molecule has 0.5e charge) as depicted in Figure 2.10.a. Therefore, if the intersite Coulomb repulsion is not considered there will be no charge ordering.

In the presence of finite $V$ and for a fixed value of the reduced onsite repulsion ($U/t_2 = 5$), it was shown that a phase transition occurs at a critical value of the intersite interaction $V_c$ between two different types of spin distributions and the charge disproportionation δ is accompanied with this transition as shown in Figure 2.10.b and Figure 2.11. This means some TMTTF molecules will have a charge of 0.5+δ (rich charge sites) and other molecules 0.5-δ (poor charge sites), and also the rich charge site will have more spin density than the poor one ($S_Z$(rich charge site) $> S_Z$(poor charge site)).

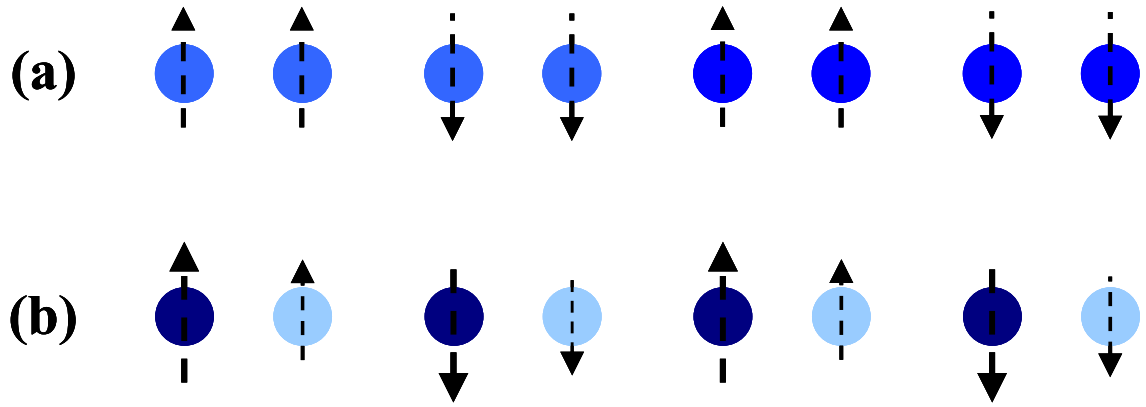


**Figure 2.10: (a) Schematic view of the quarter-filled one dimensional antiferromagnetic spin chain in case if the intersite Coulomb interaction is zero (V=0) where the charge and the spin are equally distributed between the sites (the charge of each site is 0.5 ). (b) Schematic presentation of the 1010 (rich poor rich poor) type charge ordering for V >$V_c$ and $U/t_2$=5, the length of the arrow represent the spin density on the site and the darkness of the circle represent the charge density where the charge of the dark blue sites is 0.5+δ and the light blue ones is 0.5-δ. The arrows are dashed in both cases to indicate that the electron can be in one site in the same time and not in both sites (quarter filled chain).**

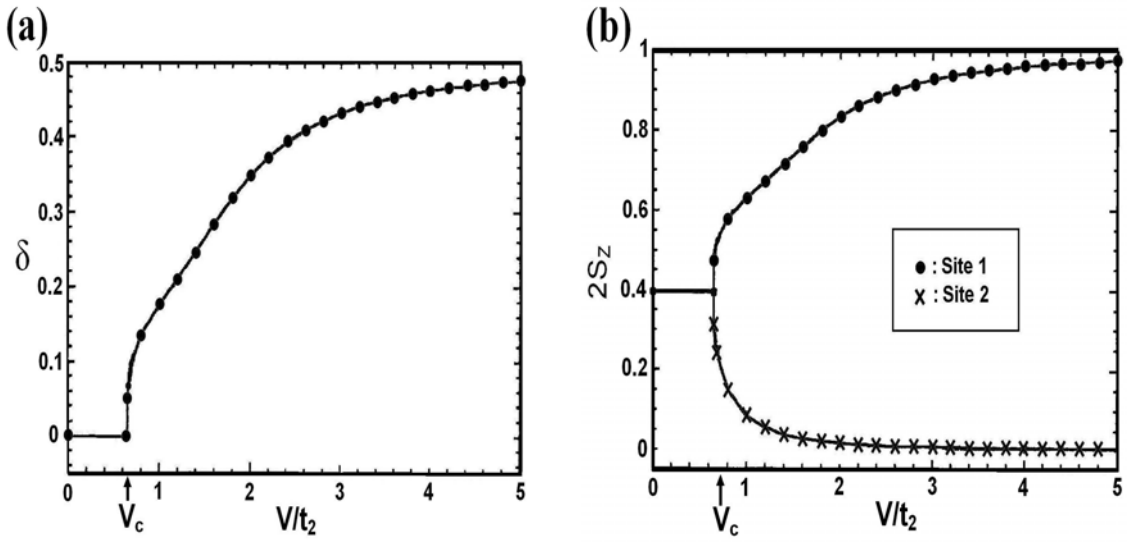


**Figure 2.11: The charge disproportionation (δ) (a) and the absolute magnitude of the spin moment per molecule $S_Z$ (b) as functions of the reduced intersite Coulomb interaction ($V/t_2$) for a fixed value of the reduced onsite Coulomb repulsion ($U/t_2$ = 5) and for $t_1/t_2$ = 1.1. From Ref. [90].**

This modulation of the charge is a $4k_F$ density wave (CDW) and this state can be considered as a Wigner crystal[I]. It was also shown that the charge disproportionation is approximately independent of the degree of dimerization.
These calculations apply for the TMTTF salts where the onsite interaction $U \approx 1$ eV and $t_2 \approx 0.2$ eV, thus the reduced onsite interaction $U/t_2 \approx 5$.
a more detailed theoretical study based on a bosonization scheme has been carried out by Yashioka et al [91]. This study is suitable for understanding the 1-D systems analytically by taking the quantum fluctuations into account.

## 2.6 Spin Density Waves (SDW)

Electron-electron interactions either attractive or repulsive, can lead to broken-symmetry ground states such as superconductivity (SC) or spin density wave (SDW). The SDW ground state is characterized by a periodic modulation of the electronic spin density which is related to the Fermi wave vector $k_F$. The spin density wave ground state can be expressed by the relation [92]:

$$S(x) = S_o \cos(q x + \phi) \qquad (2.14)$$

where $S_o$ and $\phi$ are the amplitude and the phase of the spin density, respectively.
The SDW has a well-defined magnetic character therefore magnetic investigations like ESR and NMR are powerful techniques to detect the SDW. Depending on the relation between the nesting vector $q$ and the lattice constant, the SDW can be two different types:

- If the nesting vector $q$ turns out to be an integer multiple of $\pi/a$ where $a$ is the spacing between the atoms, the spin density wave is commensurate with the lattice, a commensurate SDW results (Figure 2.12.a). An example of the commensurate SDW is the phase transition of $(TMTTF)_2SbF_6$ at 7 K.

[I] Wigner crystal was introduced for the first time by E. Wigner in 1934. He considered the effect of Coulomb interactions of electrons in metals. He found that a ground state of the electronic system where the electrons crystallize can exist, i.e. each electron is localized at a lattice site. This crystallization will occur only if the density of the electrons is low enough.

- If the nesting vector is not an integer multiple of $\pi/a$ then the spin density wave is incommensurate as shown in Figure 2.12.b. An example of the incommensurate SDW is the phase transition of $(TMTSF)_2AsF_6$ at about 12 K.

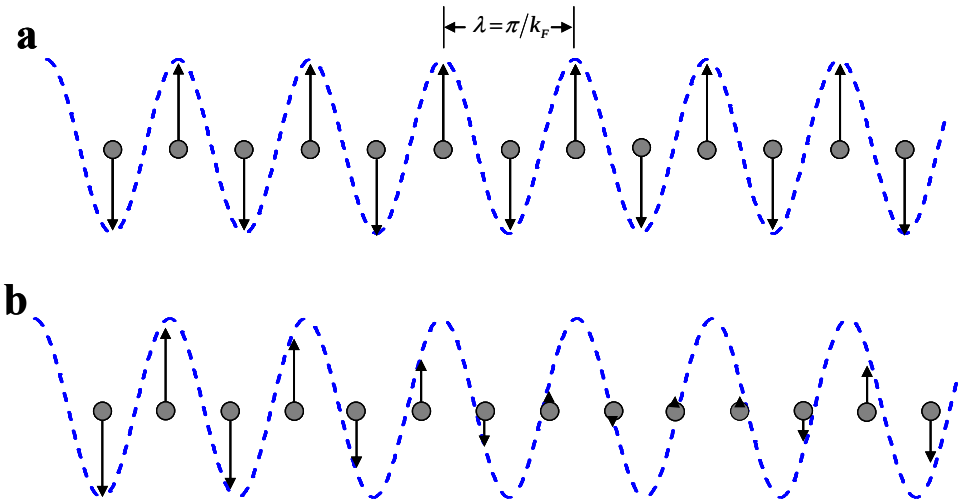


**Figure 2.12: Schematic representation of (a) the commensurate spin density wave with wave vector $q = \pi/a$ and (b) incommensurate spin density wave.**

Below the critical temperature ($T_N$) the spin susceptibility of the AFM ordered TMTTF and TMTSF salts shows a unique anisotropy. It decreases rapidly by decreasing the temperature if the magnetic field is applied parallel to the easy axis[I], while it shows a slight increase along the intermediate and the hard axes, as shown in Figure 2.13 for the $(TMTSF)_2AsF_6$ salt. This salt has a SDW transition at 12 K where the easy axis is parallel to the b'-axis, the hard and the intermediate axes are parallel to the c*- and a-axis, respectively. By increasing the magnetic field above a specific value - which is called the spin flop field - the spin susceptibility along the easy axis increases dramatically and becomes comparable to the susceptibility along the other two axes.

[I] The easy axis is the axis along which it is easy to magnetize the crystal.

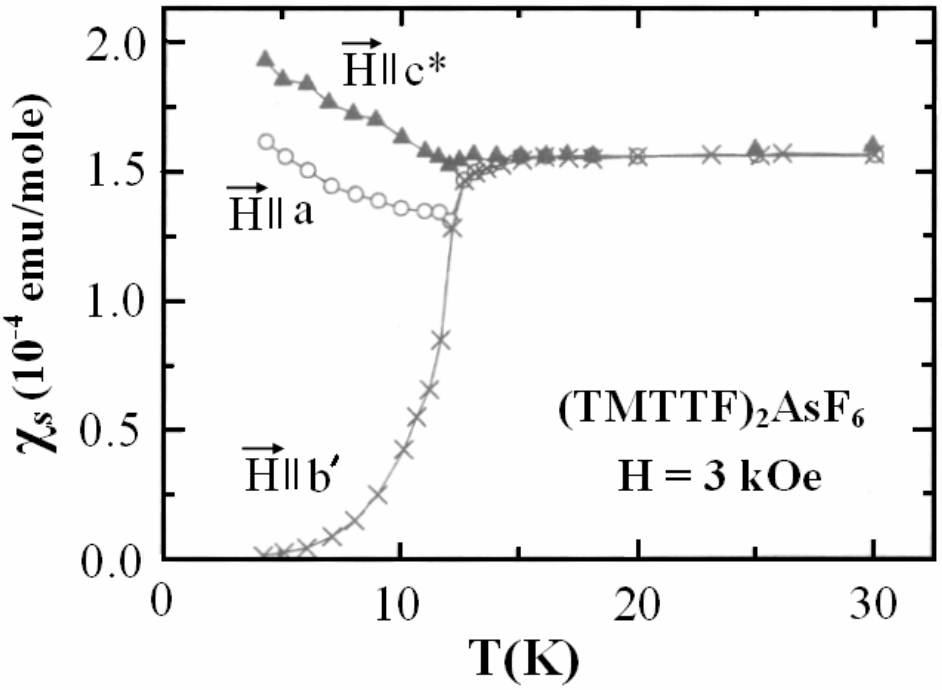


**Figure 2.13: The spin susceptibility of $(TMTSF)_2AsF_6$ with the field parallel to a, b' and c*-axes, respectively. The magnetic field H=3kOe is less than the critical spin-flop field. From ref. [93].**

## 2.7 Electrical Conductivity of 2-D Organic Conductors

Organic conductors can be divided mainly in two groups depending on their electrical conductivity. The first group includes the low-conducting semiconductors, the typical representatives of this group of organic materials are salts with 1:1 stoichiometry. Electrical conductivity of these materials at room temperature is normally in the range ($10^{-3}$-$10^{-6}$ $(\Omega\cdot cm)^{-1}$). In a wide range of temperatures the conductivity has thermally activated character (semiconducting behaviour), i.e., it is expressed by the formula

$$\sigma = \sigma_0 \exp(-E_a/KT) \tag{2.15}$$

where $E_a$ is the activation energy. The activation energy of these systems is relatively low and is most frequently limited to the range 0.1 to 0.4 eV [94]. The second group of organic conductors are the 2:1 salts whose most important

representatives are $(BEDT\text{-}TTF)_2X$ salts. These salts are organic metals at room temperature with a conductivity parallel to the conduction plane in the range of ($10^1$-$10^2$ $(\Omega \cdot cm)^{-1}$).

In conventional metals, the temperature dependence of the resistivity is given by the temperature dependence of the scattering rate $1/\tau$, this leads the resistivity to be proportional to the absolute temperature ($\rho \propto T$) at elaborated temperatures. The resistivity of the metallic organic salts, on the other hand, frequently exhibits stronger temperature dependence, as that of the quadratic relationship $\rho \propto T^2$ [57,95]. The quadratic temperature dependence is associated with electron-electron scattering [57]. However, in BEDT-TTF salts other considerations suggest that this quadratic dependence is due to the scattering by librational (twisting) modes of the organic donor molecule [95].

The most obvious electronic-transport feature is the strong anisotropy of the in-plane and out-of-plane conductivities. The real value of this anisotropy is difficult to be measured since any dislocation disturbing the in-plane transport will immediately lead to an enhanced resistance for that current direction.

## 2.8 Superconductivity in Organic Conductors

In a metal, conduction electrons obey the Fermi-Dirac statistics and Pauli's exclusion principle. As such, they are incapable of condensing in one energy state with a momentum equal to zero. Cooper has shown that if there is a slight attraction between two electrons, they can form a pair. A pair of this kind with integer spin does not obey Pauli's exclusion principle. In 1957, Bardeen, Cooper and Schrieffer [96,97] formulated a microscopic theory of superconductivity, presently known as BCS theory. According to this theory, the ground state of the whole electron system is separated from the excited state by a superconducting energy gap $\Delta(0)$:

$$2\Delta(0) = 3.54\ k_B\ T_c \tag{2.16}$$

where $k_B$ is the Boltzmann constant and $T_c$ is the superconducting transition temperature.

In the superconducting state the superconductor consists of electron-electron pairs with zero net momentum; the Coulomb repulsion between the electrons must be overcome to form these pairs. Within the BCS theory the repulsion energy between two electrons is overcome by an electron-phonon interaction, where the

lattice polarization induced by the first electron can attract a second electron of opposite momentum for some time after the second electron has moved away.

The most outstanding property of a superconductor is the complete disappearance of the electrical resistivity at the critical temperature $T_c$. The second fundamental property is the restore of the normal resistance if a magnetic field greater than a critical field $B_c$ is applied to the specimen. $B_c$ depends on both the material and the temperature. It is zero at $T_c$ and it increase as the temperature is decreased.

If a magnetic field $B_{ext.}$, which is less than $B_c$ is applied to a superconductor a persistent current will be induced in a direction which will oppose the effect of the applied field (Lenz's law). The field generated by this current will exactly cancel $B_{ext.}$ and the effective magnetic field inside the superconductor, $B_{int.}$, remains zero. If the external field is increased, when it reaches $B_c$ the persistent currents will vanish and $B_{int}$ will be equal to $B_{ext}$. If $B_{ext.}$ is now reduced then as it passes $B_c$ again, persistent currents are once more set up so that $B_{int.} = 0$ as in the initial state, this property is called the Meissner effect. The superconductor therefore acts as if it possesses a magnetic moment which opposes the external field and it is said to be perfect diamagnetic.

Superconductors are divided into two classes depending on the way in which the transition from the superconducting to the normal state proceeds when the applied magnetic field exceeds $B_c$. In type-**I** superconductors, as $B_c$ is reached, the entire specimen enters the normal state, the resistance increase above zero, the diamagnetic moment becomes zero and $B_{int.}= B_{ext.}$. In type-**II** superconductors the transition to the normal state is more gradual. At the first critical field $B_{c1}$, very small portions of the material become normal and the magnetic flux penetrate in these portions; this is called the mixed state. As the external field is further increased more normal portions are produced, each supporting a flux line, and the diamagnetic moment decreases. Only when a field $B_{c2}$ is attained the entire specimen become normal metal and the electrical resistance return. $B_{c1}$ and $B_{c2}$ are called the lower and the upper critical fields, respectively.

The superconducting properties of the organic superconductors resemble in many respects the behavior known from the cuprate superconductors. The organic superconductors are from type-**II** superconductors with low critical fields, $B_{c1}$, of only a few mT and upper critical fields, $B_{c2}$, of typically a few T (for field perpendicular to the conducting plane) [98].

# Chapter 3

# Experimental Work

In this work, different techniques were used to study the transport and magnetic properties of low-dimensional organic radical salts. In this chapter a short description of each technique will be given.

## 3.1 Electron Spin Resonance (ESR) Spectroscopy

Since the first observation by Zavoisky (1945) and the subsequent observation by Cummerow and Halliday (1946), "Electron Spin Resonance" (ESR) technique has initially been applied to non-interacting paramagnetic substances, commonly referred to as "Electron Paramagnetic Resonance" (EPR). There followed an important and fruitful period (1950-1960) of EPR research, in which much of our present-day understanding of the paramagnetic ions was established. The technique was immediately applied to ordered ferromagnets by Griffiths (1946) and Kittel (1947), referred to as "Ferromagnetic Resonance" (FMR) and antiferromagnets by Paulis (1953), and referred to as "Antiferromagnetic Resonance" (AFMR). In view of the presence of strong exchange fields and magnetic anisotropy, both FMR and AFMR in the magnetically ordered phases are completely different from ordinary EPR. They represent a coherent precession of the entire magnetization or sublattice magnetization around the effective fields and are most characterized by a nonlinear dependence of the resonance frequency on the external field, in contrast to EPR.
It was widely recognized that ESR technique is a very powerful and useful tool to study the magnetic properties from a microscopic point of view. In the past, quite a lot of ESR studies have been devoted to various ordered magnets, in order to elucidate the magnetic interactions, magnetic ground states, collective motions of interacting spin systems, critical behaviours near the phase transitions, and so on.

There are number of text books (see for example [99,100]) which extensively describe the theoretical and the experimental details of the ESR spectroscopy. In the

following sections a short introduction about the basic theory and the experimental techniques of the ESR spectroscopy will be given.

### 3.1.1 Basic EPR Theory

The phenomenon of electron paramagnetic resonance (EPR) is based on the fact that the electron is a charged particle which spins around its axis. In technical language we say: the electron has a magnetic moment $\vec{\mu}$ due to its spin $\vec{S}$:

$$\vec{\mu} = -g\mu_B \vec{S} = -\gamma_e \hbar \vec{S} \tag{3.1}$$

where $\mu_B = \frac{e\hbar}{2m_e}$ and $\gamma_e = \frac{g\mu_B}{\hbar}$

where g is the electronic g-value, for the free electron $g_e = 2.002319$, $\mu_B$ is the Bohr magneton, $\hbar = h/2\pi$ with Planck constant h, e is the elementary charge and $m_e$ the electron mass. The quantity $\gamma_e$ is called gyromagnetic ratio.

For a spin 1/2 system, in the absence of an external magnetic field, the two possible spin states with spin quantum numbers $m_s = +1/2$ and $m_s = -1/2$ will have the same energy and be equally populated. If an external magnetic field $\vec{H}_o = H_o \hat{z}$ is impressed on the system, the electron will align itself with the direction of this field and precess around this axis. Increasing the applied magnetic field will induce the electron to precess faster and acquire more kinetic energy. Practically, by applying external magnetic field the degeneracy of the spin states will be lifted (the so-called Zeeman splitting Figure 3.1). This means that the magnetic field will divide the electrons into two groups. In one group the magnetic moments of the electrons are aligned parallel to the magnetic field, while in the other group the magnetic moments are aligned antiparallel to the external field. The energy difference between the two states becomes $\Delta E = g\mu_B H_0$. If a second weaker alternating magnetic field $\vec{H}_1$ oscillating at a microwave frequency is now applied perpendicular to the static field $\vec{H}_o$ (as shown in Figure 3.2), then the electron can be tipped over when the microwave frequency is equal to the precession frequency of the electron around the magnetic field.

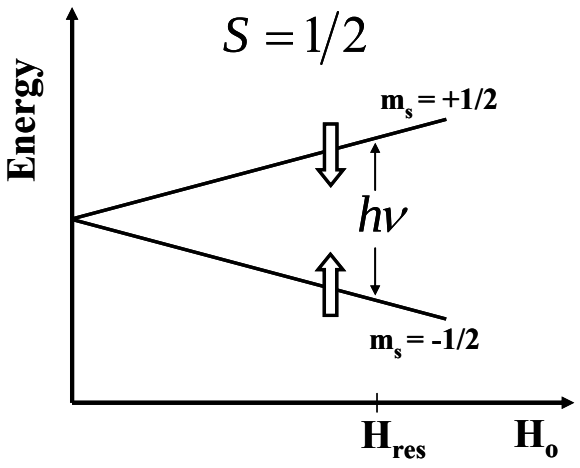


**Figure 3.1: Zeeman splitting of the free electron spin levels in an external magnetic field.**

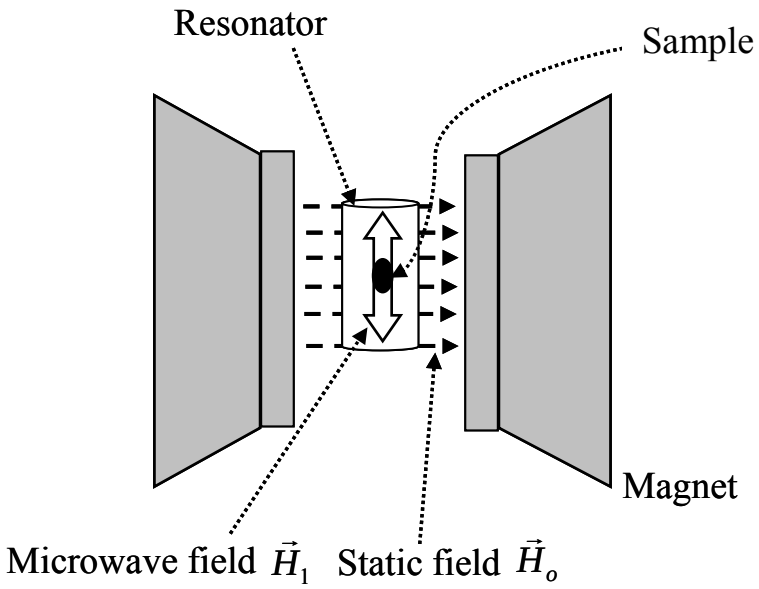


**Figure 3.2: Principle arrangement of the ESR experiment showing the direction of the microwave magnetic filed ($\vec{H}_1$) with respect to the static magnetic field ($\vec{H}_o$).**

Another way to describe the phenomenon of EPR is to say that the quanta of the incident microwaves induce transitions between the two states of the unpaired electron. When the energy $h\nu$ of these quanta coincides with the energy level separation between the two states, the resonance absorption of energy takes place as described in equation 3.2.

$$\Delta E = h\nu = g\mu_B H_{res} \tag{3.2}$$

The incoming radiation hν absorbed by the electrons in the lower energy level will induce them to jump into the higher energy state. However, the electrons in the higher energy level jump down to the lower level, a phenomenon called stimulated emission. Since the coefficients of absorption and stimulated emission are equal, no net value would be observed if the spin population were equally distributed between these two levels. In general, the population of the ground state ($n_1$) exceeds the population of the excited state ($n_2$), and a net absorption of microwave radiation takes place. The population ratio of these two states at the temperature T can in most cases be described by the Boltzmann distribution.

$$\frac{n_1}{n_2} = \exp(-\Delta E/k_B T) \tag{3.3}$$

Where $k_B$ is the Boltzmann constant. Thus the system can absorb the electromagnetic radiation from an external source of frequency ν if the basic resonance condition is fulfilled. Since ESR measures absorption, due to the slightly greater population of the lower level, this difference should be made as large as possible to enhance the measured signal. For that, one can measure at low temperatures or use a high magnetic field. The ratio $n_1/n_2$ is approximately 0.999 if one uses an X-band spectrometer ($\nu$=9.5 GHz) at room temperature, this means even with a very small difference in the population one can see the ESR signal for a lot of materials.

### 3.1.2 The ESR Apparatus.

For the ESR measurements in this work a commercial continuous wave (CW) X-band spectrometer (BRUKER ESP 300) was used. The microwave source is a

klystron tube operating at a frequency 9.5 GHz and a maximum power output 200 mW.

Figure 3.3 shows the general layout of the ESR (BRUKER ESP 300) spectrometer. The electromagnetic radiation source and the Schottky barrier detector diode are in a box called the microwave bridge. The sample is in a microwave resonator (cavity), (see section 3.1.3). The field strength of the electromagnet, which ranges from 50 to 13000 G, is measured and controlled by the field controller. The computer is used for coordinating the units for acquiring a spectrum. Although many spectrometer designs have been produced over the previous years, the vast majority of laboratory instruments are based on the simplified block diagram shown in Figure 3.3.

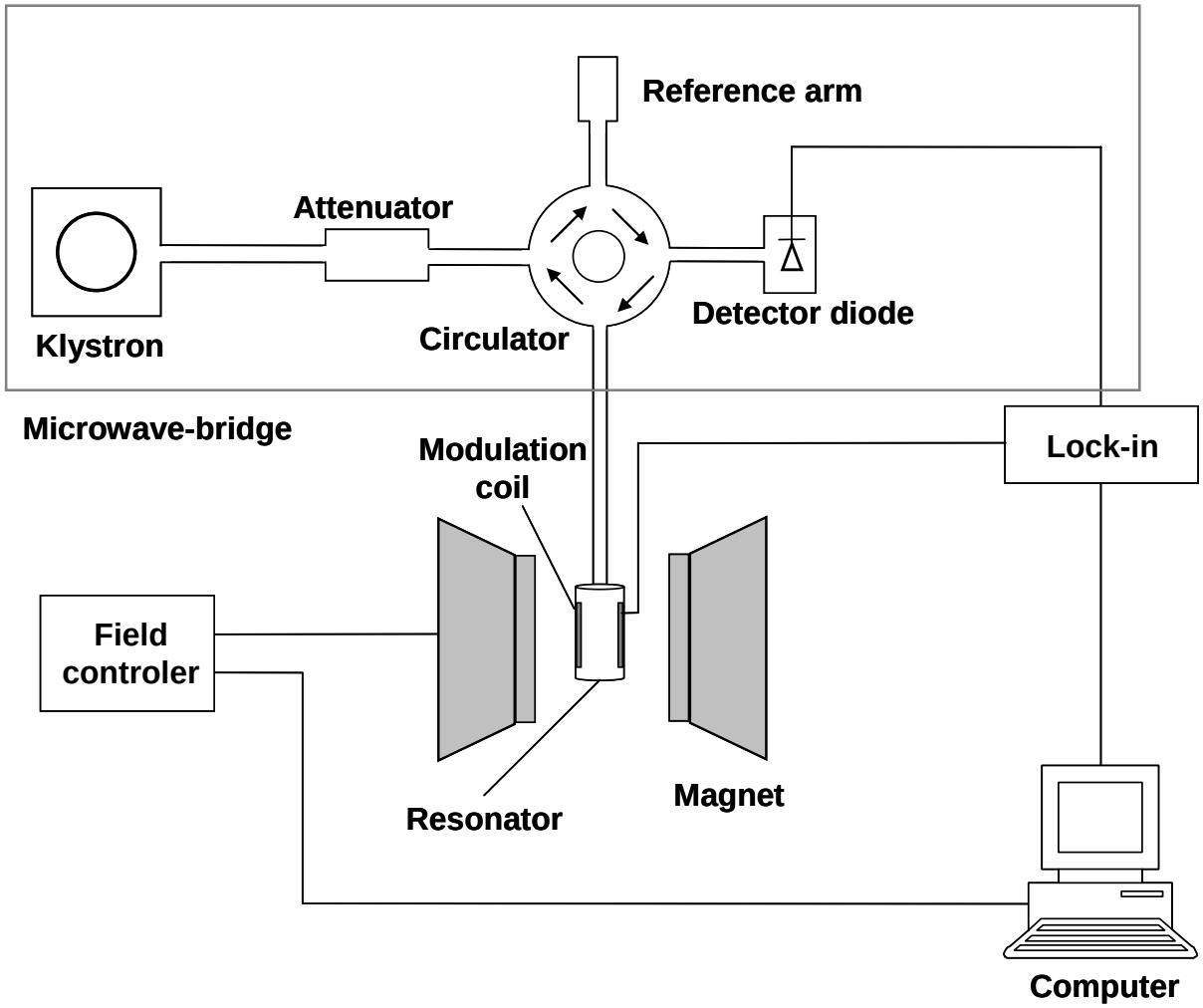


**Figure 3.3: Block diagram of the ESR (BRUKER ESP 300) spectrometer.**

The output power of the klystron can be varied using the attenuator, a device which blocks the flow of the microwave radiation. With the attenuator, one can precisely and accurately control the output microwave power.

The Bruker ESP 300 is a reflection spectrometer; this means it measures the changes (due to spectroscopic transitions) in the amount of radiation reflected back from the microwave cavity. The direction of the microwave radiation is controlled by the circulator, where the microwaves coming from the klystron through the circulator only go to the cavity and not directly to the detector, and the reflected microwaves are directed only to the detector and not back to the microwave source. The detector diode is mounted along the *E*-vector of the plane-polarized microwaves and thus produces a d.c. current proportional to the microwave power reflected from the cavity. Thus, in principle, the absorption of microwaves by the sample can be detected by noting a decrease in the d.c. current which can be measured by a micro ammeter. In practice, such a d.c. current would be far too noisy to be useful. To increase the signal-to-noise ratio, small amplitude field modulation is introduced. An oscillating magnetic field is super-imposed on the d.c. field by means of small modulation coils, usually built into the cavity walls.

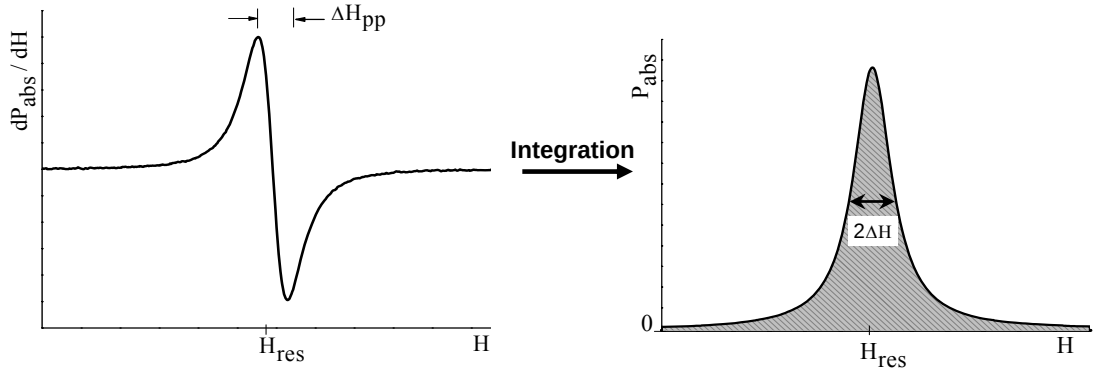


**Figure 3.4: The derivative of the ESR absorption signal $dP_{abs}/dH$ (which is measured directly by the ESR apparatus) (left), and the absorption signal $P_{abs}$ (right) as a function of the static magnetic field H. For a Lorentzian line the relation between the peak to peak linewidth ($\Delta H_{pp}$) and the half width of half maximum line (HWHM) ΔH is $\Delta H = \sqrt{3}\,\Delta H_{pp}/2$. The area under the absorption line is proportional to the spin susceptibility.**

When the field is in the vicinity of a resonance line, the modulation field is swept back and forth through part of the line, leading to an a.c. component in the diode

current. This a.c. component is amplified using a frequency selective amplifier with small bandwidth (lock in amplifier), thus eliminating a great deal of noise. The modulation amplitude is normally less than one tenth of the linewidth. Therefore the detected a.c. signal is proportional to the change in sample absorption. As a result of modulating the magnetic field, the detected signal appears as a first derivative of the absorption signal, as shown in Figure 3.4. In all ESR measurements of this work the modulation frequency was 100 kHz.

### 3.1.3 The ESR Cavity

The microwave cavity is a box fabricated normally from highly conductive metal with dimensions comparable to the wavelength. At resonance, such a cavity sustains microwave oscillations, which form an interference pattern (standing wave configuration) from superposed microwaves multiply reflected from the cavity walls. This means that the cavity stores the microwave energy; therefore, at the resonance frequency no microwaves will be reflected back from the cavity, but will remain inside it. Each particular cavity size and shape can sustain oscillations in a number of different standing wave configurations called modes.

Cavities are characterized by their quality factor (Q), which indicates how efficiently the cavity stores microwave energy. As the quality factor increases, the sensitivity of the spectrometer increases. The quality factor of a cavity is defined as:

$$Q = \frac{2\pi(power \quad stored \quad in \quad the \quad cavity)}{(power \quad dissipated \quad per \quad cycle)} \tag{3.4}$$

Energy can be dissipated to the side walls of the cavity because the microwaves generate electric current in the side walls which in turn generates heat, therefore the quality factor of the cavity depends on the conductivity of the material from which the cavity is made and the geometry of the cavity.

Since most of the samples have no-resonant absorption of the microwave via the electric field, it is the magnetic field that drives the absorption in ESR. Therefore, the sample has to be placed in the electric field minimum and the magnetic field maximum to obtain the largest signal and the highest sensitivity of the cavity. In our ESR setup we are using a Bruker cylindrical dielectric cavity (Type: ER4118X-MD) which has a $TE_{011}$ mode as illustrated in Figure 3.5. The quality factor of this cavity

at room temperature is 4000. The microwave is supplied to the cavity from the microwave bridge by a semi-rigid coaxial cable.

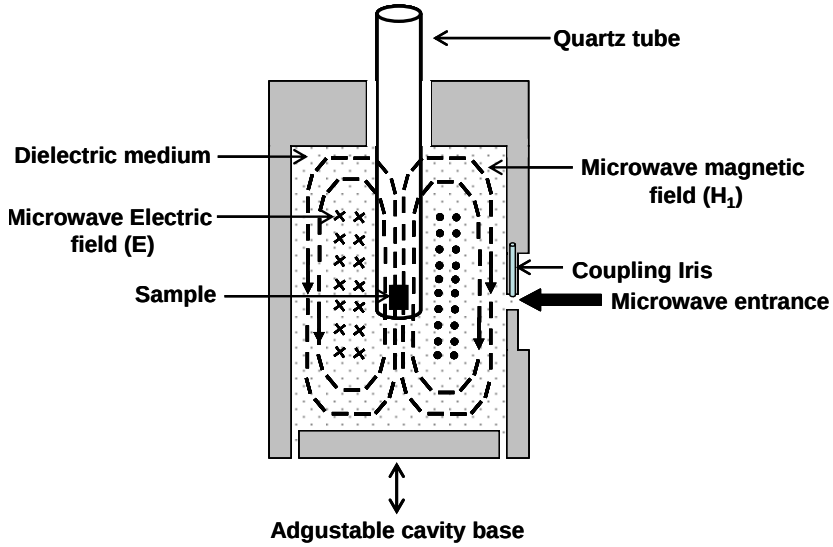


**Figure 3.5: The electromagnetic field pattern in the dielectric cavity mode $TE_{011}$. (•) Direction up from the paper; (+) direction into the paper; (--) $H_1$ lines of force.**

### 3.1.4 Low Temperature Measurements

For the low temperature measurements a Cryovac continuous-Helium flow cryostat is used (Figure 3.6). Using this cryostat, one can achieve very stable temperatures from room temperature down to 4.2 K.

The operating temperature is achieved by using a heat exchanger mounted on the bottom of the sample chamber. In the heat exchanger, a GaAs temperature control diode and a heater are installed. The ESR cavity, which contains the sample, is mounted inside the cryostat. The thermal contact between the heat exchanger and the sample is achieved by inserting $^4$He exchange gas at ambient pressure inside the sample chamber. The sample is mounted approximately 5 cm above the heat exchanger, this leads to a slight difference between the temperature reading by the GaAs sensor and the sample temperature (the real sample temperature is expected to be slightly higher). To avoid that, another temperature sensor (CGR sensor) was attached to the cavity to measure the sample temperature. The good accuracy of the temperature measurement (about 0.5 %) was checked by

measuring the spin density wave (SDW) transition temperate for a $(TMTSF)_2PF_6$ sample.

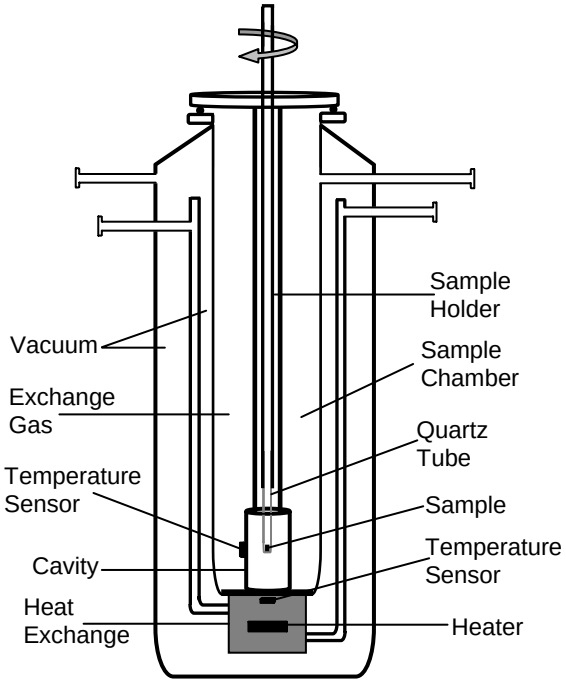


**Figure 3.6: Schematic view of the $^4$He Cryovac continuous flow cryostat with a cavity inserted.**

The samples were fixed to a 4 mm quartz tube (or rod) using silicon vacuum grease (for the BEDT-TTF salts) or paraffin (for the $(TMTTF)_2X$ salts), then they were covered by another 5 mm quartz tube to avoid soiling the cavity. The sample holder can be rotated around the vertical axis using a goniometer. To perform the ESR measurements along all crystal axis and also to perform the orientation dependence measurements along all the crystal planes, the samples were fixed to the quartz tube in different ways as shown in Figure 3.7.

The microwave power supplied into the cavity was below 1 mW in order to avoid saturation of the ESR spectra[I]. The modulation amplitude was always kept less than one-tenth of the linewidth to prevent distortion of the lineshape due to over-modulation. The g-value was determined by comparing the resonance position of the measured ESR signal with that of DPPH (1,1-Diphenyl-2-Picryl-Hydrazyl). In

[I] The physical reason for the phenomenon of saturation is that for large magnetic field $H_l$, i. e. for high microwave power, or long spin-lattice relaxation time $T_1$ the populations of the two Zeeman-split energy levels of the spin system will become more and more equal. In the limit of complete saturation there will be no population difference anymore, thus there is no net absorption of energy from the microwave field and no ESR signal can be detected.

the case of Dysonian lineshape (see below), the peak-to-peak linewidth of the pure-absorption portion was derived by assuming a linear combination of Lorentzian absorption and dispersion.

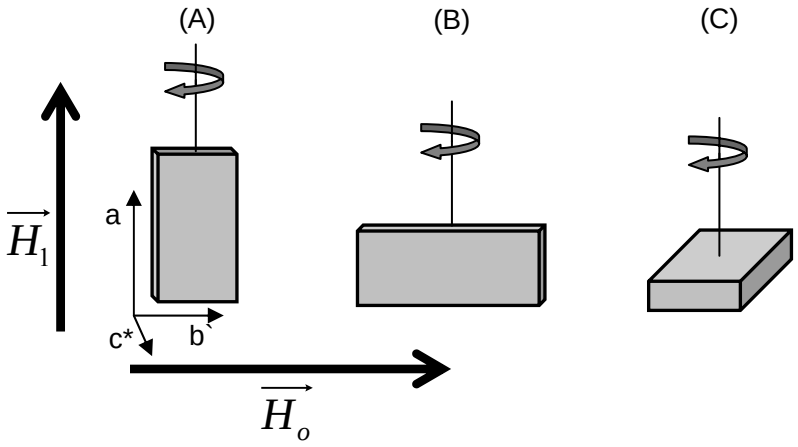


**Figure 3.7: Orientations of the crystal with respect to the static magnetic field ($H_0$), and the microwave magnetic field ($H_1$). The crystal principle axis of the $(TMTTF)_2X$ crystal are shown in (A). The crystal can be rotated around the a-axis (A), b′-axis (B) or c*-axis (C).**

### 3.1.5 Information Deduced from the ESR Signal

After the basic theoretical and experimental description of the ESR spectroscopy, it is now important to show which quantities are accessible during an ESR experiment and how the desired microscopic information can be deduced from these quantities. A lot of information can be deduced from the electron spin resonance absorption spectra. The main four characteristics which can be deduced are:

- The lineshape
- The linewidth
- The g-factor
- The spin susceptibility

A great deal of information about the studied spin system can be obtained from a careful analysis of the width and the shape of the resonant absorption line. A simple and intuitive way to investigate the dynamic behaviour of a spin system

during a continuous wave (CW) resonance experiment is to consider the relaxation effects, this is done usually by means of the Bloch equations [101].

$$\frac{d\overrightarrow{M_z}}{dt} = -(\overrightarrow{M} \times \gamma_e \overrightarrow{H})_z + \frac{\overrightarrow{M}_o - \overrightarrow{M}_z}{T_1} \tag{3.5}$$

for i = x or y one gets:

$$\frac{d\overrightarrow{M_i}}{dt} = -(\overrightarrow{M} \times \gamma_e \overrightarrow{H})_i - \frac{\overrightarrow{M}_i}{T_2} \tag{3.6}$$

where $T_1$ and $T_2$ are the spin-lattice and the spin-spin relaxation times, respectively. $\overrightarrow{M}_o$ is the equilibrium magnetization. Bloch equations describe the time dependence of the magnetization components ($\overrightarrow{M}$) along the three space coordinates in terms of $T_1$ and $T_2$ assuming that the static magnetic field ($H_o$) is applied parallel to the z-axis.

### 3.1.5.1 The linewidth

The main assumption in the Bloch equations is that the magnetization decays exponentially to reach the equilibrium. From Bloch equations, the dynamic susceptibility and therefore the shape of the absorption ESR line can be deduced. Far from the saturation, the microwave absorption power can be written as:

$$P_{abs}(H) \propto \frac{\Delta H + \alpha(H - H_{res})}{(H - H_{res})^2 + \Delta H^2} \tag{3.7}$$

where $0 \le \alpha \le 1$. For a Lorentzian absorption $\alpha = 0$ [102,103].

Note that in ESR one mostly encounters the so-called peak-to-peak linewidth ($\Delta H_{pp}$) which is defined as the distance between points of maximum slope of the absorption line (see Figure 3.4). In the first derivative this appears

simply as the distance between the maximum and the minimum of the curve, this explains its wide-spread use in ESR practice. The peak-to-peak linewidth differs from the half width at half maximum (HWHM or ΔH) by a numerical factor which depends on the particular lineshape (for a Lorentzian line $\Delta H = \sqrt{3}\Delta H_{pp}/2$).

The linewidth of a Lorentzian absorption ESR line is given by the relation [104,105]:

$$\Delta H \approx \frac{\hbar^2}{g\mu_B |J|} M_2 \tag{3.8}$$

where $M_2$ is the second magnetic moment and J is the anisotropic exchange coupling constant. The main factors which contribute in the broadening of the ESR absorption line are [105]:

- The hyperfine interaction of the electron with the nuclear spin

$$\Delta H_{h.f.}(10^4 Oe) \approx \frac{A_{\parallel}^2}{g_e \mu_B |J|} = 1.71156 \times 10^{-9} \times \frac{\left[A_{\parallel}(MHz)\right]^2}{|J(K)|} \tag{3.9}$$

$A_{\parallel}$ is the anisotropic hyperfine interaction constant of the relevant nucleus.

- The magnetic dipole-dipole interaction

$$\Delta H_{d-d}(10^4 Oe) \approx \frac{\mu_0^2 \mu_B^3 g_e^3}{(4\pi)^2 |J| d^6} = 46.3786 \ \frac{1}{|J(K)| \ \ (d(\mathring{A}))^6} \tag{3.10}$$

where *d* is the distance between each two dipoles.

- The anisotropic exchange interaction

$$\Delta H_{A.E.}(10^4 Oe) \approx \frac{|J|}{g_e \mu_B} \left(\frac{\Delta g}{g}\right)^4 = 0.04625 (\Delta g)^4 |J(K)| \tag{3.11}$$

- The anisotropic Zeeman interaction

$$\Delta H_{Zee} \approx g_e \mu_B \left(\frac{\Delta g}{g_e}\right) \frac{H_o^2}{|J|} \approx 3.36 \times 10^{-7} \frac{\left(H_o(Oe)\right)^2 \Delta g^2}{|J(K)|} \tag{3.12}$$

The conduction electron spin resonance linewidth has been correlated to the spin orbit coupling (the g-shift) and the electron scattering rate ($\tau^{-1}$) for 3D isotropic metals by use of Elliot formula [106].

$$\Delta H \propto (\Delta g)^2 \tau^{-1} \tag{3.13}$$

where $\Delta g = g - 2.0023$ measures the spin orbit coupling. However, this relation fails to give the right magnitude and temperature dependence of the ESR linewidth of quasi-one dimensional (Q-1D) organic conductors. For example, in the case of tetrathiafulvalene-tetracyanoquinodimethane (TTT-TCNQ) ΔH is three orders of magnitude lower than the expected value from the known scattering time and spin-orbit interaction, and it increases with decreasing temperature although $\tau^{-1}$ is decreasing as measured in resistivity [107]. The Elliot formula can not be applied for quasi-one dimensional metals because the on-chain scattering causes no electron relaxation. This means, in strictly 1D system, no spin relaxation can occur.

In order to account for the observed linewidth of Q-1D systems the first theoretical treatments have introduced a partial two dimensional (2-D) character of the electronic state [108,109]. In Weger's approach the measure of the 2D character was $\tau_{\|}/\tau_{\perp}$ ($\tau_{\|}$ is the on-chain scattering time and $\tau_{\perp}$ is the interchain tunnelling time), which modifies the Elliot formula to.

$$\Delta H \propto (\Delta g)^2 \tau_{\|}^{-1} \frac{\tau_{\|}}{\tau_{\perp}} = \frac{(\Delta g)^2}{\tau_{\perp}} \tag{3.14}$$

## 3.1.5.2 The lineshape

The ESR line of the examined organic conductors normally have a symmetric Lorentzian shape because of the strong exchange narrowing in these materials, nevertheless for some orientations of the crystal with respect to the static magnetic field and for high conducting big samples, one frequently detects an asymmetric lineshape known as Dysonian line. This lineshape was predicted theoretically by Dyson [102], and was observed experimentally for the first time by Feher and Kip in metals [103]. The physical origin of the Dysonian lineshape is the fact that the incident microwave field only penetrates a conductive sample to a certain depth, the skin depth ($\delta$), which is given by the relation:

$$\delta = \left( \frac{1}{\sigma \pi f \mu_o} \right)^{1/2} \tag{3.15}$$

where σ is the electrical conductivity of the material, $\mu_o$ is the permeability of the free space ( $\mu_o = 4\pi \times 10^{-7}$ (Henries/m) ) and $f$ is the frequency of the microwave. The penetration depth decreases by increasing the conductivity of the sample. The Dysonian lineshape is a mixture of the absorptive and dispersive parts of a Lorentzian line as depicted in Figure 3.8.

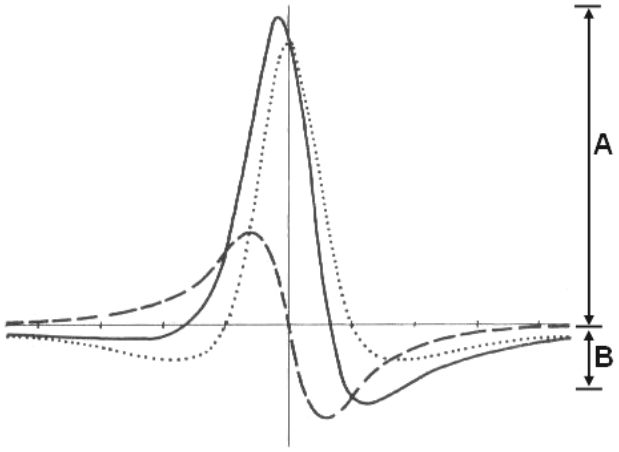


**Figure 3.8: Superposition of the derivative of a Lorentzian absorption curve (dashed) and a dispersion curve (dotted) to give a typical Dysonian lineshape (solid).**

The mixture occurs since the phase of the radio frequency (rf) field changes as it propagates into the metal. Then when the phase-sensitive detector is set to detect the absorption of electrons at the surface, it will detect a mixture of absorption and dispersion by electrons at greater depth of the sample. A frequently used and very sensitive measure of the lineshape is the $A/B$ ratio, that is, the ratio of the maximum peak to the minimum peak. For a Lorentzian absorption, $A/B = 1$, while for dispersion $A/B = 8$. For Dysonian lines the ratio $A/B$ is related to the electrical conductivity of the material [110,111].

### 3.1.5.3 The g-factor

In low dimensional organic conductors, like in any metal, the g-factor is a second rank tensor. In these materials the three components of this tensor are always close to the free electron value. Anisotropy in the g-value arises from coupling of the spin

angular momentum with the orbital angular momentum. The spin angular momentum is oriented with the field, but the orbital angular momentum, which is associated with electrons moving in molecular orbitals, is locked to the molecular wave function. The small deviation of the g-values from the free electron value is due to the effect of the internal magnetic field ($H_{int}$) which acts on the conduction electron from the surrounding environment. This means that the effective magnetic field ($H_{eff}$) which acts on the conduction electron is the vector sum of the applied magnetic field and the local magnetic field as shown in the following equation.

$$\vec{H}_{eff} = \vec{H} + \vec{H}_{\text{int}} = \frac{g}{g_e}\vec{H} \tag{3.16}$$

In this case the components of the g-tensor can be obtained by a perturbation theory, following the A. J. Stone's theory [112].

$$g_{\alpha\alpha} = g_e - 2\sum_n \sum_{i,j} \frac{\langle \psi_0 / \xi_i I_{\alpha i} / \psi_n \rangle \langle \psi_n / I_{\alpha j} / \psi_0 \rangle}{E_n - E_0} \tag{3.17}$$

where α = x, y or z, $g_e$ is the g-value of the free electron ($g_e$ = 2.002319), $\psi_0$ is the single occupied molecular orbital (SOMO), and $\psi_n$ denotes one of the double occupied or unoccupied orbitals. $E_0$ and $E_n$ are the energies of these orbitals, $\xi_i$ is the spin-orbit coupling of the atom i and $I_{\alpha i}$ is the α component of the orbital angular momentum operator for the atom i. Equation (3.17) shows that the g-tensor is essentially a characteristic property of the radical ion. Eigendirections can be deduced from the molecular symmetry, whereas corresponding eigenvalues reveal the nature of the molecular orbitals. For example, for a planar molecule like TMTTF, eigendirections are respectively along the short and the long axis of the molecule and perpendicular to the molecular plane. These axes are the local eigendirections for a single molecule; this is also the eigendirections for the whole solid if all of the molecules have the same orientation [113].

Finally, if the single crystal is rotated in the ESR cavity around one arbitrary direction the measured g-value will be a function of the orientation of the crystal with respect to the field. If the molecular axis x, y and z are the eigendirections of the g-tensor, general algebra on second rank tensor gives

$$g^2 = g_x^{\,2}\cos^2\alpha + g_y^{\,2}\cos^2\beta + g_z^{\,2}\cos^2\gamma \tag{3.18}$$

where α, β and γ are the angles between the static magnetic field H and the x, y and z axes, respectively. If the crystal is rotated in a specific plane (let us say xy-plane), and if the angle between the applied magnetic field and the x-axis is θ, then one obtains

$$g^2 = g_x{}^2 \cos^2\theta + g_y{}^2 \sin^2\theta \tag{3.19}$$

### 3.1.5.4 The spin susceptibility

For any system under magnetic resonance study the complex magnetic susceptibility $\chi(\omega)$ is given by

$$\chi(\omega) = \chi'(\omega) - i\chi''(\omega) \tag{3.20}$$

where the real part $\chi'(\omega)$ produces a frequency change in the resonance cavity and the imaginary part $\chi''(\omega)$ leads to energy absorption. The microwave absorbed power $P_{abs}$, which is proportional to the ESR signal intensity (the area under the ESR absorption signal), is proportional to $\chi''(\omega)$ [99,114].
From Kramers-Kronig relations we get for the electron spin susceptibility $\chi_e^s$:

$$\chi_e^s = \frac{2}{\pi\ H_{res}} \int_0^\infty \chi''(H)dH \ \propto \ \int_0^\infty P_{abs}(H)dH = I \tag{3.21}$$

The intensity of a Lorentzian absorption line is given by

$$I = \frac{2\pi}{\sqrt{3}} y'_{\max}\, \Delta H_{pp}^2 \tag{3.22}$$

where $\Delta H_{pp}$ is the peak to peak linewidth and $y'_{\max}$ is the maximum amplitude of the derivative of the ESR absorption signal. Since $\chi_s^e$ is proportional to *I*, only a relative value of the spin susceptibility can be measured by ESR. The absolute value of the spin susceptibility can be determined by comparing the intensity of the ESR signal with the intensity of the ESR line of a standard sample of known spin susceptibility as for example a DPPH sample. By using ESR one measures the spin susceptibility and not the bulk susceptibility of the sample as in the case of the SQUID

magnetometer or other techniques. In the other techniques one measures the bulk susceptibility which is the sum of the spin and the core diamagnetic susceptibility of the constituent atoms.

In this work the spin susceptibility could not be measured using ESR in a broad temperature range (especially on the high temperature region), because the cavity is inserted inside the cryostat and thus its temperature is changing with the sample temperature. This change of the cavity temperature affects the intensity of the measured signal because by changing the cavity temperature the conductivity of its material and the dielectric constant of the dielectric material in the cavity are changed, and thus its quality factor is a function of temperature.

### 3.1.6 Antiferromagnetic Resonance (AFMR)

When an antiferromagnetic phase transition occurs, the sample is no longer in the a paramagnetic phase. This means that the spin cannot be considered as independent species anymore and spin interactions play an important role. To describe the dynamics of these spins, the simplest description introduces an internal field superposed to the applied external magnetic field [115]. This approximation (mean field approximation) is a good approximation for temperatures not too close to the transition temperature where the magnetic ordering appears. In this critical region, more sophisticated theories may be necessary to interpret the experimental data. Antiferromagnetic resonance (AFMR) is a very sensitive technique to probe long-range magnetic order and can be performed in organic conductors, The AFMR theory [116,117] is a generalization of ESR when long-range magnetic order is present. The frequencies of the collective excitations of the spins that experience both the external field and internal fields (exchange and anisotropy) depend strongly on the orientation and magnitude of the external field.

Figure 3.9 represents the dependence of the resonance frequencies ($\omega$) for a material with maximal anisotropy at T = 0 when the field is applied along the easy axis (along which the anisotropy energy is minimum).

In a conventional spectrometer the field can be scanned to find the resonances (for a fixed frequency). When the single-crystal sample is rotated around a given axis, rotation patterns such as those shown in the

Figure 3.9 can give the resonance fields ($H_r$) as a function of the rotation angle.

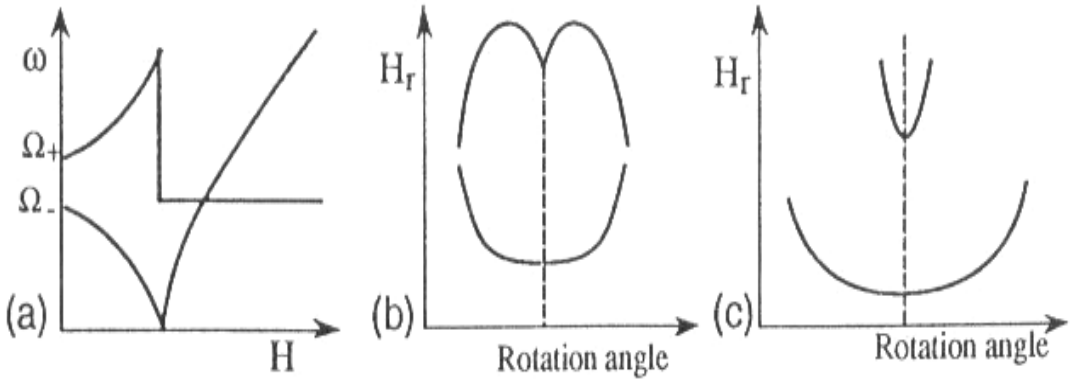


**Figure 3.9: (a) Frequency versus field when the field H is applied along the easy axis. (b) Rotation pattern in the easy–intermediate plane. (c) Rotation pattern in the easy-hard plane, $H_r$ is the resonance field, $\Omega_+$ and $\Omega_-$ are the magnetic energies. From ref. [116]**

## 3.2 The SQUID Magnetometer

A SQUID (superconducting quantum interference device) is based on the quantum interference effect in superconducting Josephson junctions. A basic SQUID consists of two Josephson junctions in parallel and relies on the interference of the currents from each junction. SQUIDs employ a quantum effect that enables cooper pairs of electrons to "tunnel" through a thin layer of insulation separating one superconductor from another. This setup is known as a Josephson junction. The amount of current able to pass through a Josephson junction is very sensitive to the magnetic environment.

The dc SQUID uses two Josephson junctions (point a and b in Figure 3.10), each of which is typically just a few microns across, to form an interferometer as shown in Figure 3.10, An electrical current tunnels through the two junctions, and the output voltage displays an interference pattern. Any change in the nearby magnetic field that is being measured produces a change in the current passing through the Josephson's junctions, and therefore a change in the interference pattern. Readout circuitry immediately applies enough voltage to the SQUID to enable it to restore its interference pattern, and that voltage is used as a measure of the change in the magnetic field. Therefore the magnetic moment of the sample can be measured using the SQUID by measuring the change in the flux due to moving of the sample

inside the SQUID loops. More details about the operation of the SQUID magnetometer can be found in books (see for example [118])

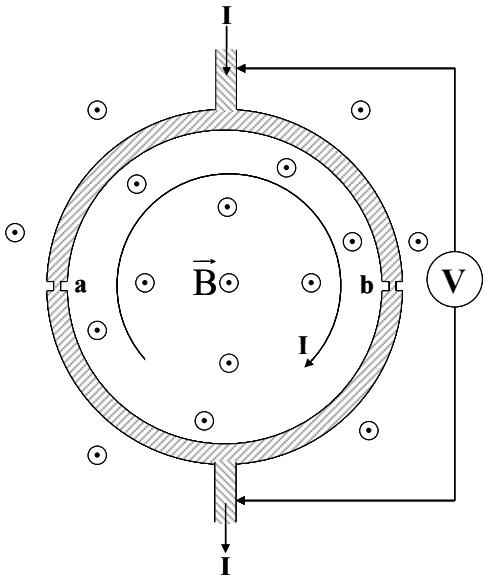


**Figure 3.10**: **The superconducting quantum interference device (SQUID)**

The high sensitivity of the SQUID ($10^{-8}$ emu or better) is the reason for choosing it for magnetization measurements. The dc magnetic susceptibility measurements in this work have been performed using a Quantum Design (MPMS) XL SQUID magnetometer. The MPMS system contains a high precision temperature control system, allowing measurements between 1.8 K and 400 K with an accuracy of 0.01 K, and a superconducting magnet, giving a field up to 7 Tesla with an accuracy of 0.1 G. The SQUID dewar consists of a liquid helium reservoir inserted inside a liquid nitrogen jacket to reduce excessive liquid helium boil off. The liquid helium is used both for maintaining the magnet in a superconducting state and for cooling the sample. Samples are mounted within a plastic straw and connected to one end of a sample rod which is inserted into the dewar. The other end is attached to a stepper motor which is used to position the sample within the center of the SQUID pickup coils. The background signal from the holder was measured and subtracted in order to obtain the intrinsic magnetization of the sample.
By the SQUID magnetometer one measures the magnetic moment of the sample. To calculate the total magnetic susceptibility one can use the relation:

$$\chi_{\text{magnetic}}\,(\text{emu/mole}) = \frac{\text{magnetic moment (emu)}}{B(\text{G})} \times \frac{M\,(\text{g/mole})}{m\,(\text{g})} \qquad (3.23)$$

where $B$ is the applied magnetic field, $M$ is the molecular mass of the sample and $m$ is the mass of sample. The magnetic susceptibility of the sample ( $\chi_{\text{magnetic}}$ ) is a sum of the diamagnetic susceptibility of the core electrons $\chi_{\text{core}}$ and the spin susceptibility $\chi_{\text{s}}$ of the conduction electrons. Therefore to calculate the spin susceptibility one can use the equation

$$\chi_{\text{s}} = \chi_{\text{magnetic}} - \chi_{\text{core}} \qquad (3.24)$$

## 3.3 The dc Resistivity Measurements

The electrical conductivity of low-dimensional organic conductors is a physical quantity which can be measured with a relative easy method (despite certain difficulties connected with electric anisotropy of these crystals as well as their very small sizes). It is a source of vital information concerning the studied material. By dc conductivity measurement one can investigate the transport properties of materials like metals, semiconductors, insulators and superconductors as a function of temperature. By this measurement, one can find the critical temperature of some phase transitions and can learn about the anisotropy of the transport properties of the examined material.

In this work the dc resistivity was measured using the standard four points method. This method was applied for the first time by Coleman [119] to measure the electrical resistivity of organic single crystals. In this method four contacts are attached on the sample, the current is initiated into the crystal by the two outside contacts and the voltage is measured over the two internal contacts (Figure 3.11 (a)). By this procedure one avoids the error of measuring the contact resistance because the voltmeter internal resistance is high and thus a small and a negligible current will flow through the contacts. From the measured current and voltage and depending on the sample dimensions which has to be measured, the electrical resistivity can be calculated.

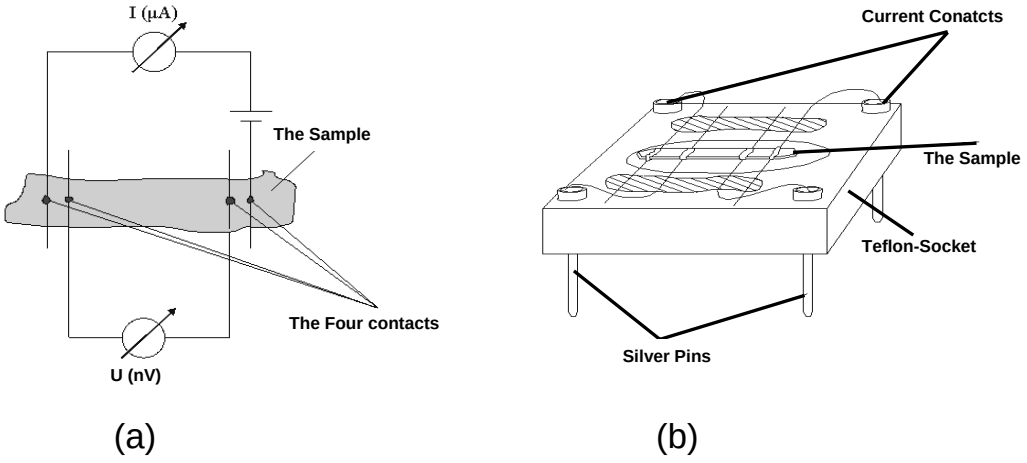


**Figure 3.11: (a) The four contacts method for the dc measurement, and (b) the sample socket.**

For a better electrical contact between the sample and the 25 μm gold wires, four thin gold films are deposited on the sample surface and the gold wires are connected to these thin films. As sample base a teflon socket (10x10x4 $mm^3$) with four silver pins at its corners and a central drilling hole for the sample is used (Figure 3.11 (b)). With a very steady low-temperature adhesive (Oxford Varnish GE7231), the four gold wires are attached over the drilling hole. The sample is connected to the four gold wires with carbon paint (Dotite paint Xc-12), whereby for easier processing, the carbon paint is diluted with a solvent (2-Butoxyethyl Acetate). The ends of the gold wires are stuck into the silver pins of the teflon socket using silver paint (Provac AG P RHC 140 20).

To perform the dc measurement along different orientations the sample can be connected in different ways as depicted in Figure 3.12.

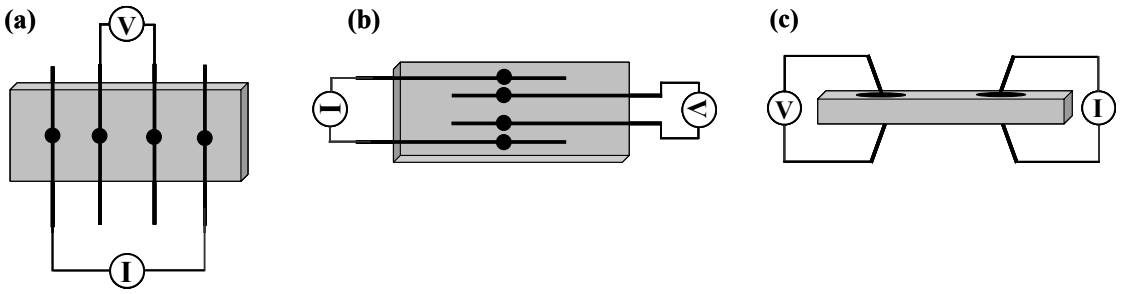


**Figure 3.12: The dc contacts along different directions of the single crystal**

For the temperature dependence measurements, a helium bath cryostat with nitrogen isolating jacket is used. Two sample sockets can be mounted on the teflon mounting plate at the lower end of a steel sample holder. Between the two sockets a temperature diode sensor type DT-470 is mounted. The sample holder is driven by a motor to the cryostat bath where it passes through the temperature gradient. The temperature inside the cryostat varies gradually from liquid Helium temperature (4.2 K) in the bottom of the cryostat to room temperature at the upper end of it. To reach 1.3 K the Helium steam can be evacuated using a vacuum pump. To control the measuring instruments and the driving motor an HP computer with a control software program is used.
The measuring procedures run now as follows:

After filling the isolating jacket with liquid nitrogen and the cryostat with liquid helium, the sample holder which holds the two samples is clamped into the mounting plate linkage above the cryostat path in such a way that it is heading inside the cryostat. The computer supervises the stability of the temperature[I] and inserts appropriate waiting periods if the temperature is instable. After the thermal stability of the samples is reached the computer creates a current signal of $10\,\mu A$ from a regulated current source to the first sample and measures its voltage. In the case that the measured voltage is situated below the measuring range of the nanovoltmeter, the computer sends a current signal of $20\,\mu A$ and measure the voltage again. Afterwards the second sample is measured in the same way. From these measurements and using the entered samples dimensions the computer calculates the electrical resistivity of each sample at the measured temperature.

After that the sample holder continues lowering down small distance inside the cryostat by the driving motor. After reaching the new temperature the above measuring procedures are repeated.

[I] The stability of the temperature is checked by measuring the sample temperature two times within 20 seconds and checking the difference between the two measurements.

# Chapter 4

# Electron Spin Resonance on $(TMTTF)_2X$ Salts

Ever since the discovery of the first organic charge transfer salt, electron spin resonance has played a major role in understanding the physical properties of these materials. ESR investigations were always from the first steps to study the new synthesized organic radical salts. This can be understood if one realizes that ESR is observable in most of the organic conductors while very few "ordinary" metals show detectable ESR signals, even at low temperatures. This feature results principally from the low dimensionality of these systems which controls the spins relaxation process [108,109]. This tendency is even reinforced by the fact that organic molecules mostly contain mainly light chemical elements like C, O, H, S,.., for which the effect of the spin-orbit coupling on the ESR linewidth is small. For this reason, even on small single crystals, electron spin resonance spectroscopy is certainly a major probe to investigate the paramagnetic state of organic conductors. Moreover, this spectroscopy is an important tool to probe different magnetic ground states.

## 4.1 Studied Materials

In this Chapter detailed electron spin resonance and SQUID investigations of single crystals of the quasi-one dimensional organic charge transfer salts $(TMTTF)_2X$ ($X=AsF_6$, $SbF_6$, $BF_4$ and SCN) will be presented and discussed. All the investigated single crystals were grown electrochemically in the crystal growth laboratory of the 1. Physikalisches Institut, Universität Stuttgart by Mrs. Gabriele Untereiner and the TMTTF molecule were synthesized in the group of Prof. H. J. Keller - the University of Heidelberg and by Prof. L. K. Montgomery - the department of chemistry, Indiana University, USA.

The electron spin resonance (ESR) spectra were measured using a continuous wave X-band spectrometer (Bruker ESP 300) operating at 9.5 GHz. For the ESR measurements a relatively small single crystal was sufficient to observe a clear ESR absorption spectrum even at room temperature, the typical dimensions of the single crystals used for the ESR measurements are: a ~ 2 mm, b' ~ 0.5 mm and c* ~ 0.1 mm, where a, b' and c* are the perpendicular three axes of the single crystal and not the unit cell coordinates (see Figure 3.7). We applied the least-square method for calculating the linewidth and the resonance field from the observed ESR spectra[I]. The g-value was determined by comparing the resonance field of the measured ESR signal with that of DPPH. In the case of a Dysonian lineshape, the linewidth of the pure-absorption portion was derived by assuming a linear combination of Lorentzian absorption and dispersion. For the different ESR measurements of the same salt, some times different crystals from the same batch were used.
The susceptibility measurements were performed using the SQUID magnetometer. A big amount of single crystals was needed to perform the susceptibility measurements. For this reason, more than one single crystal was used; the crystals were fixed parallel to each others using vacuum grease inside a plastic straw (the magnetic field was applied parallel to the a-axis for all the crystals). The masses of the crystals used for the SQUID measurements and the applied magnetic fields are listed in Table 4.1.

| | $(TMTTF)_2X$ | | | |
|---|---|---|---|---|
| X | $SbF_6$ | $AsF_6$ | $BF_4$ | SCN |
| m (mg) | 28.9 | 20.3 | 8.2 | 3.6 |
| B (G) | 2000 | 3000 | 5000 | 10000 |

**Table 4.1: The masses of the $(TMTTF)_2X$ (X= $SbF_6$, $AsF_6$, $BF_4$ and SCN) single crystals and the applied magnetic field for the SQUID measurements.**

The spin susceptibility of the sample was calculated using equation 3.23 and 3.24. The molecular masses for the different salts are listed in Table 1.1.

Several ESR and other magnetic investigations of the quasi-one dimensional organic conductors $(TMTCF)_2X$ were performed by other groups [see for example: 20,37,120,121,122,123,124,125]. These previous studies mainly focused on the

[I] We are using a software program called meascom which was provided by T. Kurz and H. A. Krug von Nidda from the Institut für experimental Physik V of the Universität Augsburg.

physical properties of the ground states of the TMTCF salts. In this work we are concentrating on the recently discovered charge-order state in the $(TMTTF)_2X$ salts. The investigated samples were additionally characterized by dc measurements as shown in Figure 1.5.

## 4.2 Room Temperature ESR Measurements

In the first step, room temperature investigations have been performed to determine the principle magnetic axes by studying the angular dependence of the linewidth and the g-value when the single crystal is rotated around the three crystal axes (a, b' and c*). At room temperature we observed a single conduction electron ESR signal ($g \sim 2$) for all investigated salts along all directions. The resulting ESR spectra for all orientations revealed a symmetric Lorentzian lineshape (in some cases a Dysonian line was observed if a big crystal is measured when the static magnetic field is applied parallel to the a-axis). The typical observed ESR spectra at room temperature for $(TMTTF)_2AsF_6$ are shown in Figure 4.1 as an example.
The resonance field ($H_{res}$) and the linewidth have a distinct anisotropy: The largest linewidth and the smallest resonance field (largest g-value) are observed when the static magnetic field ($B_o$) is applied parallel to the c*-axis (parallel to the long molecular axis of the TMTTF molecules). And the smallest linewidth and g-value are observed when the static field is applied parallel to the a-axis (perpendicular to the molecular plane of the TMTTF molecules). The same anisotropy was observed for all investigated salts at room temperature.

The anisotropy in the g-value arises from the spin orbit coupling (the coupling between the spin angular momentum and the orbital angular momentum of the conduction electron) [112,113], as shown in equation (3.17). The spin angular momentum is oriented parallel to the magnetic field, but the orbital angular momentum of the conduction electron which is delocalized on the molecular orbitals, is locked to the molecular wave function. This means that the eigendirections of the g-tensor are deduced from the molecular symmetry, i.e for a planar molecule as TMTTF the largest g-shift is observed when the static magnetic field is applied parallel to the long axis of the molecule, the intermediate value when it is applied parallel to the short axis of the molecule and the smallest when it is applied perpendicular to the molecular plane. Since the TMTTF molecules are all parallel and stacked along the a-axis as discussed in section 1.2.1 (see Figure 1.4), one expects to observe the largest g-value parallel to the c*-axis and the smallest

parallel to the a-axis as shown in Figure 4.1. This result suggests that the g-values of TMTTF-salts are essentially determined by the g-tensor of the TMTTF cations.

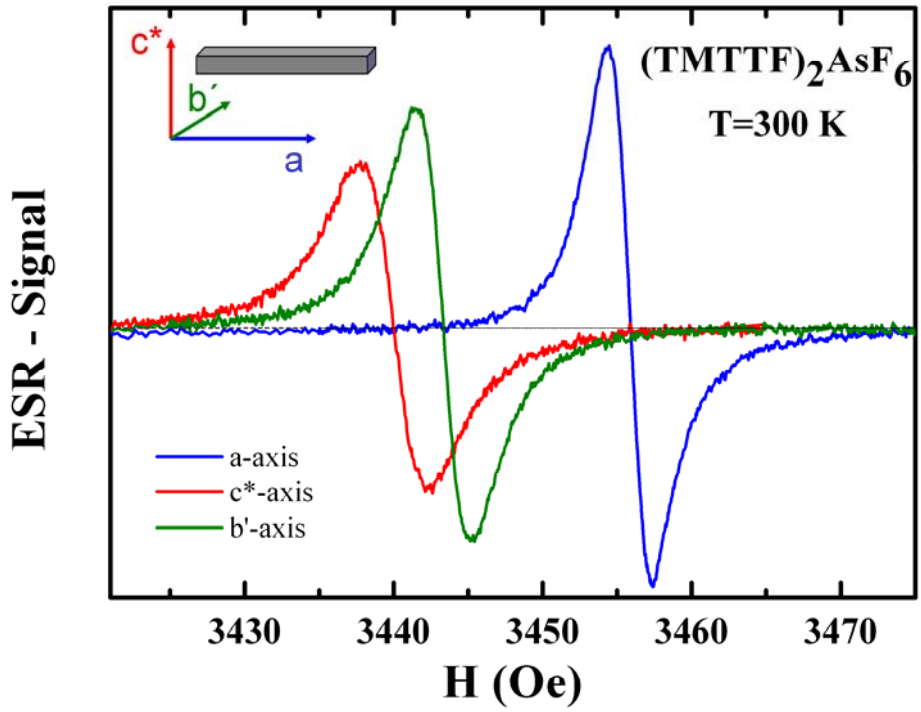


**Figure 4.1: ESR spectra of $(TMTTF)_2AsF_6$ single crystal at room temperature when the static magnetic field $B_0$ is applied parallel to the three crystal axes a, b' and c* (see the insert).**

| | | $(TMTTF)_2X$ | | | |
|---|---|---|---|---|---|
| X | | $AsF_6$ | $SbF_6$ | $BF_4$ | SCN |
| $\Delta g\ (10^{-3})$ | a | -1.04 | -0.93 | -1.06 | -1.04 |
| | b' | 6.12 | 5.78 | 6.08 | 6.00 |
| | c* | 8.10 | 7.92 | 8.17 | 7.87 |
| $\overline{\Delta g^2}\ (10^{-6})$ | | 34.71 | 32.33 | 34.95 | 33.01 |
| $\Delta H$ (Oe) | a | 2.63 | 2.51 | 2.80 | 2.87 |
| | b' | 3.09 | 3.11 | 3.39 | 3.49 |
| | c* | 4.09 | 3.91 | 4.30 | 4.43 |
| $\overline{\Delta H}$ (Oe) | | 3.27 | 3.18 | 3.50 | 3.60 |
| $\overline{\Delta H}/\overline{\Delta g^2}$ (kOe) | | 94.3 | 98.4 | 100.14 | 109.05 |

**Table 4.2: The obtained ESR linewidth and the g-shift for $(TMTTF)_2X$ (X=$AsF_6$, $SbF_6$, $BF_4$, SCN) at room temperature, where $\overline{\Delta H} = (\Delta H_a + \Delta H_{b'} + \Delta H_{c^*})/3$ and $\overline{\Delta g^2} = (\Delta g_a^2 + \Delta g_{b'}^2 + \Delta g_{c^*}^2)/3$.**

The values of the g-shift, the linewidth along the three crystal axes, the mean value of the squares of the g-shifts ($\overline{\Delta g^2} = (\Delta g_a^2 + \Delta g_{b'}^2 + \Delta g_{c^*}^2)/3$) and the reduced linewidth ($\Delta H_{red} = \overline{\Delta H}/\overline{\Delta g^2}$) where $\overline{\Delta H} = (\Delta H_a + \Delta H_{b'} + \Delta H_{c^*})/3$ of the investigated salts are tabulated in Table 4.2.

It should be mentioned that the crystals of the salts $(TMTTF)_2X$ (X = $AsF_6$, $SbF_6$ and $BF_4$) typically have the following shapes: the long crystal axis // the a-axis, the intermediate axis // the b'-axis and the short one // the c* axis. In the case of $(TMTTF)_2SCN$ the situation is different: the long crystal axis // the a-axis, the intermediate one // the c*-axis and the short one // the b'-axis, as depicted in Figure 4.2. This finding was confirmed by performing x-ray measurement on single crystal of $(TMTTF)_2SCN$ [126]. The abnormality of $(TMTTF)_2SCN$ can be due to the linear shape of the SCN anion.

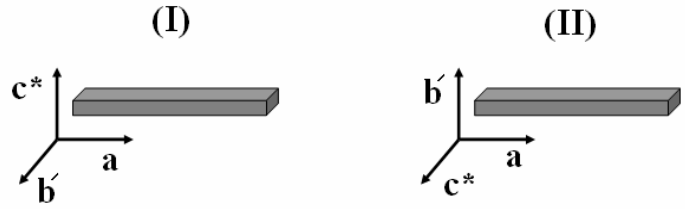


**Figure 4.2: Crystal axes of $(TMTTF)_2X$ (X=$AsF_6$, $SbF_6$ and $BF_4$) (I), and of $(TMTTF)_2SCN$ (II).**

The angular dependent measurements of the g-value and the linewidth when the crystal is rotated around the a-axis ($B_o$// b'c*-plane) and around the c*-axis ($B_o$// ab'-plane) of $(TMTTF)_2AsF_6$ at room temperature are shown in Figure 4.3. For the measurements along both planes the linewidth and the g-value have the same angular dependence (same anisotropy). This is a strong indication that the spin phonon interaction is the dominant scattering process at high temperatures.

In both cases the angular dependence of the linewidth and the g-value can be fitted by the relations:

$$\Delta H(\theta) = \left[\Delta H^2(0°)\cos^2(\theta) + \Delta H^2(90°)\sin^2(\theta)\right]^{1/2} \tag{4.1}$$

$$g(\theta) = \left[g^2(0°)\cos^2(\theta) + g^2(90°)\sin^2(\theta)\right]^{1/2} \tag{4.2}$$

where θ is the angle between the static magnetic field ($B_o$) and the b'-axis (in the case of rotation around the a-axis), and between the static magnetic field ($B_o$) and the a-axis (in the case of the rotation around the c*-axis).

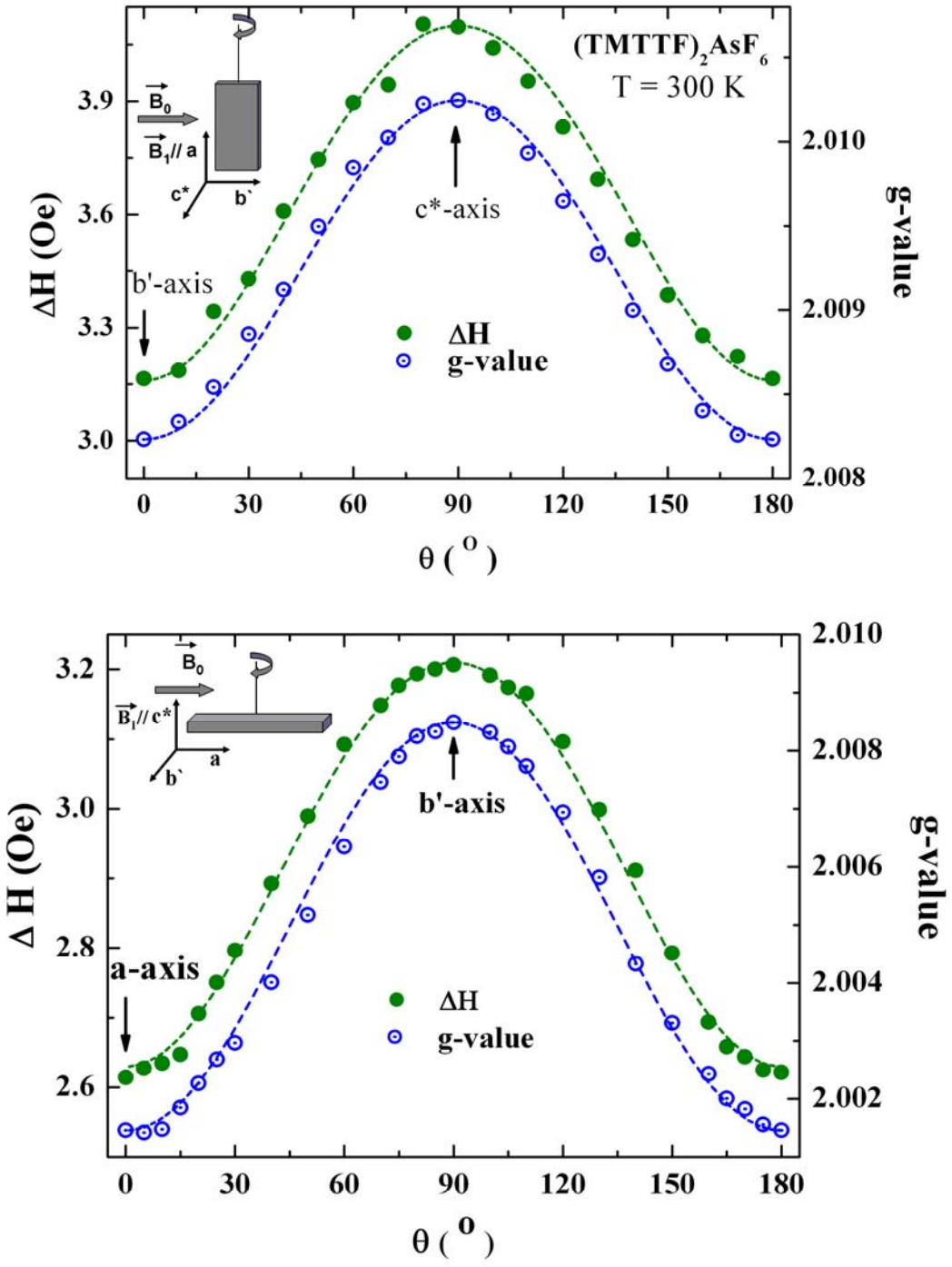


**Figure 4.3: Angular dependence of the ESR linewidth ΔH (HWHM) (closed circles), and the g-value (opened circles) at room temperature when the static magnetic field ($B_o$) is applied parallel to b'c*-plane (up), and to ab′-plane (down). The least-square fittings of the linewidth and the g-value are shown by the dashed lines. The fit parameters are $\Delta H_a$ = 2.6 Oe, $\Delta H_{b'}$ = 3.2 Oe, $\Delta H_{c^*}$ = 4.1 Oe, $g_a$ = 2.0015, $g_{b'}$ = 2.0085 and $g_{c^*}$ = 2.0102.**

The same behaviour is observed for all investigated salts $(TMTTF)_2X$ (X= $SbF_6$, $BF_4$ and SCN), where the ESR linewidth have the same angular dependence as the g-value for all planes $[\Delta H_{c^*} > \Delta H_{b'} > \Delta H_a]$ and $[g_{c^*} > g_{b'} > g_a]$. The fits of the angular dependence of the g-value and the linewidth using equations 4.1 and 4.2 are shown in Figure 4.4.

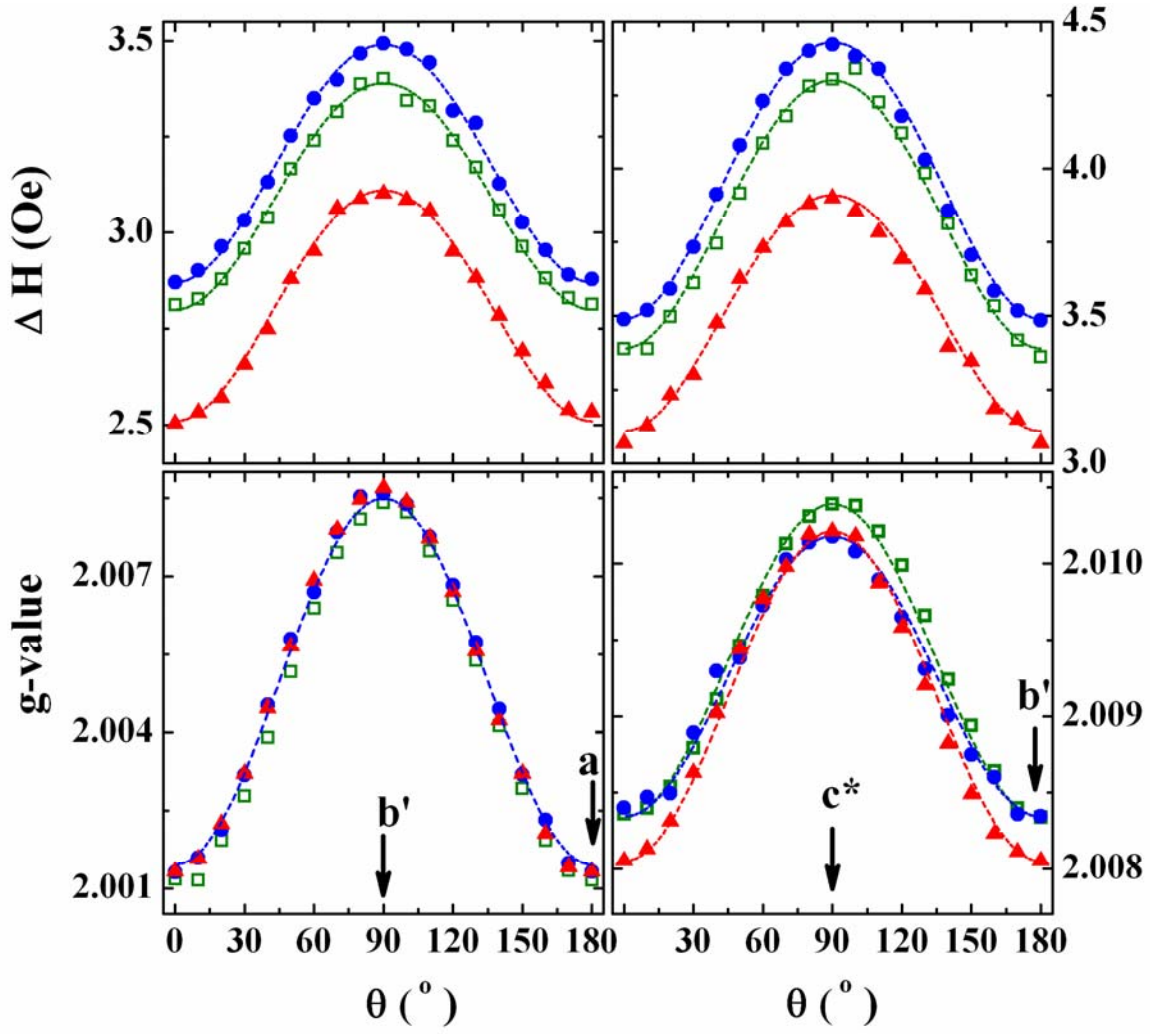


**Figure 4.4: Angular dependence of the ESR linewidth ΔH (HWHM) (up), and the g-value (down) at room temperature when the static magnetic field ($B_o$) is applied parallel to b'c*-plane (right) and ab'-plane (left) for $(TMTTF)_2X$ [X = SCN (●), $BF_4$ (□) and $SbF_6$ (▲)]. The least-square fittings of the linewidth and the g-value are shown by the dashed lines. The arrows show the position of a, b' and c* axes. The fit parameters used are: For $SbF_6$ $\Delta H_a$ = 2.5 Oe, $\Delta H_{b'}$ = 3.1 Oe, $\Delta H_{c^*}$ = 3.9 Oe, $g_a$ = 2.0014, $g_{b'}$ = 2.0081 and $g_{c^*}$ = 2.0102, for $BF_4$ $\Delta H_a$ = 2.8 Oe, $\Delta H_{b'}$ = 3.4 Oe, $\Delta H_{c^*}$ = 4.3 Oe, $g_a$ = 2.0012, $g_{b'}$ = 2.0084 and $g_{c^*}$ = 2.0105 and for SCN $\Delta H_a$ = 2.9 Oe, $\Delta H_{b'}$ = 3.5 Oe, $\Delta H_{c^*}$ = 4.4 Oe, $g_a$ = 2.0013, $g_{b'}$ = 2.0083 and $g_{c^*}$ = 2.01.**

## 4.3 Low Temperature Investigations

The temperature dependence of the ESR linewidth and the g-value for the investigated $(TMTTF)_2X$ salts was studied in the temperature range 300-4 K. The measurements were performed with the static magnetic field $B_o$ applied parallel to the three orthogonal crystal axes a, b′ and c*.

The ESR spectra of $(TMTTF)_2AsF_6$ for $B_o$ parallel to the a-axis for different temperatures are shown in Figure 4.5 as an example.

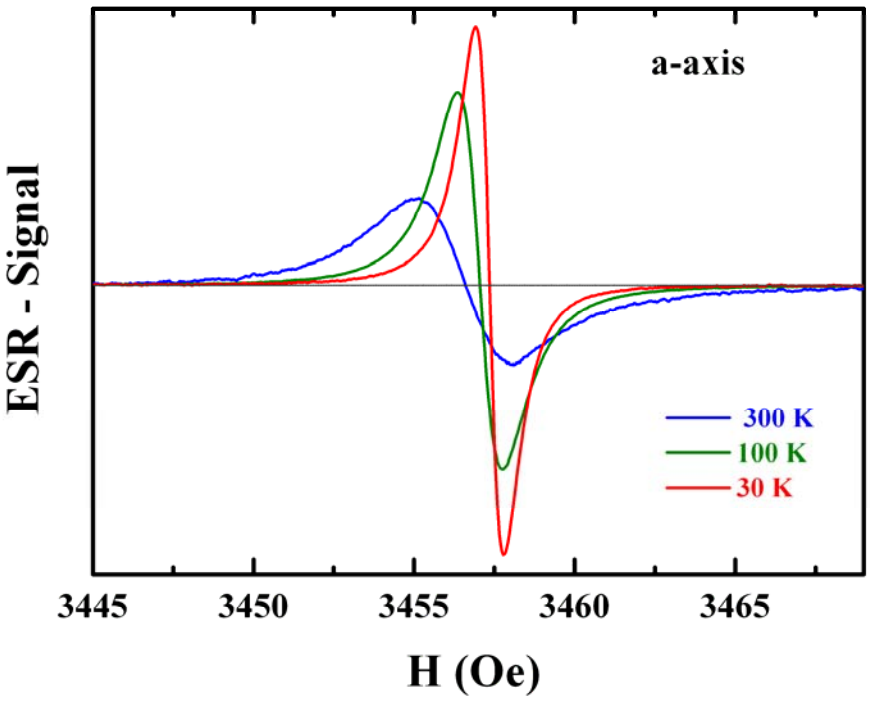


**Figure 4.5: ESR spectra of $(TMTTF)_2AsF_6$ single crystal for different temperatures when the static magnetic field is applied parallel to the a-axis.**

By lowering the temperature the linewidth decreases and the resonance field shifts slightly to higher values (the g-value decreases slightly). The same results were observed for the b'- and the c*-directions but the resonance field was decreasing slightly by lowering the temperature for the b'-direction and it was temperature independent for the c*-axis. The observed absorption line was a symmetric Lorentzian one in the whole temperature range along all orientations.

The temperature dependence of the ESR linewidth (ΔH) and the g-shift ($\Delta g = g - 2.002319$) along the three crystal axes of $(TMTTF)_2AsF_6$ and the

normalized spin susceptibility measured by the SQUID magnetometer for the magnetic field applied parallel to the a-axis are shown in Figure 4.6. In the high temperatures region ΔH is largest along the c* axis and smallest along the a-axis (as discussed in the previous section). The linewidth decreases almost linearly as the temperature decreases for all directions. At around 200 K a slight and a smooth change in the slope is observed. Below about 200 K the linewidth decreases faster down to the charge ordering transition temperature ($T_{CO}$=103K) at which a smooth hump in the linewidth for all directions is observed. The linewidth starts to decrease more slowly by decreasing the temperature below $T_{CO}$ and the anisotropy of the linewidth begins to change. Below $T_{CO}$ the anisotropy of the linewidth is $\Delta H_{c^*} > \Delta H_{b'} \approx \Delta H_a$, where by decreasing the temperature below $T_{CO}$ $\Delta H_{b'}/\Delta H_a$ decreases, $\Delta H_{c^*}/\Delta H_{b'}$ increases and $\Delta H_{c^*}/\Delta H_a$ remains temperature independent. Below about 35 K the linewidth begins to increase by lowering the temperature and then begins to fluctuate below about 16 K.

At high temperatures the g-shift for the three crystal axes shows no significant temperature dependence and a very pronounced anisotropy (it has the same anisotropy as the linewidth). The values of Δg for the three crystal axes are very small ($-1\times10^{-3}$ - $8\times10^{-3}$), Δg has a negative value when the magnetic field is applied parallel to the stacking direction (a-axis) and positive values when it is applied perpendicular to it (b'-and c*-axes). The anisotropy of the g-shift between the b' and c* axis decreases slowly by decreasing the temperature.

The spin susceptibility decreases continuously by lowering the temperature down to the spin Peierls transition temperature ($T_{SP}$ = 13 K) without any obvious change at the localization temperature $T_\rho$=220 K. Below $T_{SP}$ the susceptibility decreases rapidly by lowering the temperature as expected for a second order phase transition to a non magnetic ground state. The susceptibility does not vanish completely down to 1.8 K. No obvious effect on the g-value and the spin susceptibility is detected at $T_{CO}$=103 K.

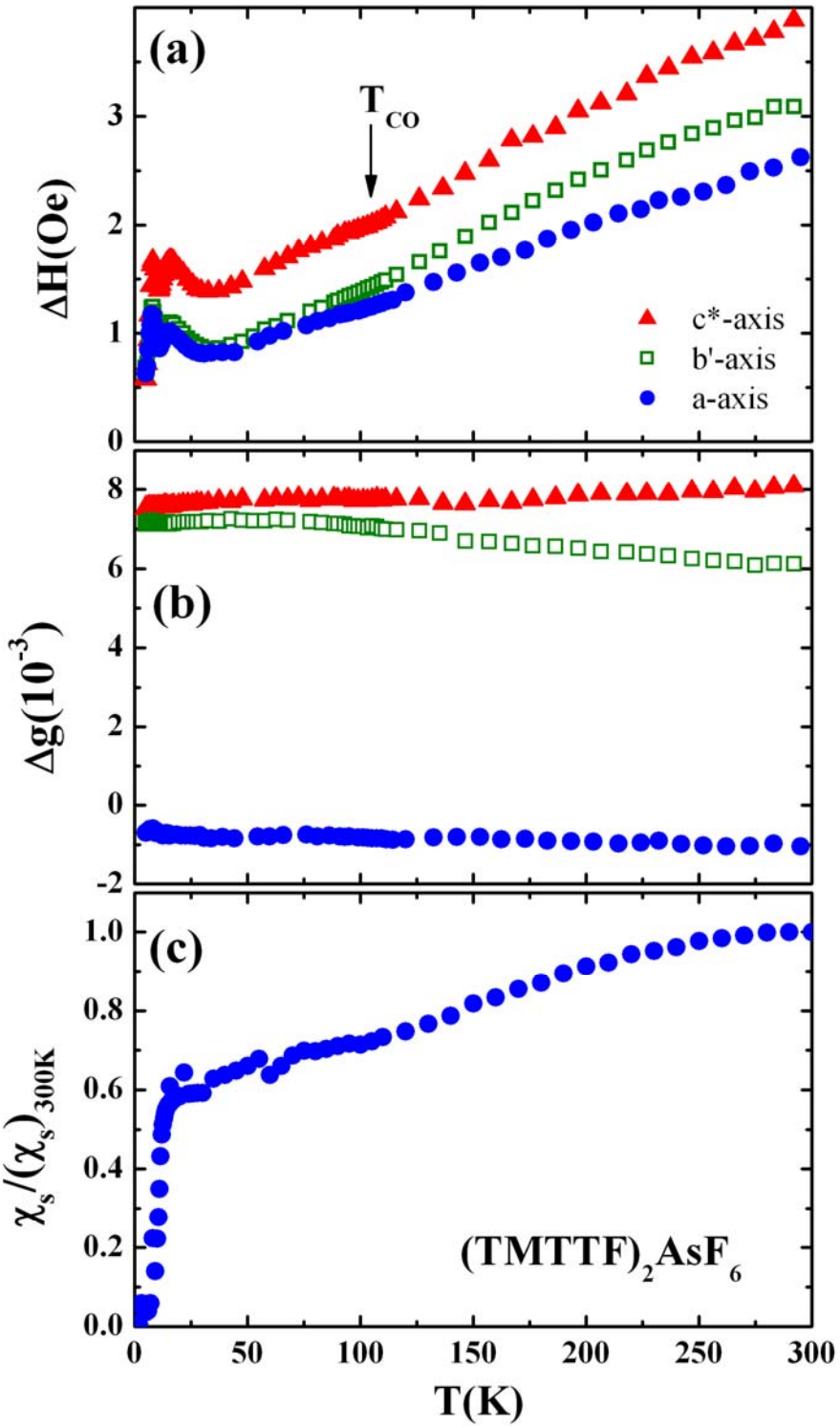


**Figure 4.6: Temperature dependence of (a) the linewidth and (b) the g-shift (Δg) along the three crystal directions and (c) the spin susceptibility normalized to the room temperature value $\left[\chi_s/(\chi_s)_{300K}\right]$ which is calculated from the SQUID magnetometer measurement along the a-axis for $(TMTTF)_2AsF_6$.**

The ESR results along the three crystal directions and the normalized spin susceptibility parallel to the stacking direction (measured by the SQUID magnetometer) for $(TMTTF)_2SbF_6$, $(TMTTF)_2SCN$ and $(TMTTF)_2BF_4$ are shown in Figure 4.7, 4.8 and 4.9, respectively. At high temperatures the ESR and the spin susceptibility results for the three salts are very similar to the results of $(TMTTF)_2AsF_6$, even the absolute values of $\Delta g$ and the linewidth (see Table 4.2). All the investigated salts show the same anisotropy in the linewidth and the g-shift at high temperature (above any phase transition). The linewidth decreases linearly by decreasing the temperature along all crystal directions for the three salts, the same change in the slope of the linewidth as observed in $(TMTTF)_2AsF_6$ is observed at around 200 K. Below about 200 K the linewidth begin to decrease faster with decreasing temperature. Also the g-shift is almost temperature independent and the anisotropy between b'- and c*-axes decreases by lowering the temperature for the three salts.

In $(TMTTF)_2SbF_6$, a clear anomaly in the linewidth for the three directions is observed at the charge ordering transition temperature $T_{CO}$=156 K. Below $T_{CO}$ the same changes as in $(TMTTF)_2AsF_6$ are observed, where the decrease of the linewidth with decreasing temperature becomes slower and the anisotropy of the linewidth begin to change. By decreasing the temperature below $T_{CO}$ $\Delta H_{b'}/\Delta H_a$ decreases, $\Delta H_{c*}/\Delta H_{b'}$ increases and $\Delta H_{c*}/\Delta H_a$ remains temperature independent. The anisotropy of the linewidth at low temperatures is the same as in $(TMTTF)_2AsF_6$ ($\Delta H_{c*} > \Delta H_{b'} \approx \Delta H_a$). Below about 45 K the linewidth for all directions begins to increase with decreasing the temperature down to $T_N$ = 7 K where the ESR spectra vanish totally for the three directions. This phase transition is accompanied by a decrease in the g-shift for b' and c*-directions and an increase in the a-direction.

In the case of $(TMTTF)_2SCN$, after a smooth hump in the linewidth at $T_{CO}$=160 K along the three directions, the linewidth begin to increase with decreasing the temperature down to about 20 K. Below 20 K $\Delta H$ begin to decrease by lowering the temperature down to 13 K, below which the linewidth increases by decreasing the temperature along the three crystal directions down to $T_N$=8 K. At 8 K the ESR spectra vanish totally for the three directions exactly as for the case of $(TMTTF)_2SbF_6$. Also this phase transition is accompanied by a decrease in the g-value for the b' and c*-directions and an increase in a-direction. Again the anisotropy of the linewidth changes below $T_{CO}$, where the anisotropy of the linewidth at low temperatures is $\Delta H_{c*} \approx \Delta H_{b'} > \Delta H_a$, which is different from the one observed in the $SbF_6$ and $AsF_6$ salts.

In $(TMTTF)_2BF_4$, the anisotropy of the linewidth along the ab′-plane becomes almost zero at about 80 K. At $T_{AO}$ = 41 K a clear step-like decrease in the linewidth is observed for all directions below which the linewidth along the a-axis becomes larger than that of the b'-axis. Below 16 K the linewidth for all directions begins to increase by decreasing the temperature down to the lowest temperature.

Again, the spin susceptibility decreases continuously by lowering the temperature for the three salts without any obvious change at the localization temperature $T_\rho$=155 K, 250 K and 210 K for the $SbF_6$, SCN and $BF_4$ salts, respectively. For $(TMTTF)_2SbF_6$, the spin susceptibility exhibits a strong decrease by decreasing the temperature from 16 K down to $T_N$=7 K below which the susceptibility begins to increase with decreasing the temperature (see the insert of Figure 4.7.c). The same behaviour of the spin susceptibility was observed for the $(TMTTF)_2SCN$ salt where the susceptibility begins to decrease rapidly with decreasing temperature below about 20 K and it increases with lowering the temperature below $T_N$=8 K (see Figure 4.8.c). At the anion ordering temperature of $(TMTTF)_2SCN$ a small dip in the susceptibility is observed, although no tetramerization of the TMTTF anions is expected along the stacks since the a-component of the anion ordering wave vector is zero ($q_{AO}$=(0,1/2,1/2)) [86]. This dip can be due to rearrangement of the spins in the perpendicular plane due to the anion ordering transition. The same behaviour was observed in previous investigations of this material [142]. The anion ordering in $(TMTTF)_2BF_4$ ($q_{AO}$=1/2,1/2,1/2) leads to a first-order structural phase transition at $T_{AO}$= 41 K [84]. This transition is accompanied by tetramerization of the TMTTF chain along the stacking direction and leads to a step-like decrease of the spin susceptibility at $T_{AO}$ below which an exponential decrease of the spin susceptibility is observed as expected for a phase transition to a non magnetic ground state. The susceptibility does not vanish completely down to 1.8 K.

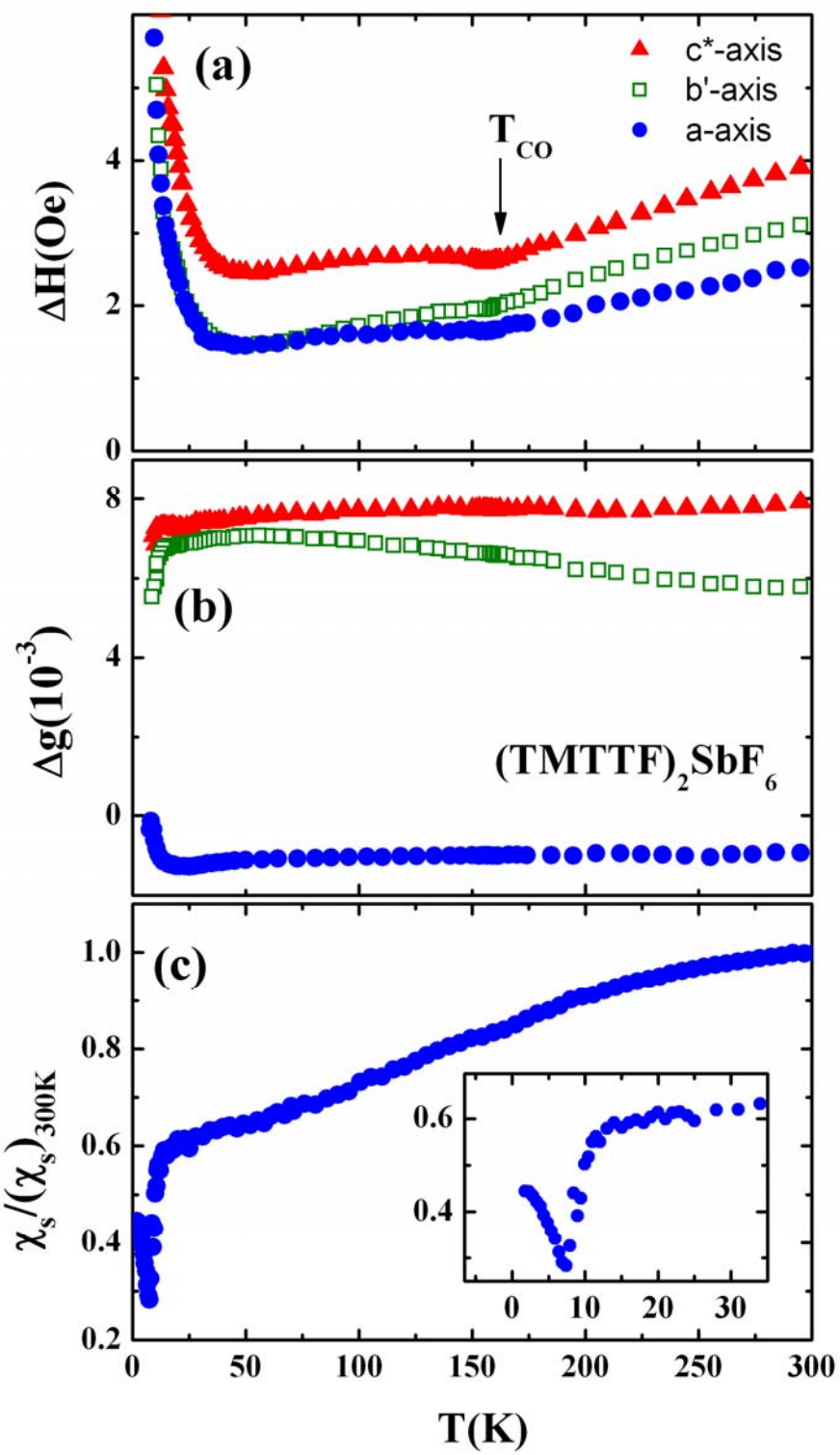


**Figure 4.7: Temperature dependence of (a) the linewidth and (b) the g-shift (Δg) in the three crystal directions and (c) the spin susceptibility normalized to the room temperature value $\left[\chi_s/(\chi_s)_{300K}\right]$ which is calculated from the SQUID magnetometer measurement along the a-axis for $(TMTTF)_2SbF_6$.**

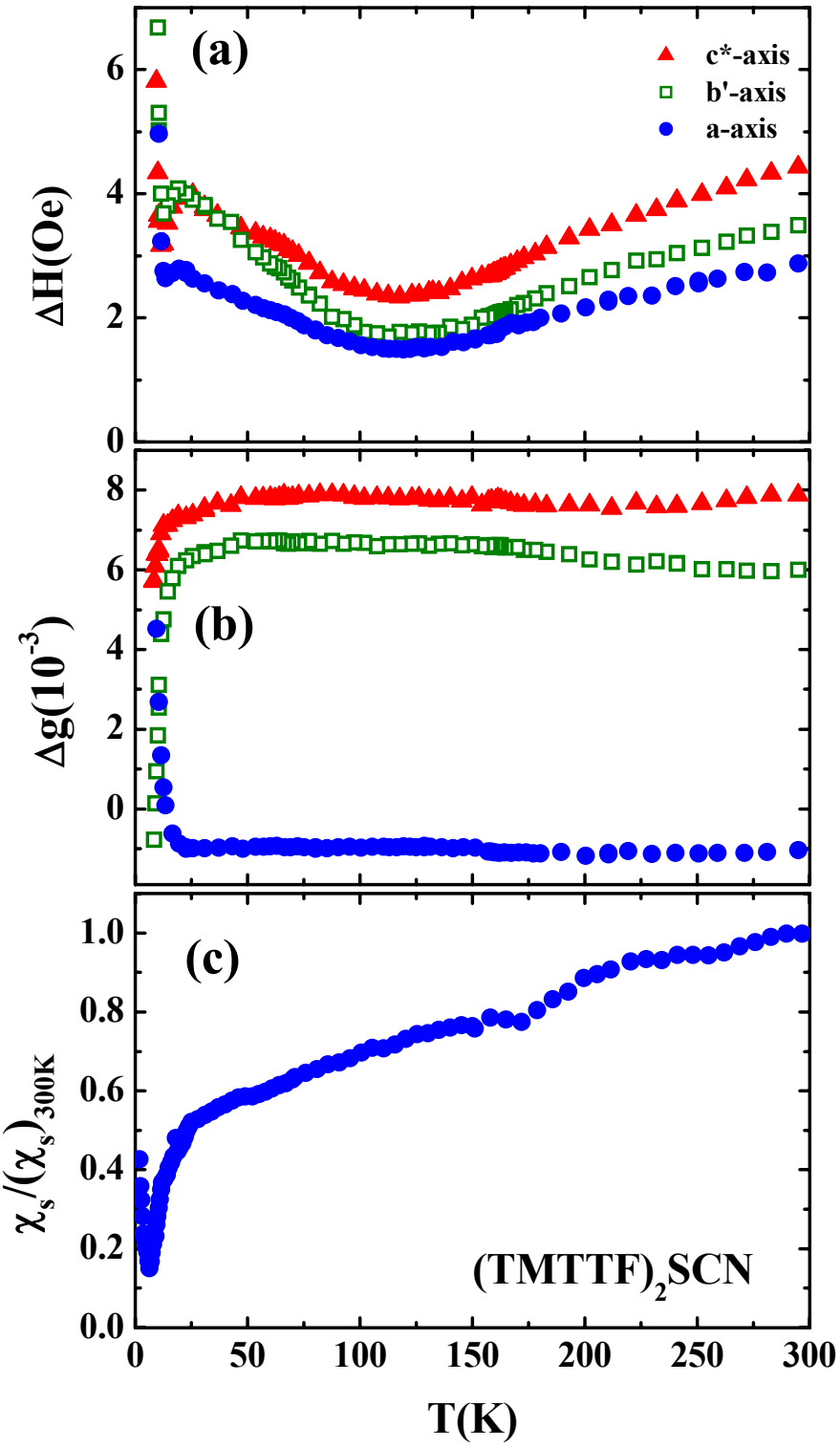


**Figure 4.8: Temperature dependence of (a) the linewidth and (b) the g-shift (Δg) in the three crystal directions and (c) the spin susceptibility normalized to the room temperature value $\left[\chi_s/(\chi_s)_{300K}\right]$ which is calculated from the SQUID magnetometer measurement along the a-axis for $(TMTTF)_2SCN$.**

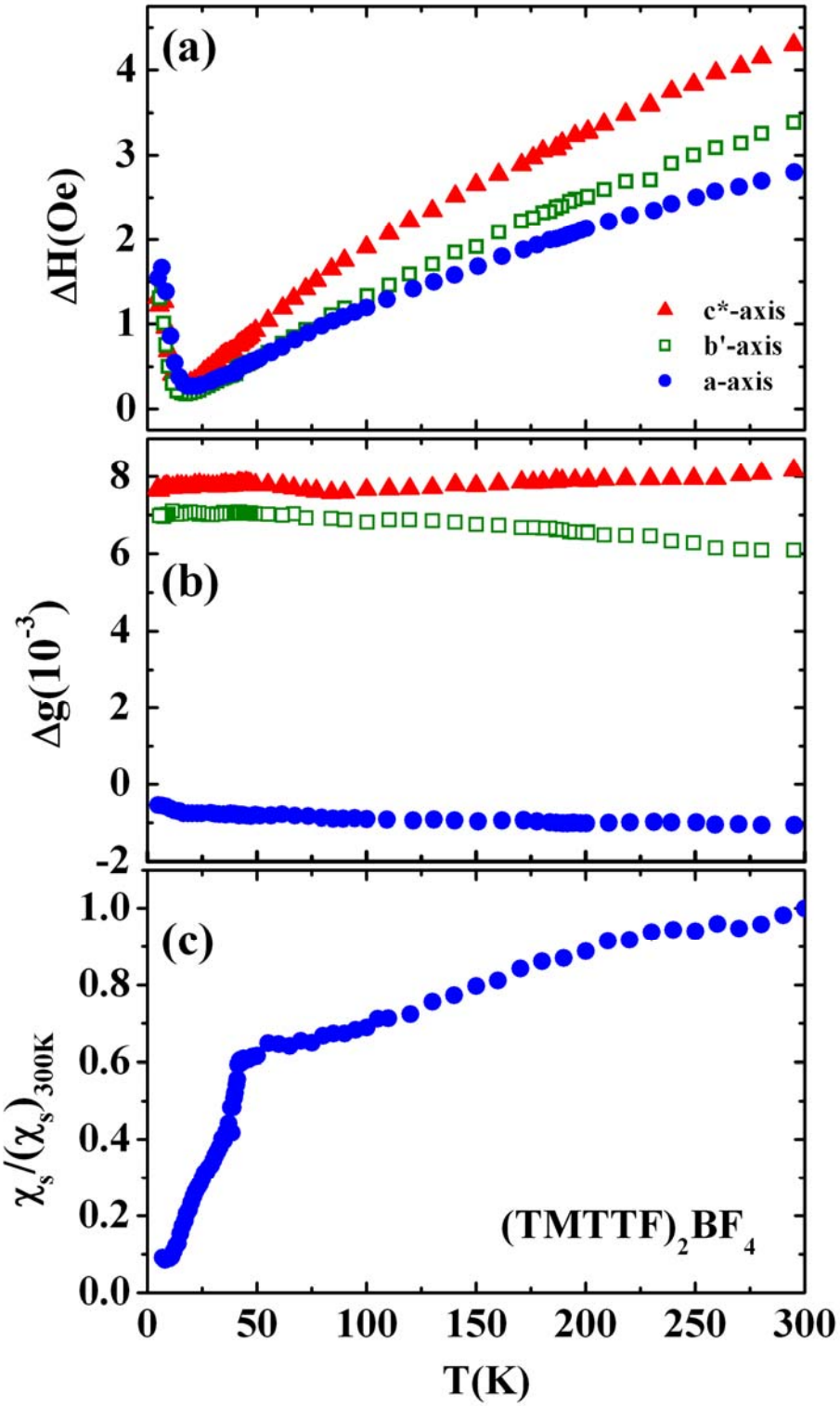


**Figure 4.9:** Temperature dependence of (a) the linewidth and (b) the g-shift (Δg) in the three crystal directions and (c) the spin susceptibility normalized to the room temperature value $\left[\chi_s/(\chi_s)_{300K}\right]$ which is calculated from the SQUID magnetometer measurement along a-axis for$(TMTTF)_2BF_4$.

## 4.4 Paramagnetic State of $(TMTTF)_2X$ Salts

The ESR linewidth and the g-value along the three crystal axes and the spin susceptibility along the stacking direction of the investigated $(TMTTF)_2X$ salts were presented in the previous section. In the following section the results in the paramagnetic range above any magnetic phase transition, where strong effects on the linewidth, g-value and the spin susceptibility are observed, will be discussed and analyzed. The charge order (CO) state will be discussed in a separated section even if it occurs in the paramagnetic region.

### 4.4.1 Spin Susceptibility

The temperature dependence of the magnetic susceptibility was found to behave the same in the paramagnetic state for TMTTF salts, where the room temperature value of the spin susceptibility is nearly independent of the counterion and is in the range $5 - 6\times10^{-4}$ emu/mole [37]. The magnetic susceptibilities were found to decrease gradually with lowering temperature. No anomaly or change in the temperature dependence of the spin susceptibility was detected at the localization temperature however a small dip at about 170 K was detected in $(TMTTF)_2SCN$ [142].

The spin susceptibility was calculated using equations 3.23 and 3.24 where diamagnetic contribution from the core electrons of $(TMTTF)_2AsF_6$ $\chi_{core} = -5.3\times10^{-9}$ $m^3$/mole [6] was subtracted from the original dataset. Since the diamagnetic contribution is mainly from the TMTTF molecules, the value of the core susceptibility was assumed to be independent of the monovalent anion.

The general behaviour of the spin susceptibility in the paramagnetic high temperature region of the $(TMTTF)_2X$ salts was described in section 4.3. The temperature dependence of the spin susceptibility of the investigated salts follow the general behaviour expected for a uniform S=1/2 AFM Heisenberg spin chain, where the susceptibility increases by decreasing the temperature to a maximum value at high temperatures ($T_{max}$) then fall slowly to a finite value at 0 K. This can be understood from the structure of the TMTTF salts, where one electron is localized on each dimer of TMTTF molecules. These dimers, each with S = 1/2, are equally spaced (the distance between each two spins equals the unit cell parameter $a=d_1+d_2$, see Table 1.1 and Table 1.2). The localized spins are antiparallel and can be oriented along any direction in the space, thus they form an AFM Heisenberg spin chain with uniform coupling constant J.

The thermal expansion coefficient along the chain direction has a large temperature dependence and hence significant effects on the temperature dependence of the spin susceptibility [120]. Therefore, to compare the experimental results (which are measured at constant pressure $(\chi_s)_p$) with the theoretical calculations (which are obtained at constant volume $(\chi_s)_v$), the spin susceptibility at constant volume has to be calculated from the spin susceptibility at constant pressure. In the case of $(TMTSF)_2PF_6$ the temperature dependence of $(\chi_s)_v$ was estimated by Wzietek *et al.* [45] by performing NMR and X-ray measurements under pressure as it was discussed in section 1.2.3. In this work we assume that the substitution of selenium by sulfur and changing the inorganic anion has no influence on the expansion coefficient of the material. Therefore we took the same ratio $(\chi_s)_v/(\chi_s)_p$ to rescale the susceptibility data for the investigated TMTTF salts.

The temperature dependence of $(\chi_s)_p$ and $(\chi_s)_v$ of $(TMTTF)_2SbF_6$ from 380 K down to 1.8 K is shown in Figure 4.10. $(\chi_s)_p$ has a smooth maximum at about T=315 K which shifts down to about 255 K for $(\chi_S)_V$. The spin susceptibility at constant volume $(\chi_s)_v$ of $(TMTTF)_2SbF_6$ resembles the well-known behaviour of a spin 1/2 Heisenberg chain with AFM exchange coupling. The spin susceptibility of such a system was studied theoretically by Bonner and Fisher [7] and Eggert, Affleck and Takahashi (EAT-model) [8] as discussed in section 2.3.1.

From the maximum temperature ($T_{\max} \approx 255K$) the AFM exchange constant can be easily estimated using the relation $T_{\max}/|J| = 0.641$, which gives $|J| \approx 400\,K$. Since the maximum of the susceptibility is very broad, it is necessary to fit the temperature dependence of $(\chi_s)_v$ numerically by equation (2.8) to obtain the accurate value of the AFM exchange constant (J).

Using Bonner Fisher [7] and EAT [8] models the $(\chi_s)_v$ of $(TMTTF)_2SbF_6$ for T >100 K can be modeled numerically using equation (2.8) [79] with $|J| = 400$ K. From the obtained J value the spin susceptibility at zero temperature [$(\chi_s)_v(T \to 0)$] can be calculated using the relation $\chi_s(T \to 0) = \Gamma/\pi^2|J|$, which gives $\chi(T \to 0) = 4.8\times10^{-9}\ m^3/mole$. Also the maximum value of the spin susceptibility can be calculated using the relation $\chi_{\max} = 0.1469\Gamma/|J|$ which gives $7.0\times10^{-9}\ m^3/mol$. The $(\chi_s)_v$ begins to deviate from the EAT model below about 100 K, where the measured susceptibility become lower than the theoretical value for $T$ <100K.

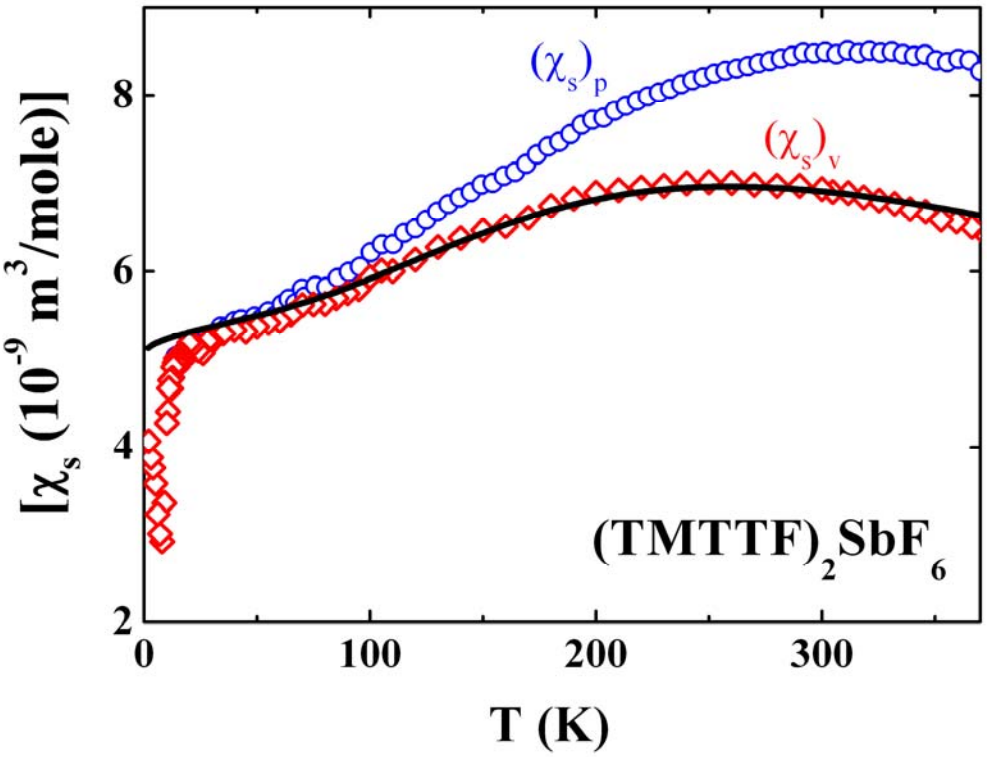


**Figure 4.10: Temperature dependence of the spin susceptibility at constant pressure $(\chi_s)_p$ (circles) and at constant volume $(\chi_s)_v$ (rectangles) of $(TMTTF)_2SbF_6$ calculated from the SQUID measurement along the stacking direction. The line corresponds to a fit using the EAT-model for a S=1/2 AFM Heisenberg chain [8] with $|J|$=400 K. The maximum value of $(\chi_s)_v$ was calculated using the relation $\chi_{max} = 0.1469\,\mu_0 N g^2 \mu_B^2 / k_B |J|$.**

The temperature dependence of the spin susceptibility at constant volume $(\chi_s)_v$ of the other investigated TMTTF salts ($(TMTTF)_2AsF_6$, $(TMTTF)_2BF_4$ and $(TMTTF)_2SCN$) are shown in Figure 4.11. The temperature dependence of $(\chi_s)_v$ was obtained from $(\chi_s)_p$ as discussed above for the case of $(TMTTF)_2SbF_6$. At high temperatures ($T \gtrsim 100\,K$) the $(\chi_s)_v$ of the three salts can also be described by the EAT model as discussed above for $(TMTTF)_2SbF_6$, where $(\chi_s)_v$ decreases gradually by lowering the temperature after passing a maximum value at $T_{max}$.

The $(\chi_s)_v$ of all compounds investigated begin to deviate from the EAT model below about 100 K, where the measured susceptibility becomes smaller than the theoretical value for $T \lesssim 100\,K$. This deviation of the measured susceptibility from the EAT model can be due to the interchain coupling where the interchain transfer integral in TMTTF salts is about $t_b \approx 12$ meV $\approx 130$ K.

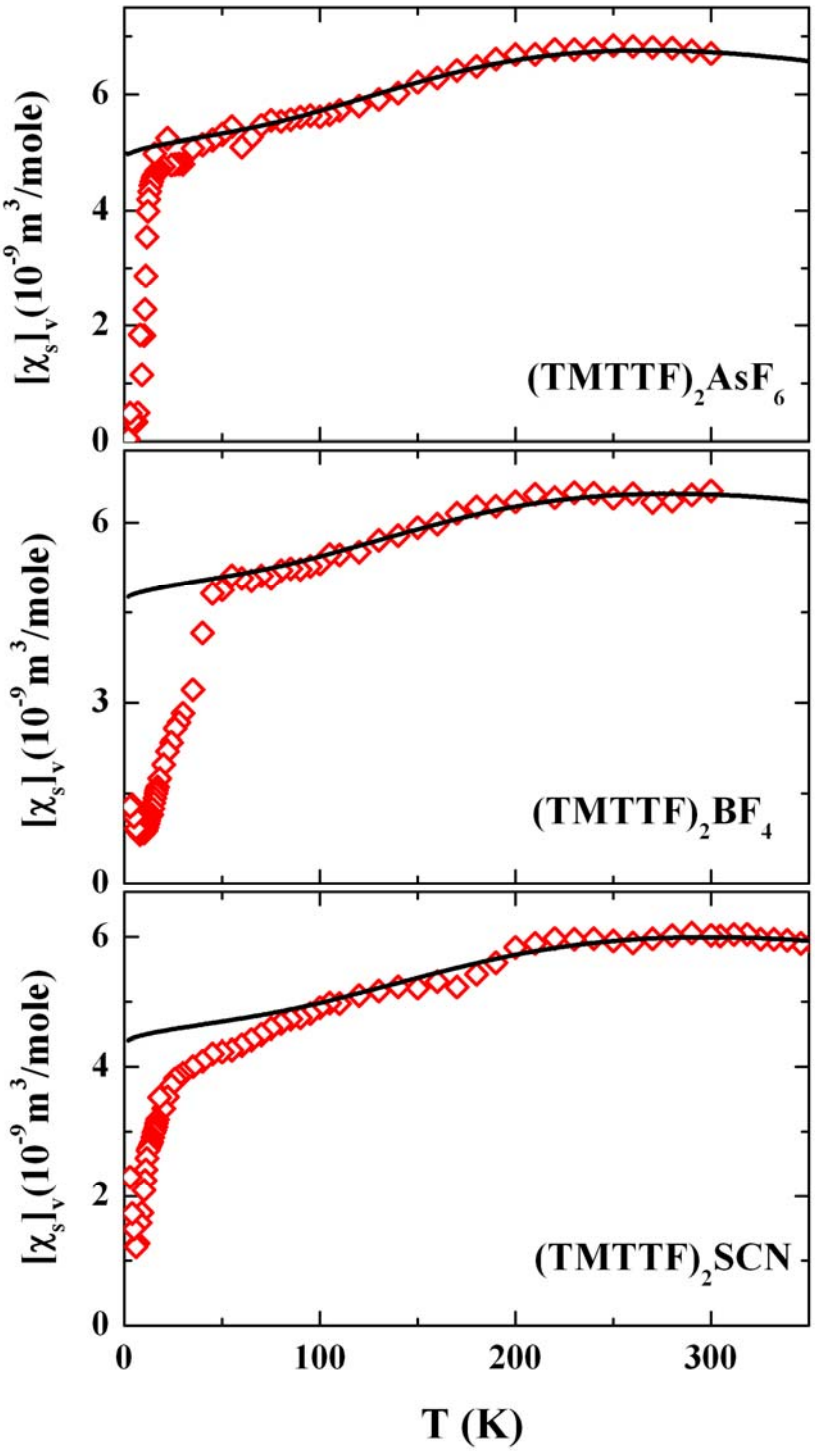


**Figure 4.11: Temperature dependence of the spin susceptibility at constant volume $(\chi_s)_v$ of $(TMTTF)_2AsF_6$, $(TMTTF)_2BF_4$ and $(TMTTF)_2SCN$ calculated from the SQUID magnetometer measurements along the stacking direction. The lines correspond to a fit using the EAT-model for the S = 1/2 AFM Heisenberg chain [8] with $|J|$=410 K, 430 K and 460 K, respectively. The maximum value of $(\chi_s)_v$ was calculated using the relation $\chi_{\max} = 0.1469\,\mu_0 N g^2 \mu_B^2 / k_B |J|$.**

This means that TMTTF salts become more two dimensional below about 100 K, and the spin susceptibility of the two dimensional AFM chain is expected to be smaller than the one dimensional chain [127], and since the EAT model was calculated for 1-D AFM spin chain, the increase of the interchain interaction can cause a decrease in the susceptibility below the expected value for a 1-D chain. The same deviation below about 100 K was observed in $(TMTTF)_2X$ (X=$ClO_4$, $PF_6$, Br) in previous studies [128,129].

In Table 4.3 the AFM exchange constant J obtained from the fit using equation (2.8), the room temperature value of the spin susceptibility at constant pressure $\left[(\chi_s)_p\right]_{300K}$ and at constant volume $\left[(\chi_s)_v\right]_{300K}$, the temperature of the maximum susceptibility $T_{max}$ and the maximum value of the spin susceptibility of the investigated salts are tabulated and compared to other previously measured compounds.

The obtained values of the AFM exchange constant $|J|$ of the $(TMTTF)_2X$ salts is correlated with the unit cell dimension along the stacking direction ($a$) (the distance between each two spins along the stacking direction see Table 4.3), where $|J|$ increases with decreasing the unit cell length $a$ as shown in Figure 4.12 for the investigated and other $(TMTTF)_2X$ salts. This is expected because by decreasing the distance between the TMTTF molecules the overlap between the molecular wave functions of the TMTTF molecules along the stacking direction will increase and therefore the exchange coupling will increase. This means, for these salts the AFM exchange constant depends primarily on the distance between the coupled spins and it increases by decreasing this distance.

In principle, the relation between $|J|$ and $a$ can be modeled theoretically by taking into account the overlap between the molecular wave functions of the TMTTF molecules along the stacking direction. However, such model has not been calculated until now up to our knowledge; therefore such theoretical calculations are needed.

In all compounds investigated no sign of the resistivity minimum was found in the susceptibility (there is no change of the susceptibility at the localization temperature $T_\rho$), this implies decoupling between the spin and the charge degree of freedom.

| | $(TMTTF)_2X$ | | | | | | |
|---|---|---|---|---|---|---|---|
| X | $SbF_6$ | $AsF_6$ | $PF_6$ | $BF_4$ | $ClO_4$ | SCN | Br |
| $\left[(\chi_s)_p\right]_{300K}$ $(10^{-9}m^3/mol)$ | 8.5 | 8.2 | 8.1 | 8.0 | 8.0 | 7.4 | 6.9 |
| $\left[(\chi_s)_v\right]_{300K}$ $(10^{-9}m^3/mol)$ | 6.9 | 6.7 | 6.6 | 6.5 | 6.5 | 6.0 | 5.6 |
| $T_{max}$ (K) | 255 | 263 | 270 | 275 | 275 | 295 | 320 |
| $\left[(\chi_s)_v\right]_{max}$ $(10^{-9}m^3/mol)$ | 7.0 | 6.8 | 6.7 | 6.6 | 6.6 | 6.1 | 5.6 |
| $\lvert J\rvert(K)$ | 400 | 410 | 420 | 430 | 430 | 460 | 500 |
| $a$ (Å) | 7.195 | 7.178 | 7.155 | 7.112 | 7.115 | 7.053 | 7.034 |

**Table 4.3: The obtained results from the spin susceptibility $(\chi_s)$ measurements of the $(TMTTF)_2X$ salts. $\left[(\chi_s)_p\right]_{300K}$ and $\left[(\chi_s)_v\right]_{300K}$ denote the spin susceptibility at constant pressure and constant volume, respectively at 300 K, $T_{max}$ is the temperature of the maximum susceptibility, $\left[(\chi_s)_v\right]_{max}$ is the maximum value of the spin susceptibility at constant volume, $\lvert J\rvert$ is the obtained AFM exchange constant from the fit using equation (2.8) and $a$ is the unit cell dimension along the stacking direction (see Table 1.1). The results of $(TMTTF)_2PF_6$, $ClO_4$ and Br are taken from Ref. [48,128,129].**

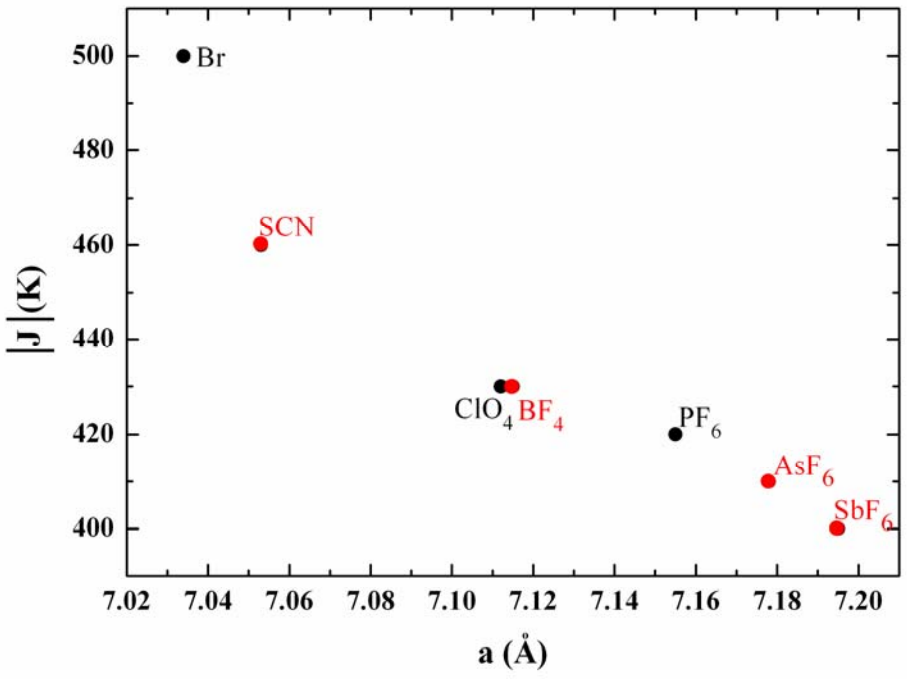


**Figure 4.12: The relation between the AFM exchange constant $\lvert J\rvert$ and the unit cell dimension along the stacking direction $a$ for $(TMTTF)_2X$ salts. The values of $\lvert J\rvert$ for $PF_6$, $ClO_4$ and Br salts are taken from Ref. [48,128,129].**

### 4.4.2 The Linewidth and the g-shift

The anisotropy of the g-value and the ESR linewidth at room temperature as well as the temperature dependence of the ESR linewidth and the g-shift (Δg) along the three crystal axes of the investigated TMTTF salts in the paramagnetic region were described in sections 4.2 and 4.3. It was illustrated that the g-value and the linewidth have the same anisotropy in this region where $g_{c^*} > g_{b'} > g_a$ and $\Delta H_{c^*} > \Delta H_{b'} > \Delta H_a$. It was also shown that the ESR linewidth of the TMTTF salts decreases upon cooling in the paramagnetic region (above the charge ordering transition temperature) independently from the temperature dependence of the electrical conductivity and that the g-value is approximately temperature independent in this region.

To understand the physics behind the anisotropy and the temperature dependence of the g-value and the ESR linewidth of TMTTF salts, the following items should be clarified:

- The broadening mechanism of the ESR linewidth of these salts.
- The origin of the anisotropy of the g-value and the linewidth in these materials.
- The temperature dependence of the linewidth in the paramagnetic region.

**1) The broadening mechanism of the ESR linewidth of TMTCF salts.**

In the previous chapter (section 3.1.5) the different factors which contribute in the broadening of the Lorentzian ESR absorption line were discussed. Applying equations 3.9-3.12 to the TMTTF salts one gets the following values for each term at room temperature.

- The linewidth due to the anisotropic hyperfine interaction:

  $\Delta H_{\text{h.f}} \approx 5\times10^{-3}$ Oe

  where $|J| \approx 430\,\text{K}$ for TMTTF salts and the value of the anisotropic hyperfine interaction constant of sulfur is $A_{||}$= 78 MHz [100].

- The linewidth due to the dipole-dipole interaction:

  $\Delta H_{\text{d-d}} \approx 8\times10^{-4}$Oe

If one takes *d* in equation (3.12) as the average distance between each two TMTTF dimers $d_1$+$d_2$ which is approximately 7 Å (see table 1.2) and $|J| \approx 430\,\text{K}$.

- The linewidth due to anisotropic exchange interaction:
  $\Delta H_{\text{A.E.}} \approx 2\times10^{-4}\text{Oe}$, where $\overline{\Delta g^2} = 33\times10^{-6}$ Oe (see Table 4.2).

- The linewidth due to anisotropic Zeeman interaction:
  $\Delta H_{\text{Zee.}} \approx 3\times10^{-5}$ Oe, where $H_o$ = 3450 Oe.

Therefore, it is clear that the contributions of the above mentioned interactions are much smaller than the measured linewidth of the investigated TMTTF salts at room temperature.

Several theoretical studies were done to explain the broadening mechanisms of the ESR line of the single chain quasi 1-D organic conductors $(TMTCF)_2X$ [108,130,131]. Spin-orbit-coupled electronic transitions between donor conduction-band states of the organic conductors $(TMTCF)_2X$ were shown to be the main ESR line broadening mechanism in these compounds. These transitions were suggested to be activated by torsional oscillations of the donor molecules around their long in-plane axis (see Figure 4.13). These oscillations break the symmetry restriction which forbids spin-orbit transitions within or between the donor stacks comprised of the same, identically oriented, centrosymmetrical molecules.

The spin-orbit interaction of the heavy chalcogen atom in the TMTCF molecule (S in TMTTF and Se in TMTSF) has a short-range nature. This nature limits the donor conduction-band states to couple via their valence $\pi$ atomic orbitals only to the states containing valence $\sigma$ atomic orbitals on the same chalcogen. Since the $\pi$ atomic orbitals are oriented perpendicular to the TMTCF molecular plane and the $\sigma$ atomic orbitals parallel to it, interstack interaction is important in the broadening mechanism of the ESR line because it leads to admixture of the chalcogen valence $\sigma$ atomic orbitals into the acceptor orbitals. This mechanism enables spin-orbit scattering between the donor and acceptor band states[I].

[I] This is the reason why the linewidth increases as the interstack interaction (the transfer integral along b′-axis) increase.

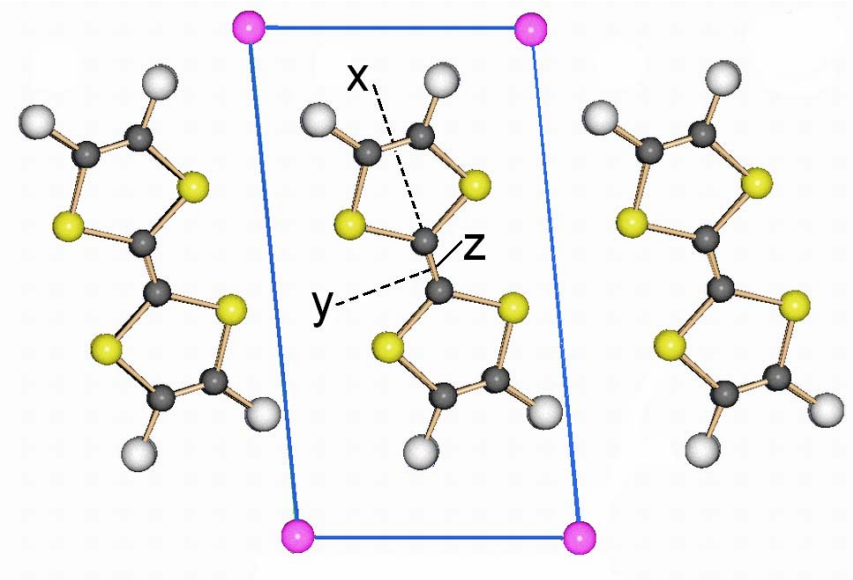


**Figure 4.13: Crystal structure of the TMTTF salts showing the possible rotational axes of the TMTTF molecule, the x and y axes are parallel to the molecular plane and the z-axis is perpendicular to it. The magenta spheres represent the monovalent anions.**

Assuming that the spin-orbit coupled electronic transitions induced by torsional oscillation is the main ESR line broadening mechanism in TMTTF salts, the ESR linewidth parallel to the stacking direction for $(TMTTF)_2PF_6$ was calculated theoretically and found to be 3.6 Oe [130], the corresponding experimental value is 2.53 Oe [120]. This fair agreement between the experimental and theoretical values is evidence that the spin-orbit coupled electronic transitions are the main ESR line broadening mechanism in TMTTF salts.

From the previous discussion the difference in the absolute value of the ESR linewidth between the TMTSF and the TMTTF salts can be understood $(\Delta H_{TMTSF}/\Delta H_{TMTTF}) \approx 25$ [120]. If one considers that the spin-orbit Hamiltonian for the chalcogen is given by the relation

$$\hat{H}_{SO} = \hbar\lambda \vec{L} \bullet \vec{S} \tag{4.3}$$

where $\lambda$ is the spin orbit coupling constant for the chalcogen atom ($\lambda = 7.2\times10^{13}\ s^{-1}$ for sulfur and $3.8\times10^{14}\ s^{-1}$ for the selenium [132]). Since the ESR linewidth is proportional to $\lambda^2$ and $\lambda_{Se}^2/\lambda_S^2 \approx 25$, this confirms that the spin orbit coupled electronic transitions are the main broadening mechanism of the ESR line of the TMTCF salts.

## 2) The anisotropy of the linewidth in TMTCF salts.

The anisotropy of the linewidth of the TMTCF salts comes from the symmetry restrictions of these materials, where the possibility that the previous mechanism of overlap-induced $\sigma$-$\pi$ mixing might produce spin-orbit scattering along the stacks comparable in magnitude to the interstack scattering is excluded by the following symmetry-based restriction [130]: Spin-orbit interactions cannot cause electronic transitions within stacks of the same, identically oriented, centrosymmetrical donor molecules. The restrictive symmetry operation is that any two donor molecules are inversion related. This symmetry precludes the intrastack spin-orbit scattering in the (TMTCF) salts. Therefore the linewidth along the stacking direction (along the a-axis) will be the smallest and along the c*-axis the largest as long as this symmetry is conserved.

The anisotropy of the ESR linewidth of the TMTCF salts can be understood by introducing the effective spin-orbit coupling magnetic field ($H_{eff}^{so}$) which is given by the relation [130]

$$H_{eff}^{so} = \frac{\lambda_{so} l_c}{\gamma_e} \tag{4.4}$$

where $l_c$ is the orbital momentum quantum number and $\gamma_e$ is the electron magnetogyric ratio. The effective spin-orbit field ($H_{eff}^{so}$) is anisotropic, having the largest component along the molecular x-axis and the intermediate one along the y-axis and the smallest component along the z-axis if the inversion symmetry is reserved (see Figure 4.13), and, consequently the relaxation rate and the ESR linewidth will depend strongly on the orientation of the external magnetic field H. And thus the ESR linewidth is expected to have the same anisotropy as the effective spin-orbit coupling magnetic field.
The anisotropy of the g-value originates from the spin-orbit coupling as discussed in section 3.1.5.

## 3) The temperature dependence of the linewidth in the paramagnetic region.

The spin-orbit coupled electronic transitions are the main broadening mechanism of the ESR line of the TMTCF salts. It was suggested that they are activated by torsional oscillations of the donor molecules around their long in-plane axis (x-axis in Figure 4.13) [130,131]. These oscillations break the symmetry restriction which forbids spin-orbit electronic transitions.

The symmetry-breaking vibrations are necessarily torsional oscillations of the donor molecules, because translational vibrational displacements do not change the molecular orientation as required to eliminate the inversion symmetry of the molecular pairs, and intramolecular vibrational distortions of the donors are generally too energetic to be considered in the relevant temperature range. From the torsional vibrations only the libration of the donor molecules around their long in-plane axis was found to be effective [130], primarily because this vibration involves the lowest moment of inertia as shown for example by the crystal-structure data of $(TMTSF)_2PF_6$ [133]. It was shown theoretically [130] that the temperature dependence of the ESR linewidth is determined primarily by the torsional vibration amplitude of the donor molecules around the x-axis ($\phi_x$) which is small at low temperatures.

This explains qualitatively why the ESR linewidth in (TMT*C*F) salts is very small at low temperatures (if there is no phase transition at low temperatures which induces an increase in the linewidth) as shown in Figure 4.9 for $(TMTTF)_2BF_4$ as example. Also it explains the increase of the linewidth with increasing temperature, in that thermally activated torsional vibrations lift the symmetry restrictions and activate spin-orbit-coupled electronic transitions.

In our investigated salts we observed a linear decrease of the linewidth in the high-temperature region. Figure 4.14 shows the temperature dependence of the ESR linewidth along the three crystal axes of $(TMTTF)_2SbF_6$. The linewidth decreases linearly from room temperature down to about 180 K with the highest slope along the c*-axis and the smallest along the a-axis. The linewidth in the high temperature region (300-180 K) can be fitted linearly for the three directions as shown by the straight lines in the figure. If the fits of the linewidths are extrapolated to low temperatures, they cross at the same negative temperature ($T_o$). The linear decrease of the linewidth at high temperatures along the three axes means in principle that the torsional vibration amplitude of the TMTTF molecules decreases linearly with decreasing the temperature in this temperature range. However the physical meaning of the negative temperature ($T_o$) is not understood yet.

The same behaviour is observed for the other investigated $(TMTTF)_2X$ (X=$AsF_6$, $BF_4$ and SCN) salts as well as slats with X=$PF_6$, Br, $ClO_4$ which were investigated in previous studies [48,120] and shown in Figure 4.15. For all TMTTF salts the linewidth decreases linearly from room temperature down to about 180 K and also the extrapolation of the linear fit for the three axes cross at a negative temperature $T_o$. The value of $T_o$ for all investigated TMTTF salts ranges between $-120$ to $-150\,\mathrm{K}$ except for $(TMTTF)_2Br$ in which $T_o \approx -200\mathrm{K}$.

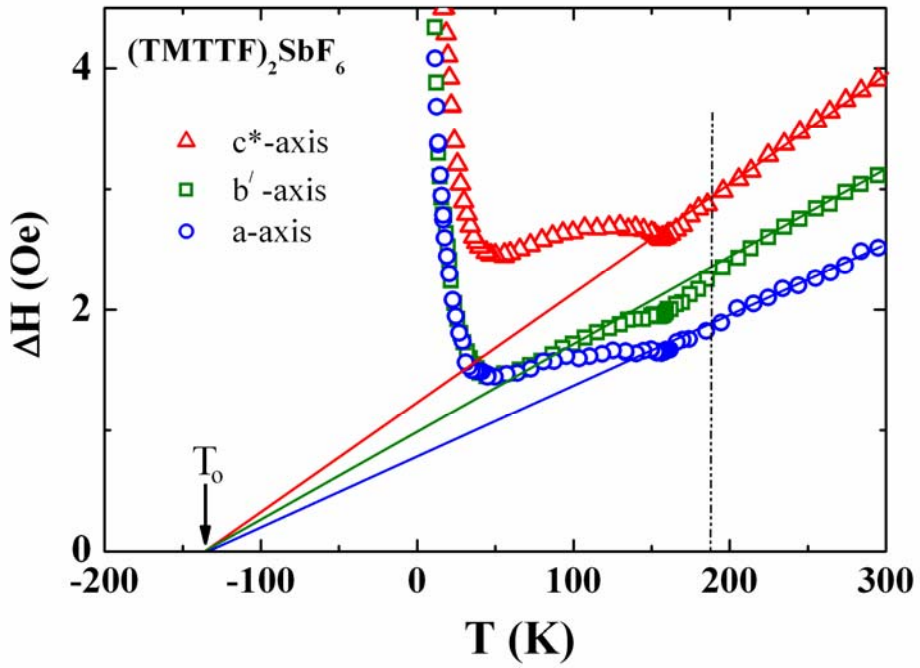


**Figure 4.14: Temperature dependence of the ESR linewidth of $(TMTTF)_2SbF_6$ along the three crystal directions. The lines show the linear fit of the linewidths in the high temperature region. $T_o$ is the temperature intercept of the linear fit along the three directions.**

The linear decrease of the linewidth with decreasing the temperature in the high temperature range seems to be a signature not only for TMTTF salts but also for TMTSF salts where the same behaviour is found in $(TMTSF)_2PF_6$ and $(TMTSF)_2AsF_6$ (see Figure 4.16), these salts were investigated previously [48,120]. In these two salts the measured linewidth deviates from the linear behaviour at about 150 K and the extrapolations of the linear fits cross at about -170 K.

The linewidth begins to decrease faster by decreasing the temperature below the kink in the linewidth along all directions for the investigated (TMTCF) salts at around (150-180 K). The cause of this could be the decrease of the phonon density below this temperature; this is expected for temperatures below the Debye temperature.

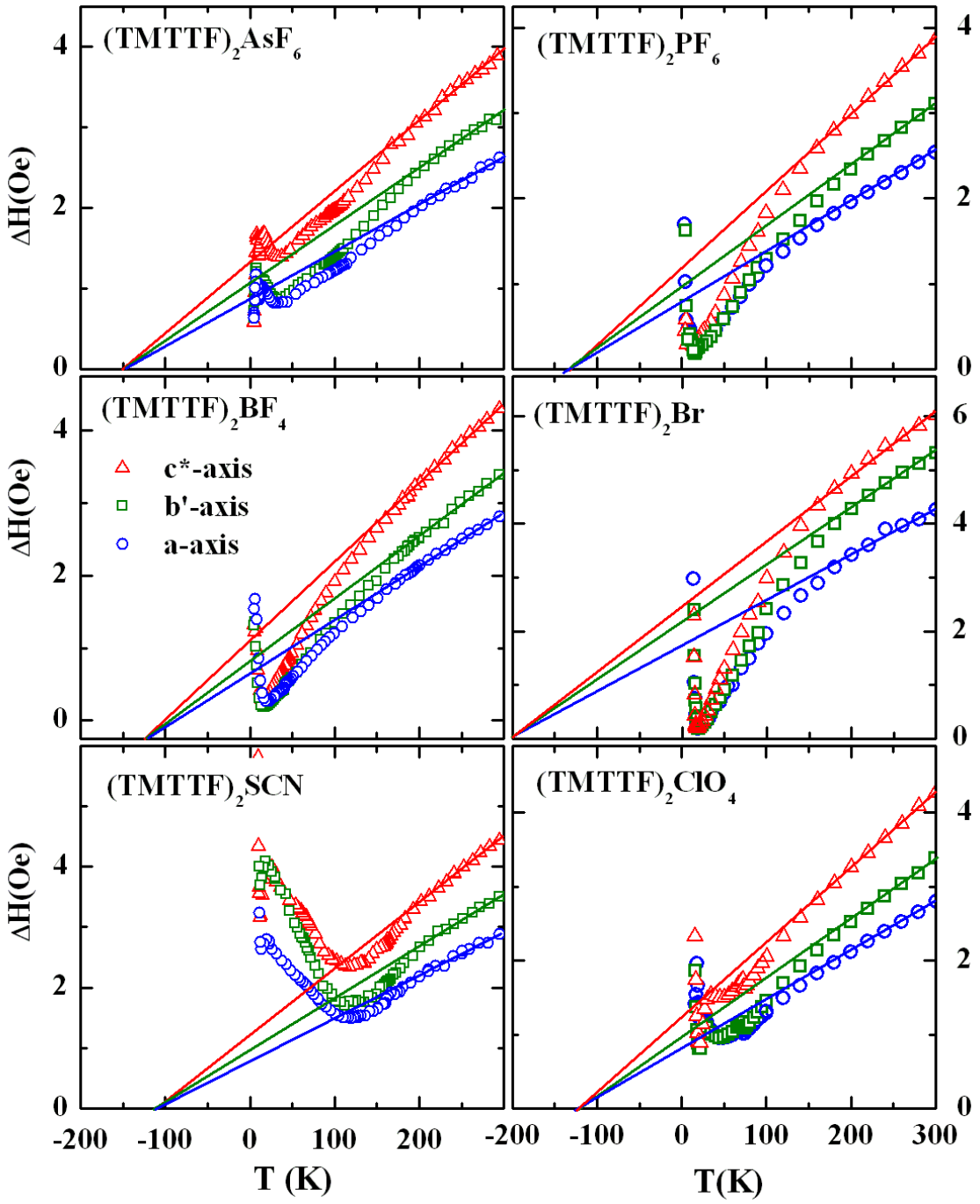


**Figure 4.15: Temperature dependence of the ESR linewidth of $(TMTTF)_2X$ (X= $AsF_6$, $BF_4$, SCN, $PF_6$, Br and $ClO_4$) along the three crystal directions. The lines show the linear fit of the linewidths in the high temperature region. The results of $(TMTTF)_2X$ (X= $PF_6$, Br and $ClO_4$) are taken from Ref. [48,120].**

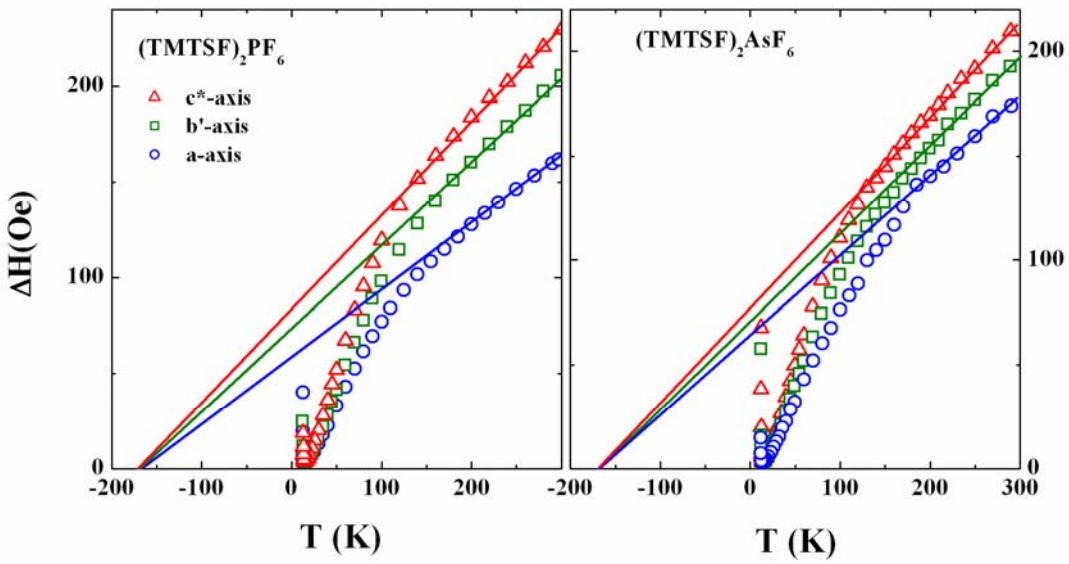


**Figure 4.16: Temperature dependence of the ESR linewidth of $(TMTSF)_2X$ (X= $PF_6$ and $AsF_6$) along the three crystal directions. The lines show the linear fit of the linewidths in the high temperature region. The results are taken from Ref. [48,120].**

Different values for the Debye temperature $\theta_D$ of the TMTCF salts are found in the literature. While the value of $\theta_D$ for $(TMTTF)_2X$ (X=$BF_4$, $ClO_4$ and $PF_6$ are in the range 50-60 K [20,37]), in other studies the $\theta_D$ of $(TMTTF)_2Br$ was found to be 236 K [134]. For $(TMTSF)_2X$ (X=$PF_6$ and $ClO_4$) the Debye temperatures were found to be 200 K and 213 K, respectively [135,136]. The latter values are in a good agreement with the measured temperature dependence of the linewidth. Significant deviations in the Debye temperatures are not expected for different salts because of the similarity of the crystal structures, therefore the deviations in $\theta_D$ might be attributed to experimental problems.

## 4.5 Charge Ordered State

The charge ordered state is a new type of phase transition which was discovered on the insulating side of the phase diagram of some $(TMTTF)_2X$ salts. In the following two sections some previous studies as well as our ESR investigations on this phase transition will be introduced.

### 4.5.1 Previous Investigations

In 1985 it has been reported that $(TMTTF)_2SbF_6$ has a structureless metal insulator phase transition at 155 K [137]. This transition was referred as structureless phase transition because X-ray analysis failed to detect any change of the crystal structure due to this transition [24]. Also no signature was found in the spin susceptibility due to this transition. This transition was identified by observing a clear anomaly in the thermopower at the transition temperature [137]. The same anomaly was observed in $(TMTTF)_2AsF_6$ at about 100 K, and through doping studies, it was possible to ensure that it is the same type of transition [137]. In the same period, a divergence in the dielectric constant $\varepsilon$ was observed at the transition temperature of $(TMTTF)_2SbF_6$ and at about 160 K for $(TMTTF)_2SCN$ [138].

Using one- and two-dimensional $^{13}C$ spin labeled NMR spectroscopy this transition was shown to be due to charge ordering (CO) [2,3]. This was one of the most exciting results of the past few years in this class of materials. The CO transition was observed in $(TMTTF)_2X$ (X=$PF_6$, $AsF_6$, $SbF_6$ and SCN) at 63, 103, 155 and 160 K, and recognized to correspond to ferroelectric (FE) and antiferroelectric (AFE) (in $(TMTTF)_2SCN$) behaviors by dielectric permittivity measurements [1,4,5]. These measurements led to the conclusion that the FE and the AFE states are associated with a charge ordering and result from the loss of the symmetry center relating the molecules on the chain. Structural studies have failed to give evidence for structural modulations associated with the ferroelectric CO transition [139]. Such deformations have been detected in $(TMTTF)_2SCN$ where the antiferroelectric CO phase is accompanied by an anion ordering transition which corresponds to the appearance of (0, 1/2, 1/2) satellite reflections [140].

In the NMR measurements two spectral lines were observed above the charge ordering transition temperature ($T_{CO}$=103K for $AsF_6$ and 156K for $SbF_6$) where each line corresponds to one $^{13}C$ nuclei in the same TMTTF molecule. This is because above $T_{CO}$ all the TMTTF molecules are equivalent, but the two $^{13}C$ nuclei in each molecule have inequivalent hyperfine coupling which results in the two spectral lines. By decreasing the temperature the NMR spectrum remains unchanged down to $T_{CO}$. Below $T_{CO}$ each of the two peaks splits into two peaks with equal absorption strength as shown in Figure 4.17 for the $(TMTTF)_2AsF_6$ salt. This splitting is a result of charge ordering developing between two inequivalent TMTTF molecules, where these two molecules have two different molecular environments, one with slightly larger electron density (rich charged site) and one with a reduced electron density (poor charged site).

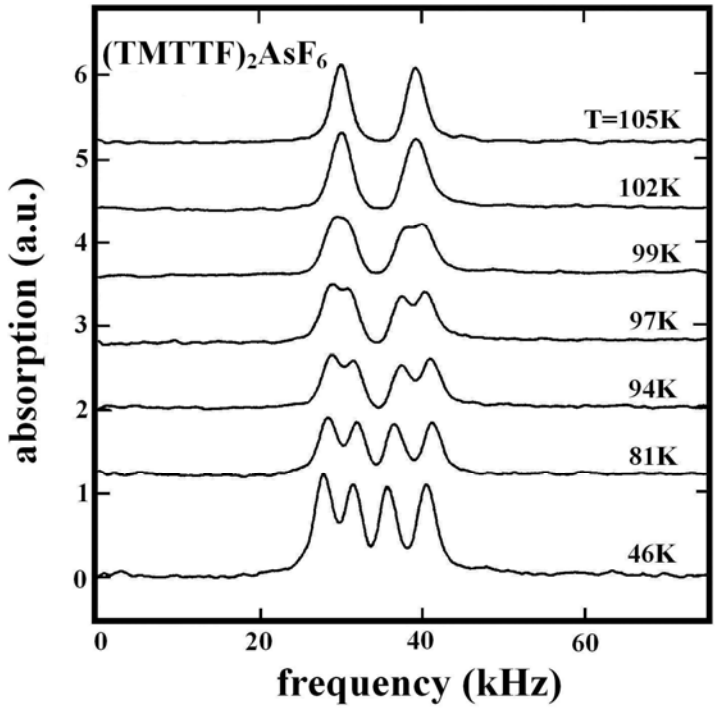


**Figure 4.17**: $^{13}C$ NMR spectra for $(TMTTF)_2AsF_6$ recorded at different temperatures. From Ref. [2].

The degree of the charge disproportionation can be estimated from the spin-lattice relaxation rates $T_1^{-1}$ ($T_{1a}^{-1}/T_{1b}^{-1} = \rho_a^2/\rho_b^2$), where $T_{1a}^{-1}$, $T_{1b}^{-1}$ are the spin lattice relaxation rates of site a and site b, respectively and $\rho_a$, $\rho_b$ are the charge densities on these sites [9]. In $(TMTTF)_2AsF_6$ the relaxation rate was found to be about one order of magnitude faster on one of the two types of molecules below $T_{CO}$ as shown in Figure 4.18. This means that the charges on the molecules of the dimers are $\rho_1 \approx 0.75$ (the rich site) and $\rho_2 \approx 0.25$ (the poor site) In other words the degree of the charge disproportionation was estimated to be 3:1 [9].

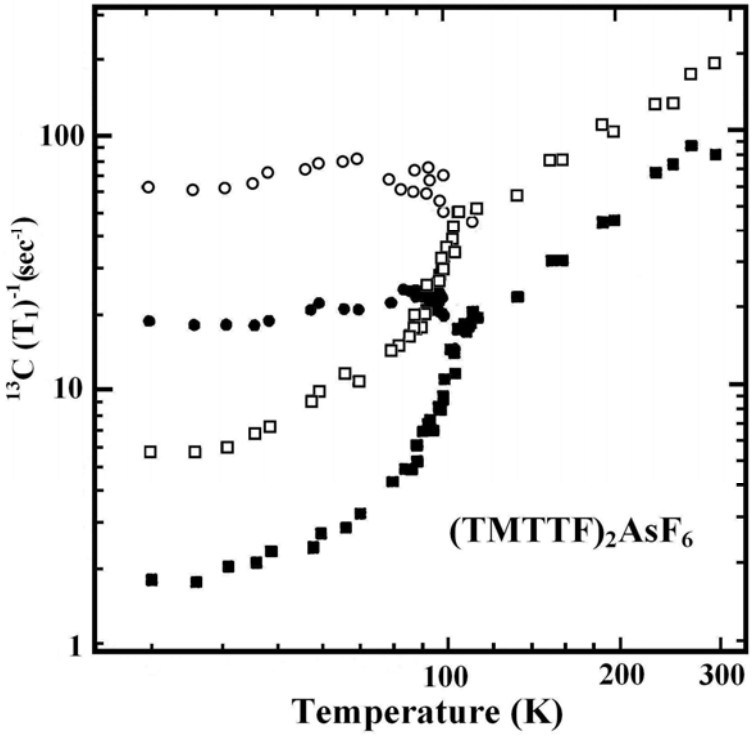


**Figure 4.18:** $^{13}C$ **relaxation rate** $T_1^{-1}$ **as a function of temperature at ambient pressure for** $(TMTTF)_2AsF_6$ **from Ref. [9]. The opened symbols correspond to one** $^{13}C$ **nuclei in the TMTTF molecule and the closed to the other** $^{13}C$ **nuclei in the same TMTTF molecule.**

The influence of charge disproportionation on the vibrational spectra of $(TMTTF)_2AsF_6$ was studied in our group [6] by performing optical reflectivity measurements as a function of temperature with the light polarized parallel to the molecular stacks (a-axis).

The resonance frequency of the $a_g(\nu_3)$ mode which gets infrared active through electron-molecular-vibration (emv) coupling strongly depends on the degree of ionization of the TMTTF molecule[I] [141]. Therefore, charge disproportionation along the molecular stacks should result in a splitting of this particular vibrational mode. Figure 4.19 shows the temperature dependence of the $a_g(\nu_3)$ mode of $(TMTTF)_2AsF_6$ in the vicinity of the charge-order transition.

[I] For neutral TMTTF the mode was observed in polarized infrared absorption spectra at $\nu_0 = 1639\ cm^{-1}$, for $TMTTF^{0.5+}$ at $\nu_0 = 1603\ cm^{-1}$, and for $TMTTF^{+}$ at $\nu_0 = 1567\ cm^{-1}$ [141].

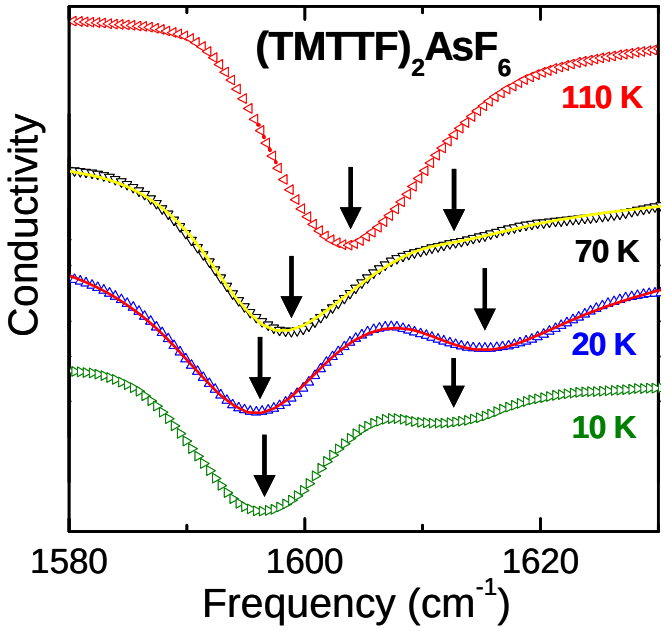


**Figure 4.19: Temperature dependence intramolecular $a_g(\nu_3)$ mode. The arrows indicate the positions of the antiresonance dips. From ref. [6].**

Above $T_{CO}$, one antiresonance mode is located at 1602 $cm^{-1}$. Well below $T_{CO}$, two antiresonance modes are observed. The mode splitting reaches its maximum at around 20 K with $\Delta\nu = 19$ $cm^{-1}$. From this value and assuming a linear shift in the resonance frequency, the difference between the charges on the two unequally charged TMTTF molecules $\Delta\rho$ can be given by $\Delta\rho = \Delta\nu/72$[I]. $\Delta\nu$ is the difference in the resonance frequency of the splited modes. This gives $\Delta\rho = 0.26$, i.e., the charges on the molecules of the dimers are $\rho_1 \approx 0.63$ and $\rho_2 \approx 0.37$. The magnitude of charge disproportionation derived from this experiment of about 2:1 is somewhat smaller than the one obtained from NMR experiments.

It was found also that $T_{CO}$ decreases with increasing pressure and the CO phase can be suppressed easily with moderate pressure of 1.5 kbar for $(TMTTF)_2AsF_6$. The effect of pressure on the ground state and the charge-ordering transition in $(TMTTF)_2SbF_6$ was studied using $^{13}C$ NMR spectroscopy [3]. It was demonstrated that the CO and SP order parameters are competing, and the AF state is stabilized when the CO parameter is large, as in the case of $(TMTTF)_2SbF_6$, where it was found that increasing the pressure reduces the amplitude of the CO and restores the SP state.

[I] The value 72 is the difference between the frequency of the neutral TMTTF and the fully charge one $TMTTF^+$ 1639-1567=72 $cm^{-1}$.

Both the CO and AFM transitions were suppressed by applying pressure of 5 kbar. There, no evidence for CO was observed, and the low temperature $^{13}C$ NMR spectrum was consistent with a singlet spin Peierls (SP) ground state. From these measurements it was concluded that the CO parameter in the $SbF_6$ is larger than in the $AsF_6$ salt. By these experiments the temperature pressure phase diagram of $(TMTTF)_2SbF_6$ was determined, as shown in Figure 4.20.

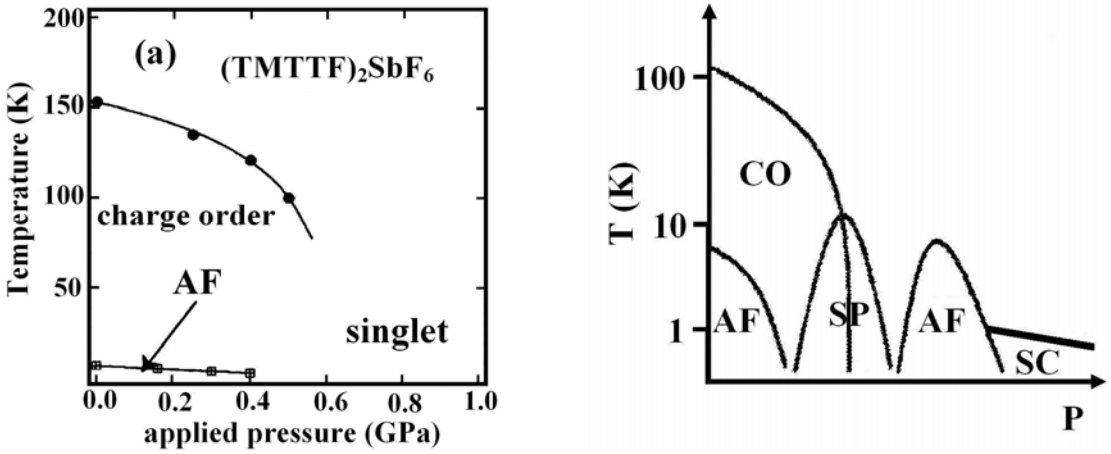


**Figure 4.20: (a) Pressure-temperature phase diagram for $(TMTTF)_2SbF_6$ and (b) a proposed generic phase diagram for the TMTCF salts. From Ref. [3].**

Using the same experiment the charge disproportionation in $(TMTTF)_2SCN$ which is triggered by anion ordering was studied [142]. Below the charge ordering temperature ($T_{CO}$=160 K), a new broad line appeared in the NMR spectra and the intensity of the distinct line is almost halved. The appearance of a new line revealed that the electronic charge is disproportionated in this salt below the $T_{CO}$.

Direct evidence for the ferroelectric nature of the CO transition at about 100 K in the $(TMTTF)_2AsF_6$ salt was obtained from the dielectric permittivity $\varepsilon'$ and the complex conductance G measurements [143]. These measurements were performed in the temperature range 10-300 K and for frequencies between $10^3$ to $10^7$ Hz. It was found that by lowering the temperature, G first increases to a maximum at $T_\rho \approx 230\,K$ as expected for a metal. Below 230 K, G was found to decrease by decreasing temperature with a thermally activated behaviour down to $T_{CO}$. At $T_{CO} \approx 100$ K, a sharp bend in G was observed and the temperature dependence of the logarithmic derivative [d(logG) / d(1/T)] shows a sharp minimum at this temperature, which is due to an increase in the activation energy. From these measurements the energy gap

due to the CO transition was calculated and found to be $\Delta_{CO}$ = 300 K. The most pronounced temperature and frequency dependence of $\varepsilon'$ was observed in a narrow temperature interval around $T_{CO}$=100 K.

With decreasing the temperature below 140 K the following behaviors were observed (see Figure 4.21):

- Increasing of the frequency dispersion of $\varepsilon'$ as the temperature approaches 100 K.
- A sharp growth of $\varepsilon'$ with a tendency to diverge at 100 K, this growth is more pronounced at low frequencies.

The growth of $\varepsilon'$ at $T_{CO}$ was attributed to the ferroelectric behaviour of the charge-ordered transition.

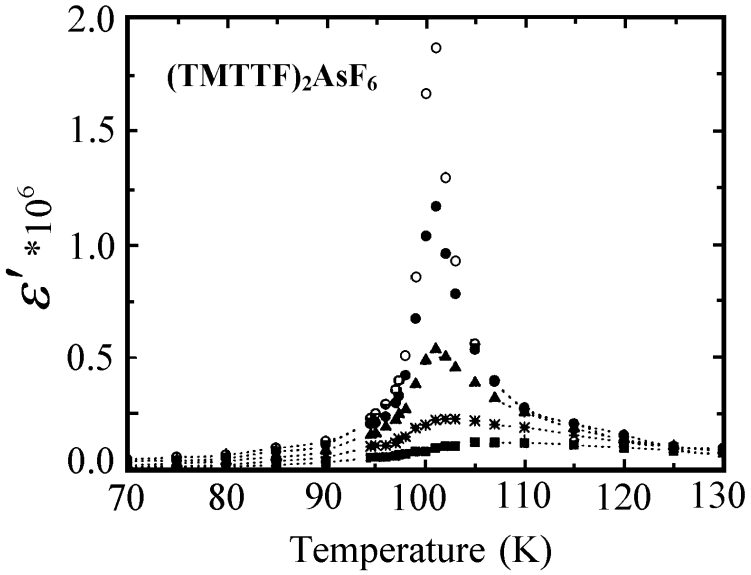


**Figure 4.21: Temperature dependence of the real part of the dielectric permittivity $\varepsilon'$ of $(TMTTF)_2AsF_6$ at frequencies: 100 kHz (○), 300 kHz (●), 1 MHz (▲), 3 MHz (∗) and 10 MHz (■). From Ref. [143].**

The same behaviors were observed for $(TMTTF)_2X$ (X= $SbF_6$ and SCN) [1,4], where a bend at $T_{CO}$ for both salts was observed in G at $T_{CO}$ ($T_{CO}$ = 154 K for $SbF_6$ and 169 for SCN). Also a narrow peak in the $\varepsilon'$(T) dependences was observed at the same temperatures (see Figure 4.22). In the SCN salt, the maximum value of $\varepsilon'$ is about two orders of magnitude smaller than the maxima in $AsF_6$ and $SbF_6$ salts, also $\varepsilon'$ drop is smooth after $T_{CO}$ not as in $AsF_6$ and $SbF_6$ salts.

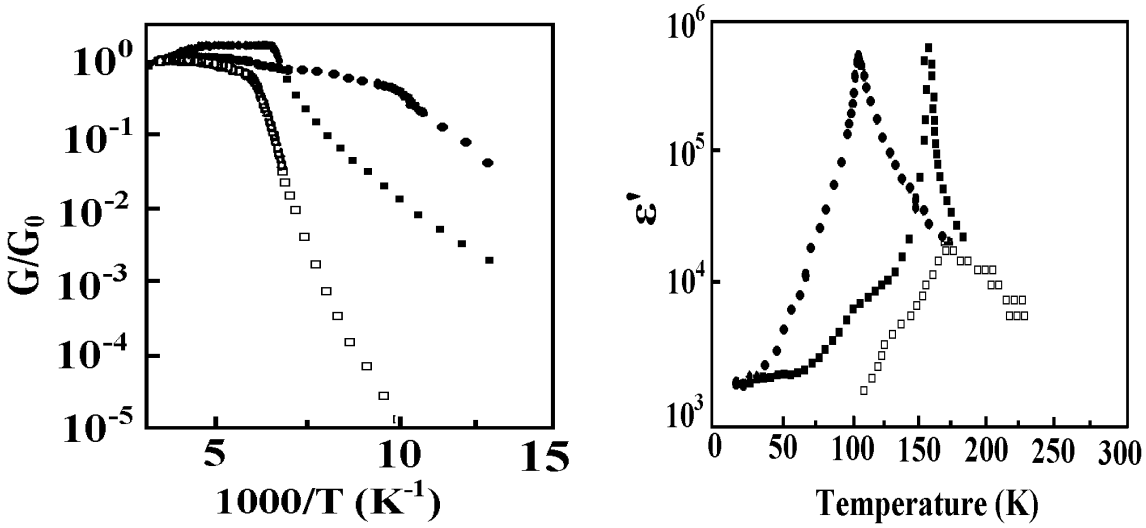


**Figure 4.22: Temperature dependence of the conductance G normalized by its value at room temperature at frequency 1 kHz (a) and dielectric permitivity $\varepsilon'$ in semilogarithmic scale at frequency 1 MHz (b). The samples are $(TMTTF)_2X$ (X= $AsF_6$ (●), $SbF_6$ (■) and SCN (□)). From ref. [4]**

In the salts with centrosymmetrical anions ($AsF_6$ and $SbF_6$) the charge ordering transition was shown to have a ferroelectric behavior [4], this transition is a second order phase transition. Such a phase transition is normally described by the Curie law $\varepsilon' = A/|T - T_{CO}|$. In the case of $(TMTTF)_2SCN$, due to the finite transverse component of $q$=(0,1/2,1/2), each anion chain can move in the opposite direction to the neighboring chains, yielding an antiferroelectric (AFE) character to the CO phase transition.

## 4.5.2 ESR Investigations of the Charge Ordered State

In section 4.3 it was shown that the linewidth begins to decrease more slowly for $(TMTTF)_2SbF_6$ and $(TMTTF)_2AsF_6$ and increases by decreasing temperature for $(TMTTF)_2SCN$ below $T_{CO}$ (See Figures: 4.6, 4.7 and 4.8). Also it was illustrated that the anisotropy of the linewidth changes in the charge order region, where for the salts with centrosymmetrical anions ($SbF_6$ and $AsF_6$ salts) the anisotropy of $\Delta H$ below $T_{CO}$ is $\Delta H_{c^*} > \Delta H_{b'} \approx \Delta H_a$, but in the case of $(TMTTF)_2SCN$ it is different where $\Delta H_{c^*} \approx \Delta H_{b'} > \Delta H_a$. These observations clearly show that the relaxation mechanism below $T_{CO}$ is different from the mechanism above it.

To illustrate the effect of the charge ordering transition on the anisotropy of the linewidth, the linewidth induced by the charge ordering $\Delta H_{CO}$ (the charge ordering linewidth) is introduced. $\Delta H_{CO}$ along any direction of the $(TMTTF)_2X$ salt can be calculated using the equation:

$$\Delta H_{CO}(x) = \Delta H(x) - \Delta H_{\text{model}}(x) \tag{4.5}$$

where $\Delta H_{CO}(x)$ is the charge ordering linewidth of the investigated salt along the x-axis (x = a, b' and c*), $\Delta H(x)$ is the measured linewidth of this salt along the same axis and $\Delta H_{\text{model}}(x)$ is the linewidth of $(TMTTF)_2PF_6$ salt [128] along the same direction normalized to the room temperature value of the linewidth of the investigated salt. $(TMTTF)_2PF_6$ is the model system of the $(TMTTF)_2X$ salts which undergoes a CO phase transition at 63 K, but the effect of this transition on the ESR linewidth is not obvious and the temperature dependence of the linewidth of this salt is the same as that of $(TMTSF)_2X$ salts.

The obtained $\Delta H_{CO}$ as a function of temperature along the three crystal axes of the three salts is shown in Figure 4.23. $\Delta H_{CO}$ equals zero along the three directions above $T_{CO}$, it begins to increase by decreasing the temperature below $T_{CO}$. Also the figure shows that below $T_{CO}$ the charge ordering linewidth of the salts with centrosymmetrical anions ($AsF_6$ and $SbF_6$) have the same anisotropy ($\Delta H_{CO}(a) = \Delta H_{CO}(b') < \Delta H_{CO}(c^*)$) and the anisotropy is different in $(TMTTF)_2SCN$ ($\Delta H_{CO}(a) < \Delta H_{CO}(b') = \Delta H_{CO}(a)$). From Figure 4.23 it is clear that the CO linewidth of $(TMTTF)_2SbF_6$ increases faster than that of $(TMTTF)_2AsF_6$ by decreasing the temperature below $T_{CO}$, this indicates a higher degree of charge disproportionation in $(TMTTF)_2SbF_6$ in agreement with the previous NMR measurements [3].

In the previous section it was clarified that the torsional oscillations of the TMTTF molecules around their long molecular axis enables the spin-orbit scattering. And that the possibility of producing intrastack spin-orbit scattering comparable in magnitude to the interstack scattering is excluded because the spin-orbit interaction can't cause electronic transitions within stacks of the same, identically oriented, centrosymmetrical donor molecules like the TMTTF molecules above $T_{CO}$. Since the inversion symmetry precludes the intrastack spin-orbit scattering in the $(TMTTF)_2X$ salts, the anisotropy of the ESR linewidth ($\Delta H_{c^*} > \Delta H_{b'} > \Delta H_a$) is reserved as long as the inversion symmetry of the donor molecules exists.

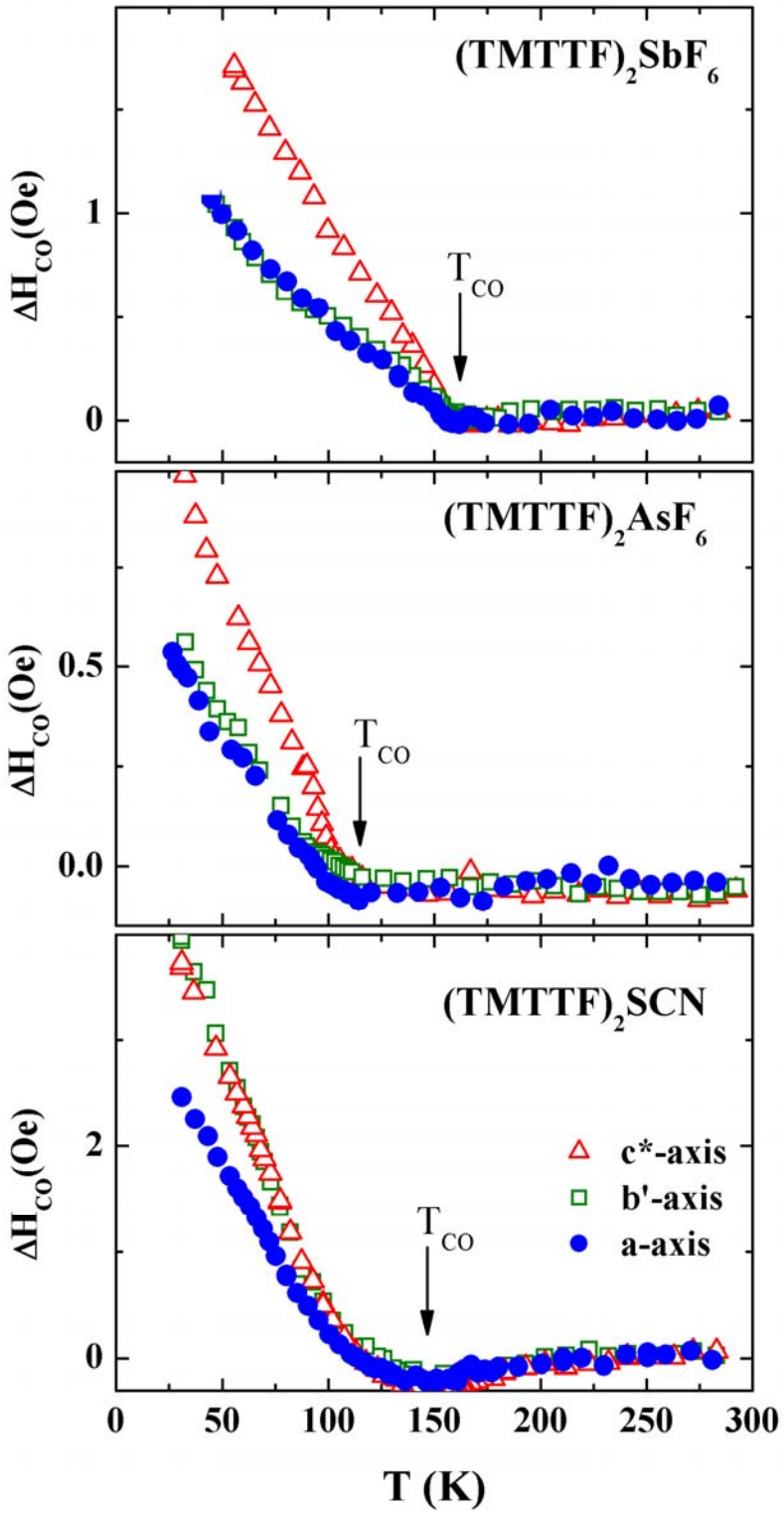


**Figure 4.23: The calculated charge ordering ESR linewidth ($\Delta H_{CO}$) for the salts $(TMTTF)_2X$ ($X=SbF_6$, $AsF_6$ and SCN) along the three crystal axes. The linewidth is calculated as explained in the text.**

From previous dielectric permittivity [1,4,5] and NMR measurements [2] it was concluded that the charge ordering transition results from the loss of the symmetry center relating the molecules of the TMTTF chain. Since the symmetry center of the TMTTF chain is lost below $T_{CO}$, one expects an increase in the scattering and therefore a change in the temperature dependence of the linewidth and change in the anisotropy of the ESR linewidth below this temperature.

The change in the temperature dependence of the linewidth below $T_{CO}$ for $(TMTTF)_2SbF_6$ is suppressed by applying pressure [144]. In other words by applying pressure there is no change in the temperature dependence of the linewidth below $T_{CO}$ and it behaves like the linewidth of $(TMTTF)_2PF_6$. This is a strong evidence that the increase in the scattering rate at low temperatures is due to charge ordering.

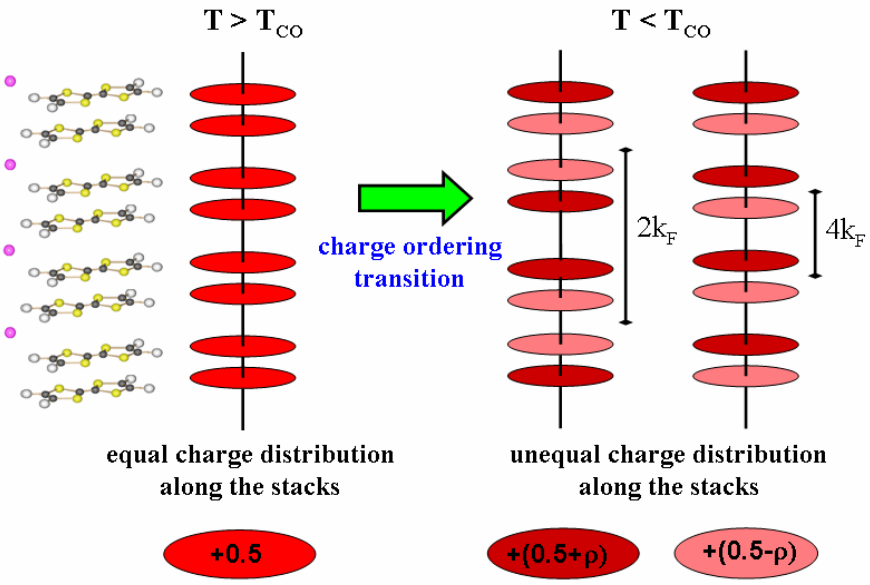


**Figure 4.24: Schematic representation of the charge ordering transition in $(TMTTF)_2X$ salts. Above $T_{CO}$ the charge is equally distributed along the stacks where each TMTTF molecule has +0.5 charge. Below $T_{CO}$ the charge is not equally distributed between the TMTTF molecules anymore where some molecules have +(0.5+ρ) charge (rich charge sites) and the others have +(0.5-ρ) (poor charge sites). The rich and the poor sites can be arranged in different ways along the stacking direction producing different charge order's wave vector ($2k_F$ or $4k_F$).**

Since the CO linewidth of the salts with centrosymmetrical anions ($AsF_6$ and $SbF_6$) have the same anisotropy it seems to be that the $(TMTTF)_2AsF_6$ and $(TMTTF)_2SbF_6$

salts have the same charge order pattern[I]. Whereas it was shown in Figure 4.23 that the anisotropy of the CO linewidth of $(TMTTF)_2SCN$ have not the same anisotropy as the two salts, therefore it seem that it has another charge order pattern as shown schematically in Figure 4.24. There was an indirect evidence from previous EPR measurements [145] that the charge order pattern changes when the symmetry of the counterion is changed. Two different charge ordering patterns along the stacking direction are schematically shown in Figure 4.24.

Since the charge ordering has a drastic effect on the linewidth, detailed angular dependent measurements of the linewidth and the g-value of the investigated salts were performed along the three crystal planes (ab', ac* and b'c*-planes) at different temperatures (above and below $T_{CO}$) to illustrate the effect of the charge ordering transition on the linewidth and the g-value. The angular dependence of the g-value along the three planes for the three compounds does not change by decreasing the temperature and has the same orientation pattern as at room temperature (see Figure 4.4). Below $T_{CO}$ the linewidth along the a-axis become almost the same as along the b′-axis for $(TMTTF)_2AsF_6$ and $SbF_6$ (see Figure 4.6 and Figure 4.7) therefore one expects no orientation dependence of the linewidth along this plane in the charge order state. However as shown in Figure 4.25 characteristic changes in the orientation dependence of the linewidth are observed for the two salts in the charge order region, where a peak in the orientation pattern appears at $45^o$ and $135^o$ instead of $90^o$ above $T_{CO}$. The two peaks are more pronounced at low temperatures.

The orientation dependence of the linewidth above $T_{CO}$ for the two salts can be modeled by equation 4.6 as was discussed in section 4.2.

$$\Delta H_{sp}(\theta) = \left[ \Delta H_{sp}^2(a)\cos^2(\theta) + \Delta H_{sp}^2(b')\sin^2(\theta) \right]^{1/2} \qquad (4.6)$$

where $\Delta H_{sp}(a)$ and $\Delta H_{sp}(b')$ are the linewidths induced by spin phonon scattering along a- and b′-axes, respectively and θ is the angle between $B_o$ and the a-axis. At the lowest temperatures (10 K in $(TMTTF)_2SbF_6$ and 5 K in $(TMTTF)_2AsF_6$) the angular dependence of the linewidth can be modeled by the relation:

$$\Delta H_{doubling}(\theta) = \left[ \Delta H^2(0^\circ)\cos^2(2\theta) + \Delta H^2(45^\circ)\sin^2(2\theta) \right]^{1/2} \qquad (4.7)$$

where $\Delta H(0^\circ)$ and $\Delta H(45^\circ)$ are the linewidths at $0^o$ and $45^o$, respectively.

[I] The charge ordering pattern means the arrangement of the rich and poor charge sites along the stacking axis, where these sites can be arranged in different ways as shown in Figure 4.24.

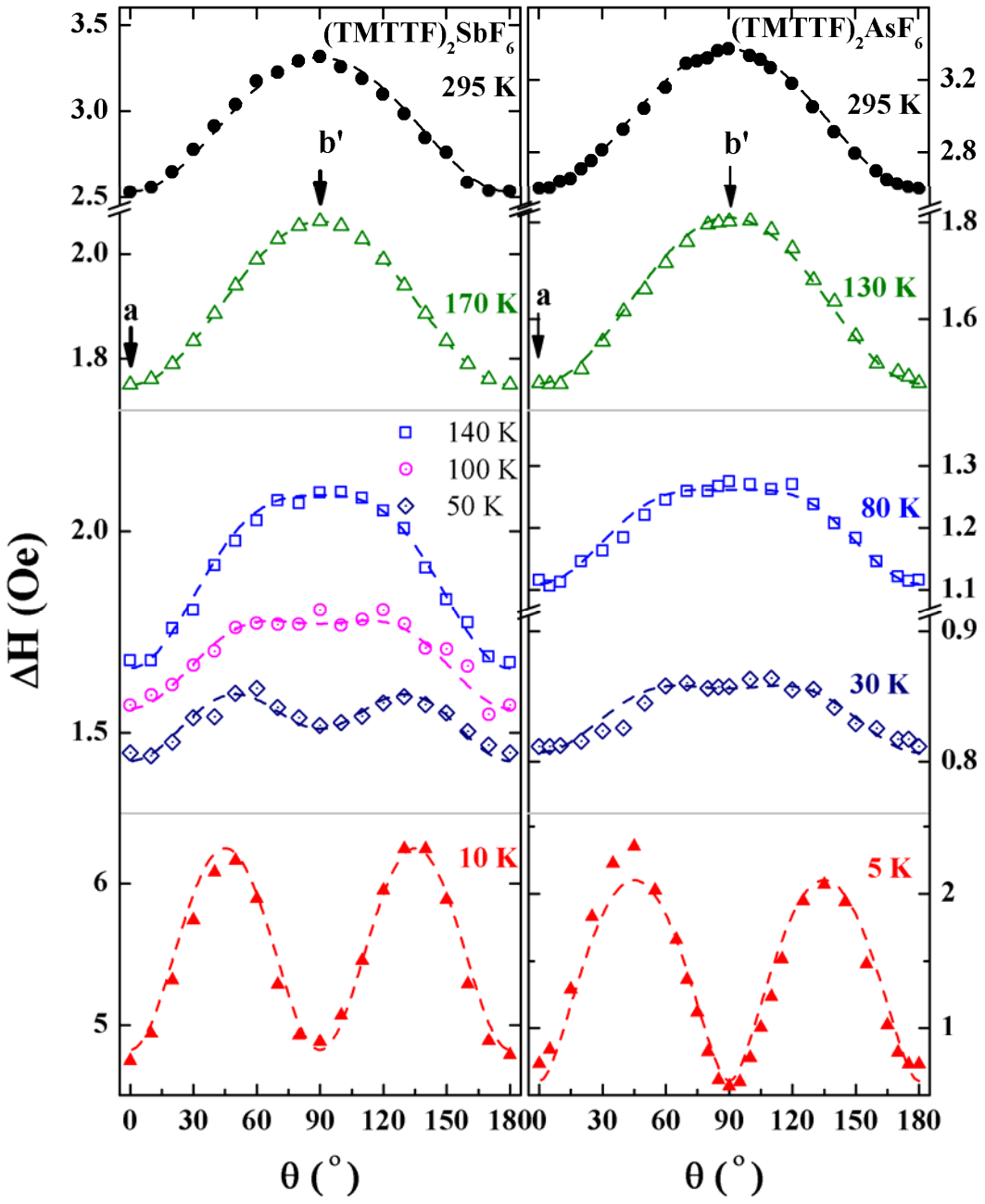


**Figure 4.25: Orientation dependence of the ESR linewidth along ab'-plane of $(TMTTF)_2SbF_6$ ($T_{CO}$=155 K) and $(TMTTF)_2AsF_6$ ($T_{CO}$=103 K) at different temperatures. The symbols represent the measured data and the dashed lines represent fittings of the linewidth using either equations 4.6 or 4.7 or the sum of both (see the text). The fit parameters used are listed in Table 4.4.**

| T (K) | $(TMTTF)_2 SbF_6$ | | | | T (K) | $(TMTTF)_2 AsF_6$ | | | |
|---|---|---|---|---|---|---|---|---|---|
| | ΔH (a) | ΔH (b') | ΔH ($0^o$) | ΔH ($45^o$) | | ΔH (a) | ΔH (b') | ΔH ($0^o$) | ΔH ($45^o$) |
| 295 | 2.53 | 3.31 | 0 | 0 | 295 | 2.59 | 3.37 | 0 | 0 |
| 170 | 1.75 | 2.06 | 0 | 0 | 130 | 1.47 | 1.81 | 0 | 0 |
| 140 | 0.91 | 1.34 | 0.75 | 0.82 | 80 | 0.61 | 0.76 | 0.5 | 0.54 |
| 100 | 0.81 | 1.02 | 0.75 | 0.82 | 30 | 0.62 | 0.67 | 0.184 | 0.202 |
| 50 | 0.45 | 0.53 | 0.98 | 1.1 | 5 | 0 | 0 | 0.6 | 2.1 |
| 5 | 0 | 0 | 4.82 | 6.25 | | | | | |

**Table 4.4: The fit parameter for the orientation dependence of the linewidth along ab′-plane of $(TMTTF)_2SbF_6$ and $(TMTTF)_2AsF_6$ using equations 4.6 and 4.7.**

For the moderate temperatures below $T_{CO}$ the orientation dependence of the linewidth can be fitted by the sum of equation 4.6 and 4.7. This means that a new scattering process which causes a doubling of the periodicity of the linewidth along ab'-plane exists below $T_{CO}$ in the salts with centrosymmetrical anions. The fit parameters used in modeling the orientation dependence of the linewidth at different temperatures are listed in Table 4.4. The detailed fitting procedures for the moderate temperatures below $T_{CO}$ are illustrated in Figure 4.26 for $(TMTTF)_2SbF_6$ at 50 K as an example.

The doubling of the periodicity in the orientation dependence of the linewidth along the ab′-plane can be due to the coexistence of two inequivalent magnetic TMTTF sites in the CO region. In this case, the EPR spectrum results from the two different magnetic species in the single crystal. Two extreme cases should be considered depending on the magnitude of $\nu_{12}$, the hopping rate between the two nonequivalent species [146]:

- Two separated signals will be observed in the "weak coupling limit", i.e., when $\nu_{12} \ll |\nu_1 - \nu_2|$, where $\nu_i$ is the Larmor frequency of the species *i*, *i*=1,2.

- A single EPR line will be observed in the "strong coupling limit", i.e., when $\nu_{12} \gg |\nu_1 - \nu_2|$, with a *g* factor and a linewidth which are the result of a weighting between the characteristics of each magnetic species.

In our measurements a single Lorentzian absorption line was observed in all the temperature range along the three crystal axes as show for $(TMTTF)_2AsF_6$ along the

a-axis in Figure 4.5 as an example. This means that the X-band frequency (9.5 GHz) is not sufficient to split the two expected ESR signals below $T_{CO}$. From this point of view performing high frequency ESR measurements (Q-band and W-band [I]) on the charge order state is very important.

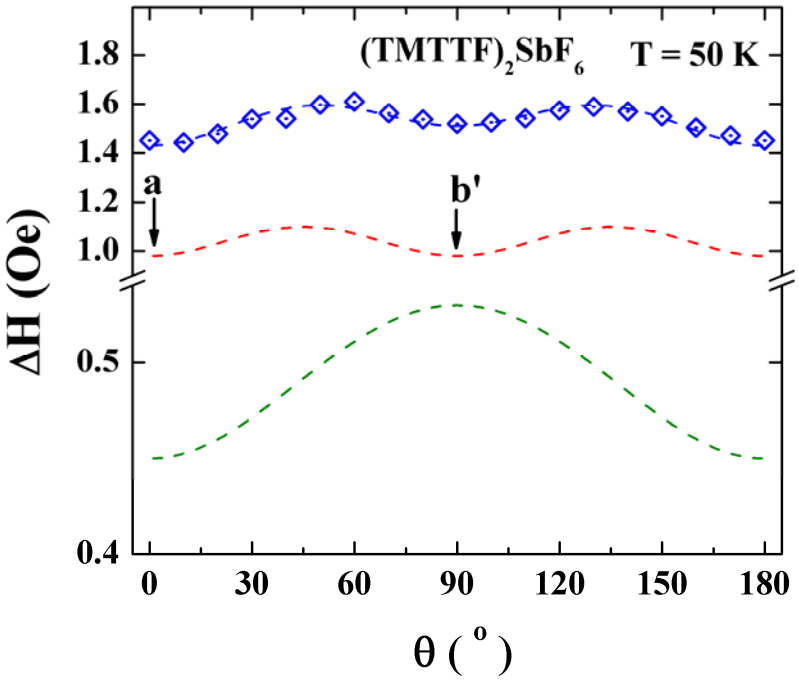


**Figure 4.26: Angular dependence of the linewidth ΔH of $(TMTTF)_2SbF_6$ in the charge order region (T=50 K). The points are the measured data, the green line represent a fit with equation 4.6 (spin phonon interaction), the red line a fit with equation 4.7 (doubling of the periodicity) and the blue line is the sum of both. The fit parameters are listed in Table 4.4.**

A doubling in the periodicity of the linewidth was also observed in the quasi one-dimensional S=1/2 AFM Heisenberg inorganic systems $CuGeO_3$ [105] and $CuSb_2O_6$ [147]. No change in the orientation pattern of the linewidth is observed along the ac* and b'c*-planes for the $(TMTTF)_2SbF_6$ and $(TMTTF)_2AsF_6$ salts as shown in Figure 4.27 for the $(TMTTF)_2SbF_6$ case.

[I] The microwave frequency in the Q-band ESR spectrometer is 35 GHz and in the W-band 94 GHz.

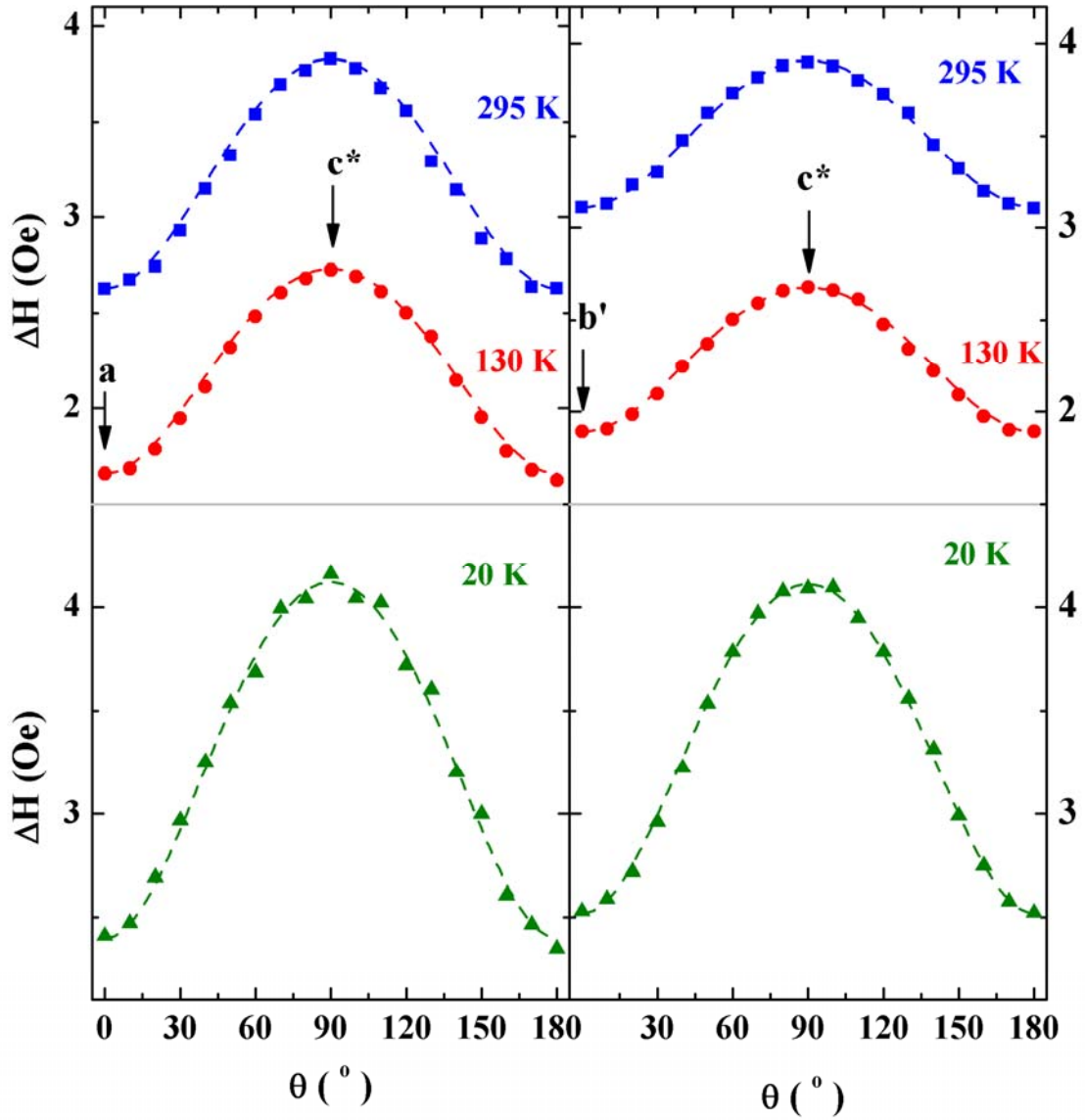


**Figure 4.27: Orientation dependence of the ESR linewidth along the ac*- and b'c*-planes of $(TMTTF)_2SbF_6$ above and below $T_{CO}$=155 K. The symbols represent the measured data and the dashed lines represent the least-square fit.**

However, no change in the orientation dependence of the linewidth in $(TMTTF)_2SCN$ along ab′-plane is observed in the charge order region as shown in Figure 4.28. Never the less, characteristic changes of the orientation dependence of the linewidth along b'c*-plane well below the charge ordering transition temperature ($T_{CO}$=160) are observed in $(TMTTF)_2SCN$ as shown in Figure 4.29.

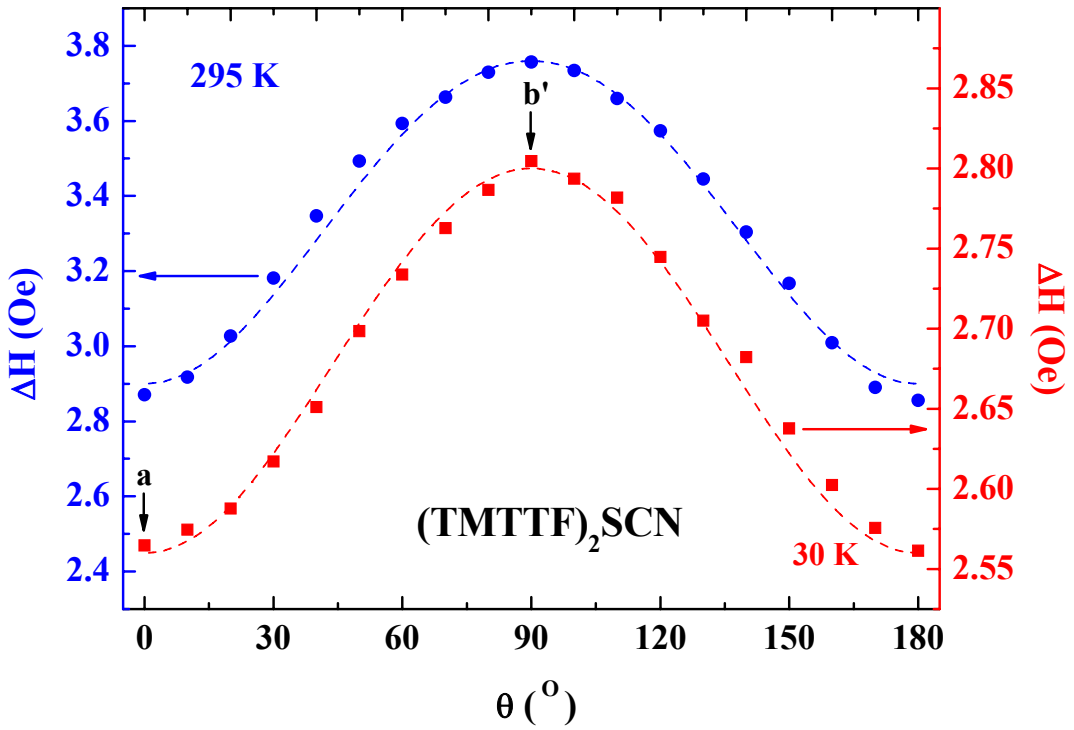


**Figure 4.28: Orientation dependence of the ESR linewidth along the ab'-plane of $(TMTTF)_2SCN$ above and below $T_{CO}$=160 K. The scattered symbols represent the measured data and the dashed lines represent the least-square fit. The fit parameters are $\Delta H_a$(295 K) = 2.9 Oe, $\Delta H_{b'}$(295 K) = 3.8 Oe, $\Delta H_a$(30 K) = 2.56 Oe and $\Delta H_{b'}$ (30 K) = 2.77 Oe**

Above $T_{CO}$ the maximum and the minimum of the linewidth are observed when the magnetic field is applied parallel to the c*- and b'-axis, respectively, the maximum and the minimum begin to shift away from the crystal axes below $T_{CO}$. At very low temperatures the maximum of the linewidth is observed along the b'-axis and the minimum along the c*-axis. At all temperatures the orientation dependence of the linewidth can be fitted by equation 4.1 after modifying it to:

$$\Delta H(\theta) = \left[\Delta H_{min}^2 \cos^2(\theta+\varphi) + \Delta H_{max}^2 \sin^2(\theta+\varphi)\right]^{1/2} \qquad (4.8)$$

where $\varphi$ is the angle at which the minimum value of the linewidth is observed. This behaviour can be due to the charge ordering transition which is triggered by the anion ordering transition which has the anion ordering critical wave vector (0,1/2,1/2) [86]. This means the unit cell is doubled along the b and c-axes due to the movement of the anion in this plane at $T_{AO}$ which can cause the shift of the minimum and the maximum of the linewidth.

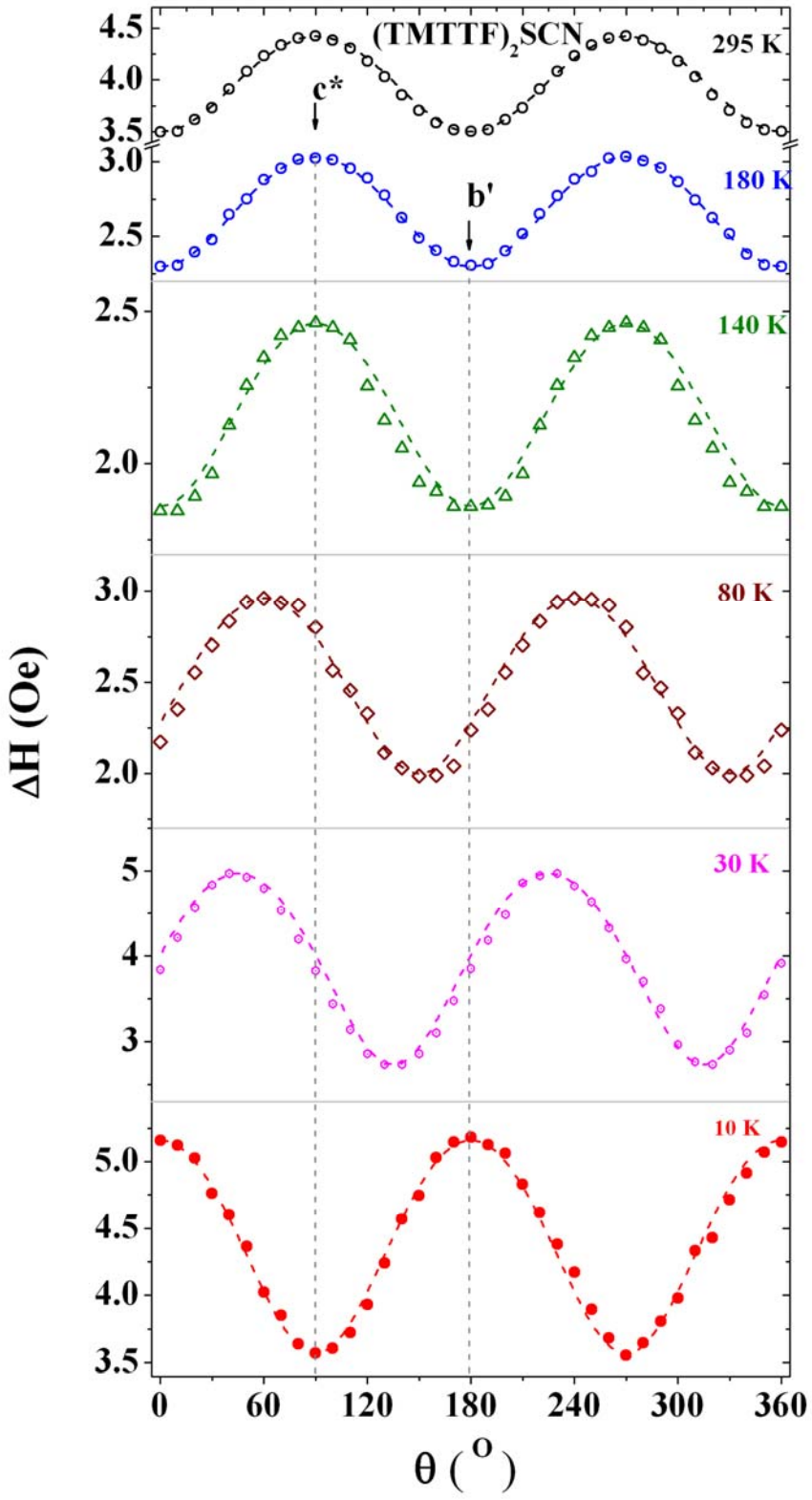


**Figure 4.29: Orientation dependence of the ESR linewidth of $(TMTTF)_2SCN$ along the b'c*-plane above and below $T_{CO}$=160 K. The symbols represent the measured data and the dashed lines represent the least-square fit using equation 4.8. The values of φ used in the fit are: 0° for T = 295 K, 180 K and 140 K, 30° for T = 80 K, 45° for T = 30 K and 90° for T = 10 K.**

## 4.6 Antiferromagnetic Fluctuations in $(TMTTF)_2SCN$ and $(TMTTF)_2SbF_6$

It was shown in Figure 4.7 and Figure 4.8 that there is a distinct increase in the ESR linewidth by lowering the temperature as the temperature approaches the AFM ordering temperature for the salts $(TMTTF)_2SbF_6$ and $(TMTTF)_2SCN$. This singularity of ΔH in the AFM fluctuation region is generally considered as the signature for the magnetic character of the ordering. A detailed theoretical analysis of the temperature dependence of the ESR linewidth in the AFM fluctuation region was done [148]. In the case of a small static magnetic field H the linewidth in the AFM fluctuation region was shown to follow the following behaviour:

$$\Delta H(T \to T_N) = C\, r_{AFM}^{-\mu} \tag{4.9}$$

where $C$ is a constant, $r_{AFM} = (T - T_N)/T_N$ and $\mu$ is a function of the critical indices[I], and the dimensionality of the AFM fluctuations $d$. If the dipole-dipole interaction is the dominant relaxation process in this critical region $\mu$ is given by $\mu = 3 - d/2$. i.e. $\mu = 3/2$ for three dimensional AFM fluctuations. The analysis of the temperature dependence of the linewidth ΔH of the two materials investigated near the antiferromagnetic phase transitions is given in Figure 4.30.

The obtained μ =1.5 for $(TMTTF)_2SCN$ confirms the three dimensional behaviour of the antiferromagnetic fluctuations which produces 3-D AFM ordering below $T_N$. This result is confirmed by NMR investigations where a critical behaviour in the relaxation rate $T_1^{-1}$ was observed [149]. The same slope (μ = 1.5) was observed for $(TMTSF)_2PF_6$ [10,120], $(TMTSF)_2AsF6$ and $(TMTTF)_2Br$ [120] as shown in Figure 4.31. Surprisingly in $(TMTTF)_2SbF_6$ we find μ = 0.5. This difference might be assigned to the different anisotropy in the spin degree of freedom, as well as to different relative magnitude of the dipole-dipole interaction and spin-orbit coupling. A similar result as in the case of $(TMTTF)_2SbF_6$ (μ = 0.5) was found in $(TMTSF)_2NO_3$ [10]

[I] The critical indices are normally obtained by the analysis of the temperature dependence of $T_1^{-1}$ in the AFM fluctuation region.

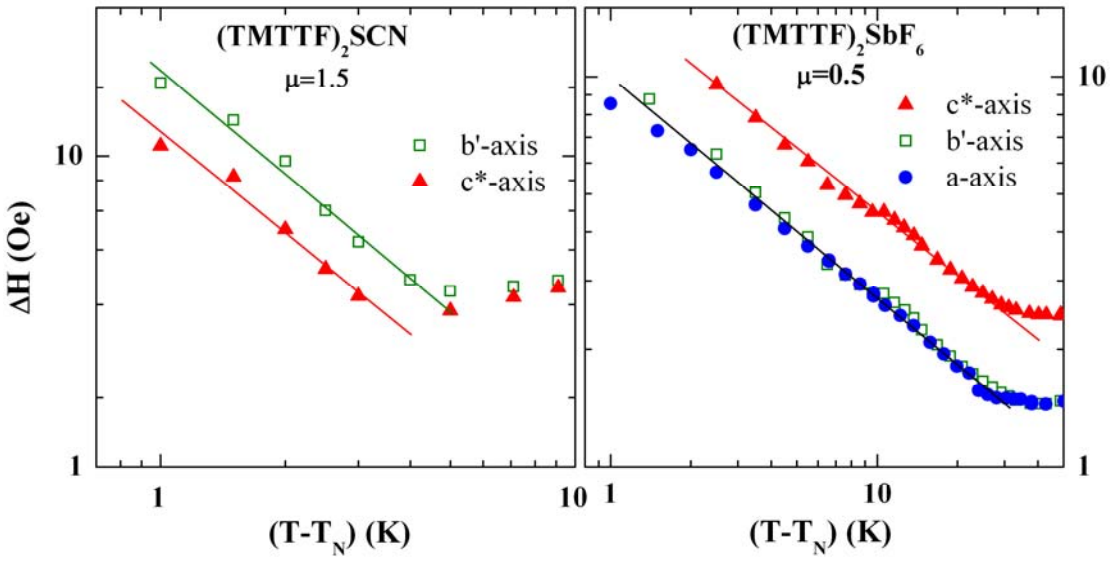


**Figure 4.30: Double-logarithmic plot of the linewidth versus $(T-T_N)$ of $(TMTTF)_2SCN$ (left) and $(TMTTF)_2SbF_6$ (right) along different directions in the antiferromagnetic fluctuation region. The lines represent the linear fit with a slope μ=1.5 in $(TMTTF)_2SCN$ and 0.5 in $(TMTTF)_2SbF_6$, $T_N$ = 8 K in the case of $(TMTTF)_2SCN$ and 7 K for $(TMTTF)_2SbF_6$.**

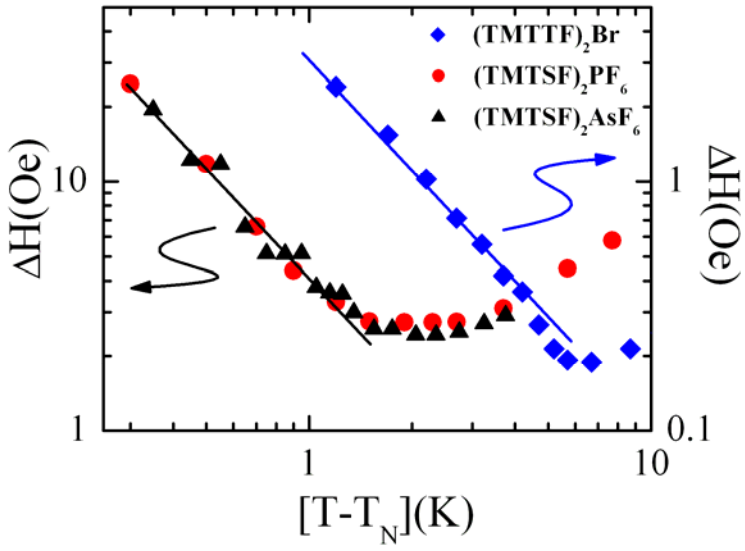


**Figure 4.31: Double-logarithmic plot of the linewidth versus $(T-T_N)$ of $(TMTTF)_2Br$ (right axis), $(TMTSF)_2PF_6$ and $(TMTSF)_2AsF_6$ (left axis) along the b'-axis near the antiferromagnetic phase transition. The lines represent the linear fit with a slope μ=1.5 for the three salts. $T_N$ = 12 K in the case of $(TMTSF)_2PF_6$ and $(TMTSF)_2AsF_6$ and 13.3 K for $(TMTTF)_2Br$. From ref. [120].**

The orientation dependence of the linewidth of both salts at room temperature was discussed in section 4.2 (see Figure 4.4). It was shown that spin phonon interaction is the main relaxation process at room temperature and therefore the linewidth have the same anisotropy as the g-value. By decreasing the temperature below the charge ordering transition temperature of $(TMTTF)_2SbF_6$ we have seen that the periodicity of the orientation pattern of the linewidth along the ab'-plane is doubled due to the coexistence of two inequivalent magnetic TMTTF molecules. Figure 4.32 shows the angular dependence of the linewidth of $(TMTTF)_2SCN$ along the ab'-plane in the region of antiferromagnetic fluctuations.

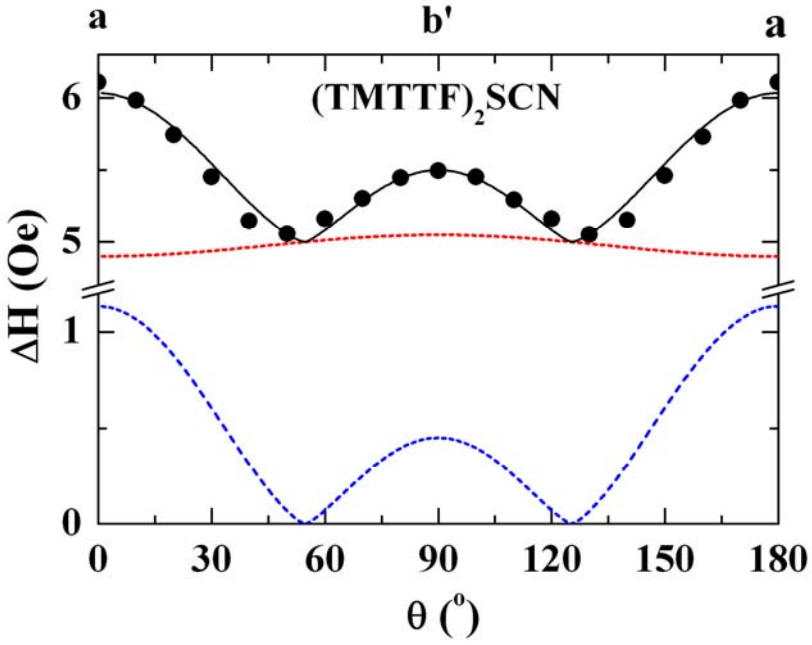


**Figure 4.32: Angular dependence of the linewidth ΔH of $(TMTTF)_2SCN$ in the antiferromagnetic fluctuation region (T=10 K). The points are the measured data, the blue line represent a fit with $\Delta H_{d\text{-}d}=\Delta H_{b'}(3\cos^2(\theta)-1)^{4/3}$ (dipole-dipole interaction)the red line a fit with $\Delta H=(\Delta H_a^2\cos^2(\theta)+\Delta H_{b'}^2\sin^2(\theta))^{1/2}$ (spin-phonon interaction) and the black line is the sum of both.**

By rotating the crystal in the ab'-plane, the broadest line is measured along the a-direction ( $\theta=0°$ ) and the smallest line at $55°$. Along the b'-direction ($\theta=90°$) the linewidth has an intermediate value. The minimum near the magic angle ($\theta=54.7°$) is a strong indication of the contribution of the of the dipole-dipole interaction in the relaxation process in this temperature range. In the case that dipole-dipole interaction is the dominant relaxation process in one-dimensional systems, an

angular dependence $\Delta H_{d\text{-}d}=\Delta H_{b'}\left[3\cos^2(\theta)-1\right]^{4/3}$ is expected. As seen in Figure 4.32 the orientation dependent measurements of the linewidth of $(TMTTF)_2SCN$ at T = 10 K can be fitted with the sum of the contributions of the dipole-dipole and spin-phonon interactions. This means that both interactions contribute in the relaxation process in this temperature range.

It was shown in section 4.3 that for both salts $(TMTTF)_2SCN$ and $(TMTTF)_2SbF_6$, the g-value become strongly temperature dependent as the temperature approaches $T_N$ (see Figure 4.7 and Figure 4.8), where it increases by decreasing the temperature along the a-axis and decrease along the b'- and c*-axes. This is expected in the case of AFM ordering, where the magnetic correlations modify the environment of a given spin. The existence of a fluctuating local field leads to a specific temperature dependence of the *g* factor, where it is expected to increase along the hard axis and decrease along the intermediate and easy axes. By performing AFM resonance measurements [150], the hard, intermediate and easy axes where shown to be close to the a, c* and b' axis, respectively.

## 4.7 Spin Peierls Transition in $(TMTTF)_2AsF_6$

The temperature dependence of the spin susceptibility of $(TMTTF)_2AsF_6$ in the low-temperature region is shown in Figure 4.33. Below $T_{SP}$ = 13K, the spin susceptibility decreases exponentially by lowering the temperature down to lowest temperatures due to the spin Peierls transition. The SP transition is a second order phase transition. The temperature dependence of the spin susceptibility below $T_{SP}$ can be described by the Bulaevskii's model for an alternating spin chain (as discussed in section 2.3.2). Bulaevskii's formula for the temperature dependence of the spin susceptibility of the alternating spin chain is given by the relation:

$$\left[\chi_s\right]_v(T)=\frac{\mu_o N g^2 \mu_B^2}{k_B}\frac{\alpha}{T}\exp\left[-\frac{J\beta'}{T}\right] \tag{4.10}$$

In the spin Peierls state, the spin susceptibility can be fitted using the previous relation with the fit parameter $J\beta'=55.7$ K as shown in the solid line in Figure 4.33. Using the obtained value of $J$ = 410 K from fitting the spin susceptibility in the high temperature region using the EAT model (as discussed in section 4.4.1), one gets $\beta'=0.1359$. Now, the values of the alternation parameter $\gamma$ and the constants $\beta$ and $\alpha$ can be obtained from Figure 2.7. We get $\gamma=0.94$, $\beta=0.131$ and $\alpha=0.051$.

Using equation (2.9) we obtain $\delta=(1-\gamma)/(1+\gamma)=0.0309$, the intradimer AFM exchange constant $|J_1|=|J|(1+\delta)=423\,\mathrm{K}$ and the interdimer AFM exchange constant $|J_2|=|J|(1-\delta)=397\,\mathrm{K}$. The singlet triplet energy gap is related to the alternation $\delta(T)$ via the relation $\Delta(T)=0.8615|J|[\delta(T)]^{2/3}$ which is assumed to be temperature dependent [12]. The energy gap between the singlet ground state and the triplet excited state (the singlet triplet energy gap in the T = 0 limit $\Delta_\sigma(0)$) can be calculated using the relation $\Delta(0)=0.8615|J|\delta^{2/3}=34.8\,\mathrm{K}$.

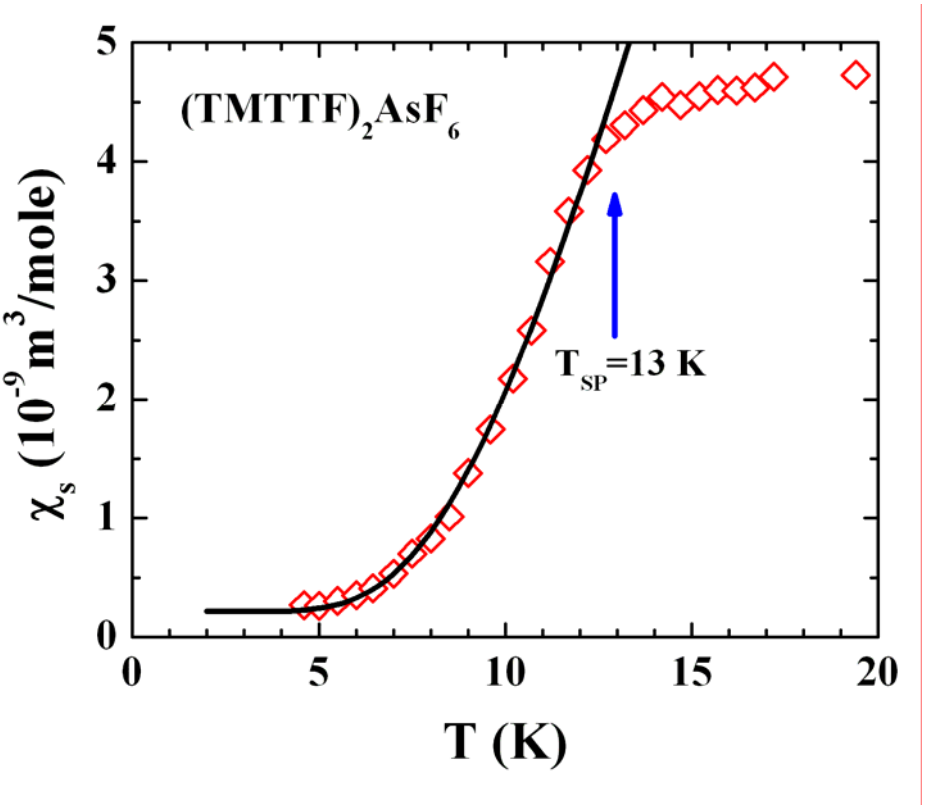


**Figure 4.33: Temperature dependence of the spin susceptibility of $(TMTTF)_2AsF_6$ in the low temperature region measured by the SQUID magnetometer along the a-axis. Below $T_{SP}$ = 13K the spin susceptibility drops exponentially, indicating a transition to a non-magnetic ground state. The line corresponds to the fit by the Bulaevskii's model using equation (4.10). The fit parameters are: α = 0.051 and Jβ′ = 55.7 K.**

The value predicted by the second order perturbation theory [12] of the ratio between the singlet-triplet energy gap and $T_{SP}$ is $\Delta_\sigma(0)/T_{SP}=2.47$. This value is in a good agreement with our results where a value of $\Delta_\sigma(0)/T_{SP}=2.67$ is obtained.
In our previous publication [6] the singlet triplet energy gap for $(TMTTF)_2AsF_6$ was calculated using the relation [151] $\Delta_\sigma=1.637\,\delta|J|=22\,\mathrm{K}$. The $(TMTTF)_2PF_6$ salt has a spin Peierls transition at $T_{SP}$=19 K, and has $|J|=420\,\mathrm{K}$ and $\delta=$ 0.0471 [120].

The singlet triplet energy gap was calculated using the relation $\Delta_\sigma = 1.637\delta|J| = 32.3\,\mathrm{K}$ [120]. If we apply the new relation [12] to calculate the singlet triplet energy gap for this salt we get $\Delta(0) = 0.8615\,|J|\delta^{2/3} = 47.1\,\mathrm{K}$. The obtained value of the ratio between the singlet-triplet energy gap and $T_{SP}$ of $(TMTTF)_2PF_6$ is $\Delta_\sigma(0)/T_{SP} = 2.48$. This value is in a very good agreement with the value predicted by a second order perturbation theory $\Delta_\sigma(0)/T_{SP} = 2.47$ [12].

## 4.8 Anion Ordering in $(TMTTF)_2BF_4$

Characteristic changes in the spin susceptibility and the linewidth are observed below the anion ordering transition temperature of $(TMTTF)_2BF_4$ ($T_{AO}$ = 41 K) as shown in Figure 4.9. Below the step-like decrease in the spin susceptibility at $T_{AO}$, an exponentially decreases in the susceptibility by decreasing the temperature is observed as depicted in Figure 4.34. The step-like decrease of the spin susceptibility indicates the first order character of this phase transition.

It was discussed in section 2.4 that $(TMTTF)_2BF_4$ has a first order anion ordering phase transition at about 41 K which is accompanied by a small specific heat anomaly and a large increase of the infrared vibronic absorption [20,40]. This ordering is achieved by the formation of a superstructure due to a structural phase transition. Since the anion ordering wave vector of $(TMTTF)_2BF_4$ is q = $(1/2,1/2,1/2)$, the stacks are tetramerized and this leads to a considerable deformation of the organic stacks. The tetramerization of the donor stacks leads to an exponentially decrease of the spin susceptibility below $T_{AO}$ because each two TMTTF dimers with spin 1/2 will be coupled and the system will go into a non-magnetic S = 0 ground state.

Using the fit parameter $J\beta' = 87.36\,\mathrm{K}$ the spin susceptibility at constant volume below $T_{AO}$ can be fitted by Bulaevskii's formula for the temperature dependence of the spin susceptibility of the alternating spin chain (equation 4.10) as shown in the solid line in Figure 4.34. Using the value of the AFM exchange constant ($|J| = 430\,\mathrm{K}$) which was obtained by fitting the spin susceptibility in the high temperature region using the EAT model (as discussed in section 4.4.1), one gets $\beta' = 0.203$. Using the same procedures as discussed in the previous section one obtains the following values for the other parameters: the alternation parameter $\gamma = 0.90$, $\beta = 0.191$, $\alpha = 0.076$, $\delta = 0.05263$, the intradimer AFM exchange constant $|J_1| = 452.6\,\mathrm{K}$ and the interdimer AFM exchange constant $|J_2| = 407.4\,\mathrm{K}$. The singlet triplet energy gap is given by $\Delta = 0.8615|J|\delta^{2/3} = 52.0\ \mathrm{K}$.

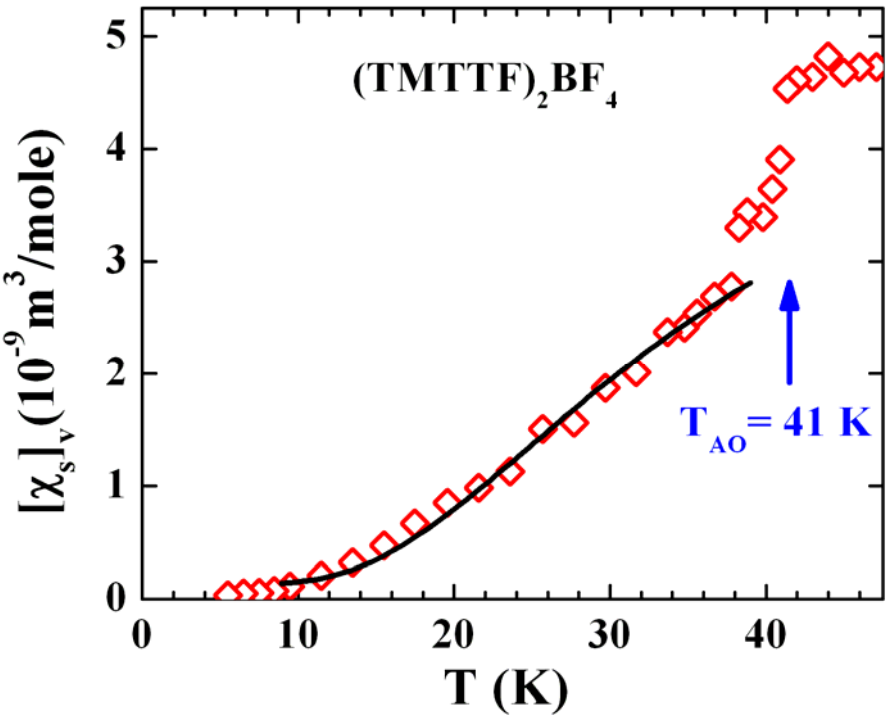


**Figure 4.34: Low temperature behaviour of the spin susceptibility at constant volume of $(TMTTF)_2BF_4$ calculated from the SQUID magnetometer measurement along the a-axis. At $T_{AO}$ = 41K a step-like drop in the spin susceptibility is observed below which the spin susceptibility decreases exponentially, indicating a transition to a non-magnetic ground state. The line corresponds to the fit by the Bulaevskii's model using equation (4.8). The fit parameters are: α = 0.076 and Jβ′ = 87.4 K.**

Figure 4.35 shows the temperature dependence of the linewidth along the three crystal axes below $T_{AO}$ of $(TMTTF)_2BF_4$. At $T_{AO}$ there is a step-like decrease in the linewidth, below this dip the linewidth along the stacking direction begins to decrease more slowly by decreasing the temperature than above, and it becomes larger than the linewidth along the b'-direction at low temperatures. In section 2.4 it was pointed out that the anion ordering transition is generally accompanied by an elastic deformation of the $P\bar{1}$ symmetry of the triclinic lattice and variations of the lattice parameters. Therefore the AO transition influences the electronic properties of the salt where it changes the electrostatic potential seen by the conduction electrons on the donor stacks. This can be the reason for changing the anisotropy of the linewidth below $T_{AO}$.

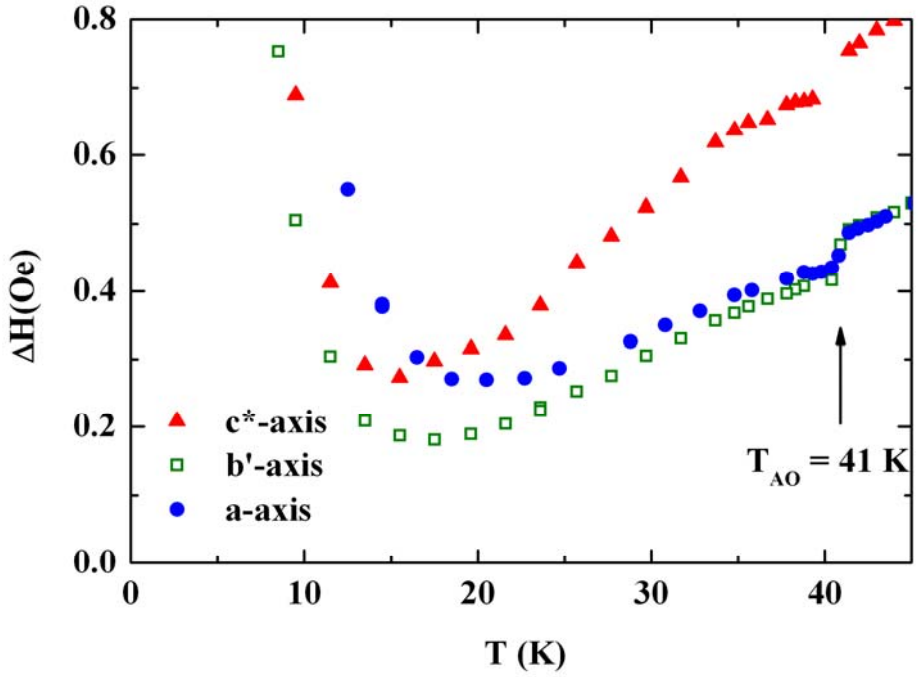


**Figure 4.35: Temperature dependence of the linewidth along the three crystal directions of $(TMTTF)_2BF_4$ at low temperatures. At $T_{AO}$ a step-like decrease in the linewidth along the three directions is observed, below $T_{AO}$ the linewidth along the stacking direction (a-axis) begin to decrease more slowly than above and it become larger than the linewidth along the b'-axis.**

# Chapter 5

# ESR and Transport Investigations of (BEDT-TTF)$_2$X Radical Salts

Electron spin resonance spectroscopy (ESR) is an extremely valuable and ideal technique for studying quasi-two dimensional metals from the (BEDT-TTF)$_2$X family. It is an ideal tool to distinguish between the different structural phases formed during the electrocystallization of BEDT-TTF salts as those formed with $I_3^-$ anions [61]. While in the most cases the main products of the electrochemical synthesis of the electron donor (BEDT-TTF) with $I_3^-$ anions were those of the α- and β-phases, in few cases the crystallization of κ- and (or) Θ-(BEDT-TTF)$_2$I$_3$ was accompanied by that of α- and β-(BEDT-TTF)$_2$I$_3$. Those phases can be distinguished by room temperature ESR measurements instead of X-ray structural experiments.
Transport and magnetic properties have been investigated by means of ESR, SQUID and dc measurements on different crystals of the organic superconductors Θ -(BEDT-TTF)$_2$I$_3$, $\Theta_T$-(BEDT-TTF)$_2$I$_3$ and the new organic conductor (BEDT-TTF)$_2$($B_{12}H_{12}$)($CH_2Cl_2$).
The electron spin resonance (ESR) spectra were measured in a continuous wave X-band spectrometer (Bruker ESP 300) at 9.5 GHz. The temperature dependent measurements in the range (300-5 K) were done using a continuous-flow helium cryostat. The samples were fixed with silicon grease to a 4 mm quartz sample holder; the sample was rotated around the vertical axis by using a goniometer. The microwave power supplied into the cavity was below 1 mW in order to avoid saturation effects of the ESR spectra. The modulation amplitude was always kept less than one-tenth of the linewidth to prevent distortion of the lineshape due to over-modulation. The g-value was determined by comparing the resonance position of the measured ESR signal with that of DPPH. In the case of Dysonian lineshapes, the peak-to-peak linewidth of the pure-absorption portion was derived by assuming a linear combination of Lorentzian absorption and dispersion. For the dc measurements the standard four probe method was used where the crystals were contacted with 25μm gold-wires by carbon paint. The current was applied parallel and normal to the highly conducting plane (see Figure 3.12). The measurement of

the magnetic susceptibility was performed in a Quantum Design SQUID magnetometer between 1.8 and 300 K where the magnetic field was applied parallel to the conduction plane. The background signal from the holder was measured and subtracted in order to obtain the intrinsic magnetization of the sample.

In this chapter the transport and the ESR measurements of the organic superconductor Θ-(BEDT-TTF)$_2$I$_3$, its tempered phase ($\Theta_T$-(BEDT-TTF)$_2$I$_3$) and the new organic conductor (BEDT-TTF)$_2$($B_{12}H_{12}$)($CH_2Cl_2$) will be presented and discussed.

## 5.1 Θ-(BEDT-TTF)$_2$I$_3$

The electrochemical crystallization procedures and the crystal structure of the investigated Θ-(BEDT-TTF)$_2$I$_3$ superconductor were discussed in section 1.3. In this study, different Θ-(BEDT-TTF)$_2$I$_3$ crystals from two different batches were investigated. The crystals in the two batches were grown following the same procedures as explained in section 1.3.

### 5.1.1 Previous Investigations

For single crystals of the organic conductor Θ-(BEDT-TTF)$_2$($I_3$)$_{1-x}$($AuI_2$)$_x$ ($x<0.02$) which have almost identical structural properties as the Θ-(BEDT-TTF)$_2$I$_3$ crystals, magnetic and transport investigations have been reported [68,71,72,152,153,154]. It was shown that among several samples few were found to show a sharp drop of the resistivity at 3.6 K, some samples have shown an incomplete drop of the resistivity (partial superconductivity), and most of them show no indication of superconductivity [68,71,72,152]. The percentage of the samples which has a sharp superconducting transition decreases with increasing amounts of $AuI_2^-$-anions up to 0.03% and the ratio of the specific resistivity ρ(300 K)/ρ(4 K) lies in the range of 40-180 [72,152]. The superconductivity of Θ-(BEDT-TTF)$_2$($I_3$)$_{1-x}$($AuI_2$)$_x$ was shown to be intrinsically a bulk one by static magnetization measurements [153]. Nevertheless in some crystals, the fractional volume of the superconducting part was very much reduced due to extrinsic factors such as twinning and disorder in the $I_3$ sublattice. On crystals of Θ-(BEDT-TTF)$_2$($I_3$)$_{1-x}$($AuI_2$)$_x$ which did not show any sign of superconductivity ESR measurements were done down to 100 K [154]. The peak to peak linewidth at room temperature was between 60 and 80 Oe depending on crystal

orientation. The linewidth decreased almost linearly with decreasing temperature down to about 100 K.

In the following sections it will be shown that the ESR and the transport measurements on the neat Θ-(BEDT-TTF)$_2$I$_3$ crystals show somewhat different results from the previous reports. It will be shown that these crystals have better quality due to the absence of twinning defects in the crystals; this can be seen by the higher resistivity ratios ($\rho(300\,\mathrm{K})/\rho(4\,\mathrm{K}) \geq 500$) and by the complete superconducting transition in the superconducting samples.

## 5.1.2 Electrical Resistivity and Magnetic Susceptibility Measurements

The temperature dependence of the dc electrical resistivity from room temperature down to 1.6 K was measured for several crystals of the organic superconductor Θ-(BEDT-TTF)$_2$I$_3$. The typical room temperature resistivity parallel to the conduction plane is about 0.04 Ω·cm and decreases to about $8\times10^{-5}$ Ω·cm at 4 K (see Figure 5.1).

The resistivity ratio ρ(300 K) / ρ(4 K) ≈ 500 indicates the high quality of the neat Θ-(BEDT-TTF)$_2$I$_3$ crystals compared to Θ-(BEDT-TTF)$_2$(I$_3$)$_{1-x}$(AuI$_2$)$_x$ crystals [68,71,72,152]. The resistivity decreases with decreasing temperature from room temperature down to the superconducting transition temperature ($T_c$ = 3.6 K) where the resistivity drops sharply. The resistivity was measured for several crystals and about 30% of them were found to show the superconducting transition as shown in the insert of Figure **5.1**. This percentage is higher than that in Θ-(BEDT-TTF)$_2$(I$_3$)$_{1-x}$(AuI$_2$)$_x$ (x<0.02). This is in agreement with the results found in previous studies [72,152] where the percentage of the superconducting samples decreases with increasing the amount of $AuI_2^-$ anions from 0.02% to 0.03%. Since in our crystals the $AuI_2^-$ is absent, the percentage of the superconducting samples is expected to increase. Also twinning defects in the $I_3^-$ sublattice have been often found in Θ-(BEDT-TTF)$_2$(I$_3$)$_{1-x}$(AuI$_2$)$_x$ crystals [67,71]. In the samples with many defects, the superconducting volume is small and the residual resistivity can be detected. This can be the reason of detecting residual resistivity in some Θ-(BEDT-TTF)$_2$I$_3$ samples.

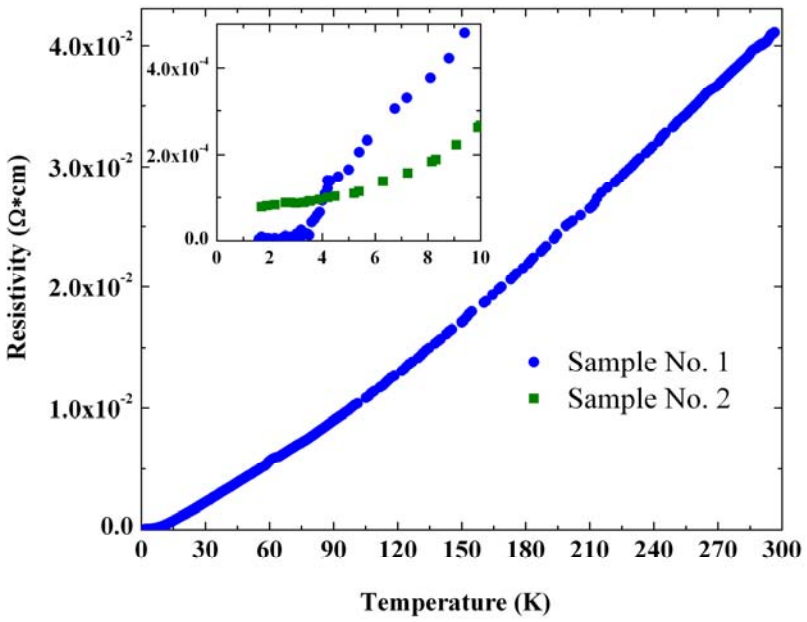


**Figure 5.1: Temperature dependence of the dc resistivity parallel to the conduction plane (ab-plane) of a superconducting crystal from Θ-(BEDT-TTF)$_2$I$_3$ salt. The insert shows the low temperature measurement for two different samples, one which shows a clear superconducting transition at 3.6 K (sample No. 1) and the other stays metallic and does not show a superconducting transition down to 1.6 K (sample No. 2).**

The temperature dependence of the static magnetic susceptibility of a superconducting sample of Θ-(BEDT-TTF)$_2$I$_3$ is shown in Figure 5.2. The mass of the measured sample was $4.5\times10^{-4}$ g (1 mole of (BEDT-TTF)$_2$I$_3$ = 1149 g). The measured susceptibility $\chi$ is the sum of the diamagnetic contribution $\chi_{\text{core}}$ from the core electrons and the paramagnetic contribution $\chi_s$ from the conduction electrons, the Pauli spin susceptibility. The value of the core diamagnetism $\chi_{\text{core}}$ = -5.2×10$^{-4}$ emu/mole was determined by measuring the susceptibility of the insulating BEDT-TTF molecules $\chi_{\text{ET}}$, at room temperature and adding to it the Pascal constants for the $I_2$ molecule plus the $I^-$ ions [155], i.e.,

$$\begin{aligned}\chi_{\text{core}} &= 2\chi_{\text{ET}} + \chi_{I_2} + \chi_{I^-} \\ &= 2(-1.96\times10^{-4}) + (-0.89\times10^{-4}) + (-0.51\times10^{-4})\ \text{emu/mole} \\ &= -5.2\times10^{-4}\ \text{emu/mole}\end{aligned} \tag{5.1}$$

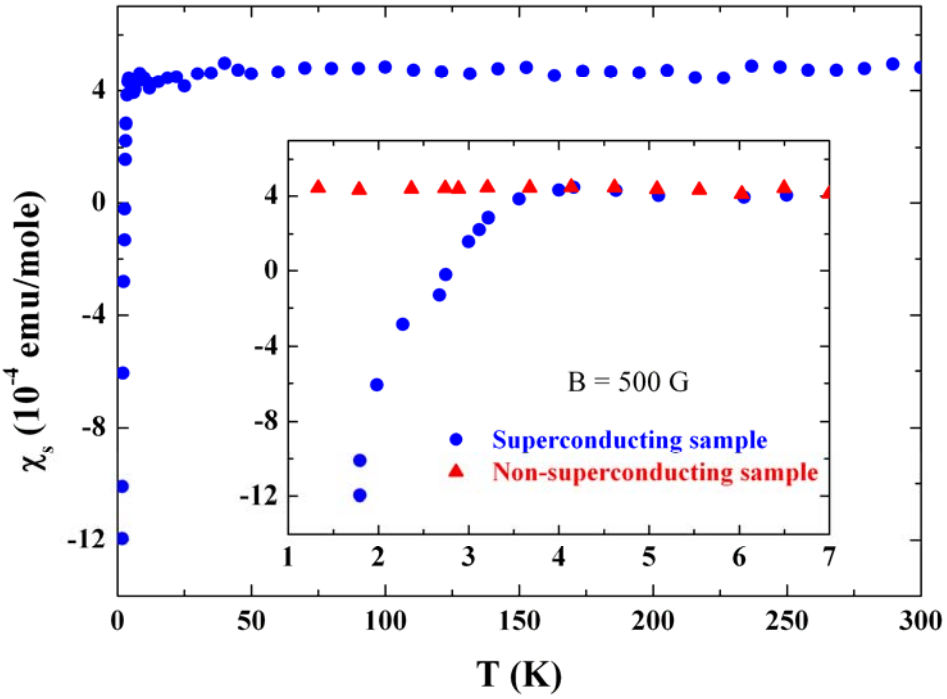


**Figure 5.2: Temperature dependence of the static susceptibility of Θ-(BEDT-TTF)$_2$I$_3$. After cooling the sample down to 1.8 K in zero magnetic field, a magnetic field of 500 G was applied parallel to the conduction plane and the magnetic susceptibility was measured during heating. The insert shows the measurement in the low temperature region for a sample which shows a bulk superconducting transition at 3.6 K (blue circles) and a sample which shows no superconducting transition (red triangles).**

At room temperature the absolute value of the spin susceptibility $\chi_s$ of Θ-(BEDT-TTF)$_2$I$_3$ is $5\times10^{-4}$ emu/mole, this value is higher than that of β-(BEDT-TTF)$_2$I$_3$ [$\chi_s(\beta\text{-(BET-TTF)}_2\text{I}_3) = 4.6\times10^{-4}$ emu/mole)] and lower than the susceptibility of α-(BEDT-TTF)$_2$I$_3$ [$\chi_s(\alpha\text{-(BET-TTF)}_2\text{I}_3) = 6.8\times10^{-4}$ emu/mole)] which were measured by Koltz *et al* [156]. The differences in the absolute values of the susceptibility can be due to the different density of states for each phase.

At high temperatures the spin susceptibility is temperature independent as expected for the Pauli susceptibility of a metal. The superconducting transition was confirmed to be a bulk property by the observation of the shielding signal for the superconducting samples (see the insert of Figure 5.2). The shielding signal was observed after cooling the sample down to 1.8 K in zero magnetic field and then a magnetic field of 500 G was applied parallel to the conduction plane. The measurement of the magnetic susceptibility was carried out during heating. The sharp drop in the susceptibility at 3.6 K is a strong indication for bulk superconductivity at this temperature. The same experiment was done for samples

which show residual resistivity, for these samples no drop in the susceptibility was observed and the susceptibility is temperature independent in the whole temperature range (see the insert of Figure 5.2). This is in agreement with the resistivity measurements.

The dimensionality of the Θ-(BEDT-TTF)$_2$I$_3$ crystals was measured by performing the dc resistivity measurements parallel and perpendicular to the conduction plane as shown in Figure 5.3. The anisotropic ratio between the resistivities perpendicular and parallel to the conducting planes at room temperature is $\rho_\perp/\rho_\parallel = 500$ indicating strong two-dimensional electronic properties. Θ-(BEDT-TTF)$_2$I$_3$ is less two dimensional than κ-(BEDT-TTF)$_2$I$_3$, where the ratio $\rho_\perp/\rho_\parallel$ at room temperature for the later one is about 1000 [157].

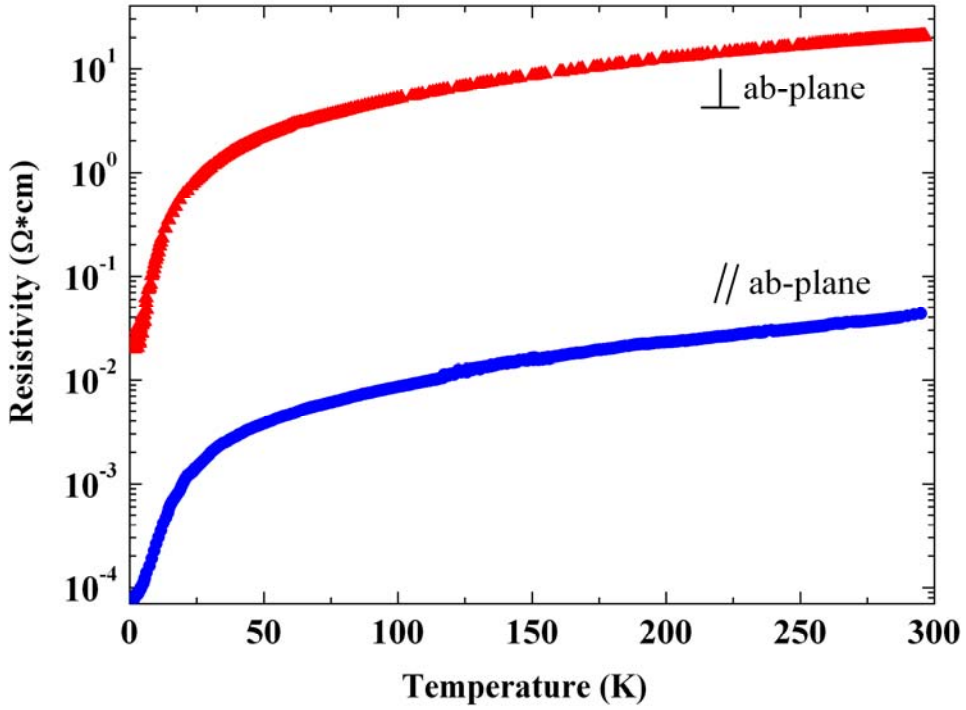


**Figure 5.3: Temperature dependence of the dc resistivity of Θ-(BEDT-TTF)$_2$I$_3$ for the current applied parallel (blue circles) and perpendicular (red triangles) to the conduction plane (ab-plane).**

At about 125 K a metal-metal phase transition seems to occur as can be seen from the change in the slope of the dc resistivity (Figure 5.4). At the same temperature a similar transition was observed in β-(BEDT-TTF)$_2$I$_3$ by resistivity and thermopower measurements [158]. The resistivity can be described here in both temperature regions (20 K to 125 K and 125 K to 300 K) by the equation:

$$\rho = \rho_o + \rho_1 T + \rho_2 T^2 \qquad (5.2)$$

with: $\rho_o = -7.3\times10^{-4}\Omega\cdot\mathrm{cm}$, $\rho_1 = 9.5\times10^{-5}\Omega\cdot\mathrm{cm\ K^{-1}}$ and $\rho_2 = 1.5\times10^{-7}\Omega\cdot\mathrm{cm\ K^{-2}}$ for $20\,\mathrm{K} \le \mathrm{T} < 125\,\mathrm{K}$ and in the high temperature region (T >125 K) $\rho_o = -5.1\times10^{-3}\Omega\cdot\mathrm{cm}$, $\rho_1 = 1.4\times10^{-4}\Omega\cdot\mathrm{cm\ K^{-1}}$ and $\rho_2 = 5.1\times10^{-8}\Omega\cdot\mathrm{cm\ K^{-2}}$.
At the metal-metal transition temperature (T = 125 K) a jump in the resistivity ratio ($\rho_\perp/\rho_\parallel$) occurs (see the insert **a** of Figure 5.4), this jump indicates a change in the anisotropy at this temperature. This transition can be due to a structural change at this temperature.

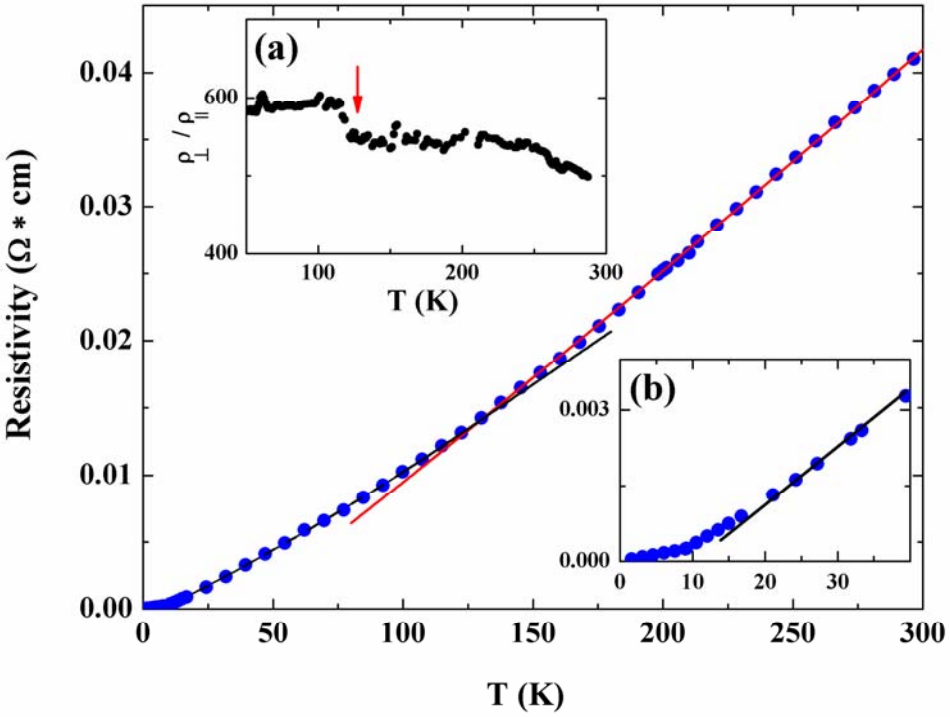


**Figure 5.4: Temperature dependence of the dc resistivity of Θ-(BEDT-TTF)$_2$I$_3$ parallel to the conduction plane. The solid curves are fits of equation 5.2. The first insert (a) shows the temperature dependence of the resistivity ratio ($\rho_\perp/\rho_\parallel$) and the arrow points at the metal-metal phase transition temperature. The second insert (b) shows the low temperature behaviour of the resistivity and the deviation from the fit below 20 K.**

At about 20 K the measured resistivity deviates from the fit using equation 5.2. Below 20 K down to the superconducting transition temperature ($T_C$ = 3.6 K) the resistivity is proportional to $T^2$ ( $\rho = aT^2$, $a = 5.5\times10^{-6}$ ) as shown in Figure 5.5.

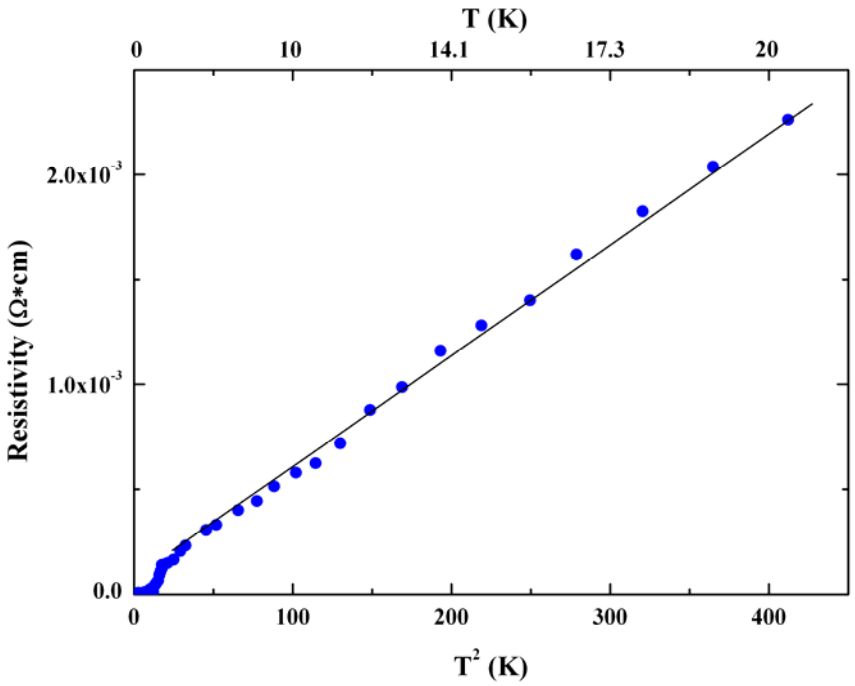


**Figure 5.5: The dc resistivity parallel to the conduction plane as a function of $T^2$ in the low temperature region (T < 20 K).**

The $T^2$ dependence of the resistivity was observed in several quasi 1-D and 2-D organic metals as (TTF-TCNQ) [159] and β- and κ- phases of $(BEDT\text{-}TTF)_2I_3$ [57,95]. Early theories accounted for this temperature dependence by electron-electron scattering [57], where the resistivity of β-$(BEDT\text{-}TTF)_2I_3$ was measured between 2 K and 20 K and the $T^2$ behaviour was observed; on the basis of this finding, Bulaevskii [57] suggested that there is no freezeout of the resistivity, and therefore the $T^2$ dependence of the resistivity is due to electron-electron scattering. He also carried out theoretical estimates of the magnitude of the resistivity, which suggested that this mechanism is strong enough to account for the observed resistivity. In contrast, in other resistivity measurements a freezeout of the resistivity at 20 K was observed [95] for β- and κ- phases of $(BEDT\text{-}TTF)_2I_3$, and also it was shown theoretically that the electron-electron scattering mechanism is too weak to account for the observed resistivity. Therefore this behaviour was attributed to electron libron scattering. In our measurements of Θ-$(BEDT\text{-}TTF)_2I_3$ no freezeout of the resistivity is observed at 20 K (see the insert **b** of Figure 5.4).

### 5.1.3 ESR Investigations

The orientation and the temperature dependent measurements of the ESR spectra of several crystals of Θ-(BEDT-TTF)$_2$I$_3$ were carried out in order to study the magnetic properties of this salt. Along all orientations and in the whole temperature range a single absorption line was observed. A nearly square platelet single crystal of Θ-(BEDT-TTF)$_2$I$_3$ which shows a clear superconducting transition at 3.6 K is used here to demonstrate the orientation and the temperature dependence of the g-value, the peak-to-peak linewidth and the ESR lineshape. The dimensions of the crystal were $1.5\times1.5\times0.07$ mm$^3$.

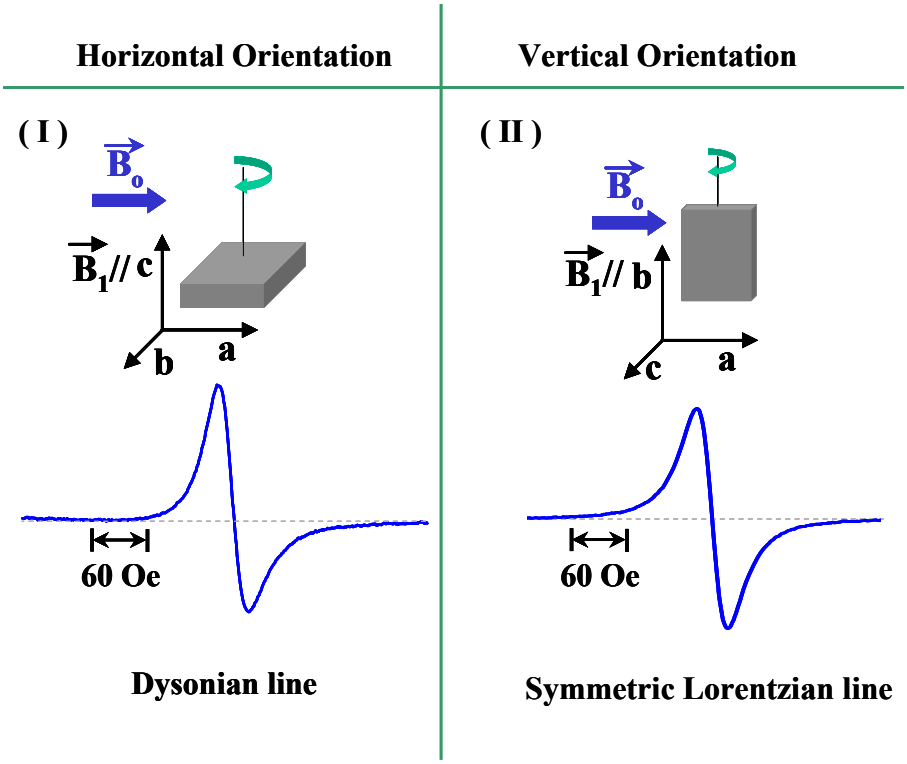


**Figure 5.6: The crystal orientations in the microwave cavity and the corresponding ESR lineshapes of a Θ-(BEDT-TTF)$_2$I$_3$ single crystal at room temperature.**

The square platelet single crystal was first oriented horizontally in the cavity, that means the microwave electric field is parallel to the conduction plane (ab-plane) and $B_1$ perpendicular to it as shown in Figure 5.6.I. The ESR spectra for the horizontal orientations have Dysonian lineshapes. After that the crystal was oriented vertically in the microwave cavity (the microwave magnetic field $B_1$ is parallel to the

conduction plane, see Figure 5.6.II). The resulting ESR spectra at these orientations revealed a symmetric Lorentzian lineshape.

The Dysonian lineshape is observed when the microwave electric field is applied parallel to the conducting plane (ab-plane). The sample and the field geometry for this case is shown in Figure 5.7.a. $B_o$ is rotated in the yz-plane (the conduction plane) and $B_1$ is always perpendicular to this plane. Therefore, the microwave electric field E which is perpendicular to $B_1$ is always parallel to the conduction plane.

The skin depth of the electromagnetic waves along z-direction is determined by the resistivity $\rho_y$ and the skin depth along y-direction is determined by $\rho_z$. Hence the skin depth $\delta_z$ and $\delta_y$ for propagation in the plane direction is determined by the equations [160].

$$\delta_z = \left( \frac{\rho_y}{\pi f \mu_o} \right)^{1/2} \tag{5.3}$$

$$\delta_y = \left( \frac{\rho_z}{\pi f \mu_o} \right)^{1/2} \tag{5.4}$$

where $\mu_o$ is the permeability of the free space ( $\mu_o = 4\pi \times 10^{-7}$ (Henries/m) ) and $f$ is the frequency of the microwaves ( $f = 9.5 \times 10^9$ Hz ).

We assume that the resistivity along the conduction plane is isotropic ( $\rho_y = \rho_z = \rho_{yz}$ ) and equals $4 \times 10^{-4}\ \Omega \cdot \mathrm{m}$ at room temperature (see Figure 5.3). Consequently, using equations 5.3 and 5.4 the skin depth $\delta_y = \delta_z = \delta_{yz}$ is estimated to be about 0.073 mm for both directions. Since the size of the crystal plane used here is $\approx 1.5 \times 1.5$ mm$^2$, thus the skin depth at room temperature is smaller than the crystal size and therefore a Dysonian line is observed[I].

[I] The same experiment was done for a smaller sample ($0.2 \times 0.2 \times 0.05$ mm$^3$) and the Dysonian line was observed at room temperature along this plane as well.

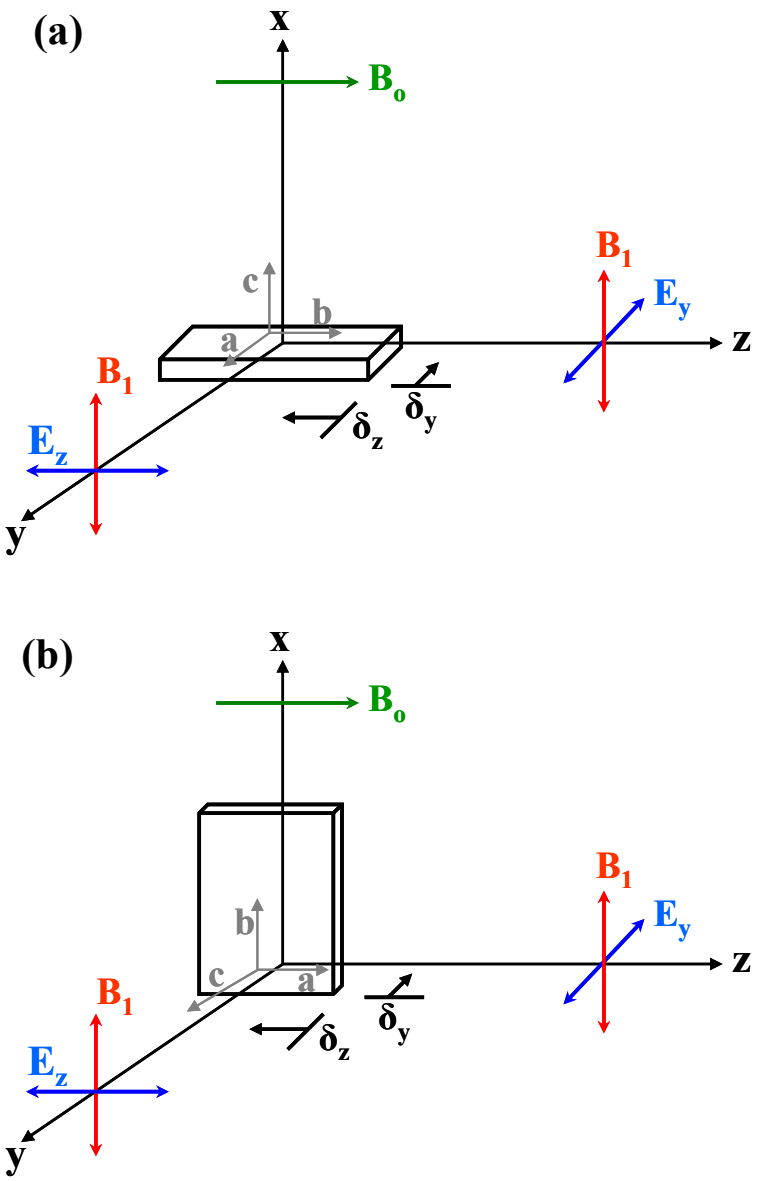


**Figure 5.7: The sample and the field geometries used in the discussion of the Dysonian and Lorentzian lineshapes, the horizontal orientation is shown in (a) and the vertical orientation in (b). The black axes represent the field axes and the gray ones the crystal axes.**

In contrast to the result mentioned above, the ESR line is symmetric Lorentzian when the microwave electric field is applied not parallel to the conduction plane as shown in Figure 5.6.II. The sample and the field geometry for this case is shown in Figure 5.7.b. In this situation, the skin depth $\delta_y$ and $\delta_z$ are estimated from $\rho_z$ and $\rho_y$, respectively. Using equations 5.3 and 5.4, and taking $\rho_z = 4\times10^{-4}\,\Omega\cdot\mathrm{m}$ and $\rho_y = 0.2\,\Omega\cdot\mathrm{m}$ (see Figure 5.3), we obtain $\delta_y = 0.073\,\mathrm{mm}$ and $\delta_z = 1.63\,\mathrm{mm}$. The

skin depths estimated are slightly larger than the size of the measured crystal (the size of the ac-plane of the crystal is $0.07 \times 1.5$ mm$^2$). Therefore no skin effect is expected for this case. By lowering the temperature - that means decreasing the resistivity - the lineshape changes to Dysonian, as will be discussed later.

Figure 5.8 shows the orientation dependence of the g-value and the peak-to-peak linewidth of Θ-(BEDT-TTF)$_2$I$_3$ at room temperature when the static magnetic field is applied parallel to ab-plane (blue circles) and ac-plane (red rectangles). The orientation of the single crystal with respect to the static magnetic field for the two cases is illustrated in Figure 5.6. The dashed lines show the simulated angular dependence by use of the following equations:

$$g(\theta) = \left[ g^2(c)\cos^2(\theta) + g^2(a)\sin^2(\theta) \right]^{1/2} \tag{5.5}$$

$$\Delta H_{pp}(\theta) = \left[ \Delta H_{pp}^2(c)\cos^2(\theta) + \Delta H_{pp}^2(a)\sin^2(\theta) \right]^{1/2} \tag{5.6}$$

The g-value is anisotropic along the ac-plane while it is isotropic along the ab-plane. This means that the g-tensor is axially symmetric around the c-axis. The same angular behaviour was observed for α-(BEDT-TTF)$_2$I$_3$ [160]. The g-value exhibits a maximum of 2.0111 along c-axis and a minimum of 2.0030 along the ab-plane.
The g-value maximum corresponds to the orientation where the static magnetic field is approximately parallel to the long molecular axis (or central C = C double bond) of the BEDT-TTF molecule (see Figure 1.11). The minimum is observed along the ab-plane. Along this plane the BEDT-TTF molecules have a zig-zag structure (see Figure 1.12.b).

The anisotropy of the g-value of the (BEDT-TTF)$_2$X salts is originated from the spin orbit coupling as discussed in section 3.1.5, where the maximum g-value ($g_1$), the intermediate ($g_2$) and the minimum value ($g_3$) are expected to be along the molecular long axis, short axis and normal to the molecular plane of BEDT-TTF molecules, respectively. In the case of the BEDT-TTF cations, the principle values of the g-tensor are $g_1 = 2.0116$, $g_2 = 2.0067$, $g_3 = 2.0023$ and they are nearly parallel to the molecular long axis, short axis and normal to the molecular plane of BEDT-TTF, respectively [161]. Since the g-tensor of Θ-(BEDT-TTF)$_2$I$_3$ crystals is axially symmetric, only $g_1 = 2.0111$[I] is obtained. The values of $g_2$ and $g_3$ are averaged at 2.0030 in the ab-plane because of the zig-zag structure of the BEDT-TTF molecules along this plane.

[I] In this case $g_1$ is the g-value along c*-axis.

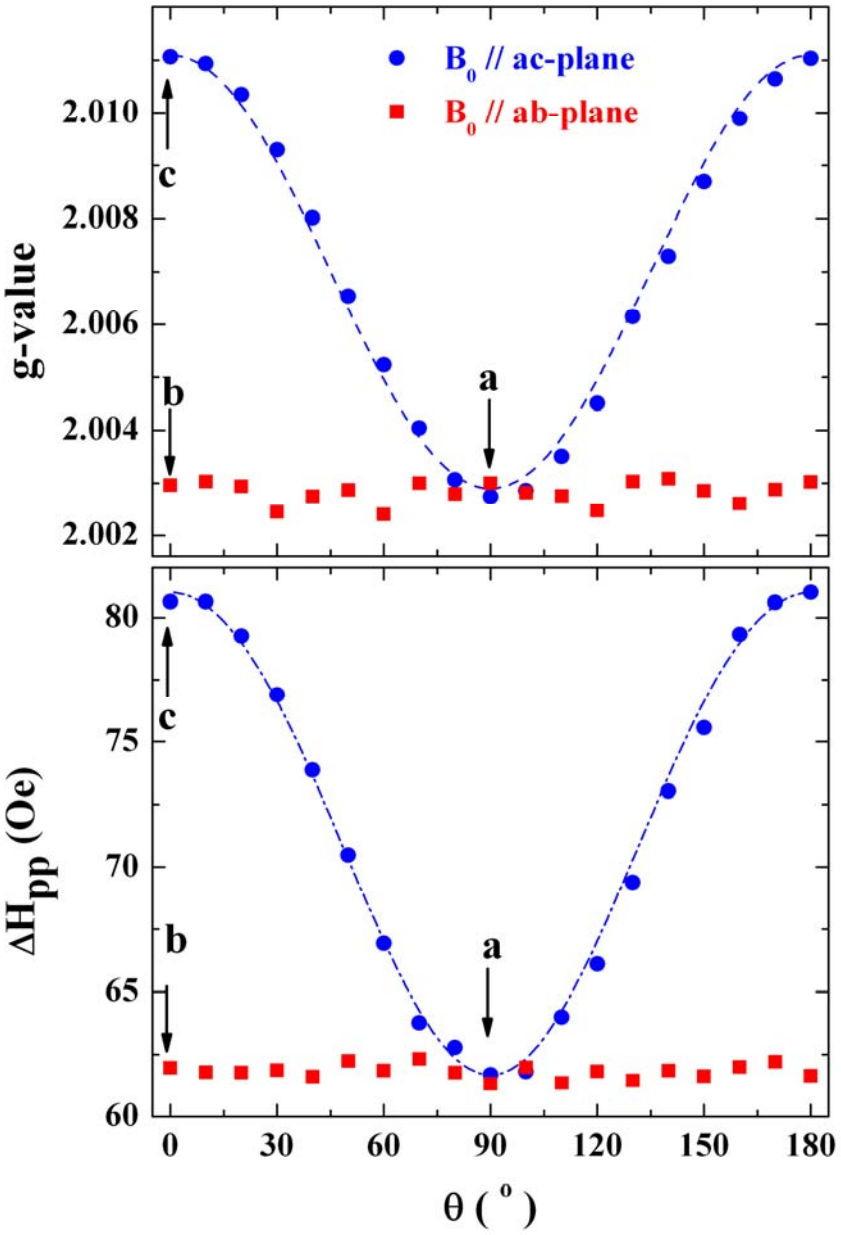


**Figure 5.8: Angular dependence of the g-value and the peak-to-peak linewidth along the ac-plane (blue circles) and ab-plane (red rectangles) of Θ-(BEDT-TTF)$_2$I$_3$ at room temperature. The least-square fittings of the g-value and the linewidth are shown by the dashed lines. The fit parameters are g(a) = 2.003, g(c) = 2.0111, $\Delta H_{pp}$(a) = 62 Oe and $\Delta H_{pp}$(c) =81 Oe.**

The anisotropy of the g-value of Θ-(BEDT-TTF)$_2$I$_3$ is well interpreted in terms of the g-tensor of the BEDT-TTF cation radical. The obtained principle values of the g-tensor of Θ-(BEDT-TTF)$_2$I$_3$ and other phases of the same salt are tabulated in Table 5.1. These results suggest that the g-values of the (BEDT-TTF)$_2$I$_3$ salts are

essentially determined by the g-tensor of the BEDT-TTF cation radical. The principle value $g_1$ obtained for $\Theta$-$(BEDT\text{-}TTF)_2I_3$ is in good agreement with that of the β- and α-phase of the same salt.

| Compound | $g_1$ | $g_2$ | $g_3$ | Reference |
|---|---|---|---|---|
| $BEDT\text{-}TTF^+$ | 2.0116 | 2.0067 | 2.0023 | [161] |
| $\Theta$-$(BEDT\text{-}TTF)_2I_3$ | 2.0111 | 2.0030 | | This work |
| α-$(BEDT\text{-}TTF)_2I_3$ | 2.0113 | 2.0033 | | [160] |
| β-$(BEDT\text{-}TTF)_2I_3$ | 2.0111 | 2.0065 | 2.0025 | [160] |

**Table 5.1: Principle values of the g-tensor for the BEDT-TTF molecule and some phases of the $(BEDT\text{-}TTF)_2I_3$ salt.**

The angular dependence of the peak-to-peak linewidth ($\Delta H_{pp}$) of $\Theta$-$(BEDT\text{-}TTF)_2I_3$ at room temperature is qualitatively similar to that of the g-value as shown in Figure 5.8, where it has a maximum value of 81 Oe along c-axis and a minimum value of 62 along ab-plane. The linewidth have the same values as for the isostructural salt $\Theta$-$(BEDT\text{-}TTF)_2(I_3)_{1-x}(AuI_2)_x$ [154].
The ESR linewidth is normally used in identifying the different crystalline phases of $(BEDT\text{-}TTF)_2X$ salts [61]. In contrast to the g-values, which usually fall within a small range as was discussed above, the linewidths are quite characteristic for each structural phase. The linewidth of the different phases of $(BEDT\text{-}TTF)_2I_3$ salts are listed in Table 5.2.

| $(BEDT\text{-}TTF)_2I_3$ | α-phase | β-phase | κ-phase | Θ -phase |
|---|---|---|---|---|
| $\Delta H_{pp}$ (Oe) | 70-120 | 17-23 | 80-125 | 62-81 |
| Reference | [61,160] | [61,160] | [162] | This work |

**Table 5.2: The ESR peak-to-peak linewidths for the different phases of the $(BEDT\text{-}TTF)_2I_3$ salt.**

The broadening mechanism of the ESR absorption line of the $(BEDT\text{-}TTF)_2X$ salts is understood by use of the theoretical treatment that correlates the relaxation rate with torsional oscillations of the organic donor molecule [130]. This means that the main broadening mechanism of the ESR line is the spin orbit coupled electronic transitions, and since the spin-orbit interaction cannot cause an electronic transition within a compound consists of inversion-related molecules the linewidth of these material is relatively small. The theory was originally developed for $(TMTCF)_2X$

salts as discussed in section 4.4.2, and has been applied to the BEDT-TTF-based salts [163]. To explain the relation between the structural phase and the ESR linewidth of the (BEDT-TTF)$_2$X salts, two schematic diagrams of the α- and β-(BEDT-TTF)$_2$I$_3$ salts are shown in Figure 5.9 [164]. In the β-type structure, there is only one kind of BEDT-TTF stacks and the inversion centers are located along and between the stacks. The α-type structure consists of two nonequivalent stacks of BEDT-TTF molecules and no inversion centers are located between them. The effect of these two packing motifs is that the interstack spin-orbit scattering is more effective in the α-phase due to the loss of the inversion centers between the stacks and therefore the linewidth is much larger (see Table 5.2). It was discussed in section 1.3.1 that the structure of Θ-(BEDT-TTF)$_2$I$_3$ crystals is very similar to that of α-(BEDT-TTF)$_2$I$_3$ but the symmetry in the Θ-phase layers is higher than in the α-phase. In addition all BEDT-TTF molecules in the Θ-phase are centrosymmetrical and equivalent to each other in the average structure as discussed in section 1.3.1 [71]. Therefore the spin orbit coupling is reduced in the Θ-phase and the linewidth is lower than in α-phase as shown in Table 5.2.

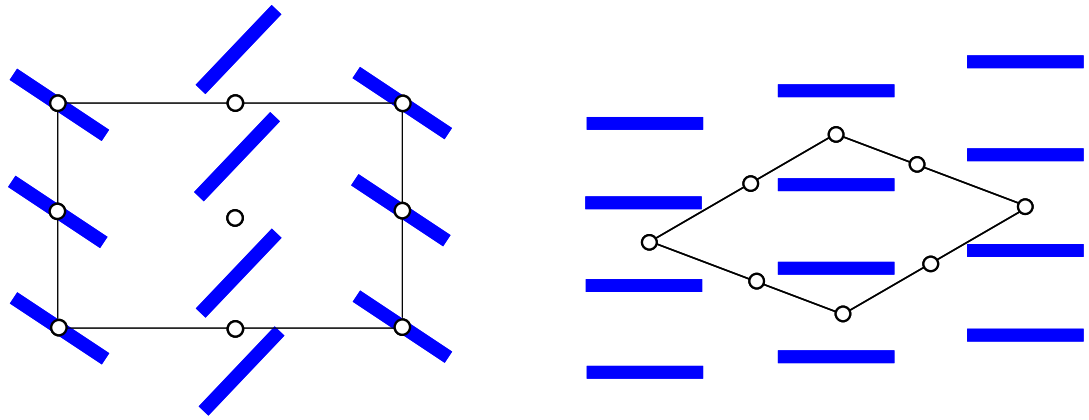

**Figure 5.9: Schematic diagrams of α-(BEDT-TTF)$_2$I$_3$ (left) and β-(BEDT-TTF)$_2$I$_3$ (right). The lines indicate the unit cell and the circles are the inversion centres.**

For the temperature dependent measurements of the ESR spectra, the sample was oriented vertically in the cavity as depicted in Figure 5.6.II. The temperature dependent measurements were carried out when $B_o$ was applied parallel to the conduction plane ($B_o$//a-axis) and perpendicular to it ($B_o$//c-axis). At room temperature the ESR line has symmetric Lorentzian lineshape along both directions as was discussed above. The Lorentzian line is gradually converted to a Dysonian

line with decreasing the temperature below about 250 K due to a significant decrease of the skin depth (increase in conductivity) as shown in Figure 5.10. The ESR spectra become more and more Dysonian by decreasing the temperature due to the decrease of the skin depth.

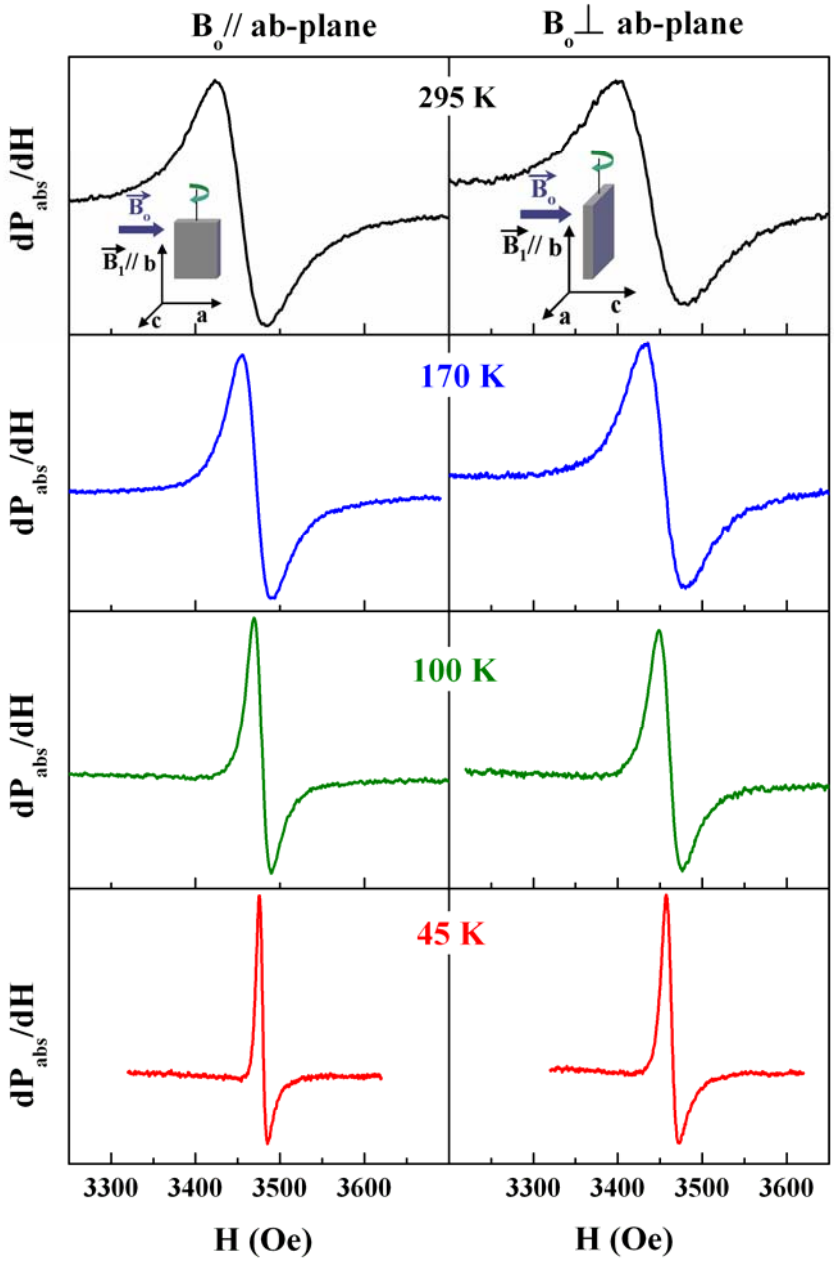


**Figure 5.10: The ESR spectra of Θ-(BEDT-TTF)$_2$I$_3$ at different temperatures when the magnetic field is applied parallel and perpendicular to the conduction plane.**

The temperature dependence of the peak-to-peak linewidth and the g-value along the two directions are shown in Figure 5.11. The linewidth decreases monotonically

from 82 Oe and 61 Oe at room temperature to 9 Oe and 6 Oe at 20 K for the perpendicular and the parallel directions, respectively. Along both orientations the linewidth increases with decreasing temperature below 20 K. The g-value along both directions is temperature independent at high temperatures and decrease with decreasing the temperature below about 20 K for the parallel direction and below about 40 K for the perpendicular one.

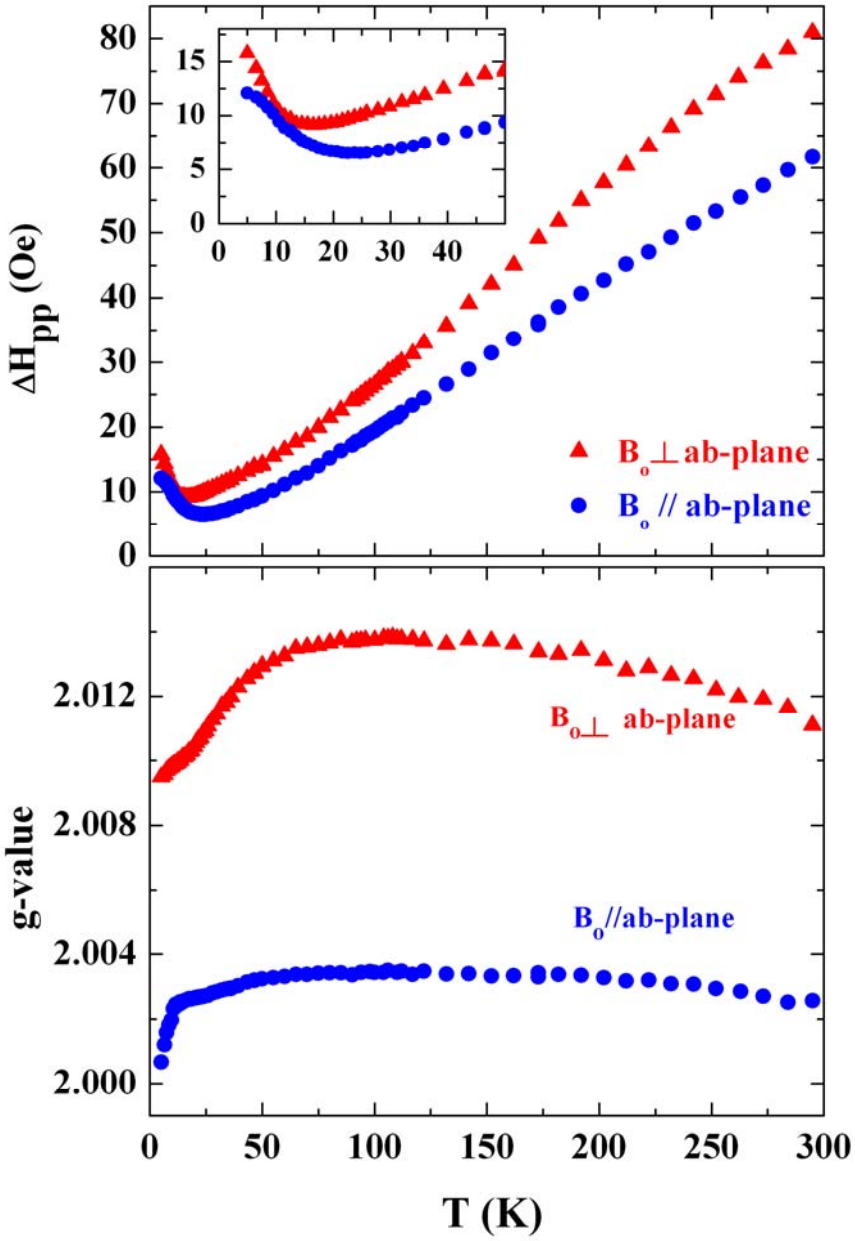


**Figure 5.11: The temperature dependence of the peak-to-peak linewidth and the g-value of Θ-(BEDT-TTF)$_2$I$_3$ when the static magnetic field is applied perpendicular (red triangles) and parallel (blue circles) to the conduction plane (ab-plane). The insert (up) shows the low temperature behaviour of the linewidth.**

The decrease of the linewidth by lowering the temperature from room temperature down to 20 K can be qualitatively understood by use of the Modified Elliott formula (equation 3.14) ($\Delta H \propto (\Delta g)^2 / \tau_\perp$)[I]. Since the g-value is temperature independent at a fixed crystal orientation in the high temperature region (see Figure 5.11), and the resistivity of the sample decreases with decreasing temperature along both directions (see Figure 5.3), the resulting linewidth is expected to decrease with decreasing temperature. The decrease of the linewidth by decreasing temperature is observed in α- and β –phase of (BEDT-TTF)$_2$I$_3$ salts as well [160,163].
Below 20 K the linewidth increases slightly down to 4.2 K for both orientations, and in the same temperature range the g-value decrease with decreasing temperature. These observations could be due to the existence of antiferromagnetic fluctuations above the superconducting transition, the same increase of the linewidth at low temperatures was observed in other κ-phase salts as $\kappa$-(BEDT-TTF)$_2$Cu(NCS)$_2$ [165].

## 5.2 $\Theta_T$-(BEDT-TTF)$_2$I$_3$

When $\alpha$-(BEDT-TTF)$_2$I$_3$ crystals which have a metal-insulator phase transition at 135 K are tempered above 70 $^o$C for several days, a high $T_c$ state is generated [166,167]. The thermally converted phase is called $\alpha_T$-(BEDT-TTF)$_2$I$_3$. This phase shows a bulk superconducting transition at 8 K [167,168]. Due to tempering $\alpha$-(BEDT-TTF)$_2$I$_3$ the ESR linewidth decreases from 120 Oe to about 25 Oe at room temperature [156]. The structure of $\alpha_T$-(BEDT-TTF)$_2$I$_3$ is very similar to that of β-(BEDT-TTF)$_2$I$_3$ as was shown by several spectroscopic techniques [166,167,169]. Nevertheless, the exact structure of $\alpha_T$-(BEDT-TTF)$_2$I$_3$ is still not known yet due to the fact that the tempered crystals have a mosaic type structure. Therefore a detailed crystal structure investigation by X-ray was not possible. The mosaic structure is a result of strong stress during the transformation [168].
The tempered crystals $\Theta_T$-(BEDT-TTF)$_2$I$_3$ were obtained by annealing single crystals of Θ-(BEDT-TTF)$_2$I$_3$ at 60-70 $^o$C for two to three hours in an oven. During the tempering process the sample was put in a glass bottle filled with nitrogen gas to avoid oxidation of the sample. Here for Θ-(BEDT-TTF)$_2$I$_3$, by annealing the

[I] The estimated value of the linewidth from the modified Elliot formula for the BEDT-TTF salts is three orders of magnitude higher than the measured value. The discrepancy is understood by the fact that the spin-orbit interaction can't cause an electronic transition within a compound that consists of inversion-related molecules.

crystals for two hours at 70 °C we got new type of crystals with somewhat different physical properties. This phase will be called $\Theta_T$-phase in the following. By tempering the crystal, the ESR linewidth changes from (81-62) Oe in the $\Theta$-phase to (27-24.5) Oe in the $\Theta_T$-phase depending on the crystal orientation as shown for one orientation in Figure 5.12.

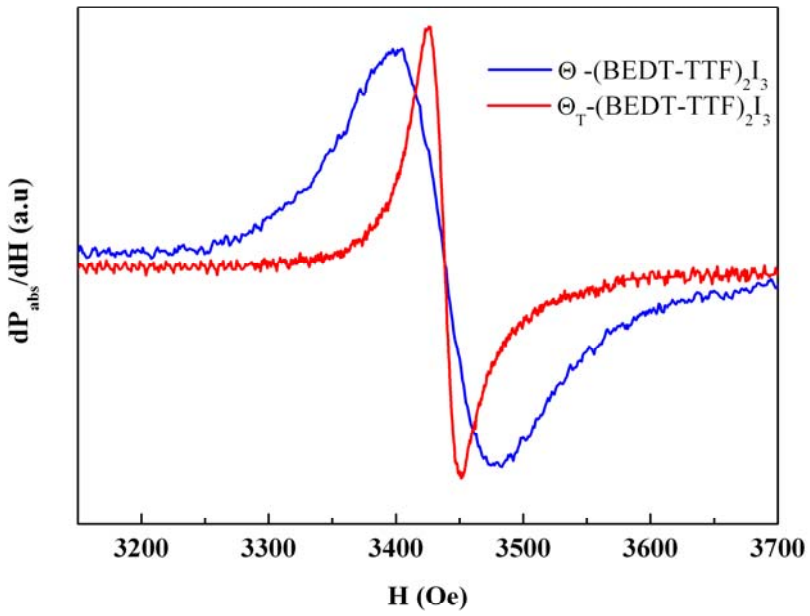


**Figure 5.12: The ESR signals of a single crystal of $\Theta$-(BEDT-TTF)$_2$I$_3$ before and after the heat treatment which transforms it into the $\Theta_T$-phase. Both signals were measured when the static magnetic field was applied perpendicular to the conduction plane. $\Delta H_{pp}$($\Theta$-phase) = 62 Oe and $\Delta H_{pp}$ ($\Theta_T$-phase) = 24.5 Oe.**

In the case of $\alpha$-(BEDT-TTF)$_2$I$_3$, annealing the crystal causes rearrangement of the BEDT-TTF molecules in the unit cell, where it become approximately similar to that of the β-phase. Therefore the drastically decrease of the linewidth in the $\alpha_T$-phase is expected, because the β-phase has inversion centers between the stacks therefore the interstack spin-orbit scattering is less effective in the β-phase as was discussed in section 5.1.3.

In the $\Theta$-(BEDT-TTF)$_2$I$_3$ case, due to the short tempering time, the tempered crystals have no mosaic type, therefore the X-ray measurements could be done [170]. X-ray investigations [170] and quantum oscillation experiments [171] of the $\Theta$- and $\Theta_T$-phases have shown that there is no change in the arrangement of the

BEDT-TTF molecules due to the tempering process. This means that the packing motive of the BEDT-TTF molecules in the $\Theta_T$-$(BEDT\text{-}TTF)_2I_3$ crystals is the same as that in the $\Theta$-$(BEDT\text{-}TTF)_2I_3$ crystals (see Figure 1.12). The only difference between the two phases is the arrangement of the $I_3^-$ anions between the BEDT-TTF molecules. In the $\Theta$-phase, every $I_3^-$ anion occupies one of two independent positions between the BEDT-TTF molecules, and the $I_3^-$ anions are statistically disordered in these different positions. In the $\Theta_T$-phase, the $I_3^-$ anions are ordered and have fixed positions between the BEDT-TTF molecules (see Figure 1.12.a). Due to the ordering of the $I_3^-$ anions in the $\Theta_T$-phase the structural symmetry is change to P2(1)/m in stead of P2(1)/c in the $\Theta$-$(BEDT\text{-}TTF)_2I_3$ crystals. The structural data of the $\Theta$-and $\Theta_T$-$(BEDT\text{-}TTF)_2I_3$ crystals are tabulated in Table 5.3. Ordering the $I_3^-$ anions in the $\Theta_T$-crystals decreases the spin-orbit coupling and therefore can be the reason for the decrease in the linewidth from 81 Oe to 26 Oe.

| | a (Å) | b (Å) | c (Å) | α (°) | β (°) | γ (°) | symmetry |
|---|---|---|---|---|---|---|---|
| $\Theta$-$(BEDT\text{-}TTF)_2I_3$ | 9.93 | 10.07 | 34.2 | 90 | 98.27 | 90 | P2(1)/c |
| $\Theta_T$-$(BEDT\text{-}TTF)_2I_3$ | 9.964 | 10.09 | 34.42 | 90 | 97.98 | 90 | P2(1)/m |

**Table 5.3: The unit cell parameters of the $\Theta$-and $\Theta_T$-$(BEDT\text{-}TTF)_2I_3$ single crystals at room temperature [170].**

## 5.2.1 Electrical Resistivity and Magnetic Susceptibility Measurements

The temperature dependence of the electrical resistivity was measured for several crystals of the organic superconductor $\Theta_T$-$(BEDT\text{-}TTF)_2I_3$. All investigated crystals show a clear superconducting transition at about 5 K in resistivity. This means that the superconductivity is a stable transition in the tempered phase unlike the $\Theta$-phase, and tempering the $\Theta$-$(BEDT\text{-}TTF)_2I_3$ crystals stabilizes the superconducting transition. The electrical resistivity as a function of temperature along the conduction plane of $\Theta_T$-$(BEDT\text{-}TTF)_2I_3$ crystal is shown in Figure 5.13.

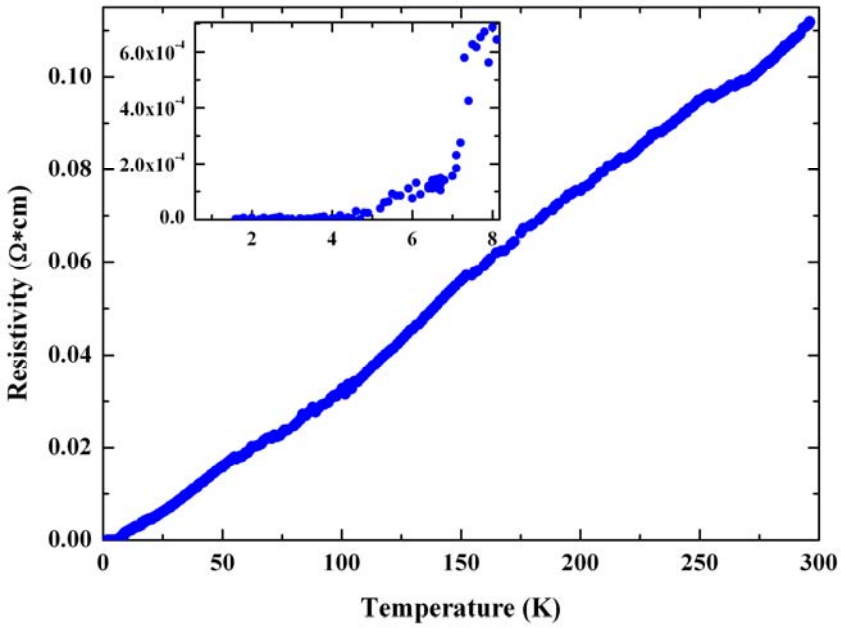


**Figure 5.13: Temperature dependence of the dc resistivity parallel to the conduction plane (ab-plane) of a $\Theta_T$-(BEDT-TTF)$_2$I$_3$ crystal. The insert shows the superconducting transition at 5 K and the onset of superconductivity at 8 K.**

While the typical resistivity at room temperature parallel to the conduction plane of $\Theta$-crystals is 0.04 $\Omega \cdot cm$, in $\Theta_T$-crystals it is about 0.10 $\Omega \cdot cm$. An increase in the room temperature resistivity was observed after tempering the α-(BEDT-TTF)$_2$I$_3$ crystals [167] as well. This increase in the resistivity can be due to creation of cracks and dislocations in the crystal and the loss of some $I_3$ molecules during the tempering process. The resistivity of $\Theta_T$-(BEDT-TTF)$_2$I$_3$ crystals shows a metallic behaviour down to low temperatures and at around 5 K a sharp superconducting transition. An onset temperature of superconductivity is observed at about 8 K (see the insert of Figure 5.13).

The superconducting transition at 4 K was confirmed to be a bulk property by observing the shielding signal as shown in Figure 5.14. At high temperatures the normalized spin susceptibility is temperature independent (Pauli susceptibility of a metal). The shielding signal was observed after cooling the sample down to 1.8 K in zero magnetic field and then applying a magnetic field of 10 G parallel to the conduction plane. The measurement of the magnetic susceptibility was carried out during heating. The sharp drop in the susceptibility at about 4 K is a strong indication for bulk superconductivity at this temperature.

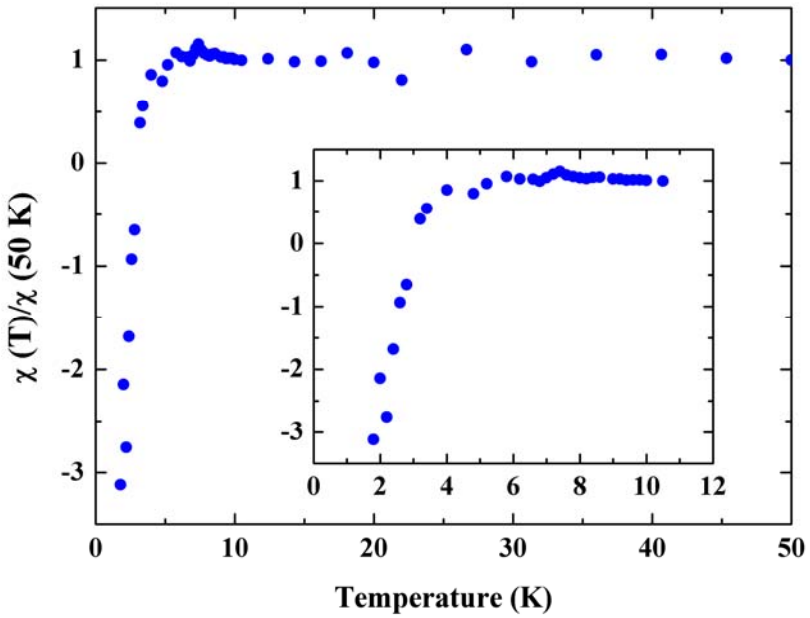


**Figure 5.14: The temperature dependence of the static susceptibility of $\Theta_T$-$(BEDT\text{-}TTF)_2I_3$ normalized to its value at 50 K. After cooling the sample down to 1.8 K in zero magnetic field, a magnetic field of 10 G was applied parallel to the conduction plane and the magnetic susceptibility was measured during heating. The insert shows the measurement in the low temperature region.**

The transition temperature here is quite different to that obtained from the dc measurements, this means that the bulk superconducting transition temperature is $4\,K$ and the drop of the resistivity at $5\,K$ can be due to the existence of a superconducting path on the crystal surface. A week onset of the diamagnetic shielding can be seen below about 7 K (see the insert of Figure 5.14) which might indicate that this onset is due to a surface effect. A similar lower transition temperature in the ac-susceptibility was already observed for β-$(BEDT\text{-}TTF)_2I_3$ crystals [172] and $\alpha_T$-$(BEDT\text{-}TTF)_2I_3$ crystals [167].

The intensity of the ESR spectra decreases by decreasing the temperature below 8 K as shown in Figure 5.15. This indicates a decrease in the spin susceptibility due to the onset of superconductivity as well.

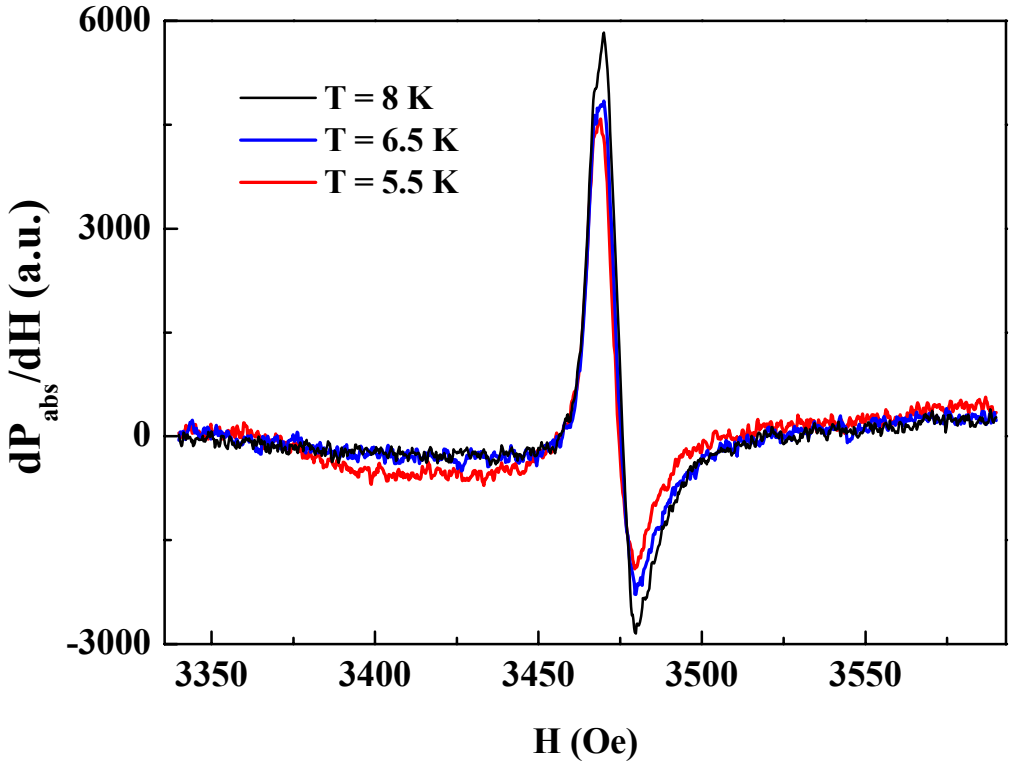


**Figure 5.15: The ESR spectra of $\Theta_T$-(BEDT-TTF)$_2$I$_3$ single crystal above and below the onset temperature of superconductivity. It can be seen that the intensity decreases by decreasing the temperature.**

## 5.2.2 ESR Investigations

The measurements of the orientation and temperature dependence of the ESR spectra of the organic superconductor $\Theta_T$-(BEDT-TTF)$_2$I$_3$ were performed along the ac-plane. Along all orientations and in the whole temperature range a single absorption line was observed indicating the complete transformation of the crystal to the tempered phase. A nearly square platelet single crystal of $\Theta_T$-(BEDT-TTF)$_2$I$_3$ was used here to demonstrate the orientation and the temperature dependence of the g-value and the peak-to-peak linewidth.

The single crystal was oriented vertically in the microwave cavity (the microwave magnetic field $B_1$ is parallel to the conduction plane; see the insert of Figure 5.16). The resulting ESR spectra at these orientations at room temperature revealed symmetric Lorentzian lines. Figure 5.16 shows the orientation dependence of the g-value and the peak-to-peak linewidth of $\Theta_T$-(BEDT-TTF)$_2$I$_3$ at room temperature

when the static magnetic field is applied parallel ac-plane. The g-value has a maximum value of 2.0091 along the c-axis and a minimum value of 2.0049 along the a-axis. The ESR linewidth has the same orientation dependence as the g-value. It ranges from 26.7 Oe along c-axis to 24.5 Oe along a-axis. The orientation dependence of the g-value and the linewidth can be modelled by equations 5.5 and 5.6, respectively as shown by the dashed lines in Figure 5.16.

The maximum g-value and linewidth is obtained for the magnetic field applied perpendicular to the conduction plane and the minimum values when the magnetic field is parallel to it. This is in agreement with what obtained for Θ-phase crystals (see Figure 5.8).

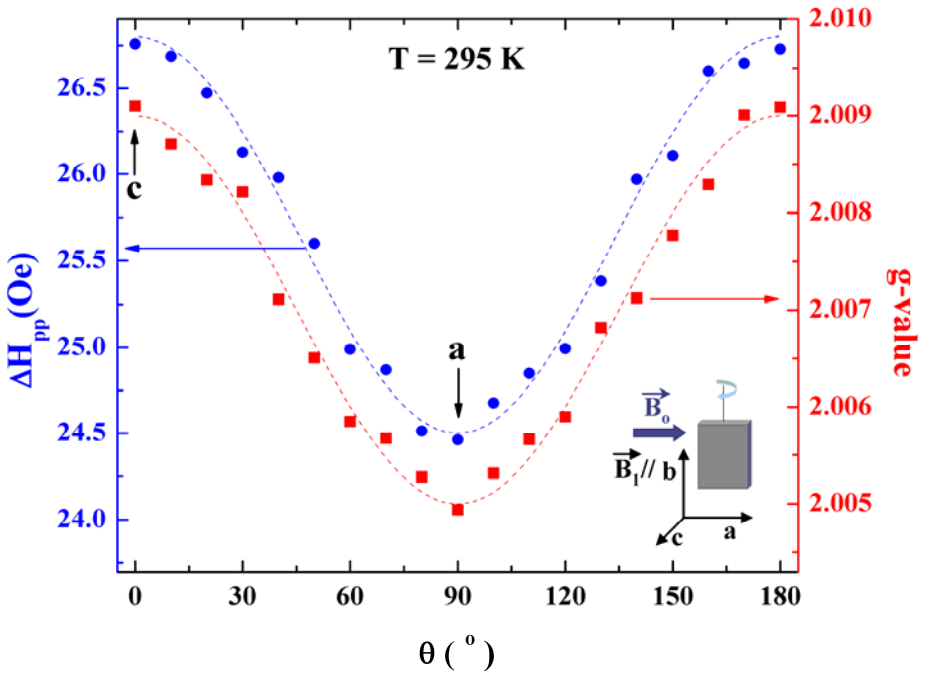


**Figure 5.16: Angular dependence of the g-value (red rectangles) and the peak-to-peak linewidth (blue circles) along the ac-plane of $\Theta_T$-(BEDT-TTF)$_2$I$_3$ at room temperature. The least-square fits of the g-value and the linewidth are shown by the dashed lines. The fit parameters are g(a) = 2.0049, g(c) = 2.0091, $\Delta H_{pp}$(a) = 24.5 Oe and $\Delta H_{pp}$(c) = 26.7 Oe.**

The temperature dependent measurements of the ESR spectra were performed when the static magnetic field ($B_o$) was applied perpendicular to the conduction plane (at $\theta = 0^o$ in Figure 5.16) and when it was parallel to the plane (at $\theta = 90^o$ in Figure 5.16). At room temperature the ESR line has symmetric Lorentzian shape along both directions as in the case of the Θ-phase. The Lorentzian line is gradually converted to a Dysonian line with decreasing the temperature below about 100 K as

shown in the insert of Figure 5.17. This change in the lineshape is due to a significant decrease of the skin depth by decreasing the temperature.

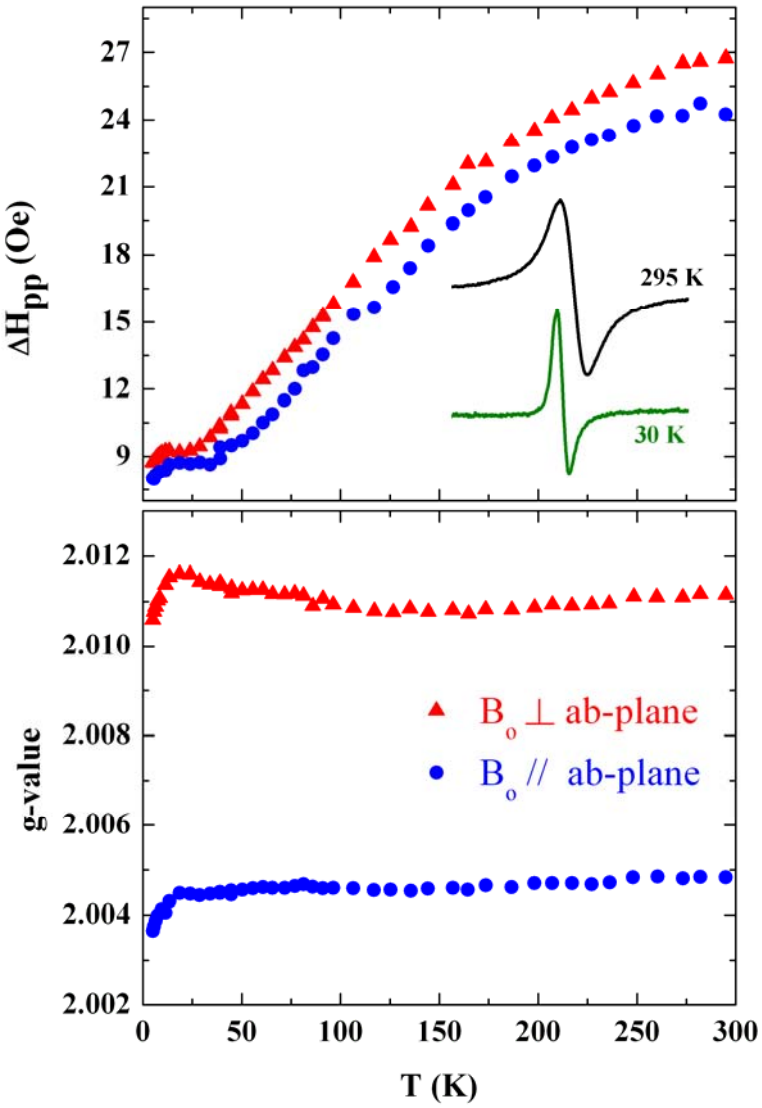


**Figure 5.17: Temperature dependence of the peak-to-peak linewidth (up) and the g-value (down) of $\Theta_T$-(BEDT-TTF)$_2$I$_3$ when the static magnetic field is applied perpendicular (red triangles) and parallel (blue circles) to the conduction plane (ab-plane). The insert shows the lineshape at different temperatures.**

The temperature dependence of the peak-to-peak linewidth and the g-value along the two directions is shown in Figure 5.17. The linewidth decreases from 26.7 Oe and 24.5 Oe at room temperature to 9.2 Oe and 8.7 Oe at 30 K for the perpendicular and the parallel directions, respectively. Along both directions the linewidth is temperature independent below about 30 K and begin to decrease again below about 12 K down to the lowest temperature. The g-value for the two directions is

temperature independent in the high temperature region and it decreases weakly by lowering the temperature below about 12 K. The increases of the linewidth by lowering the temperature below 20 K which was observed for Θ-phase is suppressed now after tempering the crystal. The decrease of the linewidth by lowering the temperature is again understood by use of the Modified Elliott formula (equation 3.14).

## 5.3 The New Organic Conductor $(BEDT\text{-}TTF)_2(B_{12}H_{12})(CH_2Cl_2)$

The most promising organic conductors are those salts of the form $(BEDT\text{-}TTF)_2X$, therefore it is always interesting to synthesis and study new $(BEDT\text{-}TTF)_2X$ radical salts.

New organic conductors based on the BEDT-TTF donor and $(B_{12}H_{12})^{-2}$ anions were prepared using $CH_2Cl_2$ as a solvent and the standard electrochemical crystallization techniques [173]. The room temperature ESR spectra were measured for several crystals from this salt. The crystals could be classified into three different types of crystals depending on the ESR linewidth at room temperature. The ESR linewidths for the different types are 1.7 Oe, 13 Oe and 45 Oe as shown in Figure 5.18. Each of these three types has a Lorentzian ESR absorption line. The difference in the linewidth is due to different packing motives of the donor-radical cations in their crystal structure (three different phases). The three phases of the organic conductor $(BEDT\text{-}TTF)_x(B_{12}H_{12})_y(CH_2Cl_2)_z$ crystallize simultaneously in the same crystallization process.

The obtained $(BEDT\text{-}TTF)_x(B_{12}H_{12})_y(CH_2Cl_2)_z$ single crystals are plates with nearly rectangular shape; the crystals have dimensions up to $(1.5\times1.5\times0.1)$ $mm^3$. The electrical resistivity parallel to the large crystal surface of several crystals from each phase of $(BEDT\text{-}TTF)_x(B_{12}H_{12})_y(CH_2Cl_2)_z$ was measured. Each of the three phases shows a semiconducting behaviour where the resistivity increases by decreasing the temperature down to the lowest temperature see Figure 5.19.a.

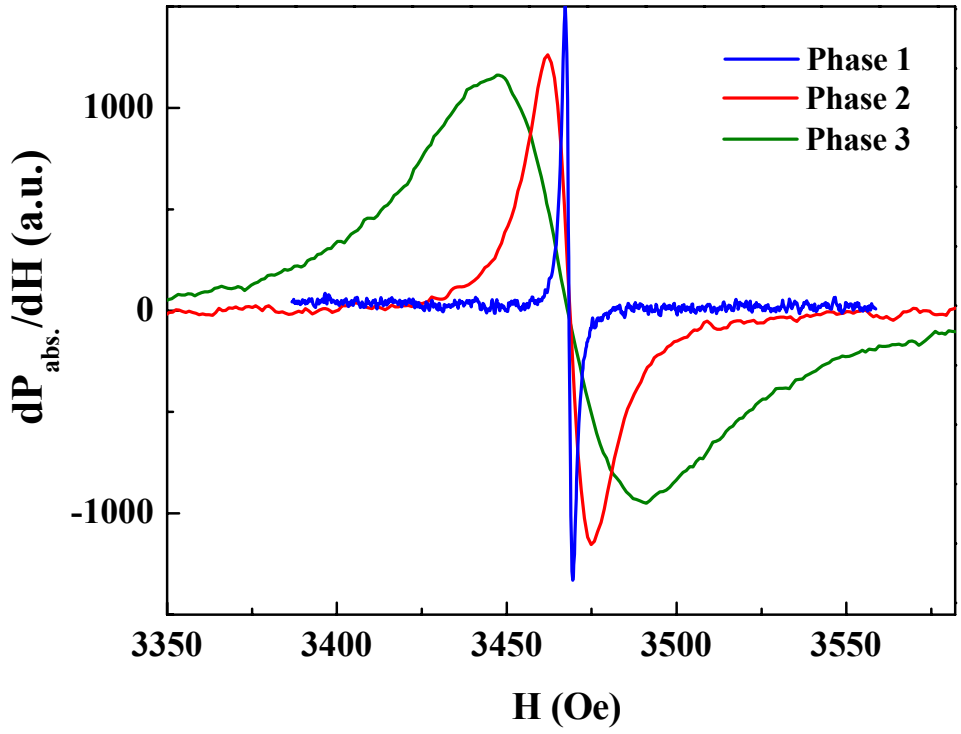


**Figure 5.18: The ESR absorption spectra for the different phase of the organic conductor (BEDT-TTF)$_x$($B_{12}H_{12}$)$_y$($CH_2Cl_2$)$_z$. The peak-to-peak linewidths are 1.7 Oe, 13 Oe and 45 Oe for phase 1, phase 2 and phase 3, respectively.**

The room temperature resistivities of the three phases are tabulated in Table 5.4. These values are small in comparison to the room temperature resistivities of other organic semiconductors which have normally values in the range ($10^2$-$10^5$) $\Omega \cdot cm$ [174]. The activation energies obtained from the linear fit of the logarithm of the conductivity (Ln(σ)) versus the inverse temperature (1/T) (see Figure 5.19.b) are tabulated in Table 5.4. The activation energies of these phases are comparable with the activation energy of other organic semiconductors, where the typical activation energies for organic semiconductors are in the range (0.1- 0.4) eV [174].

| Phase | $\Delta H_{pp}$ (Oe) | $\rho_{rt}$ ($\Omega \cdot cm$) | $E_a$ (ev) |
|---|---|---|---|
| 1 | 1.7 | 40 | 0.14 |
| 2 | 13 | 20 | 0.08 |
| 3 | 45 | 230 | 0.15 |

**Table 5.4: The room temperature peak-to-peak ESR linewidth, the room temperature electrical resistivity and the activation energy of the three different phases of the new organic conductors (BEDT-TTF)$_x$($B_{12}H_{12}$)$_y$($CH_2Cl_2$)$_z$.**

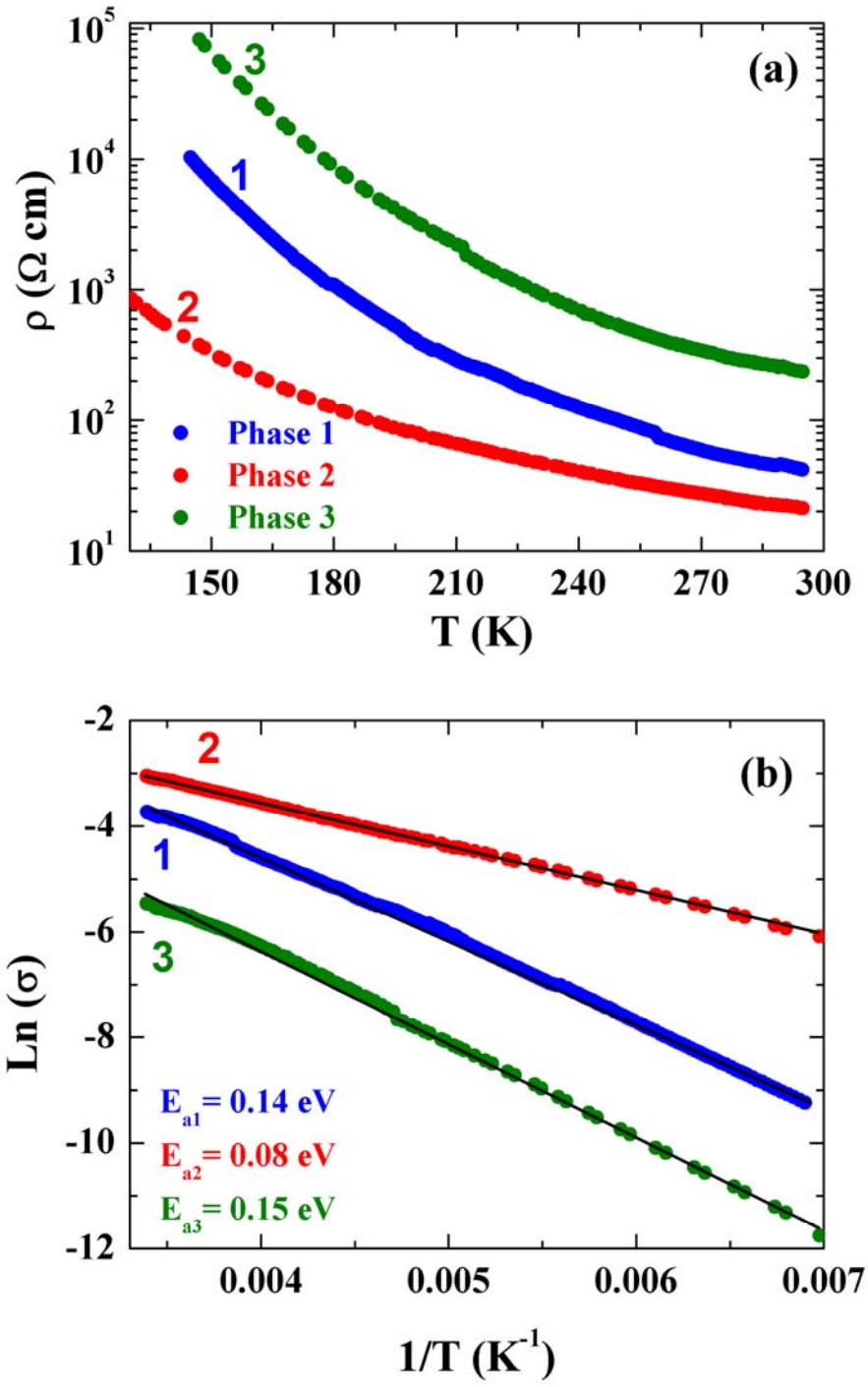


**Figure 5.19: Temperature dependence of the electrical resistivity of the three phases of the new organic conductors $(BEDT\text{-}TTF)_x(B_{12}H_{12})_y(CH_2Cl_2)_z$ parallel to the large crystal surface (a), and the logarithm of the electrical conductivity versus the inverse temperature. The obtained activation energies from the linear fit of Ln(σ) versus 1/T are: 0.14 eV, 0.08 eV and 0.15 eV for phase 1, phase 2 and phase 3, respectively.**

Up to now only the X-ray structure for phase 1 could be solved, giving a stoichiometry of $(BEDT\text{-}TTF)_2(B_{12}H_{12})(CH_2Cl_2)$. The unit cell of phase 1 is triclinic with $P\bar{1}$ symmetry and the lattice constants are: a = 8.296 Å, b = 11.498 Å, c = 12.386 Å, α = 72.73°, β = 85.93°, γ = 82.09°. The crystal structure of this phase is shown in Figure 5.20. The (BEDT-TTF) molecules are stacked along the a-axis which is the highest conductive direction (see Figure 5.20.b). The BEDT-TTF molecules are dimerized along the a-axis. This dimerization has drastic effects on the conductivity of this salt. In absence of the dimerization, the conduction band is expected to be half filled (2 $(BEDT\text{-}TTF)^{+1}$ and $(B_{12}H_{12})^{-2}$). But since the structure is dimerized along the stacking direction a gap opens in the Fermi energy, this gap results in a filled band and an empty band. Therefore an activated behaviour of the resistivity is expected as we have seen in Figure 5.19.a.

The temperature dependent measurements of the ESR linewidth and the g-value of one crystal from phase 1 are shown in Figure 5.21.a and b, respectively. The ESR measurements were performed when the static magnetic field ($B_o$) is applied parallel and perpendicular to the large crystal surface. The spin susceptibility normalized to the room temperature value which is obtained from SQUID measurements for this phase is shown in Figure 5.21.c. The peak-to-peak linewidth at room temperature varies from 1.4 Oe to 1.8 Oe for the parallel and the perpendicular directions, respectively. It increases almost linearly with decreasing the temperature for both directions down to about 25 K. Below 25 K the linewidth increases rapidly by decreasing the temperature for both directions. The g-values at room temperature are 2.0105 and 2.0067 for the perpendicular and the parallel directions, respectively. These values are in agreement with the g-values of (BEDT-TTF) radical salts (see Table 5.1). The g-value is temperature independent along both directions in the entire temperature range. The magnetic susceptibility increases slowly by decreasing the temperature down to about 25 K, below 25 K it increases faster by decreasing the temperature down to the lowest temperature.

The increase of the susceptibility by lowering the temperature is a characteristic property of paramagnetic organic semiconductors as for example $(BEDT\text{-}TTF)_2Ag_{1.6}(SCN)_2$ [175]. The rapid increase of the susceptibility below 25 K, along with the increase of the linewidth at the same temperature, can be due to a strong contribution of paramagnetic impurities [155].

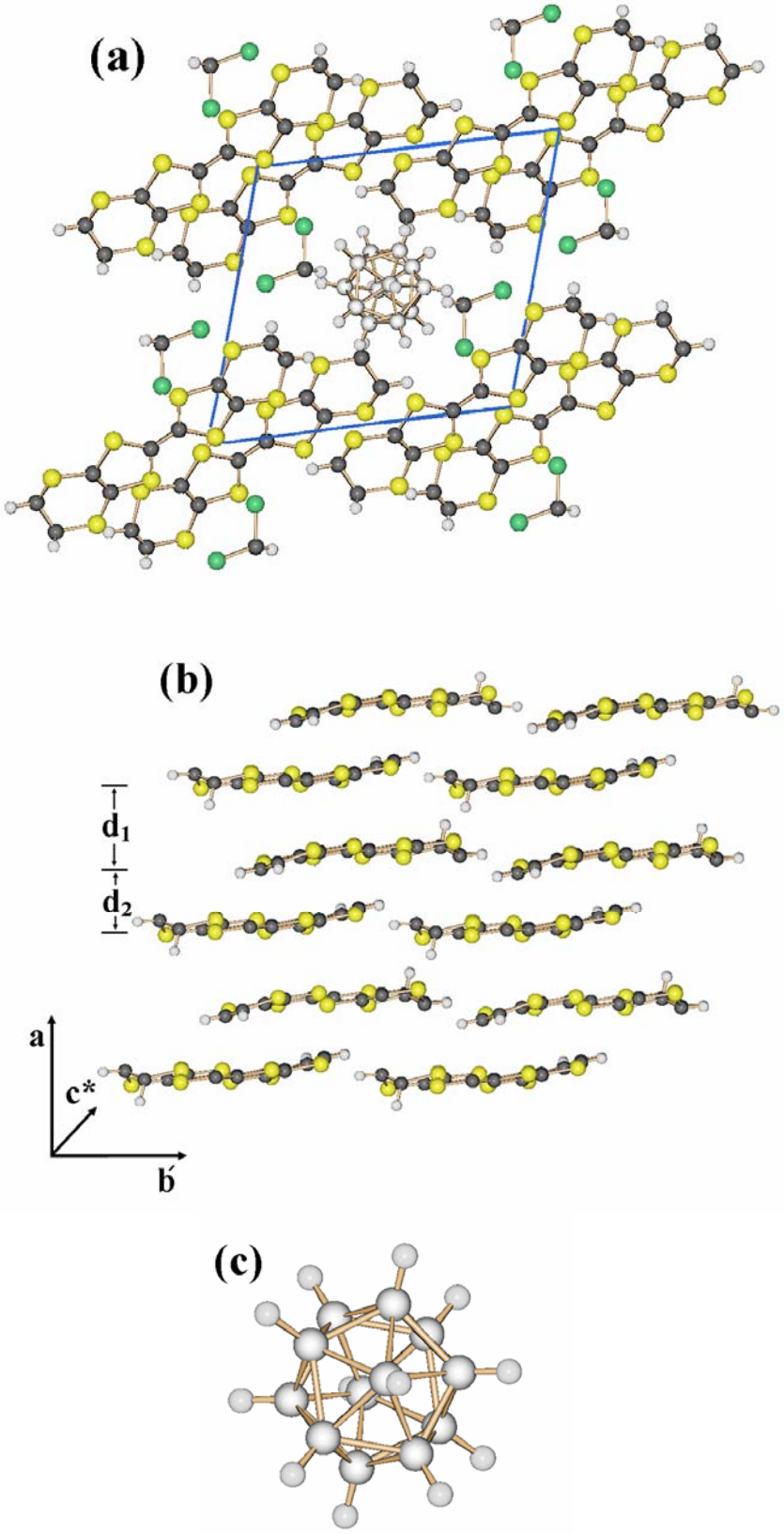


**Figure 5.20: The crystallographic structure of $(BEDT\text{-}TTF)_2(B_{12}H_{12})(CH_2Cl_2)$ (phase 1) (a). The arrangement of the BEDT-TTF molecules along the stacking direction (b), the dimerization along the a-axis can be seen by the difference in the distances $d_1$ and $d_2$ ($d_1>d_2$). (c) The structure of the $(B_{12}H_{12})^{-2}$ anions in $(BEDT\text{-}TTF)_2(B_{12}H_{12})(CH_2Cl_2)$.**

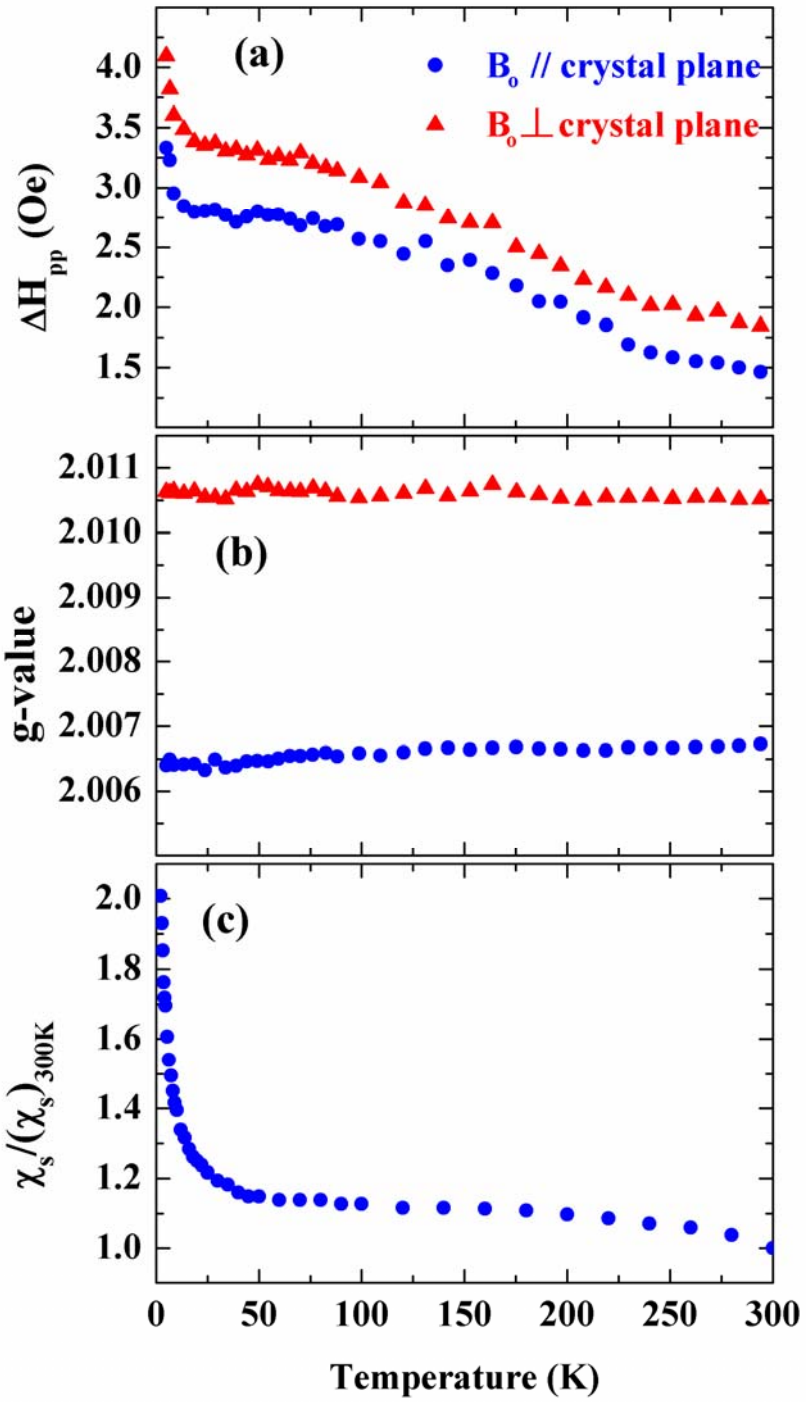


**Figure 5.21: Temperature dependence of (a) the peak-to-peak linewidth (b) the g-value when the magnetic field is applied parallel and perpendicular to the large crystal surface and (c) the spin susceptibility normalized to the room temperature value $\left[\chi_s/(\chi_s)_{300\,K}\right]$ calculated from the SQUID magnetometer measurement along the large crystal surface for $(BEDT\text{-}TTF)_2(B_{12}H_{12})(CH_2Cl_2)$.**

# Chapter 6

# Summary and Outlook

## 6.1 Results

In this work, detailed electron spin resonance and SQUID investigations on single crystals of the organic spin chain compounds $(TMTTF)_2X$ (X = $SbF_6$, $AsF_6$, $BF_4$ and SCN) were performed to explore the spin and the charge ordered states in these materials. Furthermore, the transport and ESR measurements of the neat quasi-two dimensional organic superconductor Θ-$(BEDT\text{-}TTF)_2I_3$, its tempered phase $\Theta_T$-$(BEDT\text{-}TTF)_2I_3$ and the new synthesized organic conductor $(BEDT\text{-}TTF)_2(B_{12}H_{12})(CH_2Cl_2)$ are presented and discussed.

The temperature dependence of the spin susceptibility at constant volume $(\chi_s)_v$ for $T \geq 100\,K$ of the investigated $(TMTTF)_2X$ (X = $SbF_6$, $AsF_6$, $BF_4$ and SCN) salts can be modeled using the EAT (Eggert, Affleck and Takahashi) model for a S = 1/2 antiferromagnetic spin chain. From the fits, the AFM exchange constant $|J|$ for each of the four salts was calculated. The obtained values of $|J|$ are 400 K, 410 K, 430 K and 460 K for $(TMTTF)_2X$ with X=$SbF_6$, $AsF_6$, $BF_4$ and SCN, respectively. The $(\chi_s)_v$ of all compounds investigated deviate from the EAT model below about 100 K, this deviation is due to the two-dimensional character of the TMTTF salts below about 100 K, where the interchain transfer integral in $(TMTTF)_2X$ salts is $t_b \approx 12$ meV ≈ 130 K.

The g-value and the linewidth have a distinct anisotropy for all investigated $(TMTTF)_2X$ salts. In the high temperature region, the largest linewidth and g-value are observed when the static magnetic field $B_o$ is applied parallel to the c*-axis and the smallest linewidth and g-value are observed when it is applied parallel to the a-axis. This means that the g-value and the linewidth have the same anisotropy in this region, $g_{c^*} > g_{b'} > g_a$ and $\Delta H_{c^*} > \Delta H_{b'} > \Delta H_a$. In our investigated salts we observed a linear decrease of the linewidth in the high temperature region (300-180 K). The linewidth along the three directions can be fitted linearly in this region with the highest slope along the c*-axis and the smallest along the a-axis. The extrapolations

of the fits cross at the same negative temperature ($T_o$) which is in the range (-120 to -150) K. The linear decrease of the linewidth with decreasing temperature in this region hints towards a general behaviour in these linear chain compounds. However the physical meaning of the negative temperature ($T_o$) is not understood yet.

The linewidth decreases more slowly for $(TMTTF)_2SbF_6$ and $(TMTTF)_2AsF_6$ and increases by decreasing the temperature for $(TMTTF)_2SCN$ below the charge ordering transition temperature $T_{CO}$. Also the anisotropy of the linewidth changes below $T_{CO}$, where for the salts with centrosymmetrical anions ($SbF_6$ and $AsF_6$) the anisotropy of ΔH below $T_{CO}$ is ($\Delta H_{c^*} > \Delta H_{b'} \approx \Delta H_a$), but in the case of $(TMTTF)_2SCN$ the anisotropy of ΔH below $T_{CO}$ is ($\Delta H_{c^*} \approx \Delta H_{b'} > \Delta H_a$). These observations are attributed to the loss of the inversion symmetry between the TMTTF molecules along the stacking direction below $T_{CO}$. Doubling in the periodicity in the orientation dependence of the linewidth along the ab′-plane is observed in the $(TMTTF)_2SbF_6$ and $(TMTTF)_2AsF_6$ salts in the charge order region. The linewidth have a minimum along the a-axis and the b′-axis and maximum at $45^o$ and $135^o$ between the two axes. The doubling of the periodicity in the orientation pattern can be due to the coexistence of two inequivalent magnetic TMTTF sites in the CO region.

The distinct increase of the ESR linewidth as the temperature approaches the AFM ordering temperature for the salts $(TMTTF)_2SbF_6$ and $(TMTTF)_2SCN$ is attributed to AFM fluctuations. This singularity of ΔH is a signature for the magnetic character of the AFM ordering. In this region the linewidth is proportional to $(T - T_N)^{-(3-d/2)}$ where $d$ is the dimensionality of the AFM fluctuations. The obtained $\mu = 3 - d/2$=1.5 for $(TMTTF)_2SCN$ confirms the three dimensional behaviour of the antiferromagnetic fluctuations. Surprisingly in $(TMTTF)_2SbF_6$ we find μ = 0.5, this difference might be assigned to the different anisotropy in the spin degree of freedom, as well as to different relative magnitudes of the dipole-dipole interaction and spin-orbit coupling. A similar result (μ =0.5) was found in $(TMTSF)_2NO_3$.

The spin Peierls transition in $(TMTTF)_2AsF_6$ ($T_{SP}$ = 13K) and the anion ordering transition in $(TMTTF)_2BF_4$ ($T_{AO}$=41 K) were studied. Below the transition temperature of these spin-singlet ground states, the spin susceptibility decreases rapidly by lowering the temperature down to lowest temperatures. The spin susceptibility in this region for both salts can be described by the Bulaevskii's model for alternating spin chains. By this fit we get for $(TMTTF)_2AsF_6$, the alternation parameter $\gamma = 0.94$, the intradimer AFM exchange constant $|J_1| = 423\,\mathrm{K}$ and the interdimer AFM exchange constant $|J_2| = 397\,\mathrm{K}$. The singlet triplet energy gap in the $T = 0$ limit $\Delta_\sigma(0)$ is given by the relation $\Delta(0) = 0.8615\,|J|\delta^{2/3} = 34.8\,\mathrm{K}$. The

value predicted by the second order perturbation theory for the ratio $\Delta_\sigma(0)/T_{SP}=2.47$ is in good agreement with our results, where we get $\Delta_\sigma(0)/T_{SP}=2.67$. For $(TMTTF)_2BF_4$, we obtained the parameters $\gamma=0.90$, $|J_1|=452.6\,\mathrm{K}$, $|J_2|=407.4\,\mathrm{K}$ and $\Delta_\sigma$ = 52.0 K.

The resistivity of Θ-$(BEDT\text{-}TTF)_2I_3$ crystals show a metallic behaviour from room temperature down to the superconducting transition temperature ($T_c$ = 3.6 K) where the resistivity drops sharply. About 30% of the investigated crystals show the superconducting transition. At high temperatures the spin susceptibility is temperature independent as expected for the Pauli susceptibility of a metal. The superconducting transition was confirmed to be a bulk property by the observation of the shielding signal for the superconducting samples. For the samples which show residual resistivity the susceptibility is temperature independent in the whole temperature range. The anisotropic ratio at room temperature is $\rho_\perp/\rho_\parallel=500$, where $\rho_\perp$ is the resistivity perpendicular to the conduction plane and $\rho_\parallel$ is the resistivity parallel to it. This value indicates strong two-dimensional electronic properties of the crystals. The resistivity ratio $\rho(300\,\mathrm{K})/\rho(4\,\mathrm{K})\approx 500$ parallel to the conduction plane indicates the high quality of the Θ-$(BEDT\text{-}TTF)_2I_3$ crystals.

The ESR linewidth decreases monotonically from 82 Oe and 62 Oe at room temperature when the static magnetic field is applied perpendicular and parallel to the conduction plane, respectively to 9 Oe and 6 Oe at 20 K along the same orientations. Along both orientations the linewidth increases with decreasing temperature below 20 K. The g-value along both directions is temperature independent at high temperatures and decrease with decreasing the temperature below about 20 K.

The tempered crystals ($\Theta_T$-$(BEDT\text{-}TTF)_2I_3$) were obtained by annealing single crystals of Θ-$(BEDT\text{-}TTF)_2I_3$ at 60-70 $^oC$ for two to three hours. By tempering the crystal, the ESR linewidth changes from (81-62) Oe in Θ-phase to (26.7-24.5) Oe in $\Theta_T$-phase depending on the crystal orientation. The X-ray measurements have shown that the packing motive of the BEDT-TTF molecules in Θ and $\Theta_T$-phases is the same. Nevertheless, the $I_3$ anions have fixed positions in the $\Theta_T$-$(BEDT\text{-}TTF)_2I_3$ crystals and are statistically disordered in the Θ-$(BEDT\text{-}TTF)_2I_3$ crystals. This ordering of the $I_3$ anions can be the reason of the abrupt decrease in the linewidth. All $\Theta_T$-$(BEDT\text{-}TTF)_2I_3$ crystals investigated show metallic behaviour down to 4 K where they show a bulk superconducting transition. This means that by tempering Θ-$(BEDT\text{-}TTF)_2I_3$ crystals the superconductivity is observed in all tempered crystals instead of 30% of the crystals in the Θ-phase.

The new organic conductor $(BEDT\text{-}TTF)_x(B_{12}H_{12})_y(CH_2Cl_2)_z$ was prepared using the standard electrochemical crystallization techniques. The obtained single crystals could be classified into three different phases depending on the ESR linewidth at room temperature, where the linewidths for the different phases are 1.7 Oe, 13 Oe and 45 Oe. The electrical resistivity of the three phases show semiconducting behaviour with different activation energies. The activation energies of the three phases are 0.14, 0.08 and 0.15 eV. The X-ray structure for one phase (which has 1.7 Oe ESR linewidth and an activation energy of 0.14 eV) was solved yet giving a stoichiometry of $(BEDT\text{-}TTF)_2(B_{12}H_{12})(CH_2Cl_2)$. The peak-to-peak linewidth at room temperature for this phase varies from 1.4 Oe to 1.8 Oe depending on the crystal orientation. The g-values at room temperature are 2.0105 and 2.0067 for the same orientations. The linewidth increases almost linearly with decreasing the temperature and the g-value is temperature independent from room temperature down to 4.2 K.

## 6.2 Future Work

While our results show the existence of a scattering process in the charge order region which causes doubling of the periodicity in the orientation dependence of the ESR linewidth along the ab′-plane for the $(TMTTF)_2SbF_6$ and $(TMTTF)_2AsF_6$ salts, high frequency ESR measurements in the charge order region of these salts are extremely important to clarify the responsible scattering mechanism of this doubling. By performing higher frequency ESR measurements one gains more resolution in the measured g-value, and can study the effect of the magnetic field on the linewidth thereby the relaxation process in this region can be understood. Performing orientation dependent measurements of the ESR linewidth on other materials which have charge ordering transition would be very helpful. Finally, other experimental investigations on the Θ- and $\Theta_T$-$(BEDT\text{-}TTF)_2I_3$ salts are important to understand the reason behind the absence of superconductivity in some Θ-phase crystals. Also studying the effect of the tempering time on the superconducting transition temperature of $\Theta_T$-$(BEDT\text{-}TTF)_2I_3$ would be very interesting.

# References


[1] P, Monceau, F. Nad and S. Brazovskii, Phys. Rev. Lett. **86**, 4080 (2001).

[2] D. S. Chow, F. Zamborsky, B. Alavi, D. J. Tantillo, A. Baur, C. A. Merlic and S. E. Brown, Phys. Rev. Lett. **85**, 1698 (2000).

[3] W. Yu, F. Zamborszky, B. Alavi, A. Baur, C. A. Merlic and S. E. Brown, J. Phys. IV France **114**, 35 (2004).

[4] F. Nad and P. Monceau, J. Phys. France **12**, Pr9-133 (2002).

[5] F. Nad, P. Monceau. C. Carcel and J. M. Fabre, J. Phys. Cond. Matter 13, L717 (2001).

[6] M. Dumm, B. Salameh, M. Abaker, L. K. Montgomery and M. Dressel J. Phys. IV France **114,** 57 (2004).

[7] J. C. Bonner and M. E. Fisher, Phys. Rev. **135**, A640 (1964).

[8] S. Eggert, I. Affleck and M. Takahashi, Phys. Rev. Lett. **73**, 332 (1994).

[9] F. Zamborszky, W. Yu, W. Raas, S. E. Brown, B. Alavi, C. A. Merlic and A. Baur, Phys. Rev. B. **66**, 81103 (2002).

[10] S. Tomić, J. R. Cooper, W. Kang, D. Jérome, and K. Maki, J. Phys. I **1**, 1603 (1991); P. Baillargeon, C. Bourbonnais, S. Tomić, P. Vaca, and C. Coulon, Synth. Met. **27**, B73 (1988).

[11] L. N. Bulaevskii, Sov. Phys. Solid State **11**, 921 (1969).

[12] E. Orignac and R. Chitra, Phys. Rev. B 70, 214436 (2004).

[13] D. S. Acker, R. J. Harder, W. R. Hertler, W. Mabiler, L. R. Melby, R. E. Benson and W. E. Mochel, J. Am. Chem. Soc. **82**, 6408 (1960).

[14] F. G. Wudl, G. M. Smith and E. J. Hufnagle, Chem. Commun. 1453 (1973).

[15] J. Ferraris, D. O. Cowan, V. J. Waltaka and J. H. Perlstein, J. Am. Chem.. Soc. **95**, 948 (1973).

[16] D. Jérome, A. Mazaud, M. Ribault and K. Bechgaard, J. Phys. Lett. **41**, L95 (1980).

[17] K. Bechghaard, K. Carneiro, M. Olsen and F. B. Rasmussen, Phys. Rev. Lett. **46**, 852 (1981).

[18] T. Ishiguro, K. Yamaji and G. Saito, *Organic Superconductors* ,(Springer-Verlag, Berlin 1998).

[19] K. Petukhov, Ph. D. Thesis, Universität Stuttgart, Stuttgart (2003).

[20] P. Delhaes, C. Coulon, J. Amiell, S. Flandrois, E. Torreilles, J. M. Fabre and L. Giral, Mol. Cryst. Liq. Cryst. **50**, 43 (1979).

[21] K. Bechgaard, C. S. Jacobsen, K. Mortensen, J. H. Pederson and N. Thorup, Solid State Commun. **33**, 1119 (1980).

[22] J. P. Pouget, in *Low-Dimensional Conductors and Superconductors*, ed. by D. Jérome and L. G. Caron, NATO ASI Ser. B, Physics 155, (Plenum Press, New York 1987).

[23] P. Vaca, C. Coulon, S. Ravy, J. P. Pouget and J. M. Fabre, J. Phys. I **1**, 125 (1991).

[24] R. Laversanne, C. Coulon, B. Gallois, J. P. Pouget and R. Moret, J. Phys. Lett. **45,** L393 (1984).

[25] D. Chasseau, J. Gaultier, J. L. Miane, C. Coulon, P. Delhaes, S. Flandrois, J. M. Fabre and L. Giral, J. Phys. Colloq. France **44**, C3-1223 (1983).

[26] B. Liautard, S. Peytavin, G. Brun and M. Maurin, J. Physique **43**, 1453 (1982).

[27] L. Ducasse, M. Abderrabba, J. Hoarau, M. Pesquer, B. Gallois and J. Gaultier, J. Phys. C **19**, 3805 (1986); L. Ducasse, M. Abderrabba, B. Gallois and D. Chasseau, Synth. Met. **19**, 327 (1987).

[28] S. Flandrois, C. Coulon, P. Delhaes, D. Chasseau, C. Hauw and J. Gaultier, Mol. Cryst. Liq. Cryst. **79**, 307 (1982).

[29] T. Granier, B. Gallois, A. Fritsch, L. Ducasse and C. Coulon, *Lower Dimensional Systems and Molecular Electronics* NATO-ASI (Plenu-Press 1989).

[30] B. Liautard, S. Peytavin, G. Brun and M. Maurin, J. Phys. Coll. C3 **44**, 951 (1983).

[31] J. P. Pouget and S. Ravy, J. Phys. I France **6**, 1501 (1996).

[32] J. L. Galigne, B. Liutard, S. Peytavin, G. Brun, M. Maurin, J. M. Fabre, E. Torreilles and L. Giral, Acta. Cryst. B **35**, (1979).

[33] A. Bondi, J. Phys. Chem. **68**, 441 (1964).

[34] B. Korin-Hamzić, E. Tafra, M. Basletić, and Amir Hamzić, G. Untereiner and M. Dressel, Phys. Rev. B **67**, 014513 (2003).

[35] D. Jérome and H. J. Schulz, Adv. Phys. **31**, 299 (1982).

[36] S. Tomic, J. R. Cooper, W. Kang, D. Jérome and K. Maki, J. Phys. I. France **1**, 1603 (1991).

[37] C. Coulon, P. Delhaes, S. Flandrois, R. Langnier, E. Bonjour and J. M. Fabre, J. Physique **43**, 1059 (1982).

[38] M. Dressel, P. Hesse, S. Kirchner, G. Untereiner, M. Dumm, J. Hemberger and L. K. Montgomery, Synth. Metals **120**, 719 (2001).

[39] R. Laversanne, J. Amiell, C. Coulon, C. G. Lagrange and P. Delhaes, Mol. Cryst. Liq. Cryst. **119**, 317 (1985).

[40] R. Bozio, M. Menehgetti and C. Pecille, J. Chem. Phys. **76**, 5785 (1982).

[41] J. P. Pouget, Chem. Scr. **17**, 85 (1981).

[42] K. Penc and F. Mila, Phys. Rev. B **50**, 11429 (1994).

[43] B. Gallois, J. Gaultier, F. Bechtel, A. Filhol, L. Ducasse and M. Abderrabba, Synth. Met. **19**, 321 (1987).

[44] M. Dressel, O. Klein and S. Donovan, Int. J. Infrared and Millimeter Waves **14**, 2489 (1993).

[45] P. Wzietek, F. Creuzet, C. Bourbonnais, D. Jérome, K. Bechgaard and P. Batail, J. Phys. I (France) **3**, 171 (1993).

[46] B. Gallois, J. Gaultier, C. Hauw, D. Chasseau, A. Meresse, A. Filhol and K. Bechgaard, Mol. Cryst. Liq. Cryst. **119**, 225 (1985); B. Gallois, J. Gaultier, F. Bechtel, A. Filhol, L. Ducasse and M. Abderrabba, Synth. Met. **19**, 321 (1987).

[47] C. Bourbonnais J. Phys. I (France) **3**, 143 (1993).

[48] M. Dumm, Ph. D. Thesis, Universität Augsburg, Augsburg (1999).

[49] For review, D. Jérome, Science **252**, 1509 (1991).

[50] J. Moser, M Gabay, P. Auban-Senzier, D. Jérome, K. Bechgaard and J. M. Fabre, Eur. Phys. J. B **1**, 39 (1998).

[51] W. Yu, F. Zhang, F. Zamborszky, B. Alavi, A. Baur, C. A. Merlic and S. E. Brown, Phys. Rev. B **70**, 121101 (2004).

[52] F. Creuzet, Mol. Cryst. Liq. Cryst. **119**, 289 (1985).

[53] D. Jaccard, H. Wilhelm, D. Jérome, J. Moser, C. Carcel and J. M. Fabre, J. Phys. Cond. Matt. **13**, L89 (2001).

[54] W. A. Little, Phys. Rev. A**134**, 1416 (1964).

[55] M. Mizuno, A. F. Garito and M. P. Gava, J. Chem. Soc. Chem. Comm., **18** (1978).

[56] N. Sato, G. Saito and H. Inkuchi, Chem. phys. **76**, 79 (1983).

[57] L. N. Bulaevskii, Adv. Phys. **37**,43 (1988).

[58] J. R. Cooper, L. Forró, B. Korin-Hamzic, M. Miljak and D. Schweitzer, J. Phys. France **50**, 2741 (1989).

[59] J. R. Cooper, L. Forró, B. Korin-Hamzic, K. Bechgaard and A. Moradpour, Phys. Rev. B **33**, 6810 (1986).

[60] J. R. Cooper, D. Jérome, S. Etemad, and E. M. Engler, Soild State Commun. **22**, 257 (177).

[61] I. Hennig, K. Bender, D. Schweitzer, K. Dietz, H. Enders, H. J. Keller, A. Gleiz and H. W. Helberg, Mol. Cryst. Liq. Cryst. **119**, 37 (1985).

[62] D. Schweitzer, E. Gogu, I. Hennig and T. Klutz, Phys. Chem. **91**, 890 (1987).

[63] E. B. Yagubskii, I. F. Shchegolev, V. N. Laukhin, P. A. Kononovich, M. V. Kartsovnic, A. V. Zvarykina, and L. I. Bubarvo, JETP Lett. **39**, 12 (1984).

[64] F. Creuzet, D. Jérome, D. Schweitzer and H. J. Keller, Europhys. Lett. **1**, 461 (1986).

[65] F. Creuzet, C. Bourbonnais, D. Jérome, D. Schweitzer and H. J. Keller, Europhys. Lett. **1**, 461 (1986).

[66] E. Balthes, A. Breining, S. Kahlich, J. Moldenhauer, D. Schweitzer, P. Bele, H. Brunner, I. Heinen, B. Nuber and H. J. Keller, Synth. Met. **56**, 2859 (1993).

[67] A. Kobayashi, R. Kato, H. Kobayashi, Sh. Moriyama, Y. Nishio, K. Kajita, and W. Sasaki, Chem. Lett. 2017 (1986).

[68] K. Kajita, Y. Nishio, S. Moriyama, W. Sasaki, R. Kato, H. Kobayashi and A. Kobayashi, Solid State Commun. **64**, 1279 (1987).

[69] K. Bender, I. Hennig, D. Schweitzer, K. Dietz, H. Endres and H. J. Keller, Mol. Cryst. Liq. Cryst. **108,** 359 (1984).

[70] A. Kobayashi, R. Kato, H. Kobayashi, S. Moriyama, Y. Nashio, K. Kajita and W. Sasaki, Chem. Lett. 459 (1987).

[71] H. Kobayashi, R. Kato, A. Kobayashi, Y. Nishio, K. Kajita and W. Sasaki, Chem. Lett. 789 **(**1986**)**.

[72] K. Kajita, Y. Nishio, T. Takahashi, W. Sasaki, R. Kato, H. Kobayashi and A. Kobayashi, Solid State Commun. **70**, 1181 (1989).

[73] D. Jérome, in *Organic Conductors*, ed. by J. P. Farges, (Marcel Dekker, New York, 1994).

[74] N. F. Mott, Proc. Phys. Soc. Lond. **62**, 416 (1949).

[75] N. F. Mott, Phil. Mag. **6**, 287 (1961).

[76] J. Hubbard, Proc. Roy. Soc. **A277**, 383 (1964).

[77] M. Pope and C. Swenberg, *Electronic Processes in Organic Crystals and Polymers*, (New York Oxford University Press, 1999).

[78] J. P. Ranard, in *Magnetic Phase Transitions in Low-Dimensional systems*, ed. by P. Delhaes and M. Drllon, (NATO ASI Series, Vol. 168, 1987).

[79] W. E. Estes, D. Gavel, W. E. Hatfield and D. Hodgson, Inorg. Chem. **17**, 1415 (1978).

[80] C. Bourbonnais and B. Dumoulin, J. Phys. I (France) **6**, 1727 (1996).

[81] J. P. Pouget, R. Moret, R. Comes and K. Bechgaard, J. Phys. Lett. France **42**, L543 (1981).

[82] S. S. P. Parkin., J. J. Mayerle and E. M. Engler, J. Phys. France Colloq. **44,** C3-1105 (1983).

[83] S. Ravy, R. Moret, J. P. Pouget and R. Comes, Synth. Met. **13**, 63 (1986).

[84] R. Moret, J. P. Pouget, R. Comes and K. Bechgaard, J. Phys. Colloq. France **44**, C3-957 (1983).

[85] J. P. Pouget, R. Moret, R. Comes, K. Bechgaard, J. M. Fabre and L. Giral, Mol. Cryst. Liq. Cryst. **79,** 129 (1982).

[86] C. Coulon, A. Maaroufi, J. Amiell, E. Duppart, S. Flandrois, P. Delhaes, R. Moret, J. P. Pouget and J. P. Morand, Phys. Rev. B **26**, 6322 (1982).

[87] S. S. P. Parkin, C. Coulon and D. Jérome, J. Phys. C **16**, L209 (1983).

[88] J. Moldenhauer, Ch. Horn, K. I. Pokhodnia and D. Schweitzer, Synthetic Metals, **60** 31 (1993).

[89] K. Hiraki and K. Kanoda, Phys. Rev. Lett. **80**, 4737 (1998).

[90] H. Seo and H. Fukuyama, J. Phys. Soc. Jpn. **66**, 1249 (1997).

[91] H. Yoshioka, M. Tsuchiizu and Y. Suzumura, J. Phys. Soc. Jpn. 69, 651 (2000).

[92] G. Grüner, Rev. Mod. Phys. **66**, 1 (1994).

[93] K. Mortensen, Y. Tomkiewicz and K. Bechgaard, Phys. Rev. B **25**, 3319 (1982).

[94] A. Graja, *Low-Dimensional Organic Conductors*, (World Scientific Publishing Co. Singapore, 1992)

[95] M. Weger, M. Tittelbach, E. Balthes, D. Schweitzer and H. J. Keller, J. Phys. Cond. Matt. **5**, 8569 (1993).

[96] J. Bardeen, L. N. Cooper and J. R. Schriffer, Phys. Rev. **106**, 162 (1957).

[97] J. Bardeen, L. N. Cooper and J. R. Schriffer, Phys. Rev. **108**, 1175 (1957).

[98] J. Wosnitza " in *Superconductivity in Low-Dimensional Organic Metals*" ed. by A. V. Narlikar (Nova Science Publishers, Inc.) **34**, 97 (2000).

[99] C. P. Poole, *Electron Spin Resonance*, 2nd edition (Dover Publications, INC. Mineola, 1996).

[100] J. E. Wertz and J. R. Bolton , *Electron Paramagnetic Resonance*, (Chapman and Hall, New York, 1986).

[101] F. Bloch, Phys. Rev. **70**, 460 (1946).

[102] J. Dyson, Phys. Rev. **98**, 349 (1955).

[103] G. Feher and A. F. Kip, *Electron Spin Resonance Absorption in Metals*. I. Experimental, **98 (2)**, 337 (1955).

[104] R. Kubo and K. Tomta, J. Phys. Soc. Japan **9**, 888 (1954).

[105] B. Pilawa, J. Phys. Cond. Matt. **9**, 3779 (1997).

[106] R. Elliot, Phys. Rev. **96**, 266 (1954).

[107] Y. Tomkiewicz, A. R. Taranko and E. M. Engler, Phys. Rev. Lett. **37**, 1705 (1976).

[108] A. N. Bloch, T. F. Caruthers, T. O. Poehler and D. O. Cowan, *Chemistry and Physics of one dimensional metals*, (Plenum, New York, 1977).

[109] M. Weger, J. Phys. (France) Coll. **C6**, 1456 (1978); S. Shitzkovsky, M. Weger, and H. Gutfreund, J. Phys. (Paris) **39**,711 (1978).

[110] D. H. McMahon, Phys. Rev. **134A**, 128 (1964).

[111] J. H. Pifer and R. Magno, Phys. Rev. B **3**, 663, (1971).

[112] R. S. Drago, *Physical Methods in Chemistry*, (W. B. Saunders Co., Philadelphia, 1977).

[113] C. Coulon and R. Clérac, Chemical Reviews **104**, 5655 (2004).

[114] C. P. Slichter, *principle of Magnetic Resonance*, Springer Series in Solid-State Science 1, (Springer-Verlag, Berlin, 1996).

[115] C. Kittel, *Introduction to Solid State Physics*, (Wiley and Sons, New York, 1996).

[116] C. Coulon and R. Laversanne, *Low-Dimensional Conductors and Superconductors*, NATO-ASI Series B, Physics, Vol. **155** (D. Jérome and L. G. Caron, eds.), (Plenum Press, New York, 1987).

[117] T. Nagaminya, Adv. Phys. **4:1** (1954).

[118] J. B. Ketterson and S. N. Song, *Superconductivity*, (Cambridge University Press, Cambridge, 1999).

[119] L. B. Coleman, J. A. Cohen, A. F. Garito and A. J. Heeger, Phys. Rev. B **7**, 2122 (1973).

[120] M. Dumm, A. Loidl, B. W. Fravel, K. P. Starkey, M. Montgomery and M. Dressel, Phys. Rev. B **61**, 511 (2000).

[121] M. Dumm, A. Loidl, B. W. Fravel, K. P Starkey, M. Montgomery and M. Dressel, Phys. Rev. B **62**, 6512 (2000).

[122] L. Ferró, J. R. Cooper, G. Sekretarczyk, M. Krupski and K. Kamarás, J. Physique **48**, 413 (1987).

[123] C. Coulon, J. Phys. Coll. **C3**, 885 (1983).

[124] C. Coulon, J. C. Scott and R. Laversanne, Mol. Cryst. Liq. Cryst. **119**, 307 (1985).

[125] C. Coulon, J. C. Scott and R. Laversanne, Phys. Rev. B **33**, 6235 (1986).

[126] J. Pflaum (3.Physikalisches Institut-Universität Stuttgart), private communications.

[127] M. E. Lin, J. Phys. Chem. Solids **31**, 101 (1970).

[128] M. Dumm, M. Dressel, A. Loidl, B. W. Fravel and L. K. Montgomery, Phyica B. **259-261**, 1005 (1999).

[129] M. Dumm, M. Dressel, A. Loidl, B. W. Fravel K. P. Starkey and L. K. Montgomery, Synth. Met. **103**, 2071 (1999).

[130] F. J. Adrian, Phys. Rev. B. **33**, 1537 (1986)

[131] F. J. Adrian, Phys. Rev. B. **26**, 2682 (1982).

[132] C. E. Moore, Atomic Enrergy Levels (US. GPO, Washington, D. C., 1971), Vol. **I** and **II**.

[133] N. Thorup, G. Rindorf and H. Soling, Acta Cryst. B **37**, 1236 (1981).

[134] J. C. Lasjaunias, P. Monceau, D. Starešinić, K. Biljakowić and J. M. Fabre, J. Phys. I (France) **7**, 1417 (1997).

[135] J. C. Lasjaunias, K. Biljakowić, P. Monceau and K. Bechgaard, Solid State Commun. **84**, 297 (1992).

[136] P. Garoche, R. Brusetti, D. Jérome and K. Bechgaard, J. Phys. Lett.(France) **43**, L147 (1982).

[137] C. Coulon, S. S. Parkin and R. Laversanne, Phys. Rev. B **31**, 3583 (1985).

[138] H. H. Javadi, R. Laversanne and A. J. Epstein, Phys. Rev. B **37**, 4280 (1988).

[139] S. Ravy, P. Foury-Leylekian, D. Le Bolloch and J. P. Pouget, J. Phys. IV **83**, 114 (2004).

[140] Y. Nogami and T. Nakamura, J. Phys. IV **9**, 12 (2002).

[141] M. Meneghetti, R. Bozio, I. Zanon, C. Pecile, C. Ricotta and M. Zanetti, J. Chem. Phys. **80,** 6210 (1984).

[142] Sh. Fujiyama and T. Nakamura, Phys. Rev. B. **70**, 45102 (2004).

[143] F. Nad, P. Monceau. C. Carcel and J. M. Fabre, J. Phys. Cond. Matter **12**, L435 (2000).

[144] S. E. Brown not published results "Private communications".

[145] T. Nakamura, J. Phys. Soc. Jpn. **72**, 213 (2003).

[146] A. Carrington and A. D. McLachlan, *Introduction to Magnetic Resonance*; (Andrew D. McLachlan. - New York : Harper & Row, 1967; p 204).

[147] M. Heinrich, H. A. Krug von Nidda, A. Krimmel, A. Loidl, R. M. Eremina, A. D. Ineev, B. I. Kochelaev, A. V. Prokofiev, and W. Assmus, Phys. Rev. B. **67**, 224418 (2003).

[148] C. Bourbonnais, in *Interacting Electrons in Reduced Dimensions*, D. Baeriswyl and D. K. Campdell (eds), NATO ASI Ser. B, *Physics* **213** (Plenum Press, New York 1989), P. 227.

[149] B. Liautard, S. Peytavin, G. Brun and P. Bernier, J. Phys. Coll. C3 **44**, 1087 (1983).

[150] C. Coulon, J. C. Scott and R. Laversanne, Phys. Rev. B **33**, 6235 (1986).

[151] E. Pytte, Phys. Rev. B **10**, 4637 (1974).

[152] R. Kato, H. Kobayashi, A. Kobayashi, Y. Nishio, K. Kajita and W. Sasaki, Chem. Lett. 957 (1986).

[153] M. Tamura, H. Tajima, H. Kuroda and M. Tokumoto: J. Phys. Soc. Jpn. **59** (1990), 1753.

[154] H. Wang, B. Vogt, U. Geiser, M. Beno, K. Carlson, S. Kleinjan, N. Thorup and J. Williams, Mol. Cryst. Liq. Cryst. **181,** 135 (1990).

[155] B. Rothaemel, L. Forró, J. R. Cooper, J. S. Schilling, M. Weger, P. Bele, H. Brunner, D. Schweitzer and H. K. Keller, Phys. Rev. B **34**, 704 (1986); For Pascal's constants used here, see J. Lewis and P. G. Wilkins editors "*Modern Coordination Chemistry*" (Interscience, New York, 1960), p. 417.

[156] S. Koltz, J. S. Schilling, S. Gärtner and D. Schweitzer, Solid State Comm. **67**, 981 (1988).

[157] E. Baltes, Ph. D. Thesis, Universität Stuttgart, Stuttgart (1997).

[158] S. Kahlich, D. Schweitzer and H. J. Keller, Solid State Commun. **76**, 933 (1990).

[159] J. R. Cooper, D. Jérome, M. Weger and S. Etemad, J. Phys. Lett. **36**, L219 (1975).

[160] T. Sugano, G. Saito and M. Kinoshita, Phys. Rev. B **34,** 117(1986).

[161] R. Laversanne, J. Amiell, P. Delhaés, D. Chasseau and C. Hauw, Solid state comm. **52**, 177 (1984).

[162] P. Bele, H. Brunner, I. Heinen and D. Schweitzer, Appl. Magn. Reson. **17**, 481 (1999).

[163] L. Forró, G. Sekretarczyk, M. Krupski, D. Schweitzer and H. J. Keller, Phys. Rev. B **35**, 2501 (1987).

[164] J. Williams, J. R. Ferraro, R. J. Thorn, K. D. Carlson, U. Geiser, H. Wang, A. M. Kini and M. W. Whangbo, *Organic Superconductors*, (Prentice Hall, New Jersey 1992).

[165] H. Wang, L. Montogomery, A. Kini, K. Carlson, M. Beno, U. Geiser, C. Cariss and J. Williams, Physica C **156**, 173 (1988).

[166] G. O. Baram, L. I. Buravov, L. S. Degtyarev, M. É. Kozlov, V. N. Laukhin, E. É, Laukhina, V. G. Onishchcnko, K. I. Pokhodnya, M. K. Sheinkman, R. P. Shibaeva and E. B. Yagubskii, JETP Lett (Engl. Transl.) **44**, 376 (1986).

[167] D. Schweitzer, P. Bele, H. Brunner, E. Gogu, U. Haeberlen, I. Hennig, I. Klutz, R. Swietlik and R. Keller, H. J. Z. Phys. B**. 67**, 489(1987).

[168] S. Kahlich, S. Gärtner, D. Schweitzer and H. J. Keller, Synth. Mett. **41**, 2019 (1991).

[169] I. Hennig, U. Haeberlen, I. Heinen, D. Schweitzer and R. Keller, Physica C **153**, 493 (1988).

[170] J. Strempfer Max Planck Institute for Solid State Research-Stuttgart.

[171] A. Nothardt, Ph. D. Thesis, Universität Stuttgart, Stuttgart (2005).

[172] H. Veith, C. P. Heidmann, F. Gross, A. Lerf, K. Andres and D. Schweitzer, Solid State Comm. **56**, 1015 (1985).

[173] This salt was synthesized in cooperation with the group of Prof. Th. Schleid by C. Schneck.

[174] A. Graja, *Low-Dimensional Organic Conductors*, (World Scientific Publishing Co. Singapore, 1992).

[175] U. Geiser, M. Beno, A. Kini, H. Wang, A. Schultz, B. Gates, C. Gariss, K. Carlson and J. Williams, Synth. Met. **27**, A235 (1988).

# Curriculum Vita

| | |
|---|---|
| March 26, 1975 | Born in Al Baq'ah, Jordan |
| 1980-1992 | Elementary and secondary schools study -Jordan |
| July1992 | General Secondary Education Certificate Examination - Jordan |
| 1992-1996 | Student of physics at Yarmouk University- Jordan |
| June 1996 | Bachelor degree in Physics |
| 1996-1999 | Graduate student of physics at the University of Jordan- Jordan |
| June 1999 | Master of Science, thesis: "Study of the Thermal Conductivity of Polymeric Materials", Advisor: Prof. A. Zihlif. |
| 1999-2001 | Teaching assistant (the Teachers College at Dammam - Saudi Arabia) |
| 2001-2002 | Graduate student of physics at Universität Stuttgart |
| Since January 2002 | A member of the graduate college "Modern methods of magnetic resonance in materials science" of the Faculties of Physics and Chemistry, Universität Stuttgart |
| June 2002 | Master of Science, thesis: "Temperature and Pressure Dependence Investigations of the Resistivity of Organic Conductors", Advisor: Prof. M. Dressel. |
| Since July 2002 | PhD student at the 1. Physikalisches Institut and the 3. Physikalisches Institut, Universität Stuttgart |

# List of Publications

M. Dressel, K.Petukhov, B. Salameh, P. Zornoza and T.Giamarchi.
”Scaling Behavior of the Longitudinal and Transverse Transport in Quasi One-Dimensional Organic Conductors”
*Phys. Rev. B 71, 075104 (2005).*

A. Nothardt, E. Balthes, B. Salameh, W. Schmidt, D. Schweitzer, J. Strempfer, B. Keimer, D. Maude.
”Quantum Oscillation Measurements on the Organic Superconductor $\Theta$-$(BEDT\text{-}TTF)_2I_3$”
*Materials Science-Pol. 22, 299 (2004).*

M. Dumm, B. Salameh, M. Abaker, M. Montgomery, and M. Dressel.
”Magnetic and Optical Studies of Spin and Charge Ordering in $(TMTTF)_2AsF_6$”
*J. Phys. IV France 114, 57 (2004).*

M. Dressel, N. Drichko, B. Salameh, J. Thoms, J. Schlueter, and J. Merino
”Charge ordering and superconductivity in alpha-$(BEDT\text{-}TTF)_2MHg(SCN)_4$”
*J. Phys. IV France 12, 57 (2002).*

J. A. Schlueter, U. Geiser, M. A. Whited, N. Drichko, B. Salameh, K. Petukhov and M. Dressel.
”Structural and Spectroscopic Studies of $\alpha$-$\kappa$-$(BEDT\text{-}TF)_2Hg(SCN)_3$”
*Submitted to "Chemistry of Materials".*

# Acknowledgements

First of all I would like to express my deepest gratitude to my supervisors Prof. Dieter Schweitzer and Prof. Martin Dressel, not only for giving me the opportunity to perform this project in their groups, but also for their support, encouragement and guidance during my PhD study.
I cannot express enough thanks to my advisor Dr. Michael Dumm without whom, this thesis would have not been accomplished. I acknowledge his, assistance, many fruitful discussions, suggestions, brilliant ideas, comments and proofreading of this thesis.
The single crystals of the TMTTF salts were grown in the 1. Physikalisches Institut by Gabriele Untereiner, to whom I am very grateful. Her contribution in this work is hard to be estimated.
I would like to thank the Graduate College of the Magnetic Resonance, Universität Stuttgart for the educational and financial support during this project.
I express my thanks to: Prof. Michael Mehring, Prof. Gert Denninger, Dr. J. U. von Schütz, Dr. Jürgen Rahmer and Dr. Stephan Mair for their collaborations and discussions.
Furthermore I thank all of my colleagues at Prof. Dressel's and Prof. Schweitzer's groups especially my intimate friends Axel Nothardt and Wolfgang Schmidt for their assistance especially in the first steps of this project and for their kind friendship in the laboratory.
The software program "meascom" which was used for the spectra fitting in this project was provided by T. Kurz and Dr. H. A. Krug von Nidda from the Institut für Experimental Physik V of the Universität Augsburg. I am very thankful for them.
The technical support and help of the low temperature work shop headed by Jürgen Maurer and of the glass work shop is greatly appreciated.
Finally, I am forever indebted to my parents and my family for their understanding, endless patience and encouragement when it was most required. I am very grateful for their support.